Terms and Conditions of Use of Digitised Theses from Trinity College Library Dublin

Copyright statement

All material supplied by Trinity College Library is protected by copyright (under the Copyright and Related Rights Act, 2000 as amended) and other relevant Intellectual Property Rights. By accessing and using a Digitised Thesis from Trinity College Library you acknowledge that all Intellectual Property Rights in any Works supplied are the sole and exclusive property of the copyright and/or other IPR holder. Specific copyright holders may not be explicitly identified. Use of materials from other sources within a thesis should not be construed as a claim over them.

A non-exclusive, non-transferable licence is hereby granted to those using or reproducing, in whole or in part, the material for valid purposes, providing the copyright owners are acknowledged using the normal conventions. Where specific permission to use material is required, this is identified and such permission must be sought from the copyright holder or agency cited.

Liability statement

By using a Digitised Thesis, I accept that Trinity College Dublin bears no legal responsibility for the accuracy, legality or comprehensiveness of materials contained within the thesis, and that Trinity College Dublin accepts no liability for indirect, consequential, or incidental, damages or losses arising from use of the thesis for whatever reason. Information located in a thesis may be subject to specific use constraints, details of which may not be explicitly described. It is the responsibility of potential and actual users to be aware of such constraints and to abide by them. By making use of material from a digitised thesis, you accept these copyright and disclaimer provisions. Where it is brought to the attention of Trinity College Library that there may be a breach of copyright or other restraint, it is the policy to withdraw or take down access to a thesis while the issue is being resolved.

Access Agreement

By using a Digitised Thesis from Trinity College Library you are bound by the following Terms & Conditions. Please read them carefully.

I have read and I understand the following statement: All material supplied via a Digitised Thesis from Trinity College Library is protected by copyright and other intellectual property rights, and duplication or sale of all or part of any of a thesis is not permitted, except that material may be duplicated by you for your research use or for educational purposes in electronic or print form providing the copyright owners are acknowledged using the normal conventions. You must obtain permission for any other use. Electronic or print copies may not be offered, whether for sale or otherwise to anyone. This copy has been supplied on the understanding that it is copyright material and that no quotation from the thesis may be published without proper acknowledgement.

Ruthenium(II) Metal Complexes for Photodynamic Therapy(PDT) or as Imaging Agents

Thesis submitted for the

Degree of Doctor of Philosophy

Marialuisa Erby

Supervisor Prof. DC Williams

School of Biochemistry and Immunology

Trinity College

Dublin

Ireland

September 2013

Declaration

This thesis has not been submitted as an exercise for a degree at this or any other University.

The work herein is entirely my own work with the exception of:

- Structures and UV/visible, excitation and emission spectra of the compounds performed by Robert B. P. Elmes;
- Sub-cellular localisation of RE37 with mitochondria, lysosome and ER shown in figure 3.47 performed by Suzanne Cloonan;
- TEM of RE37 shown in figure 3.48 performed by Suzanne Cloonan;
- Mitochondrial membrane potential studies using the radioactivity protocol shown in figure 3.49 performed by Suzanne Cloonan for compound RE37 and by Sandra Bright for RE34;
- Temperature dependent uptake studies and investigation in the involvement of the microtubule network in the transport of RE37 to the nucleus using microtubule inhibitors shown in figure 3.50 performed by Suzanne Cloonan;
- Comet assay of RE34 and 37 shown in figure 3.51 performed by Sandra Bright

I agree that the Library may lend or copy the thesis upon request.

Abstract

Photodynamic therapy (PDT) represents a new localised method of treatment in cancer. The therapeutic effect is mediated by the generation of reactive oxygen species (ROS) and/or the formation of singlet oxygen ($^1O_2$), a process that depends on the photosensitizing agent's interactions with light and oxygen. The photophysical and DNA binding properties of a cationic water-soluble organic derivate of dppz, has previously been reported and its suitability for PDT has been suggested.

In the first part of this study, the organic pdppz derivative, RE33, was investigated as a DNA probe and photocleavage agent potentially suitable in PDT. Localisation studies in HeLa cells using confocal microscopy showed uptake but the lack of intense luminescence when inside the cells, suggested RE33 to be unsuitable as a molecular probe. Moreover, flow cytometry analysis showed RE33 to be toxic to the cells with little difference in cell toxicity upon photoirradiation if incubated at high concentrationa and at long time points suggesting RE33 to be also unsuitable as a PDT agent.

In the last few decades, coordination complexes based on metal centres, in particular Ru(II) centres, and polypyridyl ligands have been developed as DNA binding agents. In this regard, it was thought beneficial to add a ruthenium (Ru(II)) centre to the structure of RE33 to produce Ru(II) polypyridyl complexes. Three compounds based on a novel extended, aromatic, polypyridyl ligand, RE30, 34, 37, were investigated as candidates for potential cancer therapeutics as well as spectroscopic DNA probes.

Among these compounds only RE37 induced light dependent cell death at a low concentration with little toxicity when not illuminated. Most of the subsequent experiments were set up with this compound. Localisation studies in HeLa cells using confocal microscopy showed the uptake of RE37 into cells within 4h. FACS analysis demonstrated RE37 to induce apoptosis in HeLa cells in a light-dependent manner and in a caspase-dependent manner. However, caspase-3 did not appear to be involved in the apoptotic process. Moreover, cell death was related to ROS production. Co-localisation studies of RE37 in HeLa cells showed the compound localised in the mitochondria, which became clustered with a peri-nuclear localisation. This relocation of mitochondria with RE37 is not microtubule dependent. Furthermore, it was shown that RE37 decreased the mitochondrial membrane potential within 4h of treatment. These results are constant with a process called mitophagy where gross insult of the mitochondria results in Ru(II) loaded mitochondrial peri-nuclear clustering.

RE37 thus shows potential to be a good candidate for PDT. On the other hand, compounds RE30 and 34 presented properties potentially suitable for a fluorescence imaging application because they were rapidly taken up into the cells and they were also non-toxic to the cells with no phototoxicity.

Continuing in the search for DNA-binding compounds which can be used as molecular probes or as photosensitizers in PDT it was thought to investigate two bis-Ru(II) compounds based on bis-1,8-naphthalamide derived Tröger's bases, RE84 and 85, whose structure allows tight binding to DNA. In HeLa cells, localisation studies using confocal microscopy showed that RE84 and 85 were taken up inside the cells within 2h and a reduction in cell viability was shown at low concentrations in a light-dependent manner. It has been shown using different techniques that compounds RE84 and 85 are localized to the mitochondria which became localised to the edge of the nucleus. They rapidly and extensively reduced the mitochondrial membrane potential without illumination and, spinning disk studies showed that the compounds led the mitochondria to undergo fission after light exposure in a short time. Moreover, isolation of mitochondrial and nuclear fractions of HeLa cells after compound treatment showed localization of the compounds in the mitochondria. Compounds RE84 and 85 induced DNA damage as shown with the Comet assay, which is likely to be an indirect effect of the ROS and/or $^1O_2$ production and diffusion from mitochondria to DNA. Confocal images also showed light dependent damaged-tubulin, but not actin filaments, around the nucleus suggesting that it may contribute to mitochondrial clustering around the nucleus which may also contribute to PDT-induced cell death. Investigation on the mechanism of cell death showed RE84 and 85 to induce apoptosis which is implicated in examples of phototoxicity which implies that mitochondrial photodamage can directly initiate apoptosis resulting in DNA and cellular fragmentation with these fragments engulfed by adjoining cells without necrotic effects. Furthermore, it has been shown that by changing the concentration of the RE84 and by changing the laser used to illuminate the cells, results changed in terms of mechanism of cell death and mitochondrial damage probably through dysfunction of the mitochondrial transition pores or/and dysfunction of the ROS generation and detoxification which lead to 'oxidative stress'. All the above, make RE84 and 85 potentially good candidates for PDT because there was little toxicity in cells when not illuminated and because of the big difference in cell toxicity upon photoirradiation at low concentrations.

Acknowledgements

First and foremost, I would like to thank my supervisor Dr. Clive Williams for giving me the opportunity to do my PhD in his group, for his valuable guidance and support throughout the project.

I would also like to thank Dr. Thorfinnur Gunnlaugsson from the School of Chemistry for his advice during the collaboration and Dr. Derek Nolan for his precious suggestions.

To the members of DCW lab – Trevor, who helped me a lot with my English, Kim and Suzanne. Particularly, I want to thank Sandra, who has been so supportive, encouraging and for her patience in going through all my transfer report and final thesis.

A note of thanks to Rob, from the School of Chemistry, for his fantastic compounds, support and time during the collaboration.

I would like to thank Gavin Mc Manus for his suggestions, help with the confocal facilities and for his patience in listening to me all the times I was giving out and Barry Moran for his help with the flow cytometry facilities.

I would like to thank Giorgio Carta for helping me during my stay in Dublin at the beginning of my PhD, Salim Dastan for helping me to solve all the technical problems in the preparation of the final version of the thesis and videos and Alessia De Luca for her contribution in revising the last version of the thesis.

Also I am extremely grateful to all my English teachers in the English Academy, who helped me to greatly improve my English.

Finally, but most importantly, I would like to thank my family, my friends and dear ones for their patience, support and encouragement throughout my studies and especially during my thesis.

I remain grateful to all of them.

This work was funded by the "Programma Master and Back - Avviso Pubblico 2009 - Alta Formazione Regione Autonoma della Sardegna" and by TCD for financial support.

Dedicated to:

My dear parents

Felice Erby and Ester Marongiu

Table of Contents *Page Number*

Chapter 3

Investigation on organic pdppz derivative and on Ru(II) complexes based on a novel extended aromatic polypyridyl ligands as a DNA probe and photocleavage agent

Chapter 4

Investigation of 4-Amino 1,8-Naphthalimide Derived Tröger's Bases

Chapter 5

Investigation on the mechanism of action of compounds RE84 and 85 in HeLa cells

Chapter 6
Overall Discussion

Abbreviations

(KCl)TEM	Potassium chloride transmission electron microscopy
[^{3}H]TPMP	[^{3}H]triphenylmethylphosphonium
^{3}MC	Upper triplet metal centre state
^{3}MLTC	Lowest lying triplet MLTC state
53BP1	p53 binding protein 1
AB	Alamar Blue
Ac-DEVD-AMC	N-acetyl- (Asp-Glu-Val-Asp)-7-amino-4-methylcoumarin
ADP	Adenosine diphosphate
AIF	Apoptosis-inducing factor
AIS_4Pc	Aluminium tetrasulfonate phthalocyanine
APS	Ammonium persulphate
ATM	Ataxia Telangiectasia Mutated
ATP	Adenosine trisphosphate
BCA	Bicinchoninic acid
BER	Base Excision Repair
bpy	Bipyridine
BRCT	Brca1 carboxy-terminal
$C_3H_3NaO_3$	Sodium pyruvate
Ca^{2+}	Calcium ion
$CaCl_2$	Calcium chloride
cdks	Cyclin-dependent kinases
CFP	Cyan fluorescent protein
Cisplatin	Cis-diammineplatinum(II) dichloride
CKI	Cdk inhibitors
CMA	Centre for Microscopy and Analysis, TCD
CO_2	Carbon dioxide
Cu^{+1}	Cuprous cation
Cu^{+2}	Cupric cation

DAPI	4',6-diamidino-2-phenylindole
DBD	DNA Binding Domain
DCF	2′,7′-dichlorofluorescein
DCFH-DA	2',7'-dichlorofluorescein-diacetate
DD	Death Domain
DFF	DNA Fragmentation Factor
DHE	Dihematoporphyrin ester
DMEM	Dulbecco's modified eagles medium
DMSO	Dimethyl sulphoxide
dppz	Dipyrido[3,2-a:2',3'-c] phenazyne
DR	Death Receptors
DSB	Double Strand Break
DTT	Dithiothreitol
EBV	Epstein-Barr Virus
ECL	Enhanced chemiluminescence
ECM	Extracellular matrix
EDTA	Ethylenediaminetetraacetic acid
EGFR	Epithelial Growth Factor Receptor
EGTA	Ethyleneglycoltetraacetic acid
ER	Endoplasmic Reticulum
FACS	Fluorescence Activated Cell Sorter
FADD	Fas-Associated Death Domain protein
$FADH_2$	Flavine adenine dinucleotide, reduced
FasL	Fas ligand
FasR	Fas receptor
FBS	Fetal Bovine Serum
FCCP	Carbonyl cyanide 4-(trifluoromethoxy)phenylhydrazone
FCS	Fetal Calf Serum
FI	Fluorescent Intensity

FITC	Fluorescein isothiocyanate
FLT3	Fms-like tyrosine kinase 3
FMNH	Flavin mononucleotide semiquinone
GFP	Green Fluorescent Protein
GFs	Growth Factors
GI	Gastrointestinal tract
GSH	Glutathione
GSSG	Glutathione homodimer
GTPases	Guanosine triphosphatases
HCl	Hydrogen Chloride
Hepes	4-(2-hydroxyethyl)-1-piperazine ethanesulfonic acid
HPD	Hematoporphyrin derivative
HY	Hypericin
IAPs	Inhibitors of apoptosis
IC_{50}	Half maximal inhibitory concentration
INT	Tetrazolium salt
IR	Inhibition Rate
ISC	Intersystem crossing
JNK	Jun N-terminal kinases
LDH	Lactate dehydrogenase
LMPA	Low Melting Point Agarose
MDC1	Mediator of DNA damage checkpoint 1
$MgCl_2$	Magnesium chloride
MLTC	Metal ligand charge transfer
MMP	Mitochondrial Membrane Potential
MOMP	Mitochondrial Outer Membrane Permeabilisation
mtDNA	Mitochondrial DNA
MTOC	Microtubule-organizing center
mTOR	Mammalian target of rapamycin

MTT	(3-(4,5-Dimethylthiazol-2-yl)-2,5-diphenyltetrazolium bromide
Nac	N-acetyl-L-cysteine
NaCl	Sodium chloride
NAD	Nicotinamide adenine dinucleotide
NADH	Nicotinamide adenine dinucleotide reduced
NADPH	Nicotinamide adenine dinucleotide phosphate
$NaNO_2$	Sodium nitrate
NaOH	Sodium hydroxide
NER	Nucleotide Excision Repair
NMPA	Normal Melting Point Agarose
NO	Nitric oxide
PAR	Poly (ADP-ribose)
PARP-1	Poly (ADP-ribose) polymerase
PBS	Phosphate Buffer Saline
PCD	PARP Catalytic Domain
PDGFR	Platelet-Derived Growth Factors Receptor
PDH	Pyruvate Dehydrogenase
pdppz	Ppyrazino[2,3-h]dipyrido[3,2-a:2',3'-c]phenazine
PDT	Photo Dynamic Therapy
Pen-Strep	Penicillin Streptomycin
PET	Photoinduced Electron Transfer
phen	Phenanthroline
PI	Propidium Iodide
PI(3)K	Phosphatidyl-inositol-3-OH kinase
PIKKs	Phosphatidyl-inositol-3-OH kinase –like kinases
pmc	Perinuclear Mitochondrial Clustering
pRb	Tumour Suppressor Protein
PS	Phosphatidylserine
PTP	Mitochondrial permeability transition pore

PVDF	Polyvinylidene difluoride
RB	Retinoblastoma
RDS	Radioresistant DNA Synthesis
REDOX	Oxidation-reduction
RER	Rough Endoplasmic Reticulum
ROS	Reactive Oxygen Species
SCFR	Mast/Stem Cell Growth Factor Receptor
SDS	Sodium Dodecyl Sulphate
SDS-PAGE	Sodium dodecyl sulphate-polyacrylamide gel electrophoresis
SSBR	Single Strand Break Repair
TAP	Tetraaza-phenantrene T
TBS	Tris-Buffered Saline
TBST	Tris-buffered saline and Tween 20
TEM	Transmission electron microscopy
TEMED	N,N,N',N',-tetramethylethylenediamine
TK	Tyrosine Kinase
TNF	Tumour -Necrosis Factor
TNF-R	Tumour -Necrosis Factor- Receptor
TPB	Sodium Tetraphenylboron
TRADD	TNF-R-associated Death Domain protein
TRITC	Tetramethylrhodamine
TSP-1	Thrombospondin- 1
U	Uracil
VDAC	Voltage-Dependent Anion Channel
VEGF-A	Vascular Endothelial Growth Factor-A
VEGFR	Vascular Endothelial Grow Factor Receptor
WR	Working Reagent
Z-VAD-FMK	Carbobenzoxy-valyl-alanyl-aspartyl-[O-methyl]- fluoromethylketone
$\Delta\Psi$	Membrane potential

Chapter 1: General Introduction

1.1 Oncogenesis

Tumors are complex tissues composed of multiple distinct cell types that participate in heterotypic interactions with one another. Tumour cells have a different morphology, have a larger interstitial volume and often contain a larger fraction of macrophages. They have a microvasculature, poor lymphatic drainage, a low extracellular pH, a relatively large amount of newly synthesized collagen and tumour tissues also contain many receptors for lipoproteins [1].

There are six biological hallmarks acquired during the multistep development of human tumors that allow cancer to survive, proliferate and disseminate. These hallmarks of cancer, originally proposed in 2000 by Hanahan and Weinberg, are acquired in different tumour types via distinct mechanisms and at various times during the course of multistep tumorigenesis. They include sustaining proliferative signalling, evading growth suppressors, resisting cell death, enabling replicative immortality, inducing angiogenesis and activating invasion and metastasis, as illustrated in figure 1.1 [2].

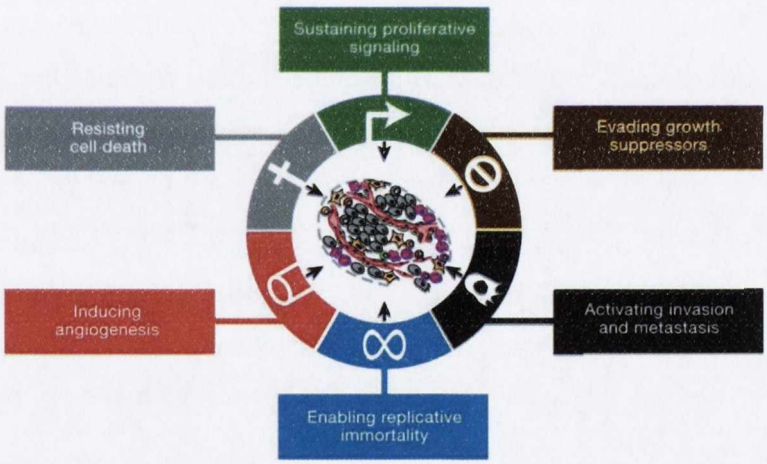

Figure 1.1: Illustration of the six hallmarks of cancer taken from [2].

The acquisition of the hallmarks of cancer is made possible by two enabling characteristics. The most prominent is the development of genomic instability in cancer cells [2, 3].

This development has been set in the discovery of mutations that produce oncogenes with dominant gain of function and tumour suppressor genes with recessive loss of function [4]. In general, proto-oncogenes, which are normal genes found within the DNA of a living species, code for proteins that help to regulate cell growth and differentiation. Somatic

cells are diploid: they carry two copies (alleles) of each autosomal gene (all the genes present in non-sexual chromosomes). Dominant negative mutations of these genes confer the acquisition of a new function that is called gain of function. This gain of function occurs when a mutation arises in the genome of one allele and can influence the activity of a cell if the change results in a dominant effect on the "healthy allele". This phenomenon, typically observed in mutations of proto-oncogenes, can generate an increase of a protein's activity or a loss of the normal homeostatic controls. The non-mutated protein, encoded by the healthy allele, continues to perform its normal functions while, the mutated protein, encoded by mutated allele is functionally independent. On the other hand, to have a loss of function, both alleles must be mutated. When a proto-oncogene is altered it becomes an oncogene, a gene that has the potential to cause cancer. There are several ways in which an oncogene can be generated. Firstly, it can be caused by an alteration in its regulation or production, for instance, an over expression of normal proteins or gene amplification. When gene amplification occurs, the regulatory mechanism is still normal, but there are multiple copies of the proto-oncogene in the cell, which results in a higher number of proteins. This increase creates an anomalous situation. Oncogenes can also be caused by an alteration in the region that encodes the protein. In this case, both the gene product and the functions are abnormal. Thirdly, oncogenes can be formed by chromosomal rearrangement. The gene product is a fusion protein, derived from the combination of two different genes to form a single new gene. In this case we obtain a protein with a new feature that leads to over expression and differences in the regulatory system.

A second enabling characteristic that makes the acquisition of the hallmarks of cancer possible involves the inflammatory state of premalignant and frankly malignant (the tumour is cancer) lesions that is driven by cells of the immune system, some of which serve to promote tumor progression [2, 5].

The first hallmark of cancer is the cancer cell's ability to sustain chronic proliferation. In general, the proliferative signals operating within normal tissues are poorly understood. In contrast, the mitogenic signaling in cancer cells is better understood. What is known about normal tissues is that they carefully control proliferative signaling, which is conveyed in large part by growth factors (GFs) that bind cell-surface receptors, ensuring a homeostasis of cell number as well as maintenance of a normal tissues architecture and function [2]. On the other hand, cancer cells can acquire the capability to sustain proliferative signaling in a number of alternative ways: they may produce growth factor ligands themselves; cancer

cells may send signals to stimulate normal cells within the supporting tumor-associated stroma; receptor signaling can also be deregulated by elevating the levels of receptor proteins displayed at the cancer cell surface; the same growth factor independence may also be derived from the constitutive activation of components of signaling pathways operating downstream of these receptors [2, 6].

The second biological hallmark is that cancer cells circumvent programs that negatively regulate cell proliferation by evading growth suppressors. Many of these programs depend on the actions of tumor suppressor genes such as RB (retinoblastoma) and p53 proteins. The RB protein integrates signals from diverse extracellular and intracellular sources and, in response, decides whether or not a cell should proceed through its growth-and-division cycle; p53 receives inputs from stress and abnormality sensors that function within the cell's intracellular operating systems: if the degree of damage to the genome is excessive, or if the levels of nucleotide pools, growth-promoting signals, glucose, or oxygenation are suboptimal, p53 can call a halt to further cell-cycle progression until these conditions have been normalized [2, 7]. Cancer cells can override these signals.

The third biological hallmark is related to several abnormalities in sensors that play key roles in tumor development by inhibiting cell death. For example, tumor cells evolve a variety of strategies to limit or circumvent apoptosis. Most common is the loss of p53 tumor suppressor function, which eliminates the critical DNA-damage sensor that functions via the p53 tumour suppressor from the apoptosis-inducing circuitry [2, 8]. Alternatively, tumors may achieve similar ends by increasing expression of antiapoptotic regulators (Bcl-2, Bcl-xL), or survival signals (Igf1/2) by downregulating proapoptotic factors (Bax, Bim, Puma), or by short-circuiting the extrinsic ligand-induced death pathway [2, 9].

The fourth biological hallmark is that cancer is a disease in which there is a reduction in control over cell proliferation and cell death. Moreover, by 2000, it was widely accepted that cancer cells require unlimited replicative potential in order to generate macroscopic tumors [2].

Normal cells of adult tissues are not all of the same proliferative status as each other. The first category of cells, for example, mature neurons, myocardium, and mature pre-fertilization cells of the female germ line, do not proliferate at all. The second category of cells, in conditionally renewing tissues such as liver cells, vascular endothelium, and cells of the extracellular matrix (ECM) are not usually replicative, but can proliferate if need be,

for example, during wound healing. The third category is of cells that under normal conditions are always in the cell cycle, for example, the epithelium that lines the gastrointestinal (GI) tract, all blood cell precursors, and some cells at the basal level of the epidermis [10].

This limitation to pass through only a limited number of successive cell growth-and-division cycles has been associated with two distinct barriers to proliferation: senescence, a typically irreversible entrance into a non-proliferative but viable state, and crisis, which involves cell death. Rarely, cells emerge from a population in crisis and exhibit unlimited replicative potential. This transition has been termed immortalization, a trait that most established cell lines possess by virtue of their ability to proliferate in culture without evidence of either senescence or crisis [2]. The presence of telomerase, the specialized DNA polymerase that adds telomere repeat segments to the ends of telomeric DNA, either in spontaneously immortalized cells or in the context of cells engineered to express the enzyme, is correlated with a resistance to induction of both senescence and crisis/apoptosis; conversely, suppression of telomerase activity leads to telomere shortening and to activation of one or the other of these proliferative barriers, has been rationalized as crucial for anticancer defenses [2, 11].

The fifth biological hallmark of cancer is angiogenesis induction which is the physiological process through which new blood vessels form from pre-existing vessels. The development of the vasculature during embryogenesis evolves the birth of new endothelial cells which assembled into tubes (vasculogenesis) and the angiogenesis process. After this morphogenesis, the normal vasculature becomes largely quiescent but only transiently (angiogenic switch). In fact, in the adult, angiogenesis is turned on as part of physiologic processes such as wound healing and female reproductive cycling. In contrast, during tumor progression, angiogenesis is almost always active, causing new vessel formation that helps sustain expanding neoplastic growths [2]. Angiogenic regulators of the ''angiogenic switch'' are signaling proteins that bind to stimulatory or inhibitory cell surface receptors displayed by vascular endothelial cells. The well-known prototypes of angiogenesis inducers and inhibitors are vascular endothelial growth factor-A (VEGF-A), and thrombospondin-1 (TSP-1), respectively [12]. The VEGF-A gene encodes ligands that are involved in organising new blood vessel growth and its expression can be upregulated both by hypoxia and by oncogene signaling. The counterbalance in the angiogenic switch is TSP-1, which also binds transmembrane receptors displayed by endothelial cells evoking

suppressive signals that can counteract proangiogenic stimuli. Historically, angiogenesis was envisioned to be important only when rapidly growing macroscopic tumors had formed, but more recent data indicate that angiogenesis also contributes to the microscopic premalignant phase of neoplastic progression [2, 12].

The sixth biological hallmark is invasion and metastasis. The best characterized alteration to higher pathological grades of malignancy involved the loss by carcinoma cells of E-cadherin, a key cell-to cell adhesion molecule. E-cadherin helps to assemble epithelial cell sheets and maintain the quiescence of the cells within these sheets by forming adherens junctions with adjacent epithelial cells [2, 13]. Moreover, expression of genes encoding other cell-to-cell and cell-to-ECM (extracellular matrix) adhesion molecules are demonstrably altered in some highly aggressive carcinomas. Adhesion molecules that promote cytostasis are also typically downregulated. Conversely, adhesion molecules, such as N-cadherin which is normally expressed in migrating neurons and mesenchymal cells during organogenesis, are normally associated with the cell migrations that occur during embryogenesis and inflammation are often upregulated in many invasive carcinoma cells [2]. The multistep process of invasion and metastasis is often termed the invasion-metastasis cascade, which envisions a succession of cell-biologic changes: beginning with local invasion, then intravasation by cancer cells into nearby blood and lymphatic vessels, transit of cancer cells through the lymphatic and hematogenous systems, followed by escape of cancer cells from the lumina of such vessels into the parenchyma of distant tissues (extravasation), the formation of small nodules of cancer cells (micrometastases), and finally the growth of micrometastatic lesions into macroscopic tumors, this last step being termed ''colonization'' [2, 13].

1.2 The need for new targeted anti-cancer therapies

Cancer is the second most common cause of death of people around the world and for decades, traditional cytotoxic chemotherapy has been the treatment for cancer.

Traditional cytotoxic chemotherapy works primarily through the inhibition of cell division targeting rapidly dividing cells. In addition to cancer cells, there are other rapidly dividing cells in our body (hair, gastrointestinal epithelium, bone morrow) which are affected by these drugs resulting in many patients experiencing the classic toxicities of alopecia,

gastrointestinal symptoms, and myelosuppression [14, 15]. The traditional chemotherapeutic drugs can be divided into alkylating agents, which interfere with DNA base pairing, leading to strand breaks and arresting DNA replication; topoisomerase inhibitors, which prevent DNA uncoiling; taxanes and alkaloids, which interfere with microtubule function required for cell mitosis; and antimetabolites, which block the formation and use of nucleic acids essential for DNA replication [15].

In the past decades, strong efforts have been made to find new harmless and effective solutions: although traditional cytotoxic chemotherapy remains the treatment of choice for many malignancies, targeted therapies are now a crucial component of treatment for many types of cancer (breast, colorectal, lung, and pancreatic cancer, as well as lymphoma, leukemia, and multiple myeloma) [15, 16].

In contrast to cytotoxic chemotherapy, targeted therapy preferentially blocks the proliferation of cancer cells by interfering with specific molecules required for tumour development and growth expanding the concept of individually tailored cancer treatment because some of these drugs may be effective in patients whose cancer have a specific molecular target, but they may not be effective in the absence of such a target. Some of these targeted molecules may be present in normal tissues, but they are often modulated or overexpressed in tumours [17]. For example, CD20 (an activated-glycosylated phosphoprotein expressed on the surface of all B-cells) is present on lymphoma and normal lymphoid cells; HER2/neu (transmembrane receptors of the erbB family) is present on 25 percent of breast cancer cells, and VEGFR (vascular endothelial grow factor receptor) is present on normal tumour-associated vasculature; small molecular inhibitors can target some of the downstream intracellular signalling molecules.

Targeted therapy is divided into two main types which are monoclonal antibodies and small molecule inhibitors. Monoclonal antibodies are identical antibodies produced by a single type of immune cell and in targeted cancer therapy they are directed against molecules unique to, overexpressed in, or mutated in cancer cells; small molecule inhibitor drugs interfere with the function of molecules (most commonly they interfere with tyrosine kinases) involved in the development and progression of cancer.

Receptors of the tyrosine Kinase (TK) family play principal rules in the interpretation of extracellular signals to produce an appropriate developmental or proliferative response in the cell as they integrate a multitude of external stimuli with specific internal signals and responses allowing the cell to respond correctly to its environment. In particular one family

of TK receptors, known as the erbB family EGRF family, is critical for mediating the proliferation and differentiation of normal cells and current knowledge suggests that aberrant activation of the kinase activity of these receptors is important in the development and/or progression of human cancer. The erbB family consists of four closely related transmembrane receptors termed erbB1, 2, 3, 4 (also termed (HER1, 2, 3, 4) [18]. There is strong clinical evidence that trastuzumab (Herceptin), a monoclonal antibodies targeting the HER, is an important component of first-line treatment of patients with HER2-positive metastatic breast cancer. Results from large phase III trials evaluating adjuvant therapy in HER2-positive early breast cancer indicate that the addition of trastuzumab to chemotherapy improves disease-free and overall survival. The use of lapatinib, a dual TK inhibitor of both HER1 and HER2, in combination with capecitabine in the second-line treatment of HER2-positive patients with metastatic breast cancer previously treated with trastuzumab has also been established: there is a modest, but still insufficient, support that the compound passes the blood-brain barrier [19].

Nevertheless, both cytotoxic and targeted therapies have some limitations. Chief among these is the potential for cells to develop resistance to therapy. Carcinogenesis is characterized by progressing genetic changes: some patients can develop resistance to some drugs, which can be due to changes in the shape of the protein so that it no longer binds the front line drug as well. In most cases, another cytotoxic or targeted therapy that could overcome this resistance is available, although with lower efficacy. It is for this reason that therapies may work best in combination, either with other targeted therapies or with more traditional therapies. Resistance to current treatments, side effects of treatments and an inability to cure certain types or advanced stages of tumour has lead to the need to develop novel therapies for cancer.Moreover, some targeted drugs have multiple targets such as sorafenib (Nexavar), which targets BRAF (serine-threonine protein kinase), VEGFR, EGFR (epithelial grow factor receptor), and PDGFR (platelet-derived growth factors receptor) for renal cell cancer and hepatocellular carcinoma [20]; sunitinib (Sutent), which targets VEGFR, PDGFR, c-kit (mast/stem cell growth factor receptor (SCFR), also known as proto-oncogene c-Kit or tyrosine-protein kinase Kit or CD117), and FLT3 (Fms-like tyrosine kinase 3 also known as cluster of differentiation antigen 135 (CD135)) for renal cell cancer gastrointestinal stromal tumours [21]; imatinib (Gleevec), which targets BCR-ABL (breakpoint cluster region-Abelson), c-KIT and PDGFR for acute lymphocytic leukemia, chronic myeloid leukemia, gastrointestinal stromal tumours, hypereosinophilic

syndrome, systemic mastrocytosis [22]; dasatinib (Sprycel), which targets BCL-ABL, SRC family (non-receptor tyrosine kinases), c-Kit, PDGFR for chronic myeloid leukemia, acute lymphocytic leukemia [23].

A lot has been done in cancer research on stem cell biology and striking parallels can be found between stem cells and cancer cells: tumours may often originate from the transformation of normal stem cells, similar signalling pathways may regulate self-renewal in stem cells and cancer cells, and cancer cells may include 'cancer stem cells', which are rare cells with indefinite potential for self-renewal that drive tumourigenesis. The most important and useful property of stem cells is that of self-renewal. Moreover, the proof that stem cells exist in the haematopoietic system has given way to the prospective isolation of several tissue-specific stem and progenitor cells, the initial delineation of their properties and expressed genetic programmes, and the beginnings of their utility in regenerative medicine [24-26].

1.3 Cell cycle

The cell cycle is the way individual cells within organisms reproduce and it entails the division of a "parent cell" into two "daughter cells" [27], which includes different stages. Mitosis, or M phase, is where the actual division process takes place: the replicated chromosomes are separated and each daughter cell gets a copy of each chromosome during cell division. The period between the end of a mitosis at the beginning of the next one is called interphase, which is divided in different stages. The first one, which is called G1, is a check point gap in which the cell starts synthesizing RNA and proteins and where the cell increases its size. The second stage, which is called S, is the phase where DNA synthesis occurs and chromosomes are copied. The DNA changes from 2n (diploid cells: cells with a full set of chromosomes) to 4n (tetraploid cells: cells with a double set of chromosomes). G2, which is the third stage, is another check point gap where the control of the replication of all chromosomes occurs. In this phase, the DNA has a 4n content. Mitosis consists of prophase, metaphase, anaphase, telophase and finally cytokinesis. In eukaryotic cells this sequence of events is repeated every 18-24 hours. G1 usually takes between 6 and 12 hours, the S phase between 6 and 8 hours, the G2 is the shortest interphase phase and the

M phase takes about 1 hour to complete. The synthesis of RNA and proteins occur continuously during the cycle, while the synthesis of DNA is only during the S phase. Some cell types exit irreversibly from this cell cycle (terminally differentiated cells), others enter a state of quiescence called G0 so that cells can be stimulated to leave G0 and go back into the cell cycle.

In the regulation of cell cycle progression two classes of proteins have a key role: the cyclin-dependent kinases (cdks) and cyclins. The cdks are serine-threonine kinases whose catalytic subunit is activated by conformational changes after binding to specific cyclins, which are their regulatory subunits. The cyclins are so called because their levels vary in a "cyclical" way in certain phases of the cell cycle, before being degraded.

The variation of the expression of cyclins and the resulting fluctuations in the activity of cdks, sets out the basis of cell cycle progression. Several cyclin/cdk complexes are formed during the different phases of the cell cycle and are guided to the appropriate cdk substrates [7].

Cyclins in eukaryotic cells involved in the transition from G1 to S phase are those of type D and E [28]. There are 3 types of D cyclins (cyclin D1, D2 and D3) and 2 types of cyclin E (E1 and E2). The D-type cyclins are synthesized in G1 in response to mitogenic signals and are associated with cdk4 or cdk6 [29]. The levels of cyclin E increase during the progression from G1 to S phase by activating cdk2 [30]. pRb (retinoblastoma protein, a tumour suppressor) is the protein that acts as a switch for the R (restriction) point (which is described in more detail below) playing a crucial role in controlling cell proliferation. pRb activity is controlled by post-translational modifications in particular through phosphorylation and dephosphorylation (figure 1.2) [31].

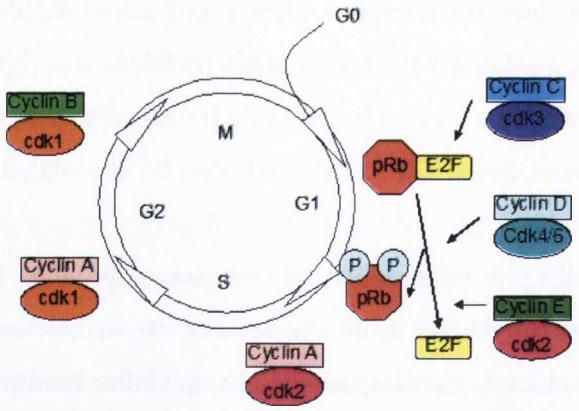

***Figure 1.2*:** pRb and the cell cycle. pRb and pRb-p, respectively, represent the non-phosphorylated and phosphorylated form of the protein pRb. In G0 and early G1 phase, pRb is physically associated with E2F factors and blocks their transactivation domains. In late G1, pRb releases E2F-p, allowing the expression of genes encoding products required for progression into S phase

In the hypophosphorylated state, the cell cycle progression is suppressed because pRb is physically associated with E2F transcription factors preventing the entry into S phase. pRb is phosphorylated by the complex cyclin D1/cdk4 or D1/cdk6 in early G1 and, later from the complex cyclin E/cdk [32, 33] which determines its functional inactivation.

pRb can also adjust the transition from G0 to G1 phase [34]. In fact, when a cell is in phase G0 pRb is hypophosphorylated and helps to maintain the cell at this stage by repressing the transcription of ribosomal (r)RNA and transfer (t)RNA genes. The complex cyclin C/cdk3 mediates the release from the G0 phase through the phosphorylation of pRb.

The phosphorylation state is also regulated indirectly by a class of proteins called cdk inhibitors (CKI) that bind the cyclin/cdk complex, inactivating it and preventing the phosphorylation which results in the inactivation of pRb [35]. CKI inhibitors, p15, p16 and p17 play a specific role in inhibiting cyclin D/cdk4 or cdk6 complexes, while p21, p27 and p57 act on all other cyclin/cdk complexes.

In a normal cell there are checkpoint controls with the function to ensure that chromosomes are intact and that critical stages of the cell cycle are completed before the following stage is initiated.

The decision of normal cells to replicate DNA and duplicate itself is influenced by extracellular signalling such us GFs which are necessary to initiate and maintain the transition through G1 phase leading to S phase. The restriction (R) point is the point in G1 at which commitment occurs and the cell no longer requires GFs to complete the cell cycle.

The restriction point has been temporally mapped at 2-3 hours prior to the onset of DNA synthesis. R-protein is a functionally short-lived (labile) regulatory protein, whose synthesis is sensitive to GFs, and must accumulate to a critical amount before a cell can pass the restriction point and proceed towards DNA synthesis [6, 36].

Initiation of the activation of the PIKKs (PI(3)K (phosphatidyl-inositol-3-OH kinase) –like kinases), ATM (ataxia telangiectasia mutated) and ATR (ATM-and Rad3-related) are the first steps in the activation of signal transduction pathways that inhibit cell cycle progression after DNA damage [37, 38]. The ATM kinase seems to primarily be activated following DNA damage whereas the ATR kinase seems to be critical for cellular responses to arrest of DNA replication forks (the DNA structure formed during replication). Some kinds of DNA damage result both in the direct damage of the DNA and the arrest of DNA replication forks, ATM and ATR seem to participate together in many cellular-stress responses [37, 38]. Checkpoint factors seems to modulate the activity of ATM/ATR facilitating the interaction of ATM/ATR with their substrates and mediating spatio-temporal assembly of multiprotein complexes in the chromatin regions surrounding the sites of DNA damage [37].

The ATM-related mediators include MDC1 (mediator of DNA damage checkpoint 1; also known as NFBD1), 53BP1 (p53 binding protein 1) and BRCA1 which is a large multi-domain protein that contains two tandem BRCT (Brca1 carboxy-terminal) domains at its C-terminus [37]. The BRCT domains have recently been shown to serve as protein-phosphoprotein-binding modules, suggesting a possible mechanism for how the mediator proteins could promote the transient multiple interactions of checkpoint and repair proteins near the DNA-damage sites [38]. The ATM-independent recruitment of the mediators to sites of DNA damage depends on ATM-mediated phosphorylation of histone H2AX, a modification that marks chromatin regions spanning megadaltons of DNA flanking each double strand break (DSB) [37, 38]. The MDC1 protein functions as a molecular bridge between the phosphorylated H2AX (γ-H2AX) and the NBS1 component of the MRN complex, and helps provide a platform for a myriad of dynamic interactions for these and additional checkpoint and DNA-repair proteins (including the activated ATM and BRCA1) within the vicinity of the damage sites [38]. Although the mediator proteins are unlikely to initially target the activated ATM to sites of DNA damage (this might be the role of the candidate damage sensors such as the MRN complex), the sustained multiprotein interactions mediated by MDC1, 53BP1 and BRCA1 seem to facilitate ATM signalling

and the processing/repair of the lesions, thereby contributing to the biological outcome of the checkpoint responses [37]. Cells that lack any of these three mediators show enhanced sensitivity to DNA-damaging agents such as ionizing radiation, and impaired intra-S-phase and G2/M cell cycle checkpoints. Reminiscent of the roles of MDC1, 53BP1 and BRCA1 in proper localization, timing and velocity of the ATM-controlled signalling, the ATR-controlled checkpoint signalling, at least towards the Chk1 kinase that is activated by ATR, relies on claspin, which is a mediator/adaptor protein that is structurally unrelated to the mediators involved in response to DSBs. Claspin selectively interacts with chromatin structures created by active replication forks, and is required for ATR-mediated phosphorylation, and so for proper activation, of Chk1 [37, 38].

The G1 checkpoint (or DNA-damage checkpoint) arrests the cell cycle in response to DNA damage until the damage is repaired. Cells that have incurred DNA DSBs during G1 phase activate p53 primarily via an ATM-dependent pathway. In cells that express both ATM/ATR, the activation of p53 is reinforced and maintained by ATR. ATM regulates p53 accumulation by an indirect pathway involving the Chk2-mediated phosphorylation of serine 20 on p53, by promoting casein kinase-I-dependent phosphorylation of serine 18, and by directly phosphorylating MDM2 on serine 395. ATR may influence serine 20 phosphorylation through activation of Chk1. In response to extensive DNA damage, p53 also activates genes that induce apoptosis [36, 38, 39].

The ATM-dependent pathway in the S-phase checkpoint is initiated by the presence of DNA DSBs in an S-phase cell. This checkpoint response leads to the proteosome-mediated degradation of Cdc25A (is a member of the CDC25 family of dual-specificity phosphatases, CDC25A, B, C), followed by the failure to maintain activation of cyclin·cdk2 complexes resulting in inhibition of DNA synthesis. Disruption of this pathway yields the radioresistant DNA synthesis (RDS) phenotype. The checkpoint pathway can also be triggered by intrinsic events or environmental insults that impair replication fork progression during S phase. The pathway is governed primarily by ATR, and may use members of the Rad family of checkpoint proteins as damage sensors and as scaffolds for the assembly of checkpoint signaling complexes. The operation of this pathway prevents mitotic catastrophe that results from incomplete or inaccurate DNA replication, and orchestrates high-fidelity DNA repair through homologous recombination. Complete loss of this pathway is likely incompatible with viability, even in the absence of genotoxic agent-induced DNA damage [36, 38, 39].

The ATM and ATR pathway in G2 checkpoint is activated when cells incur DNA damage before completion of S phase, and is governed primarily by ATR. The pathway is also activated by DNA damage during the G2 phase itself, and depends largely on the activation of ATM. Both these activities converge on the Cdc25C phosphatase, and prevent activation of the mitotic cyclin B/cdc2 complex by inducing the cytoplasmic sequestration and/or catalytic inhibition of Cdc25C [38, 39].

The spindle-assembly checkpoint, which prevents premature initiation of anaphase, utilises Mad2 and other proteins to regulate the APC/C specificity factor Cdc20 (regulator of cell division) that targets securin for polyubiquitination (ubiquitination and subsequent protein degradation by the proteasome) [40]. Securin is a protein involved in control of the metaphase-anaphase transition and anaphase onset, orientation of chromosome pairs and inactivation of the spindle checkpoint system, which includes producing an abrupt stimulus that induces highly synchronous chromosome separation in anaphase. The APC/C, an anaphase-promoting complex also called the cyclosome, triggers the events leading to destruction of cohesin which is a protein complex that regulates the separation of sister chromatids during cell division.

The spindle-position checkpoint prevents telophase and cytokinesis until daughter chromosomes have been properly segregated, so that the daughter cell has a full set of chromosomes. In the spindle-position checkpoint, the small GTP-ase Tem1 controls the availability of Cdc14 phosphatese (a protein phosphatase), which in turn activates the APC/C specificity factor Cdh1 that targets B-type cyclins for degradation, causing inactivation of mitosis-promoting factor (MPF), a heteromeric protein, composed of a mitotic cyclin and CDK, that trigger entrance of a cell into mitosis by phosphorylating multiple specific proteins [40].

1.4 Cell death

Programmed cell death is a conserved physiological cell death process which the cell uses to remove unwanted cells, and to defend against damage or infected cells. Apoptosis is also important in controlling cell number and proliferation as part of normal development. Cell death can be induced by a variety of stress responses, such as heat shock response, when the vital processes are slowly or only partially inhibited. These responses involve detection

of the damage, transduction of signals, and activation of the response, such as production of heat shock proteins, proteases, or chaperones. Apoptosis, one particular type of programmed cell death, leads to well-known morphological changes including cell shrinkage and the release of small membrane-bound apoptotic bodies which are generally engulfed by other cells. Furthermore, nuclei condense and DNA is fragmented, but the intracellular constituents are not released into the extracellular milieu where they might have deleterious effects on neighbouring cells.

The mitochondrial proteins, for example, are of particular interest in drug design as apoptosis can be initiated in the mitochondria, as well as by other pathways, for instance, by the Fas/FasL pathway [41].

In contrast to apoptosis, necrosis is a different non-programmed kind of cell death in response to tissue damage and necrotic cells exhibit very different morphological changes: cells swell and burst, releasing their intracellular contents, which can damage surrounding cells and cause inflammation.

There are two main pathways for the induction of apoptosis, the extrinsic or receptor-mediated pathway, and the intrinsic or mitochondrial pathway [41]. Both of these pathways converge to a final common pathway involving the activation of caspases, a class of intracellular cysteine proteases that are responsible for the cleavage of a variety of cellular substrates and the morphological changes attributed to apoptosis [41].

The **extrinsic pathway** is activated by the interaction of a specific death ligand with its cell surface death receptors (DR), which are members of the tumour-necrosis factor (TNF) superfamily [42].

Fas receptor (FasR) and Fas ligand (FasL) are examples of plasma membrane proteins whose interaction triggers major apoptotic pathways. First, FasR forms a homotrimer following interaction with its ligand. Second, the assembled trimer can result in the large grouping together or aggregation of trimers. Only the interaction between FasL and FasR can lead to activated downstream signalling pathways. FasR is a surface receptor related to TNF-R (tumour necrosis factor receptor). Each ligand family includes a series of trans-membrane proteins and there are different ways that lead to cell death: it can be triggered by a cell-cell interaction, in which the ligand on the surface of a cell interacts with the surface receptor of the other cell. Both Fas and TNF receptors can trigger apoptosis. Fas and TNF ligands can be cleaved to generate soluble proteins that function as diffusible factors. Mutant versions of the receptors demonstrate that the apoptotic response is

triggered by an intracellular domain of 80 amino acids near the C-terminus. This region is poorly conserved (28% approximately) between Fas and TNF-R1 (one of the receptors in the TNF family) and is called the death domain (DD) [41, 42].

Ligand-receptor interaction triggers the activation of a caspase protease (caspase-8) which leads to the release of cytochrome c from mitochondria (figure 1.3). This in turn activates a series of proteases, whose actions culminate in the destruction of cellular structures.

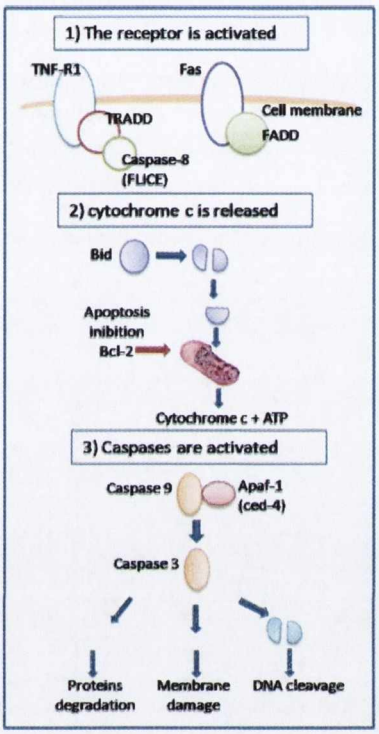

Figure 1.3: The "classic" apoptotic pathway adapted from [27]. Apoptosis can be triggered by the activation of surface receptors. Caspases are activated in two different stages. Caspase-8 is activated by the receptor which leads to the release of cytochrome c from mitochondria. Apoptosis can be blocked at this stage by Bcl2. Cytochrome c activates the intrinsic pathway.

The TNF receptor binds a protein called TNF-R–associated death domain protein (TRADD), which in turn binds a protein called Fas-associated death domain protein (FADD). Fas receptor binds FADD directly. In both cases, the protein FADD binds caspase-8 (or FLICE), which possesses both a death domain and a protease catalytic activity. Autocatalytic cleavage of caspase-8 activates a common pathway of apoptosis and the triggering event is the oligomerization of the receptor. Caspases have a catalytic cysteine and they cleave their targets at aspartate residues in a major and minor subunit. Individual enzymes have related but not identical targets. Human caspases are involved in

inflammatory and immune responses (caspase-1, 4, 5) however the majority of caspases are involved in apoptosis [27].

Some of the procaspases that operate in apoptosis act at the start of the proteolytic cascade and are called initiator procaspases (caspase-2, 8, 9, 10). When they are activated they cleave and activate downstream executioner procaspases (caspase-3, 6, 7) which then cleave and activate other executioner (or effector) procaspases, as well as specific target proteins in the cell. Among the many target proteins cleaved by executioner caspases are, for example, components of the cytoskeleton and cell-cell adhesion proteins that attach cells to their neighbours helping apoptotic cells to round up and detach from its neighbours in order to engulf it easily [43].

Fas can activate apoptosis through either caspases or through the activation of the jun N-terminal Kinases (JNK), whose substrate is the important transcription factor c-Jun (figure 1.4).

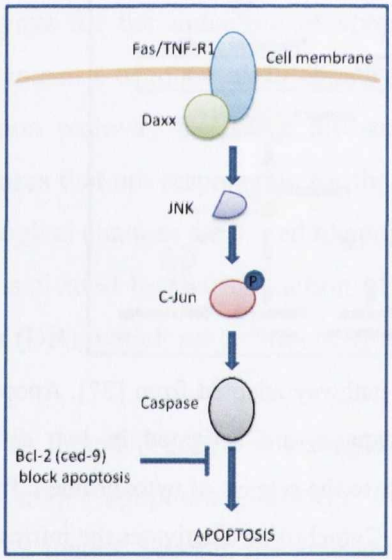

Figure 1.4: The JNK pathway adapted from [27]. Fas can trigger apoptosis through a JNK-mediated pathway.

The Fas cell surface receptor induces apoptosis upon receptor oligomerization. This pathway is mediated by the signalling protein Daxx (which has no death domain). The binding of FADD and Daxx to Fas is independent with each adapter recognising a different site of Fas. In fact, Daxx specifically binds the Fas death domain. The TNF receptor can activate JNK through distinct adapter proteins. Overexpression of Daxx enhances Fas-mediated apoptosis and activates JNK patway. A C-terminal portion of Daxx interacts with

the Fas death domain, while a different region activates both JNK and apoptosis. The Fas-binding domain of Daxx is a dominant-negative inhibitor of both Fas-induced apoptosis and JNK activation, while the FADD death domain partially inhibits death but not JNK activation. The Daxx apoptotic pathway is sensitive to both Bcl-2 and dominant negative JNK pathway components and acts cooperatively with the FADD pathway [44]. Thus, Daxx and FADD define two distinct apoptotic pathways downstream of Fas.

Another apoptotic pathway is triggered by cytotoxic T lymphocytes, which kill target cells in a process that involves the release of granules that contain serine proteases and other lytic components. One of these components is a perforin, which can produce holes in the membrane of target cells and under some conditions can kill them. The serine proteases, called granzymes, are present in the granules. In the presence of perforin, granzyme B can induce many of the features of apoptosis, including DNA fragmentation, by activating a caspase called Ich-3, which is necessary for this form of apoptosis [27].

The **intrinsic pathway** can be activated by a variety of stimuli, including growth factor withdrawal, heat shock, oncogene activaction, DNA-damaging agents, ROS, excessive cytosolic calcium and other cellular stresses [44]. These agents cause mitochondrial outer membrane permeabilization (MOMP) and the release of cytochrome c and other proteins into the cytosol. MOMP can occur as a result of either a change in the mitochondrial permeability transition pore (PTP) or by the action of pro-apoptotic members of the Bcl2 family of proteins. The PTP complex is composed of the voltage-dependent anion channel (VDAC) in the outer membrane, the inner mitochondrial membrane and the soluble matrix protein cyclophilin D [42].

The intrinsic pathway starts when caspase-8 cleaves a protein called Bid resulting in the release of the C-terminal domain. This domain then moves to the mitochondrial membrane causing the release of cytochrome c (figure 1.5).

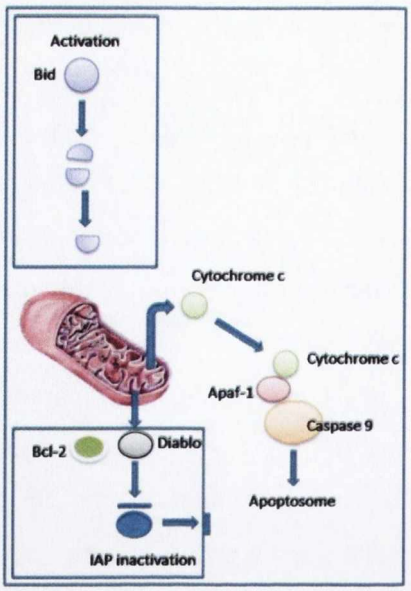

Figure 1.5: The mitochondrial apoptotic pathway adapted from [27]. The mitochondrion plays a central role in apoptosis by releasing cytochrome c, a phenomenon triggered by Bid and inactivated by Bcl2. Cytochrome c binds to Apaf-1 and pro-caspase-9 to form the apoptosome. The activition of the proteolytic caspase-9 can be inhibited by IAP proteins. Proteins that antagonize the IAP proteins are also released from the mitochondria.

Bid is a member of the Bcl2 family. Some members of this family, the pro-apoptotic Bcl2 proteins, are required for apoptosis, while the anti-apoptotic Bcl2 proteins, such as Bcl2 itself, work in an opposite way, which inhibit apoptosis in many cells. Bcl2 has a C-terminal membrane anchor which is located in the outer mitochondrial membrane, in the nuclear membrane and endoplasmic reticulum (ER). In contrast to the function of Bid, Bcl2 functions to prevent cytochrome c release.

The anti-apoptotic Bcl2 proteins are a class of proteins that cause tumourigenesis when proliferation is uncontrolled, members can heterodimerize and homodimerize. Two other members of this family are bcl-x and Bax. Bcl-x is produced in different forms due to alternative splicing. Each one of them has different properties.

Combinatorial associations and the ratio of Bcl2 family members can influence the susceptibility of a cell to undergo apoptosis [42].

Once cytochrome c is released, it triggers the interaction of the cytosolic protein Apaf-1 with caspase-9 in a complex called the apoptosome (figure 1.6).

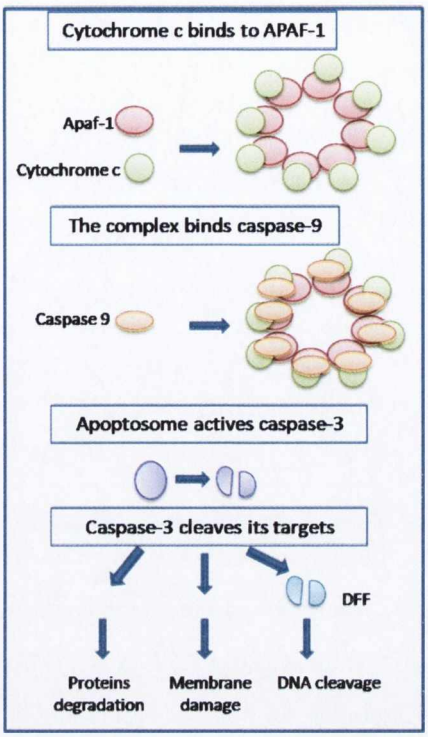

Figure 1.6: Formation of the apoptosome adapted from [27]. Cytochrome c leads the interaction of Apaf-1 with caspase-9, which activates caspase-3 followed by cleavage of target proteins that cause apoptosis.

This reaction takes place in several stages. Cytochrome c binds to the Apaf-1 protein, allowing it to bind adenosine triphosphate (ATP). This leads to oligomerization, which causes a conformational change that exposes the caspase-binding domain of Apaf-1. Apaf-1 then binds caspase-9. The incorporation of caspase-9 inside the apoptosome triggers self-cleavage and activation. Caspase-9 in turn cleaves and activates caspase-3 -6 and -7. A well-known target of this protease activity is the PARP enzyme (poly [ADP-ribose] polymerase), whose degradation is not essential, but is a useful diagnostic marker of apoptosis [45].

It has been identified as a pathway that leads to DNA fragmentation. The caspase-3 enzyme cleaves a subunit of a dimer called DFF (DNA fragmentation factor). The other subunit then activates a nuclease that degrades the DNA.

DNA degradation is also directly triggered by the release of an enzyme from the mitochondria called endonuclease G. Its normal function, inside the mitochondria, is related to DNA replication, but in apoptotic cells the enzyme is released and degrades nuclear DNA. This enzyme is important during the apoptotic process, although it is not that necessary for the eventual death of the cell. Apoptosis regulation involves not only

components that inhibit the signalled pathway but also those that trigger it. The apoptotic pathway can also be inhibited during the catalyzed stage by effector caspases. Proteins, called IAPs (inhibitors of apoptosis), can bind to pro-caspases and activated caspases in order to block the activity. The blocking activity of IAPs can be inhibited to allowed apoptosis to proceed. Mammalian cells contain a protein called Diablo/Smac, which is released from mitochondria together with cytochrome c followed by binding to IAPs [27].

1.5 PARP

PARP is a family of enzymes that consist of 18 nuclear proteins. They have roles in the repairing and regulation of DNA damage, in gene transcription, cell cycle progression, in chromatin function, in genomic stability and cell death. However the main function of these enzymes is the polymerization of linear or branched chains of ADP-ribose from a donor molecule NAD^+ and the transfer to acceptor proteins through covalent bonds [46].
PARP is composed of 3 main distinct regions: a N-terminal DNA-binding domain (DBD), which is composed of two zinc finger motifs, a central auto-modification domain, and a C-terminal catalytic domain. The caspase-cleaved domain is at Aspartic Acid 214 and Glycine 215 [47]. In the presence of damaged DNA (base pair-excised), the DNA-binding domain will bind the DNA and induce a conformational shift. It has been shown that this binding occurs independent of the other domains. This is integral in a programmed cell death model based on caspase cleavage inhibition of PARP. The auto-modification domain is responsible for releasing the protein from DNA after catalysis. Also, it plays an integral role in cleavage-induced inactivation. Upon DNA cleavage by enzymes involved in cell death, PARP can deplete the ATP of a cell in an attempt to repair the damaged DNA. ATP depletion in a cell leads to lysis and cell death followed by PARP cleavage separating the protein into a 24kDA (which include the DNA-binding domain) and 89kDA (which includes the auto-modification domain and catalytic domain) segment. The putative mechanism of PARP catalytic domain (PCD) activation via PARP inactivation relies on the separation of the DNA-binding region and the auto-modification domain. The DNA-binding domain, even if cleaved, is able to bind DNA but it is unable to dissociate from it without the auto-modification domain. As a consequence, the DNA-binding domain will attach to a damaged site and be unable to affect repair, as it no longer has the catalytic

domain. Moreover, it prevents other, non-cleaved PARP from accessing the damaged site and initiating repairs. PARP also has the ability to directly induce apoptosis, via the production of poly(ADP-ribose) (PAR), which stimulates mitochondria to release AIF (Apoptosis-inducing factor) a flavoprotein normally confined to the mitochondrial intermembrane space. This mechanism appears to be caspase-independent.

Poly (ADP-Ribose) polymerase-1 (PARP-1) is the most studied isoform of this family: it acts as a sensor of DNA damage and recruits complexes, repair proteins and chromatin remodelling [48]. The homology of its primary structure is high among vertebrates: the percentage of matching amino acid sequences between the human enzyme and the traditional murine enzyme is 92% and reaches 100% homology in the active site, which is the main family characteristic. PARP-1 has a molecular weight of 116 kDa and it is organized into 3 functional domains: the N-terminal DNA-binding domain (DBD) of 42kDa; the 16kDa self-modification domain; the 55kDa C-terminal domain with the catalytic activity. The DBD contains 2 zinc fingers and 2 helix-turn-helix motifs that recognize and bind to altered DNA structures [49]. In addition, codon 214 begins with a sequence recognized by caspases, which cleave the enzyme during apoptosis, inhibiting its activity. Cleavage of PARP-1 is recognised as a classical hallmark of apoptosis.

PARP-2 is responsible for only 10–15% of the total PARP activity fully stimulated by DNA strand-breaks in cells. Its catalytic domain is conserved among all the other family members to that of PARP-1 with 69% similarity. PARP-2 is a nuclear protein whose DNA binding domain differs from that of PARP-1 and targets DNA gaps but not nicks. The N-terminal domain of PARP-2, is responsible both for the localization of PARP-2 to the nucleus and the recognition of DNA interruptions. It displays homology with the SAP domain found in various nuclear proteins like APE-1 and Ku70, involved in chromosomal organization and in DNA repair [50].

PARP-2 acts as a chromatin modifier targeting histone H2B while PARP-1 targets histone H1. PARP-2 interacts with PARP-1, they share common partners involved in the single strand break repair (SSBR) and base excision repair (BER) pathways: XRCC1, DNA polymerase-, and DNA ligase III suggesting that they are both engaged in the same DNA repair complex [50, 51]. PARP-1 and PARP-2 interact also with proteins involved in the kinetochore structure and in the mitotic spindle checkpoint. However, specific partners of PARP-2 are hypostasised to act as the telomeric protein TRF2 suggesting a link with the control of telomere integrity.

The early response to DNA strand breaks is mediated by PARP-1. Recent studies reveal that the immediate synthesis of PAR at a DNA strand break constitutes an initiating event in a damaged cell triggering the subsequent co-ordination of DNA strand-breaks detection by PARP-1 and signaling to the SSBR pathway (the whole process being performed in less than 15 s) [51].

PARP-1 has different functions including [50]:

1. efficient sensing of the DNA break;
2. translation and amplification of the damage signal in a posttranslational modification of PARP-1 itself (automodification) and of histones H1 and H2B (heteromodification) that triggers chromatin structure relaxation and increases the access to the break;
3. PAR-dependent recruitment of XRCC1 to the damaged site mediated by its BRCT1 motif that displays high affinity to PAR and PARP-1.

XRCC1 has a scaffold protein with no known enzymatic function plays a critical role in the co-ordinated handling of the damaged DNA, from one repair enzyme to the next, in the BER pathway. The absence of PARP-1 or the inhibition of its enzymatic activity totally prevents the dynamic recruitment of XRCC1 to the break, thus explaining the important delay in strand-break rejoining that causes a severe DNA repair. However, the absence or inhibition of PARP-2 cannot be attributed to a lack of XRCC1 recruitment, since this step still occurred following DNA breakage. Rather, PARP-2 activity seems to be associated to a subsequent step in the SSBR pathway [50, 51].

PARP-1 activity induced by high levels of DNA breaks renders PARP-1 a risky cellular factor when the genome is being degraded during cell death. Therefore, to limit futile DNA repair during apoptosis and to preserve the NAD^+ and ATP pools, PARP-1 is inactivated by a caspase-dependent cleavage. A quite different scenario takes place in acute pathophysiological conditions such as necrosis or caspase-independent cell death (chromatinolysis) where PARP-1 is instrumentalized by the AIF. In response to DNA injury, AIF in concert with the endonuclease G translocates rapidly to the nucleus and degradates the chromatin into 50 kb fragments [50]. This large scale DNA fragmentation overactivates PARP-1 and kills the cells in a caspase-independent manner, thus leading to inflammatory injury in the corresponding tissue. Dawson and colleagues provided evidence that PARP-1 initiates a nuclear signal that propagates to mitochondria and triggers the release of AIF that leads to cell death. In relation to that, PARP-1-deficient

cells or pharmacologically inhibited wild-type cells are fully protected against excessive damage showing that the activation of PARP-1 has two opposed meanings depending upon the cell type and the extent of the DNA damage [50, 51]:

Survival: in replicating cells, limited damage to DNA induces PARP activity and stimulates the activation of DNA repair pathways through the recruitment of DNA repair factors (i.e. XRCC1). The decision for the cell to engage the apoptotic pathway after genotoxic stress takes place downstream of p53 activation, but the molecular determinants that switch between DNA repair and cell-cycle arrest or apoptosis are not yet fully understood. When apoptosis is induced, PARP-1 and -2 as survival factors are cleaved by caspases and are thus inactivated.

Cell death: In post-mitotic cells, reactive oxygen species (ROS) damage DNA, activates PARP and trigger AIF translocation to the nucleus. The resulting DNA fragmentation overactivates PARP and leads to nuclear condensation. Understanding the switch between these two facets of PARP biology might ultimately improve pharmacological strategies to enhance both antitumor efficacy as well as the treatment of a number of inflammatory and neurodegenerative disorders.

1.6 Mitochondria

The mitochondrion is a cellular organelle which morphology varies widely among different cell types (fibroblast mitochondria, for example, are usually long filaments with 1-10 μm in length and a fairly constant diameter of approximately 700nm) [52]. Mitochondria are found in all eukaryotic cells with some exceptions such as red blood cells. They are absent in prokaryotic cells like bacteria, where respiratory functions are performed by enzymes. It consists of a double membrane: the outer membrane allows the passage of small molecules; the inner membrane is selectively permeable and is folded in a number of windings, indentations and protrusions called mitochondrial cristae [52]. The function of these structures is to increase the membrane surface area allowing for a greater number of ATP synthase complexes thus providing more energy. The two membranes partition two different regions: the intermembrane space between the outer and inner membrane, and the matrix, the space circumscribed by the inner membrane [52]. The two sides of the inner membrane are called the matrix side and the cytosolic side or the N side

and P side because of the differing membrane potentials (neutral in the cytosolic side and positive in the inside intermembrane space). Mitochondria are the organelles involved in cellular respiration, containing respiratory enzymes, which are concentrated in the cristae. Oxygen is introduced inside mitochondria by using both cellular respiration and the food-derived catabolites and passing them down through the electron transport chain from which emerge both energy (ATP) and water [53].

Mitochondria change shape continuously through the combined action of fission, fusion, and motility. Fusion helps mitigate stress by mixing the contents of partially damaged mitochondria as a form of complementation whereas fission is needed to create new mitochondria, but it also contributes to quality control by enabling the removal of damaged mitochondria and can facilitate apoptosis during high levels of cellular stress [52, 54]. It has been discovered that disruptions in these processes affect normal development, and they have been implicated in neurodegenerative diseases, such as Parkinson's [54].

Mitochondrial fission and fusion processes are both mediated by large guanosine triphosphatases (GTPases) in the dynamin family that are well conserved between yeast, flies, and mammals [52]. Their combined actions divide and fuse the two lipid bilayers that surround mitochondria: the mitochondrial inner membrane, which encloses the matrix, is folded into cristae that contain membrane-bound oxidative phosphorylation enzyme complexes and the bulk of the soluble electron transport proteins such as cytochrome c, whereas the smooth mitochondrial outer membrane encapsulates the inner membrane and an intermembrane space [54].

Fission is mediated by a cytosolic dynamin family member (Drp1 in mammals). Drp1 is recruited from the cytosol to form spirals around mitochondria that constrict to sever both inner and outer membranes. Mid49, Mid51 and Mff recruit Drp1 to mitochondria, often at sites where mitochondria make contact with the endoplasmic reticulum [52]. Fusion between mitochondrial outermembranes is mediated by membrane-anchored dynamin family members named Mfn1 and Mfn2 in mammals, whereas fusion between mitochondrial inner membranes is mediated by a single dynamin family member called Opa1 in mammals. Mitochondrial fission and fusion machineries are regulated by proteolysis and posttranslational modifications [54].

The rates of mitochondrial fission and fusion respond to changes in metabolism and each of these effects is consistent with a model in which mitochondrial dynamics help to maximize the capacity for oxidative phosphorylation under stressful conditions [55].

Mitochondrial fusion occurs when [54]:

1. they are forced to rely on oxidative phosphorylation by withdrawing glucose as a carbon source;
2. it is necessary to maximize the fidelity for oxidative phosphorylation by stimulating complementation among mitochondria;
3. treatments directly or indirectly inhibit protein synthesis;
4. mTOR (mammalian target of rapamycin) inhibition–induced autophagy
5. starvation-induced autophagy by increasing the reliance on oxidative phosphorylation through the metabolism of lipids and proteins. Alternatively, starvation may evoke a specific stress response called stress induced mitochondrial hyperfusion, or it may inhibit fission to protect mitochondria from autophagic catabolism when they are most needed.

Mitochondrial stress-damage can be due to environmental insults such as radiation and toxic chemicals or genetic mutations in genes for metabolic processes or repair pathways. Some mitochondrial damages are spontaneous such as ROS generation, a by-product of the electron transport chain which leads to protein, lipid and DNA damage [52]. The problem caused by this damage can be the loss of metabolic functions such as ATP synthesis by ROS-damaged proteins in the electron transport chain which lead to the generation of even more ROS. Alteration of the electron transport chain may lead to the ATP synthase to consume ATP to generate membrane potential instead of making ATP. The cellular responses to the mitochondrial damage are different [52]. For example, mitochondria use quality control proteases to eliminate damaged proteins and respond to unfolded protein stress in the matrix through transcriptional induction of chaperone expression. Moreover, damaged mitochondrial outer membrane proteins also may be removed by the ubiquitin proteasome quality-control pathway [52, 54]. Mitochondria respond to genotoxic damage by some, but not all, of the DNA repair pathways found in the nucleus. These proteotoxic and genotoxic damage-response pathways target individual molecules for quality control, thereby rescuing mitochondria with minor damage without the need for altered fission or fusion rates. Elimination of mitochondria by autophagy is another level of quality control which is a process that is linked to mitochondrial fission and fusion [54].

During autophagy, cells form double-membraned vesicles, autophagosomes, which sequester organelles, proteins, or portions of the cytoplasm for delivery to the lysosomes [56]. The sequestered contents are degraded in the lysosome, allowing cells to eliminate

damaged or harmful components through catabolism and recycling to maintain nutrient and energy homeostasis. Autophagy constitutes a major protective mechanism that allows cells to survive in response to multiple stressors and that helps defend organisms against degenerative, inflammatory, infectious and neoplastic diseases [56]. Autophagy has been seen as an adaptive response to survival, whereas in other cases it appears to promote cell death and mitophagy [56]. It has been shown that mitophagy could be prevented with a dominant negative mutant of Drp1, suggesting that fission is required in mitophagy [54].

When stressed cells cannot repair the damage, apoptosis occurs. High levels of cell stress that lead to apoptosis also lead to excessive fission of mitochondria [54].

Mitochondria are very dynamic organelles, capable of changing size and shape and mitochondria motility was found to be regulated by Calcium (Ca^{2+}) [57, 58]. Additionally, they undergo short- and long-distance vectorial transport mediated by association with the cytoskeleton and there is evidence that mitochondria need to be strategically localised at particular subcellular sites both for providing energy supply and for participating in intracellular signalling [57, 58].

Various studies on biogenesis and dynamics of mitochondria during the cell cycle have shown that entry of cells into the G1 phase of the cycle is associated with a burst of mitochondrial activity and it appears that progression through the cycle is supported by non-respiratory modes of energy generation [55]. In fact, very recent findings in cells of mammals indicate that cyclin D1 which is involved in the phosphorylation and inactivation of the pRB, marking the entry of cells into the S phase of the cycle, inhibits mitochondrial function and represses the activity of NRF-1, a nuclear factor that masters the transcriptional expression of nuclear-encoded mitochondrial genes [55].

The regulation of the expression of β-F1-ATPase is exerted at the level of translation. The β-F1-ATPase mRNA (β-mRNA) further provides an example of a mitochondria localized mRNA in both mammalian and lower eukaryotic cells whose efficient translation depends on the 39 non-translated region (39UTR) of the mRNA [55]. In other words, the relevance that the 39UTR of β-mRNA has for the synthesis of the protein at G2/M illustrates the role that a regulatory mRNA sequence has for the appropriate biogenesis of mitochondria in the daughter cells with the same bioenergetic phenotype than that of the parental cell highlighting a previously unappreciated relationship between the control of translation at G2/M and the biogenesis of mammalian mitochondria that is likely to influence the cancer field [55]. The knowledge of the timing of the biosynthesis of the different mitochondrial

constituents and on the mechanisms that regulate their biosynthesis during cellular proliferation is scarce or remains largely unknown. Moreover, even less explored are the dynamics and changes in mitochondrial morphology during mitosis, a process that is likely to impact on the development of mitochondrial function and on the segregation of the organelles during progression through the cell cycle [55].

1.6.1 Energy production

The mitochondrion is able to perform multiple functions including roles in apoptosis; cell cycle regulation; redox regulation of the cell; heme synthesis; cholesterol synthesis (which is a phenomenon that occurs in the cell cytoplasm and that starts with the acetylCoA) and heat production. However, energy production is the main function of mitochondria and is performed using the main products of glycolysis: pyruvate and NADH. They are exploited in two processes: the Krebs cycle and oxidative phosphorylation.

Oxidative phosphorylation is a metabolic pathway during which electrons are transferred from electron donors to electron acceptors in redox reactions. These redox reactions release energy to form ATP and they are carried out by a series of proteins complexes within mitochondria called electron transport chains. The energy release by electrons flowing through this electron transport chain is used to transport protons across the inner mitochondrial membrane, in a process called *chemiosmosis*, which generate a potential energy in the form of a pH gradient and an electrical potential across this membrane. Oxidative phosphorylation consists of two reactions, which are dependent one to the other (one reaction cannot occur without the other): using energy-releasing chemical reactions (the electron transport chain) to drive energy-requiring reactions (ATP synthesis). The electron transport chain is a process where the electrons are transferred from electron donors such as NADH and $FADH_2$ to electron acceptors such as oxygen: this is an exergonic process that leads to the electrochemical gradient across the membrane called *proton-motive force*. ATP synthesis, which is an endoergonic reaction, occurs through phosphorylation of ADP by the enzyme ATP synthase with rotational catalysis: the enzyme ATP synthase release this stored energy allowing protons to flow down the electrochemical gradient, from the positive side of the membrane (P-side) back to the

negative side (N-side). The two components of the proton-motive force are thermodynamically equivalent.

After ATP synthesis, in order to restore the concentration of NADH into the matrix, the malate-aspartate shuttle is exploited. The malate-aspartate shuttle is a system for translocations of electrons produced during glycolysis across the semi-permeable inner membrane of the mitochondrion for oxidative phosphorilation. This system is required because NADH cannot cross the mitochondrial inner membrane. In the cytosol, malate dehydrogenase reacts with oxaloacetate and NADH to produce malate and NAD^+: two electrons generated from NADH and an accompanying H^+, are attached to oxaloacetate to form malate. Once malate is formed, the first antiporter called malate-alpha-ketoglutarate imports the malate from the cytosol into the mitochondrial matrix and simultaneously exports alpha-ketoglutarate from the matrix into the cytosol. After malate reaches the mitochondrial matrix it is converted into oxaloacetate by mitochondrial malate dehydrogenase, during which NAD^+ is reduced to form NADH and an H^+. Oxaloacetate is then transformed into aspartate (since oxaloacetate cannot be transported into the cytosol) by mitochondrial aspartate aminotransferase. The amino radical is supplied by glutamate, which is transformed into alpha-ketoglutarate in the process by the same enzyme. The second antiporter, the glutamate-aspartate, imports glutamate from the cytosol into the matrix and exports aspartate from the matrix to the cytosol. Once in the cytosol, aspartate is converted by cytosolic aspartate aminotransferase to oxaloacetate [59]..

Briefly, mitochondria synthesize ATP from adenosine diphosphate (ADP) and inorganic phosphate in a process called oxidative phosphorylation. Mitochondria burn food in the presence of oxygen to produce ATP. The process, greatly simplified, has three main steps.

1. The citric acid cycle breaks down the pyruvate (a product of the metabolism of glucose) and the β-oxidation pathway metabolises fatty acids. Both require energy to reduce the electron carrier NAD^+, producing NADH, and FAD, yielding $FADH_2$.
2. The electron transport chain in cells with mitochondria (called the respiratory chain) uses the energy of electrons to pump hydrogen ions (protons) into the intermembrane space. The electron transport chain consists of five complexes named from I to V.
3. ATP synthesis takes place in complex V of the electron transport chain, which uses the energy from the protons refluent in the matrix in order to attach phosphate

atoms to the ADP molecules, producing ATP. ATP comes out through the channel of adenosine nucleotide translocase (ANT), where ATP is exchanged for ADP.

1.6.2 Stoichiometry

For each molecule of NADH oxidized, 2.5 molecules of ATP are produced. For each molecule of $FADH_2$ 1.5 molecules of ATP are produced. Through the glycolytic oxidation of one molecule of glucose, the subsequent conversion of the molecules acetylCoA into pyruvate and the Krebs cycle, 8 molecules of NADH and 2 $FADH_2$ are synthesized in total. The energy value stored in these molecules is converted to a total of 23 molecules of ATP.

It is important to note that these values are only theoretical, but in fact the yield of the synthesis of ATP is lower because of the permeability of the membrane to protons.

Some molecules are able to inhibit some steps of oxidative phosphorylation. For this reason, they have the same effects as toxins.

1.7 PDT and photosensitizing agents

1.7.1 History of PDT

Different methods used until now to treat cancer, cited above, are sometimes not effective, so research is continuing to be able to understand the mechanisms of cancer evolution and find new ways to effectively deal with it. Such research has led in the last years to photochemotherapy or photodynamic therapy [16]. Photodynamic therapy (PDT) represents a new method of treatment in cancer characterized by the combination of a light source with a photosensitizing agent that causes a cytotoxic event against tumour tissues. The therapeutic effect is mediated by the generation of ROS and/or the formation of singlet oxygen ($^1O_2$), a process that depends on the photosensitizing agents interactions with light and oxygen [14].

PDT has a long history that begins a century ago. In 1888, Moracci claimed, without presenting data that the toxicity of quinine and cinchonamine to enzymes, plants and frog eggs was greater in the light than in the dark [60]. Quinine is a bitter crystalline alkaloid

obtained from cinchona bark that is used as a flavouring agent, has antipyretic and analgesic properties, and is administered orally in the form of its salts (as the hydrated sulfate) as an antimalarial. Cinchonamine is a white crystalline alkaloid obtained from some South American shrubs (genus Remijia) of the Madder family that has been used as a substitute for and is more toxic than quinine. At that time, the discovery was not given significance, but a decade later, Professor Hermann von Tappeiner and Oscar Raab observed that the toxicity of acridine to paramecia (unicellular ciliate protozoa) increased with the amount of sunlight in the laboratory [16], as published in 1900. Acridine is a colourless crystalline compound occurring in coal tar and important as the parent compound of many dyes and pharmaceuticals. Professor Hermann von Tappeiner, who follow his observations, then coined the German term that translated to "photodynamic action", and conducted the first clinical test of PDT with eosin for skin cancer and other skin conditions [60]. Eosin is a red fluorescent dye obtained by the action of bromine on fluorescein and used in particular in cosmetics and as a toner; also: its red to brown sodium or potassium salt is used as a biological stain for cytoplasmic structures. However, it wasn't until the mid-century that there was interest in the effects of photodynamic action, when it was reported that injected hematoporphyrin accumulated in tumours in rats and, upon illumination, led to necrosis of the tumour. Schwarts, Winkelman and Lipson published a series of papers demonstrating that the fluorescence of the porphyrin photosensitizers, in particular, the preparation known as hematoporphyrin derivative (HPD), could be used to detect tumours [61]. The HPD is a complex mixture of porphyrin derived from hematoporphyrin [62]. Porphyrins are a group of organic compounds that can bind metals: a porphyrin without metal in its cavity is a free base; a porphyrin containing iron is called heme. Heme-containing proteins, or hemoproteins, are found extensively in Nature, such as the pigment in red blood cells, heme. In the 1970s, Thomas J. Dougherty initiated the "modern photodynamic therapy" recognising the potential of PDT for tumour treatment and demonstrated that HPD had efficacy in the treatment of human tumours metastatic to the skin. The hydrophobic fraction of HPD was termed dihematoporphyrin ether/ester (DHE) and, after original name changes, is now referred to as Photofrin® (porfimer sodium) (figure 1.7).

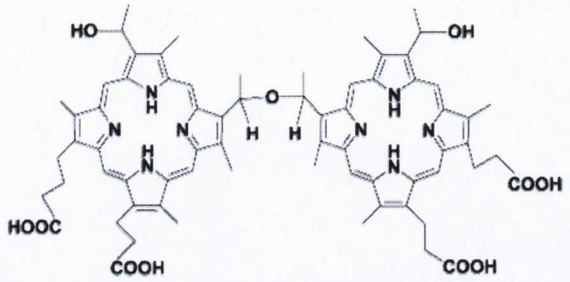

Figure 1.7: Compound Photofrin® taken from [63]

Photofrin was approved as a PDT compound for the first time in 1993 in Canada for the treatment of bladder cancer at an early stage. After that, the approval of PDT therapy in oncology has been obtained in other countries for the treatment of various cancers including oesophageal and lung cancer [64, 65]. Moreover, confirmation was obtained of the validity of this methodology in localized cases at an early stage with few side effects. In addition, PDT seems to be suitable as palliative therapy for untreatable patients. Since the discovery of the effectiveness of experimental photoactivated Photofrin in its clinical use, several years have passed. In fact, Photofrin is not the optimal photosensitizer for PDT in clinics for different reasons. First of all, it absorbs at 630 nm. Most relevant to PDT is visible light, which covers the limited range of 400-700nm of all electromagnetic radiation. However, in practice, the range of light used in PDT is mainly 600-900nm, since endogenous molecules, such as haemoglobin, have a strong absorption below 600nm and therefore capture most of the incoming photons. The 900nm upper limit is due to the energy content of the photons at higher wavelengths, which is not sufficient to induce the generation of $^1O_2$. In most cases oxygen is required to obtain an effective biological response. Use of photosensitizers which absorb light at higher wavelengths between these limits has been an important focus of research, since light at longer wavelengths can penetrate deeper into the tissue [1].

What is more, Photofrin is a mixture of unstable products and has a poor selectivity for cancer cells. Generally, the selective tumour uptake is probably not due to special properties of tumour cells, but rather to differences in the physiology between tumours and normal tissues as described in the previous paragraph [1].

Finally, Photofrin triggers side effects against healthy tissues include skin necrosis and skin ulcers [66]. This forces the patient to stay away from direct sunlight during the period of photosensitivity. In most cases, the patient requires lengthy hospital stays. However, with the discovery of second generation photosensitizers, with greater ability to penetrate

tissue and fewer side effects, PDT has raised more interest in oncology and in other branches of medicine.

1.7.2 Second generation photosensitizers

The use of visible light for phototherapeutic purposes rose with the increase in knowledge on the optical properties of tissues: the light in the spectral region between 600-1000nm (phototherapeutic window) has full power of penetration in most tissues of the human body. This is related to the low absorption coefficient of cellular constituents in this region and to its inefficient scattering of red light by these cellular organelles. The recent introduction of "second generation" photosensitizers has been a significant success for different reasons: they have provided greater selectivity of antitumour action, a more efficient photo-activation and a notable lower incidence of side effects. Moreover, they have a better pharmacokinetic profile than original PDT compounds due to an excitation range greater than 650nm, the possibility of action against deep tumours and also a faster time of drug elimination, resulting in fewer photosensitivity skin side effects. This allows the patient to be exposed to direct sunlight only a few days after treatment.
An example of a second generation photosensitizer is Foscan® (figure 1.8), which was approved in Europe for the palliative treatment of neck and head cancers in 2001.

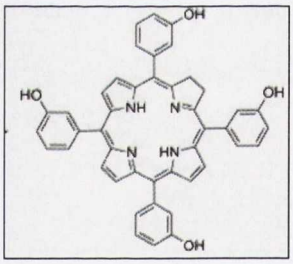

Figure 1.8: Compound Foscan® adapted from [67]

It is excited at 652 nm using a diode light and the penetration in tissues is about 8-10mm. The illumination time for Foscan is 200 sec. Foscan is a temoporfin, a single pure chlorine derivative and its chemical name is meso-tetra-hydroxyphenyl-chlorine [68]. It is an anticancer drug activated by light and is currently used for squamous carcinomas of the head and neck. In clinical practice, Foscan has been used in patients with advanced cancer who have failed previous treatment or who are not candidates for surgery, radiotherapy or

chemotherapy. Moreover, it has been used as a palliative treatment with the objectives of reducing the size of the tumour, reducing symptoms, preventing complications and preserving organ function.

Clinical trials have already been performed on the effectiveness of Foscan PDT in the treatment of carcinoma of the oral cavity. D'Cruz *et al.,* have conducted a multicentre study of 128 patients with recurrent/refractory squamous cell carcinoma of the head and neck in an advanced state who had failed previous therapy or had no indication to be treated with traditional methods [69]. The results obtained were encouraging. Hopper *et al.,* have conducted a multicenter study to test the validity of Foscan PDT in patients with oral cancer in its early stages [70]. It maintained functional integrity of the mouth and excellent cosmetic healing. Copper *et al.,* also carried out a study of 25 patients with squamous carcinoma cell of the oral cavity and oropharynx [71]. Once again with Foscan, PDT has proven a viable alternative to surgery and radiotherapy and has also demonstrated a high efficacy and long-term reduction in morbidity.

1.7.3 Mechanism of action of photosensitizers

Upon illumination, the photosensitizer is excited from a ground state (S_0) to the first excited single state (S_1), followed by conversion to the triplet state (T_1) via intersystem crossing. The longer life time of the triplet state enables the interaction of the excited compound with the surrounding molecules, the generation of the cytotoxic species produced during PDT occurs whilst in this state. The singlet excited photosensitizer either decays back to the ground state, resulting in fluorescence or undergoes intersystem crossover to the longer lived triplet excited state. Tumour destruction is most efficient using compounds with a long triplet half-life and a high quantum yield for the triplet excited state for the generation of $^1O_2$ [72].

The interaction of the triplet sensitizer with surrounding molecules results in two types of photo-oxidative reactions:

The **Type I** pathway involves electron or hydrogen atom transfer, producing radical forms of the photosensitizer or the substrate. These intermediates may react with oxygen to either form ROS such as superoxide anions (O^-_2) or hydroxyl radicals (·OH), which initiate free radical chain reactions.

The **Type II** mechanism is mediated by the energy transfer process from the photosensitizer triplet to ground state molecular oxygen ($^3O_2$) to generate $^1O_2$, a non radical but highly reactive form of oxygen. The in situ generation of $^1O_2$ via the type II pathway appears to play a central role in photodynamic cytotoxicity because of the highly efficient interaction of the $^1O_2$ species with different biomolecules.

A simplified energy level diagram representing the activation of a PDT agent, leading to the formation of $^1O_2$ is shown in figure 1.9.

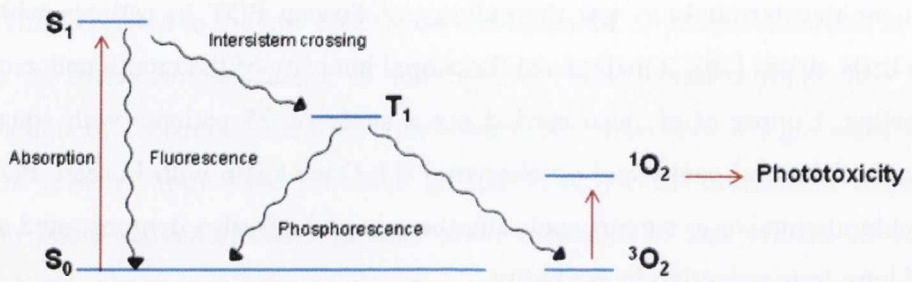

Figure 1.9: A simplified energy level diagram representing the activation of a PDT agent, leading to the formation of $^1O_2$ adapted from [73]

Any number of subcellular targets can be attacked during PDT including mitochondria, lysosomes, plasma membranes and nuclei and the exact target can affect whether cell death occurs by necrosis or apoptosis (see section regarding cell death) [74-77]. The site of the primary localization of the sensitizer strongly depends on the lipophilic or hydrophilic character of the drug considered and because of limited migration of $^1O_2$ from the site of its formation, sites of initial cell or tissue damage of photosensitization are closely related to the localization of the sensitizer [72]. In general, hydrophobic drugs attack the tumor cells mainly by direct interactions. In contrast, water-soluble sensitizers kill hyperproliferating cells indirectly by damaging blood vessels and interrupting the supply of oxygen and other essential nutrients [72]. Finally, it has been shown that PDT can induce inflammation and other tumour-specific immune reactions. The exact method of PDT-induced tumour destruction depends on the photosensitizers used and varies greatly depending on the condition being treated and the light dose used.

1.7.4 ROS production in PDT

As mentioned before, oxygen is required for the photodynamic effect in most cases. PDT requires the same localisation of the photosensitizer, light and oxygen to induce a photodynamic reaction and response. Several studies have shown that PDT efficacy is oxygen dependent, which is mediated by $^1O_2$, the ROS responsible for most photodynamic processes in biological systems [1]. Only recently, has it been possible to detect $^1O_2$ *in vivo* [78]. Other ROS such as $^{\cdot}OH$ and O^{-2} may well be equally involved [79]. ROS are generated in many processes within the cell. Membrane proteins, cytosolic enzymes (such as cyclooxygenase), lipid metabolism in peroxisomes all involve production of a small amount of free radicals.

Another site of ROS production is the nucleus. Despite the fact that NADPH-dependent $O^{\cdot}_2$ production by the nucleus was discovered over three decades ago, the regulation and function of nuclear $O^{\cdot}_2$ remain largely uncharacterized [80].

The vast majority of ROS (estimated at around 90%) is produced by mitochondria during oxidative phosphorylation. During this process, nicotinamide adenine dinucleotide (NADH) or flavine adenine dinucleotide ($FADH_2$) is used to generate a proton gradient between the matrix and intermembrane space. Normally the electrons generated by NADH pass through the respiratory chain and are used to produce water and to transfer protons into the intermembrane space, generating a membrane potential.

But sometimes these electrons can react with a molecule of oxygen to give the $O^{\cdot}_2$. This $O^{\cdot}_2$ can be converted to hydrogen peroxide (H_2O_2) by the enzyme manganese superoxide dismutase (located in the matrix) or by the enzyme superoxide dismutase copper/sulfur (localized in the cytoplasm and the intermembrane space). H_2O_2 is more stable than $O^{\cdot}_2$ and it can diffuse through the membranes outside the mitochondria to the nucleus or it can be inactivated by the enzyme glutathione peroxidase or the catalase enzyme. However, in the presence of reduced transition metals, H_2O_2 can also be converted into the highly reactive $^{\cdot}OH$ species. In general, because mitochondria are the main source of ROS in the cell, they are more affected by the effect of cellular oxidative stress than other organelles.

Free radical synthesis is also, if properly controlled, a process that can act against certain microorganisms. During inflammation, for example, polymorphonuclear leukocytes are subject to a mass production of these radicals by activation of the enzyme nicotinamide adenine dinucleotide phosphate (NADPH) oxidase. To cope with the presence of free

radicals, which could result in serious damage, the cell has to use specific systems suitable for their elimination [59]:

- Catalase, is an enzyme that catalyzes the reaction of elimination of H_2O_2 ($2H_2O_2 \rightarrow O_2 + 2H_2O$);
- Glutathione (GSH) results in the elimination of free radicals using a sulfhydryl group in its reduced form ($H_2O_2 + 2GSH \rightarrow$ GSSG (glutathione homodimer) + $2H_2O$, $2OH^{\bullet} + 2GSH \rightarrow GSSG + 2\ H_2O$);
- Other antioxidants such as ascorbic acid, vitamins A and E and the superoxide dismutase group also have roles in protecting against ROS.

1.7.5 Ruthenium properties suited to biological applications

The current use of ruthenium-based drugs is varied and the activity of each compound is a function of the oxidation state of the metal and the nature of the attached ligands. Ruthenium-based drugs are used as immunosuppressant clinical agents in the treatment of a broad range of diseases, including aplastic anaemia, severe eczema, glomerulonephritis, psoriasis, systematic sclerosis and psoriatic arthritis. Moreover, ruthenium can be coordinated to organic antibiotic compounds, which often results in higher *in vitro* activity. Nitric oxide (NO) plays a central role in many physiological processes including signalling, regulation of cardiovascular function and immunological response to microorganisms and tumour cells. Malfunction of NO production results in many physiological symptoms. Ru(III)-based drugs have been shown to enhance the activity of vasoconstrictor drugs and are proposed for the treatment of diseases that involve overproduction of NO including stroke, septic shock, arthritis, inflammatory bowel disease, epilepsy and diabetes. Basically, Ru(III) binds NO rapidly and strongly, resulting in the reduction of the metal ion to form a linear Ru(II)-NO adduct. Last but not least, ruthenium-based drugs have anticancer activity. Many Ru(II), Ru(III) and Ru(IV) complexes with different ligands have been found to bind DNA. However, many of these compounds are barely soluble in aqueous solution, which is necessary to allow efficient administration and transport. In NAMI-A (figure 1.10), for example, solubility has been increased by using dialkyl sulfoxide derivatives, which is now recognised as the most successful ruthenium-based anticancer compound. NAMI-A shows a strong efficacy against solid tumour metastases such as lung cancer [81]. Moreover, it has concluded a

phase I clinical evaluation, showing a relatively low toxicity and the absence of renal toxicities at the maximal tolerated dose.

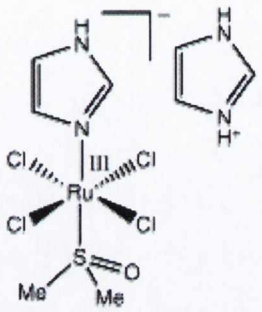

Figure 1.10: Compound NAMI-A adapted from [82]

In general, even if NAMI-A can bind DNA, *in vivo* DNA damage does not appear to be part of its anticancer mechanism on metastasis. Conversely, NAMI-A was shown to bind tightly to serum albumin and serum transferrin, two representative plasma proteins, suggesting that binding of specific proteins may represent the molecular basis for its peculiar biological activity. It was also suggested that binding of Ru(III) complexes to serum transferrin might help to target cancer cells taking advantage of the specific receptor-binding mechanism of transferrin, but these results remain controversial [83]. What is expected from a drug is to bring about apoptosis, which is a programmed and a controlled cell death compared to necrosis (another kind of cell death), which causes inflammation and damage to adjacent cells. What is more, some ruthenium complexes have been shown to damage DNA, either directly or indirectly, for example, by positioning radiosensitisers close to DNA. Moreover, they can interact with proteins, and it is likely that both activities contribute to the anticancer properties of the compounds. The biological properties of ruthenium in medicine have been reviewed in [84].

The main properties of ruthenium compounds are as follows:

Firstly, the rate of ligand exchange is an important determination of biological activity, as very few metal drugs reach their biological target without being modified. As the rate of ligand exchange is dependent on the concentration of the exchanging ligands in the surrounding solution, diseases that alter these concentrations in cells or in the surrounding tissues can have an effect on the activity of the drug.

Moreover, the range of accessible oxidation states, which are Ru(II), Ru(III) and Ru(IV), are all accessible under physiological conditions. In these oxidation states the ruthenium

centre is predominantly hexacoordinate with octahedral geometry. Ru(III) complexes tend to be more biologically inert than related Ru(II) and Ru(IV) complexes. The redox potential of a complex can be modified by varying the ligands and thus exploited to improve the effectiveness of drugs in the clinic. In many cases, the altered metabolism associated with cancer and microbial infection results in a lower oxygen concentration in these tissues compared to healthy ones and this promotes a reductive environment. If the more active Ru(II) complex leaves the low oxygen environment, it may be converted back to more inert Ru(III) by a variety of biological oxidants. Cancer cells are also known to have higher levels of glutathione and a lower pH than healthy tissues, also creating a strongly reducing environment. Mitochondrial and microsomal electron transfer proteins can catalyze the reduction of Ru(III) to Ru(II). Transmembrane electron transport systems can also reduce Ru(III) complexes outside of the cell and this is highly relevant to the mechanism of action of a ruthenium based drug in clinical use which has anticancer activity independent of cell entry.

Finally, ruthenium has the ability to mimic iron in binding to certain biological molecules, including serum transferrin and albumin and this may be the reason for the low toxicity of ruthenium drugs. These two proteins are used by mammals to solubilise and transport iron, thereby reducing its toxicity. Since rapidly dividing cells, such as cancer cells, have a greater requirement for iron, they increase the number of transferrin receptors located on their cell surfaces, thereby sequestering more of the circulating metal-loaded transferrin.

All of the biological properties of ruthenium described above make this element a suitable choice for the basis of designing novel compounds which preferentially target cancer cells over healthy cells [84].

1.7.6 Photophysical properties of Ru(II) polypyridyl complexes

In order to understand the interaction between Ru(II) polypyridyl complexes with DNA, an explanation of their photophysical properties is necessary. The energy level diagram in figure 1.11 describes the photophysical mechanism of the complex $Ru(bpy)_3^{2+}$, which is the most studied one [85]. Upon irradiation in the visible absorption band of $Ru(bpy)_3^{2+}$, the exited state of a single metal to ligand charge transfer (MLCT) is populated. This state deactivates rapidly by intersystem crossing (ISC) to lowest lying triplet MLCT state (^{3}MLCT), which correspond to three energy states. These three energy states are very close

in energy to each other and a fourth state is slightly higher in energy. The deactivation of ^{3}MLCT state can occur via radiative deactivation, which is responsible for the observed emission in the wavelength region of 600nm; radiationless activation, which generally controls the lifetime of the ^{3}MLCT state in many of Ru(II) complexes; conversion to the upper triplet metal-centred state (^{3}MC) by thermal activation.

Both the ^{3}MLCT and ^{3}MC states exhibit two types of exited states reactivities: ^{3}MLCT exhibits both oxidation and reduction depending on the conditions; ^{3}MC state usually results in the loss of the ligand.

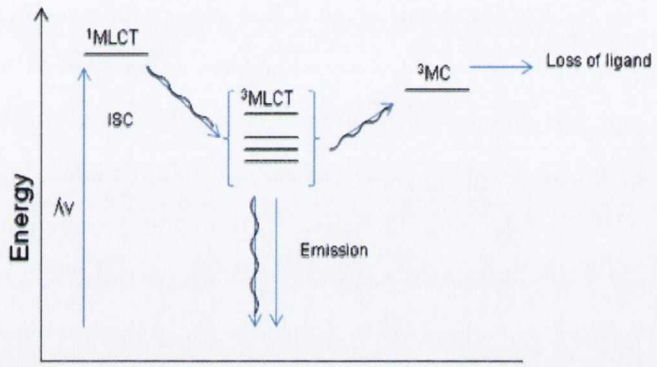

Figure 1.11: Energy level diagram for the lowest excited states of $Ru(bpy)_3^{2+}$ adapted from [73]

1.8 DNA structure and metal binding

The cationic character of metal ions and complexes, their three-dimensional structural profiles, and propensity for performing hydrolysis, redox, or photoreactions, leads to a natural aptitude for interacting with DNA. DNA being the base of cellular transcription and translation, the binding to single-stranded and double-stranded DNA and its cleavage is an obvious target for therapeutic intervention and the development of diagnostic structural probes. This is the reason why new metal complexes have been designed with the aim of utilising or creating open coordination positions for DNA binding and hydrolysis, generating ROS or other radicals for DNA oxidation, or perform direct redox reactions with DNA. Some Ru(II) compounds have been shown to bind DNA, for example, antitumour monodentate Ru(II) arene compounds bind preferentially to N-7 of guanine residues in double-stranded DNA [86].

DNA whose structure was first discovered by James D. Watson and Francis Crick, consists of a double anti-parallel helix polymer of simple units called nucleotides, with backbones made of sugars and phosphate groups joined by ester bonds. Attached to each pentose sugar (2-deoxyribose), there is one of the four bases found in DNA which are classified into two types: the purines, adenine (A) and guanine (G) (heterocyclic compounds) and the pyrimidines, cytosine (C), and thymine (T). A fifth pyrimidine nucleobase, uracil (U), usually takes the place of thymine in RNA and differs from thymine by lacking a methyl group on its ring. The sequence of these complementary nucleobase pair (purines form hydrogen bonds to pyrimidines, with A bonding only to T, and C bonding only to G) along the backbone encodes the genetic information, which specifies the sequence of the amino acids within proteins. The code is read by copying stretches of DNA into the related nucleic acid RNA in a process called transcription. The double helix is joined together by phosphate groups that form phosphodiester bonds between the third and fifth carbon atoms of adjacent sugar rings. The DNA double helix is stabilized primarily by two forces: hydrogen bonds between nucleotides and base-stacking interactions among the aromatic nucleobases. The grooves are the spaces between the strands in the double helix, which are adjacent to the base pairs and may provide a binding site. As the strands are not directly opposite each other, the grooves are unequally sized: the major groove, in which the edges of the bases are more accessible to proteins like transcription factors, and the minor grove. B-DNA is the classic helical structure described by Watson and Crick, which is the right handed anti-parallel double helix of DNA structure. As hydrogen bonds are not covalent, they can be broken and rejoined relatively easily for example either by a mechanical force or high temperature. DNA exists in many possible conformations that include also A-DNA and Z-DNA forms, although, only B-DNA and Z-DNA have been directly observed in functional organisms. The conformation depends on the hydration level, DNA sequence, the amount and direction of supercoiling, chemical modifications of the bases, the type and concentration of metal ions, as well as the presence of polyamines in solution. Compared to B-DNA, the A-DNA form is a wider right-handed spiral, with a shallow, wide minor groove and a narrower, deeper major groove. The A form occurs under non-physiological conditions in partially dehydrated samples of DNA. Segments of DNA where the bases have been chemically modified by methylation may undergo a larger change in conformation and adopt the Z form. In this case, the strands turn about the helical axis in a left-handed spiral, the opposite of the more common B form. Molecular recognition of B-

DNA can take place in 5 distinct ways: major grove recognition, minor grove recognition, electrostatic binding (due to the broad electronegative cloud that surrounds the phosphate backbone), covalent binding to the bases and intercalation (due to the possession in many chemical species of an extended heteroaromatic ring system, a chromophore, which is approximately the same size as a DNA base pair).

1.9 Introduction to the compounds studied in this thesis

The development of low molecular weight agents with good water solubility, rapid cellular uptake, and selective localisation, which lead to programmed cell death, as cancer therapeutics for targeting DNA, is a highly topical area for research [87]. Thomas *et al.*, reported on the photophysical and DNA binding properties of a cationic water-soluble organic derivate of dppz (figure 1.12A) creating an improved synthesis of it: ethylene-bipyridydilyum-phenazyne (figure 1.12C) [88] This organic derivative of dppz is non-toxic in plants despite its structural similarity with the well-known weed killer, diquat (figure 1.12B). Moreover, it showed good water solubility and distinctive photophysical properties that allowed the interaction with DNA at relatively long wavelengths, without the need for Ru(II) centre.

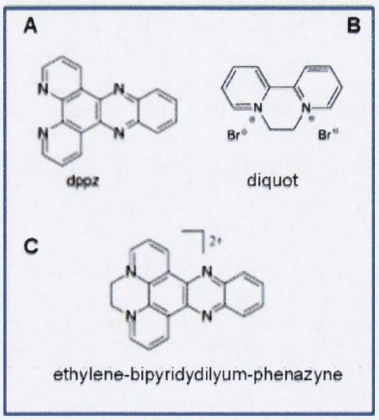

Figure 1.12: Structure of the water-soluble derivative of dipyrido[3,2-a:2′,3′-c]phenazine (dppz) (A), of the weed killer diquot (B) and of the compound ethylene-bipyridydilyum-phenazyne (C) adapted from [88]

In addition, studies revealed the cationic derivative of ethylene-bipyridydilyum-phenazyne exhibited an enhanced affinity for DNA with a binding constant calculated to be comparable to that of mononuclear [Ru(II)(dppz)] complexes [89]. Furthermore, it showed more affinity for GC over AT sequences, and a luminescence increase in the presence of $[poly(dAdT)]_2$ and a luminescence decrease in the presence of $[poly(dGdC)]_2$.

Taking into consideration all the above the organic pdppz derivative as a DNA probe and photocleavage agent potentially suitable in PDT, RE33 (figure 1.13), was synthesised by Robert B. P. Elmes from the Thorfinnur Gunnlaugsson research group, School of Chemistry at Trinity College Dublin.

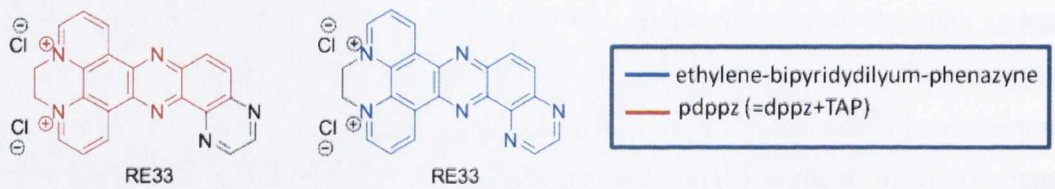

***Figure 1.13*:** Structure of the compound RE33

Other interesting examples in the literature of cationic dyes include xanthylium dye rhodamine 123 (Rh-123) (figure 1.14A) and thiopyrylium dye AA1 (figure 1.14B), which is related in structure to Rh-123. The importance of these cationic dyes is their affinity for mitochondria which is a driving force for investigating such molecules as photosensitizers for PDT.

Localization studies of Rh-123 showed that this cationic dye accumulates selectively in the mitochondria of certain cancer cell types. It is selectively toxic to certain cancer cell lines and gives prolonged survival *in vivo* in tumour-bearing animals. On the other hand, Rh-123 is a poor photosensitizer for PDT because of its low triplet yield, which limits its ability to produce $^1O_2$ so irradiation of Rh-123-treated cancer cells *in vitro* gives little if any added phototoxicity, irradiation of Rh-123-treated, tumour-bearing animals also gives no further increase in post-treatment survival [90].

AA1 inhibits mitochondrial ATP-ase activity, inhibits growth of the human colon carcinoma cell line CX-1 *in vitro*, and gives prolonged survival in mice implanted with several different tumour lines. As in studies with Rh-123, irradiation of either AA1-treated cancer cells *in vitro* or AA1-treated tumour-bearing animals gives no increase in either toxicity or survival [90]. Another example of a cationic dye used in PDT is a synthetic monocationic porphyrin which was tested as a photosensitizer toward cells in culture and

the RIF tumour (RIF-1 fibrosarcoma) *in vivo*. The aim of that study was to determine whether a positively charged porphyrin would show increased uptake by mitochondria and enhanced effectiveness as a photosensitizer for PDT. It was shown to be localized in the membranous structures of the cells, especially the plasma membrane, not in the mitochondria as expected. The inhibition of tumour growing *in vivo* that was observed was mainly due to vascular damage and not due [90] to direct cell kill as might be expected for a cationic compound

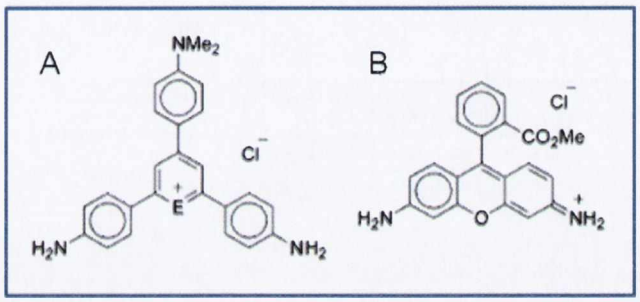

***Figure 1.14*:** Structure of the cationic dyes Rh-123 (A) and AA1 (B) adapted from [90].

With the aim to ameliorate the structure of the compound in order to increase the potentiality in binding DNA, Robert B. P. Elmes synthesised three novel Ru(II) complexes based on novel extended aromatic polypyridyl ligands, compounds RE30, 34 and 37 (figure 1.15).

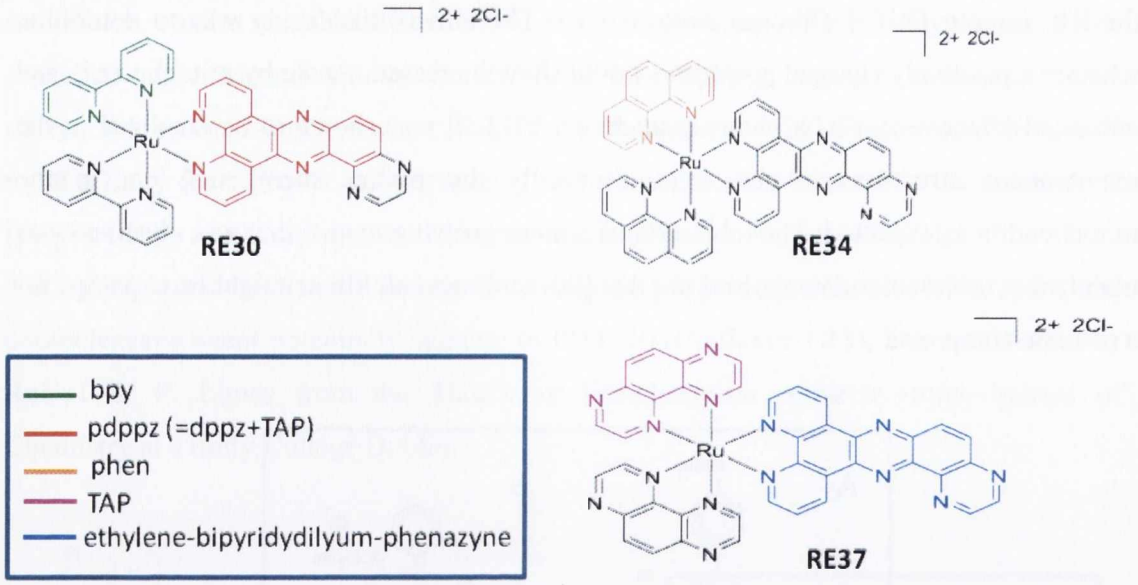

***Figure 1.15*:** Structure of compounds RE30, 34 and 37.

The different properties that make Ru(II) polypyridyl metal complexes excellent candidates for potential cancer therapeutics as well as spectroscopic DNA probes and photoreagents are: the photophysical properties (described in "Mechanism of action of Photosensitizers" section in the first Chapter); the positive charge of the Ru(II) polypyridyl metal complex which binds tightly to DNA via electrostatic binding to the phosphate backbone and water solubility. Moreover, by varying the ligands around the metal centre it has been possible to modify the interaction, where they may also bind by either groove binding or intercalation [91]. The simplest systems were based on bipyridine (bpy), and phenanthroline (phen) complexes of ruthenium. It was observed that while the first, $[Ru(bpy)_3]^{2+}$ bound to DNA weakly through electrostatic interaction, the second one $[Ru(phen)_3]^{2+}$was much stronger. This is due to the cationic nature of those complexes. It is also well established that both $[Ru(bpy)_3]^{2+}$ and $[Ru(phen)_3]^{2+}$ cause cleavage of DNA upon photoirradiation. Moreover, as described in "Mechanism of Action of Photosensitizers" section (in the first Chapter), these species are strongly oxidizing in the excited state and can abstract electrons from species which have high oxidation potential. In most cases the base oxidation responsible for DNA cleavage is as a result of $^1O_2$ formation [92], which diffuses along the helices, resulting in a single strand break.

The complex $[Ru(phen)_3]^{2+}$, with slightly extended heteroaromatic ligands, improves their intercalation ability. Among the complexes with extended aromatic heterocylic ligands, the most interesting is the incorporated dipyrido[3,2-a:2',3'-c] phenazyne (dppz) ligand. The large, planar surface area allows it to be inserted between the base-pairs of B-form double-stranded DNA. Barton *et al.*, described the interaction of the complex with DNA [91], and showed that in aqueous solution no photoluminescence was observed at ambient temperature, but in the presence of double helical DNA intense photoluminescence was observed; the difference between the 'on' and 'off' state of this complex has been described as the "light switch" effect [91]. Intercalation between the base-pairs provides protection from aqueous solvent molecules. This is very important because the complex $[Ru(phen)_2 (dppz)]^{2+}$ in aqueous solution has a low excitation state but the reason why this occurs still remains unclear.

In order to confer a strong oxidizing excited state on the complex, electron accepting ligands, such as tetraazaphenantrene (TAP), have been added to the Ru(II) complex. This state results in a photoinduced-electron transfer (PET) between guanine and the ^{3}MLCT state of the complex, which can result in both single-strand followed by double-strand cleavage, as observed with plasmid DNA [73].

Examples in literature of Ru(II) complexes as photodynamic therapy or cellular imaging include the amphiphilic Ru(II) polypyridyl-porphyrin conjugate, Ru-L (em = 675nm; ex = 800nm) (figure 1.16A), which showed great potential to be a bi-functional tumour-imaging and photodynamic therapeutic agent [93]. Cell-based studies of this complex conjugate were conducted using human nasopharyngeal carcinoma HK-1 and cervical carcinoma HeLa cells on which Ru-L showed rapid cellular uptake, low dark-cytotoxicity, and high photo-cytotoxicity [93]. Moreover, a series of Ru(II) polypyridyl complexes containing N,N-chelating ligands, RuPOP (figure 1.16B), showed antiproliferative activity and ability to induce mitochondria-mediated and caspase-dependent apoptosis in human cancer cells, which make it a potential candidate for further evaluation as a chemopreventive and chemotherapeutic agent for human cancers, especially for melanoma [94].

Ru(III) compound (NAM1-A) (figure 1.10), which has been shown to prevent the development and growth of pulmonary metastases in all the solid tumours on which it has been tested and has successfully completed the first round of clinical trials, and another Ru(II) compound (RAPTA-T) (figure 1.16C), which has shown similar activity *in vivo,* are both emerging as potential drugs for treating secondary tumours [95]. Furthermore, in the

last few years, there have been an increasing number of reports of the design and application in cellular studies of a diverse range of Ru complexes tailor-made for imaging applications where the design principles, uptake and cellular localisation of this new class of imaging agents were presented [96].

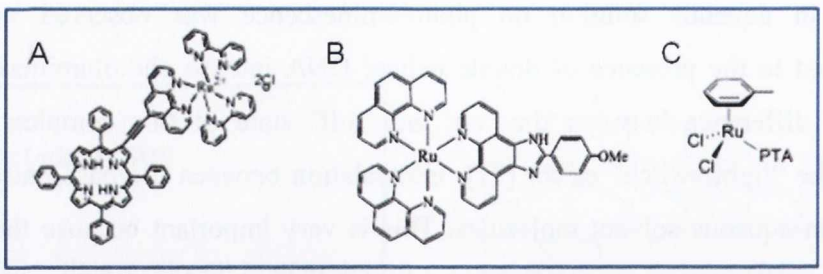

Figure 1.16: Structure of compounds Ru-L (A), RuPOP (B) and RAPTA-T (C) adapted from [93-95]

The compounds RE84 and 85 (figure 1.17) based on 4-Amino 1,8-Naphthalimide Derived Tröger's Bases were synthesised by Robert B. P. Elmes in order to increase even more the potency of this class of compounds in binding DNA increasing their potential in being used as molecular probes or as photosensitizers in PDT.

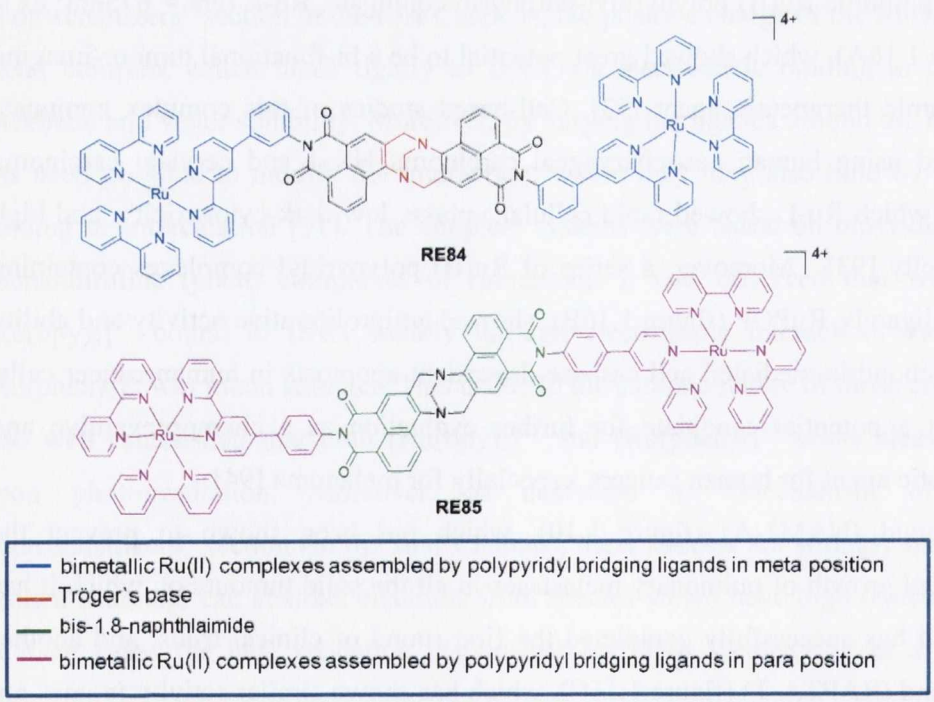

Figure 1.17: Structure of compounds RE84 and 85

The interest in Tröger's bases is due to the central bicyclic framework which results in the two aromatic rings being fused nearly perpendicular to each other, creating a rigid V-shaped molecular scaffold. It was seen to offer a nanometer-sized building block for molecular designs. Moreover, due to the blocked conformation of the two nitrogens of the methanodiazocine bridge, the molecule is chiral with a C_2 axis of symmetry, giving it the potential for enantiospecific recognition of molecules [97]. The chirality of the Tröger's base framework plays an important role in their interaction with DNA and it is expected that such species may give rise to enantiospecific binders of DNA.

Ruthenium polypyridyl complexes have been extensively studied during the last three decades for their strong and sequence-selective DNA binding [98]. In order to further improve DNA affinity and target more specific structure have resulted in an increasing interest in binuclear complexes, and to date, there are several examples of binuclear ruthenium complexes showing potential for therapeutic use or for direct imaging of DNA structure in living cells [98, 99].

For example, the pure enantiomers of two structural isomers of $[\mu\text{-bipb(phen)}_4\text{Ru}_2]^{4+}$ (figure 1.18A) were shown to be promising for future applications as cellular imaging probes [98]. Moreover, their DNA-condensing properties, make them interesting as potential gene delivery vectors [98]. Another study of the potential of two dinuclear Ru(II) polypyridyl complexes (1 and 2) (figure 1.18B) as cellular DNA stain showed one of them to be successfully taken up by living cells and to act as multifunctional biological imaging agents staining the DNA of eukaryotic and prokaryotic cells for both luminescence and transition electron microscopy [99].

The 4-Amino-1,8-naphthalimide is a fluorophore, which has a strong absorption band in the visible region and emits at long wavelengths and is often combined with metals in order to create complexes that can have different applications as probes or as therapeutic agents. For example, 4-Amino-1,8-naphthalimide-based Tröger's bases called 1, 2 and 3 (figure1.18C) have been shown to bind strongly DNA in competitive media at pH 7.4, with concomitant modulation in their fluorescence emission and also undergo uptake, being localized within the nucleus a few hours and are cytotoxic against HL60 (promyelocytic leukemia) and K562 (chronic myeloid leukemia) [100].

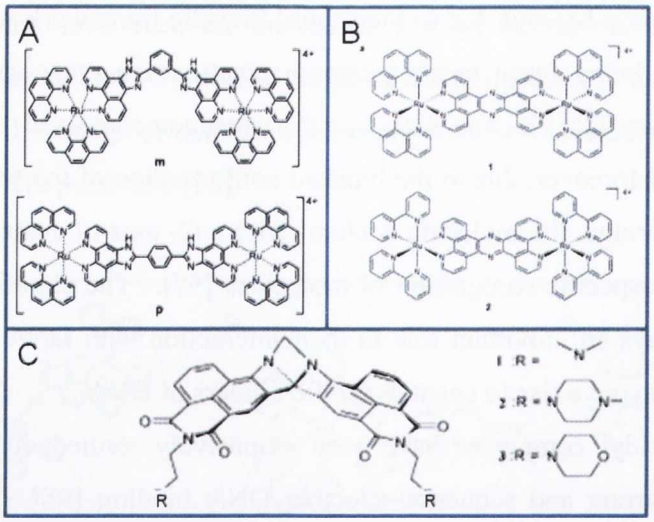

***Figure 1.18*:** Structure of the two structural isomers of $[\mu\text{-bipb(phen)}_4Ru_2]^{4+}$ (A), of the two dinuclear Ru(II) polypyridyl complexes 1 and 2 (B) and of the 4-Amino-1,8-naphthalimide-based Tröger's bases called 1, 2 and 3 (C) adapted from [98-100]

The combination of Tröger's bases with a bimetallic Ru(II) complexes assembled by polypyridyl bridging ligands and the 1,8-naphthlaimide units can lead to novel bimetallic species, which are expected to be capable of binding DNA with further possible applications in cellular imaging and therapy for different reasons: the Tröger's base framework may orientate the two functional units, the Ru(II) centre and the organic derivative bis-1,8-naphthlaimide containing the bipyridyl ligand, in a rigid architecture that may enable DNA binding; the bimetallic Ru(II) character may enable cellular localisation; the highly positive charge would be likely to further increase the DNA binding ability of such a system through electrostatic interactions. In the synthesis of these bimetallic species, the Ru(II) would have either a meta or para arrangement with respect to each other and they can be isolated as a mixture of enantiomers.

1.10 Aims of this project

Ruthenium compounds are promising in the clinic as antitumour agents in PDT or they can be proposed as molecular markers [84] because of the cationic character of metal ions and complexes, which have a natural aptitude for interacting with certain biological molecules; their photophysical characteristic; the redox potential between the different accessible oxidation states occupied by ruthenium that enables the body to catalyse

oxidation/reduction reactions; because of the alteration of the physiological environment that accompany disease which enables ruthenium compounds to be selectively activated in diseased tissues making PDT less invasive than conventional chemotherapy.

Many ruthenium compounds have been extensively studied as PDT agents. PDT, as mentioned previously, in combination with visible light, a photosensitizer and oxygen, can produce lethal cytotoxic agents that can inactivate tumour cells. This enables a dual selectivity towards diseased tissue which is produced by both a preferential uptake of the photosensitizer by the diseased tissue and the ability to confine activation of the photosensitizer to this diseased tissue by restricting the illumination to that specific region leaving normal tissue intact.

In connection with that, the aim of my project is to test novel Ru(II) compounds, which are designed for binding DNA, in different cancer cell lines. Attempts were made to verify if they show phototoxicity and if they are toxic without being exposed to light. This is important in order to understand if they are more suitable as molecular probes, in which no toxicity in the dark is required, or as therapeutic agents, in which phototoxicity is required.

Furthermore, studies were made to show if they are taken up by the cells and the uptake time to enter the cells. It is very relevant in order to understand the accumulation time of the drug within tumour cells for either compounds suitable as molecular probes or as anticancer agents. In relation to that, this work also aimed to identify the localisation and eventual co-localisation of the compounds in order to verify if the compounds bind specifically to DNA or other organelles within the cells. Moreover, the mechanism of cell death was investigated studying any ROS production leading to cell death and the recovery and elimination of the compounds in order to verify their PDT efficacy. The purpose of studying their mechanism of action is to understand any further improvements which may be necessary in those compounds to be more effective as either molecular markers or PDT compounds.

Ru(II) compounds are proposed as having similar properties to molecular probes or kill tumour cells. The compounds which can enter the cells and be well tolerated by the cells might find use as imaging agents. The compounds which can be photo-activated may find use as PDT agents especially if selectivity can be arranged by either selective uptake/retention in cancer cells, or by selective targeting to rapidly dividing cells, or by selective photoreaction.

In summary the aims of this project are to investigate the:

- Uptake and localisation of the compounds inside the cells
- Effect of the compounds in cells with and without light treatment
- Co-localisation of the compounds with some organelles in cells
- Effect of the compounds in cell organelles
- ROS production
- Mechanism of action of cell death

Chapter 2: Materials and Methods

2.1 Materials and Methods

Materials

2.1.1 Source of materials

Materials	Suppliers
6-well plates	Greiner Bio-One
96-well plates	Greiner Bio-One
AB	Invitrogen
Ac-DEVD-AMC	Enzo Life Science
Alexa fluor 488 Phalloidin probe	Invitrogen
Amersham molecular weight marker	GE Healthcare
AnnexinV-FITC	IQ Products
Anti-mouse Alexa 633 mAb	Bioscience
Anti-mouse IgG HRP	Promega
Anti-mouse-Lamin A mAb	Santa Cruz
Anti-mouse-PARP-1 (Ab-2) mAb	Calbiochem
Anti-mouse-PDH E1-α mAb	Mito Sciences
Anti-mouse-α-tubulin mAb	Millipore
Anti-mouse-β-actin mAb	AbCAM
Aprotinin	Sigma-Aldrich
APS	Sigma-Aldrich
BCA protein assay kit	Pierce
Bromophenol blue	Sigma-Aldrich
BSA	Sigma-Aldrich
$C_3H_3NaO_3$	Sigma-Aldrich
CHAPS	Fluka Biochemical
Cisplatin	Sigma-Aldrich
Complete protease inhibitor cocktail	Roche Diagnostics
CytoTox 96® Non-Radioactive Cytotoxicity Assay	Promega
DAPI blue nuclear stain	Invitrogen

DCFH-DA	Invitrogen
DMEM	Invitrogen
DMSO	Sigma-Aldrich
DRAQ-7	Biostatus
Dried milk	Marvel
DTT	Sigma-Aldrich
EDTA	Sigma-Aldrich
EGTA	Sigma-Aldrich
Ethanol	Lennox
FBS	Invitrogen
FCCP	Sigma-Aldrich
Glass bottom dish plates (Ø 22 mm for Confocal Microscopy)	Greiner Bio-One
Glucose-6-phosphate dehydrogenase	Sigma-Aldrich
Glycerol	Sigma-Aldrich
Glycine	Sigma-Aldrich
Hepes (cell culture)	Sigma-Aldrich
Immobilon Western chemiluminescent HRP substrate (ECL)	Millipore
JC-1	Invitrogen
KCl	Sigma-Aldrich
Leupeptin	Sigma-Aldrich
LMPA	Sigma-Aldrich
Methanol	Lennox
Microscope slides	Thermo Scientific
Mitochondria isolation kit for cultured cells	Pierce
N-acetyl-L-cysteine	Sigma-Aldrich
NaCl	Sigma-Aldrich
Nonidet P-40	Sigma-Aldrich
PBS	Oxoid chemicals
Pen-Strep	Bioscience
PI	Sigma-Aldrich
PMSF	Sigma-Aldrich
ProLong gold antifade reagent with DAPI	Invitrogen
Protogel™ acrylamide mix	National Diagnostics

PVDF	Sigma-Aldrich
RapiDiff nuclear and cytoplasmic staining kit	Sigma-Aldrich
RNAse A	Sigma-Aldrich
RPMI 1460 medium	Invitrogen
SDS	Fluka Biochemical
Shandon filter cards	Thermo Scientific
Stripping buffer	Chemicom
Sucrose	Sigma-Aldrich
TEMED	Sigma-Aldrich
Tissue culture flasks	Greiner Bio-One
Triton-X-100	Sigma-Aldrich
Trizma base (Tris)	Sigma-Aldrich
Trypsin-EDTA (10x)	Sigma-Aldrich
Tween-20	Sigma-Aldrich
Urea	Sigma-Aldrich
X-Omat LS film	Kodak
Z-VAD-FMK	MBL International
α-thioglycerol	Sigma-Aldrich

2.1.2 Source of cell lines

Mesothelioma cell lines CRL and One 58 were obtained from Prof. Ken O'Byrne (Institute of Molecular Medicine, St. James Hospital and Trinity College Dublin, Ireland). Burkitt's lymphoma cell lines MUTUI (c179) and DG-75 were provided by Dr. Dermot Walls (School of Biotechnology, Dublin City University, Ireland). HeLa cells were provided by Prof. Mary Meegan from the School of Pharmacy and Pharmaceutical Sciences, Trinity College Dublin, Ireland. HeLaDsRed were provided by Dr. Gavin Davey from School of Biochemistry and Immunology, Trinity College Dublin.

2.1.3 Source of the compounds

Compounds were synthesised and characterised by Robert B. P. Elmes from the Thorfinnur Gunnlaugsson research group, School of Chemistry at Trinity College Dublin. Compounds were characterised by ^{1}H NMR spectra, ^{13}C NMR, high resolution mass spectrometry (MALDI), infra read spectroscopy, elemental analysis, absorption spectroscopy, emission spectroscopy (emission and excitation spectra). The results of detailed characterisation studies on the compounds are reported in Robert B. P. Elmes thesis [73].

Methods

2.2 Cell culture

2.2.1 Mesothelioma cell lines

ONE 58 is a human adherent malignant mesothelioma cell line derived from pleural effusions. CRL is a human adherent malignant mesothelioma cell line derived from lung effusions.

Cells were maintained in 75cm^2 tissue culture flasks at 37°C in a humidified atmosphere of 95% oxygen (O_2) and 5% carbon dioxide (CO_2).The above cell lines were cultured in RPMI-1640+ Glutamax medium supplemented with 10% (v/v) FBS, penicillin and streptomycin (pen-strep, 100µg/ml). Cells were maintained in 75cm^2 tissue culture flasks at 37°C.

2.2.2 Burkitt's lymphoma cell lines

MUTU I c179 is a Burkitt's lymphoma suspension cell line derived from biopsy that was Epstein-Barr virus (EBV) positive. DG75 is a Burkitt's lymphoma suspension cell line derived from pleural effusion.

The above cell lines were cultured in RPMI-1640 + Glutamax medium supplemented with 10% (v/v) FBS, pen-strep (100µg/ml). The MUTU-I cell line required the additional supplements of α-thioglycerol (5mM in phosphate-buffer saline (PBS) with 20µM

bathocuprione disulphonic acid), sodium pyruvate ($C_3H_3NaO_3$) (100μM) and HEPES (1mM).

Cells were maintained in 75cm^2 tissue culture flasks at 37°C.

2.2.3 HeLa cell line

HeLa is a human adherent cervix epithelial adenocarcinoma cell line. The above cell line was cultured in DMEM + Glutamax medium supplemented with 10% (v/v) FBS, pen-strep (100μg/ml). Cells were maintained in 75cm^2 tissue culture flasks at 37°C.

2.2.4 HeLaDsRed cell line

HeLa cells were stably transfected with pDsRed2-mito plasmid (Clontech, CA, USA) by Dr Stephen R. Quinn from Gavin Davey's group. The plasmid encodes a fusion fluorescent protein and mitochondrial targeting sequence from subunit VIII of human cytocrome c oxidase. The plasmid contains cytomegalovirus (CMV) promoters and confers neomycin resistance in *E.Coli.*

2.3 Cell maintenance

Growth media was stored at 4°C and when required was heated to 37°C in a water bath before being added to cells. Cells were sub–cultured three times weekly depending on cell viability and growth. When required for an experiment, cells where centrifuged at 300xg for 5min in a Sorvall T436 centrifuge and the pellet suspended in 5ml of growth medium before the cell number was counted using a haemocytometer. The specified amount of cells for each experiment was seeded accordingly in the relevant medium.

2.4 Cell storage-cryopreservation

6-7 million cells were suspended in 60% growth medium, 30% (v/v) FBS and 10% (v/v) dimethyl sulphoxide (DMSO) and aliquoted into cryotubes, each containing 1.5ml.

The cryotubes were incubated in a polycarbonate container containing isopropyl alcohol (provides the critical, repeatable, 1°C/min cooling rate required for successful cryopreservation of cells) in a -70°C freezer overnight before being transferred to long-term storage at -180°C in liquid nitrogen. When required, an aliquot of cells was removed and quickly thawed, followed by suspension in 9ml of 37°C growth medium.

Cells were centrifuged for 5min at 300xg to wash off the DMSO. The supernatant was discarded and the cells resuspended in 5ml of growth medium in a sterile 25cm^2 flask. Once confluent, the cells were maintained in 75cm^2 tissue culture flasks at 37°C.

2.5 Investigation of photo-toxicity

To induce photo-toxicity, cells were irradiated at >450nm using a xenon lamp (figure 2.1) at 6Mw/cm^2 which was measured by a photometer ILT1400-A to give light doses of 12.66J/cm^2. In addition, a sodium nitrate ($NaNO_2$) liquid filter was used to exclude light at wavelengths lower than 390nm. The temperature at 37°C was checked using a thermometer.

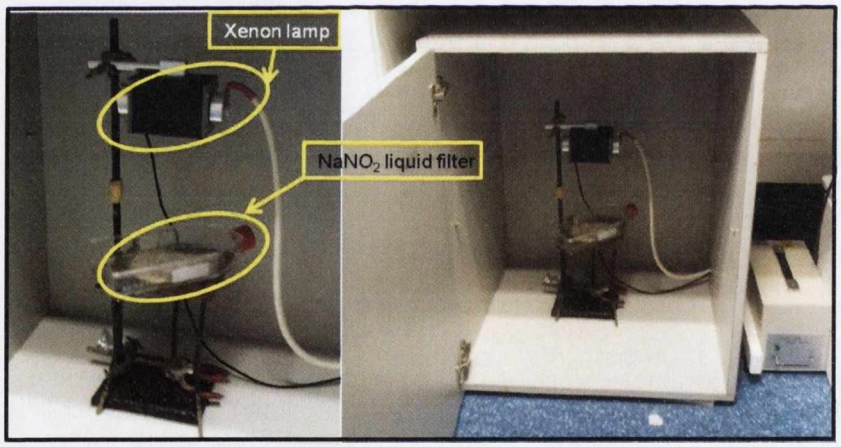

Figure 2.1: Xenon lamp

2.5.1 *In vitro* cytotoxicity using Alamar Blue fluorescence assay

Alamar Blue (AB) is a safe, non toxic, soluble, aqueous dye that is stable in culture medium that is used to assess cell viability and cell proliferation. It consists of an

oxidation-reduction (REDOX) indicator that yields a colorimetric change and a fluorescent signal in response to metabolic activity. The oxidized form of AB enters the cytosol and is converted to the reduced form by mitochondrial enzyme activity by accepting electrons from NADPH, FADH, FMNH (flavin mononucleotide semiquinone), NADH as well as from the cytochromes. This redox reaction is accompanied by a shift in colour of the culture medium from indigo blue to fluorescent pink, which can be easily measured by fluorimetric reading. The number of viable cells is expressed as percentage of AB reduction of control samples.

$0.5x10^4$ cells/well CRL, HeLa and ONE58 cells, $0.8x10^5$ cells/well MUTUI cells and $4x10^4$ DG75 cells were seeded in 96-well flat bottomed microtitre plates (200µl total volume/well). Adherent cells were incubated at 37°C overnight before treatment. Each concentration of compound was plated in triplicate and compared to dark-treated controls. Following 24h of compound treatment, the treated cells were either exposed to light for 1h to give a light dose of 12.66 J/cm^2 or maintained in the dark as is schematized in figure 2.2. Following 23h of incubation an AB assay was performed adding 20µl of AB dye per well followed by 5-6h incubation at 37°C in the dark until the shift in colour occurred. The background fluorescence of media without cells plus AB was subtracted from the values for each group, and the control untreated cells was used to represent 100% cell viability. The number of viable cells is expressed as a percentage of AB reduction of untreated controls. Fluorescence was measured using a Spectramax Gemini fluorometric plate reader using a SOFTmax Pro version 4.0 (Molecular Devices) software package (excitation 544nm, emission 590nm). Data was graphed as the mean ± S.E.M in GRAPHPAD Prism software.

The antiproliferative potency of each compound was determined by non-linear regression analysis calculating an approximate IC_{50} value ([Dose] when response is equal to 50% cell viability).

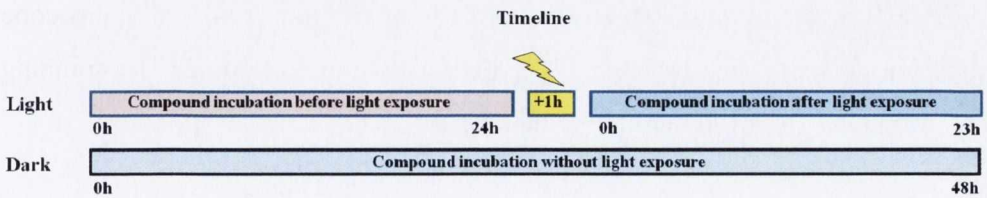

Figure 2.2: Treatment scheme: the cells treated with the compound were either exposed to light for 1h to give a light dose of 12.66 J/cm^2 or maintained in the dark.

2.6 Cytospin

The cytospin technique uses a high speed centrifuge to concentrate the cells onto a slide in a uniform monolayer 6mm in diameter. The monolayer distribution enhances the morphological appearance of the cells present.

Cells were seeded at a density of $0.25x10^6$ cells/ml, treated with the indicated compounds for 24h and exposed to light for 1h or maintained in the dark. After incubation at 37°C for another 23h, an aliquot of cells (150µl) were cytocentrifuged onto poly-l-lysine coated slides at 500xg for 2min using a Cytospin 3 (Shandon). The slides were removed and left to air-dry at room temperature for 2min.

Staining was carried out using the RapiDiff kit containing solution A (100% methanol), solution B (Eosin Y) and solution C (methylene blue). The cells were fixed by dipping them ten times in solution A. The nucleus of the cells was stained pink by dipping the slide ten times in solution B and the cytoplasm was stained blue by dipping eight times in solution C. Excess dye was washed off with dH_2O. After allowing the slides to air dry, cells were examined under a light microscope using 40x magnification.

2.7 Laser scanning confocal microscopy and spinning disk confocal microscopy

Laser scanning confocal microscopy is typically used for ultra-thin sectioning on fixed or live specimens. Alternatively, spinning disk confocal microscopy is suitable for 4D (time-lapse) imaging of living cells for investigation of dynamics.

Using laser scanning confocal microscopy, the excitation laser source is scanned across the specimen in a point-by-point raster pattern, so that, over time, a complete image of the focal plane is collected. By compiling multiple optical sections of the specimen sequentially it can provide images of extremely thin optical sections of specimens.

Spinning disk confocal microscopy, is preferred to the laser scanning confocal microscope when transmission, or speed, is a higher priority than ultra-thin sectioning. The spinning disk light only penetrates the specimens perpendicularly.

2.7.1 Live imaging using laser scanning confocal microscopy

$1x10^5$ cells/well HeLa and CRL cells were seeded in glass bottom dish plates (Ø 22 mm; 2ml total volume/well). Adherent cells were incubated at 37°C overnight before treatment. The cells were then treated with the compounds at different concentrations and incubated at different time points. Cells were washed twice in PBS followed by the addition of fresh media and 4',6-diamidino-2-phenylindole (DAPI) (Blue nuclear stain at 0.2µg/ml; 1/50,000 dilution), followed by viewing using Olympus FV1000 confocal microscopy with a 60x oil immersion lens. Image analysis was performed using FluoView Version 7.1 Software. Compounds were excited by a 488nm argon laser, and DAPI was exited by a 405nm diode laser.

2.7.2 Overnight live video using laser scanning confocal microscopy

$1x10^5$ cells/well HeLa cells were plated in glass bottom dish plates (Ø 22 mm; 2ml total volume/well). Cells were incubated at 37°C overnight before treatment. The cells were then treated with RE37 (100µM) and incubated for a further 24h or treated with RE84 at different concentrations (1 and 3µM) for 30min. Cells were washed twice in PBS followed by the addition of fresh medium before viewing using Olympus FV1000 confocal microscopy with a 60x oil immersion lens. Image analysis was performed using FluoView Version 7.1 Software.

During the 12h overnight video, cells were at 37°C, 5% CO_2 and images were taken every 10min at 5% 488nm laser intensity (laser was only on when the images were taken).

Different experiments were performed:

- control cells ± irradiated for 30min at 5% 488nm laser intensity and incubated overnight;
- cells + RE37 were irradiated for 30min at 5% 488nm laser intensity and incubated overnight;
- cells + RE37 were not irradiated for 30min at 5% 488nm laser intensity and incubated overnight.
- cells + RE84 (1 and 3µM) without irradiation at 4% 488nm laser intensity and incubated overnight.

The percentage of cell death was analysed and graphed as the mean ± S.E.M in GRAPHPAD Prism software.

2.7.3 Short live video using laser scanning confocal microscopy

$1x10^5$ cells/well HeLaDsRed cells were plated in glass bottom dish plates (Ø 22 mm; 2ml total volume/well). Cells were incubated at 37°C overnight before treatment. The cells were then treated with RE84 (5µM) and incubated for 2h before confocal microscopy. Cells were washed twice in PBS followed by the addition of fresh medium before viewing using Olympus FV1000 confocal microscopy with a 60x oil immersion lens. Image analysis was performed using FluoViev Version 7.1 Software.
During the 20min video cells were at 37°C, 5% CO_2, images were taken every 2min at 4% laser intensity for the 543nm laser and at 10% intensity for the 488nm laser.

Two different experiments were performed:

- control cells + 543nm laser + mercury bulb;
- cells + compound + 543nm laser (on all the time) ± mercury bulb ± 488nm laser (on for 20sec).

The 543nm laser was always on because it was used for viewing the DsRed. The mercury bulb (white-green region) is normally used for visualising the cells from the base of the confocal.

2.7.4 Live video using spinning disk confocal microscopy

$1x10^5$ cells/well HeLaDsRed cells were plated in glass bottom dish plates (Ø 22 mm; 2ml total volume/well). Cells were incubated at 37°C overnight before treatment. The cells were then treated with the compound RE84 at different concentrations (1, 3 and 5µM) and incubated for 30min. Cells were washed twice in PBS followed by the addition of fresh medium before viewing using Olympus IX81-DSU Spinning Disk Confocal Microscope with a 60x oil immersion lens. Image analysis was performed using IQ2 Software.

During the 30min video cells were at 37°C, 5% CO_2 at 4% laser intensity for the 543nm laser and at 10% intensity for the 488nm laser (laser was only on when the images were taken).

Different experiments were performed:

- control cells + 543nm laser ± 488nm laser;
- cells + compounds + 543nm laser ± 488nm laser;

2.8 Fixed cells

Effect/co-localisation studies were carried out with the compounds and different molecular markers in HeLa cells.

2.8.1 Effect of the compounds with F-actin

The marker Alexa Fluor 488 Phalloidin (Ex/Em: 495/518nm) is an actin (F-actin) probe conjugated to a bright, photostable, green-fluorescent Alexa Fluor 488 dye.
$3x10^5$ cells/well HeLa cells were seeded on coverslips and placed inside a 6-well plate. Adherent cells were incubated at 37°C overnight before treatment. The cells were treated with the indicated compounds and incubated for 24h. Following 24h incubation the treated cells were exposed to light for 1h to give light doses of 12.66 J/cm^2. Following a further 23h of incubation cells were washed twice with pre-warmed PBS pH 7.4. Samples were fixed in 3% paraformaldehyde solution in PBS for 10min at room temperature followed by 2 or more washes with PBS. Staining solution (5% BSA+0.2% Triton X-100 in PBS + phalloidin 488 (1/100 dilution) was added to the cells for 20-30min at room temperature. To avoid evaporation, the coverslips were kept inside a covered 6-well plate during the incubation, followed by 2 or more washes with PBS. The cells on the coverslips were then transferred onto glass slides and DAPI gel (blue nuclear stain in gel specific for fixed cells) was added and left overnight at room temperature before confocal microscopy. Image viewing was performed using Olympus FV1000 confocal microscopy with a 60x oil immersion lens. Image analysis was performed using FluoView Version 7.1.The sample was excited with a 488nm laser diode and the emission of the compounds was monitored

and captured at 600-700nm. Simultaneously DAPI was excited by a 405nm diode laser. The sample was then excited again with a 488nm laser diode and the emission of phalloidin was monitored and captured at 500-600nm. Both images were then overlaid and analysed using the Imaris 3D software analyser (Bitplane).

2.8.2 Effect of the compounds on microtubules

$3x10^5$ cells/well HeLa cells were seeded on coverslips and placed inside a 6-well plate. Adherent cells were incubated at 37°C over night before treatment. The cells were treated with the compound and incubated for 24h. After 24h incubation the treated cells were exposed to light for 1h to give light doses of $12.66J/cm^2$ followed by incubation at different time points. Cells were then washed twice with pre-warmed PBS pH 7.4. Samples were fixed in 3% paraformaldehyde solution in PBS for 10min at room temperature followed by 2 or more washes with PBS. In order to confine the flow of reagents to a defined area, a Super Pap Pen liquid blocker, which has hydrophobic properties, was used to draw barriers on the coverslips. Staining solution (5% BSA+ 0.2% Triton X-100 in PBS) with monoclonal anti-α-Tubulin (1/500 dilution) was added to the cells overnight at 4°C. To avoid evaporation, the coverslips were kept inside a covered container during the incubation on top of wet paper. Cells were washed twice with PBS pH 7.4 before adding the staining solution with anti-mouse Alexa 633 (1/1,000 dilution) on the coverslips for 1h at room temperature. The cells on the coverslips were then transferred onto glass slides and DAPI gel was added and left overnight at room temperature before confocal microscopy. Image viewing was performed using Olympus FV1000 confocal microscopy with a 60x oil immersion lens. Image analysis was performed using FluoViev Version 7.1. The sample was excited with a 488nm laser diode and the emission of the compound was monitored and captured at 551-651nm. Simultaneously DAPI was excited by a 405 diode laser and the emission was monitored and captured at 425-475nm; anti-mouse Alexa 633 was excited by a 633nm laser and the emission was monitored and captured below 650nm. 3D images were analysed using the Imaris 3D software analyser (Bitplane).

2.8.3 Investigation on the toxicity of the compounds in the dark

$3x10^5$ cells/well HeLa cells were seeded on coverslips and placed inside a 6-well plate. Adherent cells were incubated at 37°C over night before treatment. The cells were treated with the compound and incubated for 48h. Cells were then washed twice with pre-warmed PBS pH 7.4. Samples were fixed in 3% paraformaldehyde solution in PBS for 10min at room temperature followed by 2 or more washes with PBS. The cells on the coverslips were then transferred onto glass slides and DAPI gel was added and left overnight at room temperature before confocal microscopy. Image viewing was performed using Olympus FV1000 confocal microscopy with a 60x oil immersion lens. Image analysis was performed using FluoViev Version 7.1. The sample was excited with a 488nm laser diode and the emission of the compound was monitored and captured at 551-651nm. Simultaneously DAPI was excited by a 405nm diode laser and the emission was monitored and captured at 425-475nm.

2.9 FACS (Fluorescence Activated Cell Sorting) experiments using FACS Calibur and CyAn

Flow cytometry is a technique for analysing cells, by suspending them in a stream of fluid and passing them through an electronic detection apparatus. It allows simultaneous multiparametric analysis of the physical and/or chemical characteristics of up to thousands of cells per second. One of the first major applications of flow cytometry, the DNA content of the cell cycle, can provide a great deal of information about the cell cycle and consequently the effect on the cell cycle of added stimuli. The FACS Calibur is equipped with 2 lasers (488nm, 635nm) and the CyAn is equipped with 3 lasers (488nm, 635nm and405 nm).

2.9.1 PI cell cycle analysis using a FACS Calibur

Propidium iodide (PI) (Ex/Em: 535/617nm) is a fluorogenic compound that binds stoichiometrically to nucleic acids so that fluorescence emission is proportional to the DNA (and RNA, which has to be removed if DNA is to be measured) content of a cell

providing information about the cell cycle. PI can be excited at 488nm and has an emission centred around 600nm. When apoptotic cells are stained with PI and analyzed with a flow cytometer, they display a broad hypodiploid (pre-G1) peak, which can be easily discriminated from the narrow peak of cells with normal (diploid) DNA content in the red fluorescence channel. When the cells enter into the G2/M phase of the cell cycle, the DNA contracts and occupies less space resulting in a lower fluorescence release, while the cells entering the G1 and S phases have a greater amount of loosely associated DNA and thus release greater fluorescence. The laser beam can distinguish different phases in the cell cycle and also the difference of the diameter of a typical nucleus in the different phases. The stage at which the cells are at in its cell cycle will have a characteristic DNA profile consisting of a series of different peaks.

2.9.2 Time and dose experiments

$1x10^5$ HeLa cells were seeded in 6-well plates (2.5ml total volume/well) or $0.25x10^6$ cells were seeded in T25 flasks (5ml total volume/flask). Adherent cells were incubated at 37°C overnight before treatment. The cells were treated with different concentrations of the compound, following 24h incubation the treated cells were exposed to light for 1h to give light doses of 12.66 J/cm^2. After light exposure the percentage of cell death was analyzed at different time points. The percentage of cell death was compared with the equivalent cells maintained in the dark. Following 23h of incubation the cells were fixed as described below, section 2.9.6.

2.9.3 ROS involvement: detection with N-Acetyl-L-Cysteine

N-Acetyl-L-Cysteine (Nac) is an antioxidant and mucolytic agent. It increases cellular pools of free radical scavengers.

$1x10^5$ HeLa cells were seeded in 6-well plates (2.5ml total volume/well). Adherent cells were incubated at 37°C overnight before being treated. The cells were treated with 5mM Nac followed by the compound 1h after and incubated for 24h before exposure to light for 1h to give light doses of 12.66 J/cm^2. The percentage of cell death was compared with the equivalent cells maintained in the dark and with the control cells treated only with Nac.

Following 23h of incubation the cells were fixed as described below in the cell fixation section.

2.9.4 Determination of caspase involvement in cell death using a caspase inhibitor

Z-VAD-FMK (carbobenzoxy-valyl-alanyl-aspartyl-[O-methyl]- fluoro methyl ketone) is a caspase inhibitor (CI) that irreversibly binds to the catalytic site of caspase proteases and can inhibit induction of caspase-dependent apoptosis. The peptide is O-methylated in the P1 position on aspartic acid, providing enhanced stability and increased cell permeability. $1x10^5$ HeLa cells were plated in 6-well plates (2.5ml total volume/well). Adherent cells were incubated at 37°C overnight before being treated. The cells were treated with 40μM of CI followed by the compound 1h after and incubated for 24h before exposure to light to give light doses of 12.66 J/cm^2. The percentage of cell death was compared with the equivalent cells maintained in the dark and with the control cells treated only with CI. Following 23h of incubation the cells were fixed as described in cell fixation section.

2.9.5 Dark toxicity test

$0.25x10^6$ cells were seeded in T25 flasks (5ml total volume/flask). Adherent cells were incubated at 37°C overnight before treatment. The cells were treated with different concentrations of the compounds for 24h and then washed with PBS followed by the addition of fresh media. Following a total of 48-96h incubation the cells were then fixed as described below. The percentage of cell death was compared with the equivalent non-treated cells.

2.9.6 Cell fixation

Adherent cells were trypsinised and harvested by centrifugation at 300xg for 5min and washed with 1ml of ice cold PBS. The cells were centrifuged again at 300xg for 5min and the pellet was resuspended in 500μl of ice cold 70% ethanol. The cells were left to fix overnight at 4°C. After fixation, the cells were pelleted by centrifugation at 300xg for 5min and the ethanol was removed. The pellet was resuspended in 300μl of PBS in FACS microtubes, 25μl of RNAse A (10mg/ml) and 75μl of PI (1mg/ml) were then added. The

tubes were incubated at 37°C in the dark for 30min. Flow cytometry analysis was performed on a FACS Calibur (Bectin Dickson). Cell cycle analysis was performed using appropriate gates counting 10,000 cells using Cell Quest software. The percentage of cell death was analysed mean ± S.E.M. in GRAPHPAD Prism software.

2.9.7 Cellular uptake of the compounds

Uptake in cells was quantified by flow cytometry measuring the compound fluorescence in cells and the difference in fluorescence over time. $0.25x10^6$ cells were seeded in T25 flasks (5ml total volume/flask). Adherent cells were incubated at 37°C overnight before treatment. The cells were treated with different concentrations of the compounds and kept in the dark for different incubation times. Adherent cells were trypsinised and harvested by centrifugation at 300xg for 5min and washed twice with 1ml of ice cold PBS. The cells were centrifuged again at 300xg for 5min and the pellet was resuspended in 400µl of ice cold PBS supplemented with 2% FBS in FACS microtubes. Flow cytometry analysis was performed on a FACS Calibur (Bectin Dickson). Cell analysis was performed using appropriate gates counting 10,000 cells and the CELLQUEST software package. The compounds were excited by a 488nm argon laser, with emission observed at 515 and 630nm. The percentage of fluorescence in the cells was analysed and graphed as the mean ± S.E.M in GRAPHPAD Prism software.

2.9.8 AnnexinV/PI staining

During the early stages of apoptosis, phosphatidylserine (PS, a negatively charged phospholipid) becomes exposed on the outside of the cell membrane. This can be specifically detected by PS binding proteins in the presence of calcium (Ca^{2+}), such as, AnnexinV. Fluorescein isothiocyanate (FITC) conjugated AnnexinV makes it possible to identify and to quantify apoptotic cells on a single-cell basis by FACS. Staining cells simultaneously with AnnexinV (FITC) and the PI allows the discrimination of intact cells (FITC-PI-), early apoptotic (FITC+PI-) and late apoptotic or necrotic cells (FITC+PI+).

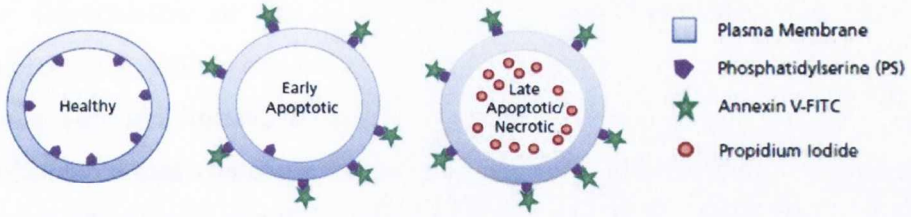

Figure 2.3: Diagram showing healthy and apoptotic cells with markers for detection of apoptosis adapted from [101].

$0{,}25x10^6$ HeLa cells were seeded in T25 flasks (5ml total volume/flask). Adherent cells were incubated at 37°C overnight before treatment. The cells were treated with different concentrations of the compounds and incubated for 24h followed by either light exposure for 1h to give light doses of 12.66 J/cm^2 or maintained in the dark. After light exposure, cells were incubated for further 23h before AnnexinV/PI staining.

Cells were trypsinised and harvested by centrifugation at 300xg for 5min and resuspended in 500µl of 1X AnnexinV binding buffer (20X Ca^{2+} Annexin V Binding buffer: 10.9mM Hepes, 140mM NaCl, 2.5mM $CaCl_2$ (calcium chloride), pH 7.4 in PBS). Cells were then harvested by centrifugation at 300xg for 5min and stained with Annexin V by resuspending the pellet in 50µl of anti-Annexin V antibody (1/33.3 dilution in binding buffer). Samples were then vortexed and incubated for 10min in the dark on ice followed by the addition of 500µl of binding buffer before being harvested by centrifugation at 300xg for 5min. The pellet was then resuspended in 500ul PI (1mg/ml PI diluted 1/2000 in binding buffer). Cells were kept on ice until being analysed on a FACS CyAn machine.

The 488nm laser was used to excite the FITC conjugated Annexin V and the PI: FITC Annexin V was detected in FL1 (Em: 530nm), PI was detected in FL3 (Em: 613nm) and the compounds were detected in FL4 (Em: 680).

Cell analysis was performed on the CyAn using appropriate gates counting 10,000 cells and using Summit software package. The standard compensation was performed using the untreated control, cells stained only with Annexin V or PI, cells stained with both AnnexinV/PI and by excluding the fluorescence of the compounds. The percentage of fluorescence into the cells was analysed using Flow Jo software. The percentage of cell death was analysed and graphed as the mean ± S.E.M in GRAPHPAD Prism software.

2.9.9 Determination of intracellular ROS

DCFH-DA (2',7'-dichlorofluorescein-diacetate) is a dye used for determining the amount of ROS produced in cells. Chemically reduced and acetylated forms of 2',7'-dichlorofluorescein (DCF) and calcein are non-fluorescent until the acetate groups are removed by intracellular esterases and oxidation occurs within the cell. Esterase cleavage of the lipophilic blocking groups yields a charged form of the dye that is retained by cells. Oxidation of DCFH-DA can be detected by monitoring the increase in fluorescence with a flow cytometer, or fluorescence microscope, using excitation sources and filters appropriate for fluorescein. As DCFH-DA is susceptible to photo-oxidation, low light conditions should be used for fluorescence microscopy applications whenever possible.

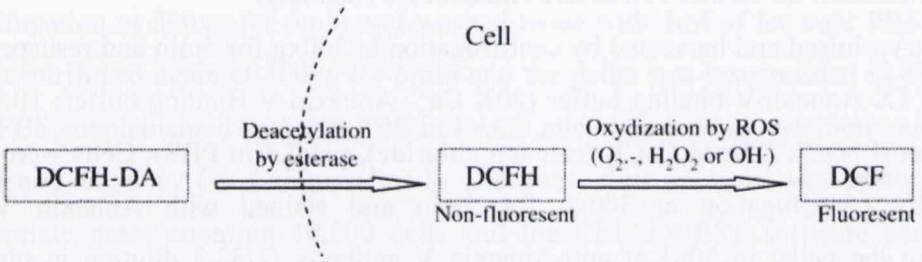

Figure 2.4: Scheme of the ROS production assay adapted from [102]

$3x10^5$ cells were seeded in T25 flasks. Cells were incubated at 37°C overnight before treatment. The cells were treated with the compounds at different concentrations. After 24h incubation the treated cells were exposed to light for 1h to give light doses of 12.66J/cm^2 or maintained in the dark. Cells were then incubated at different time points after light exposure followed by one wash with warm PBS. Pre-warmed media containing 10µM DCFH-DA was placed on the cells and incubated for 30min at 37°C. Cells were then harvested by trypsinisation and pelleted by centrifugation. Cells were washed with ice cold PBS before being resuspended in ice cold PBS. DRAQ-7 (1.5µM) was added 20min before analysis to exclude dead cells.

The 488nm laser was used to excite the DCFH-DA and the 435nm laser was used to excite the DRAQ-7. DCFH-DA was detected in FL2 (Em: 575nm), DRAQ-7 was detected in FL8 (Em: 665nm) and the compounds were detected in FL4 (Em: 680nm).

Cell analysis was performed on the CyAn using appropriate gates, counting 10,000 cells and using Summit software package. The necessary compensations were made to exclude

the fluorescence of the compounds and the dead cells. The percentage of mean fluorescence within the cells was analysed using Flow Jo software, which generates histograms, and graphed as the mean ± S.E.M in GRAPHPAD Prism software. The statistical analysis of the data was performed using unpaired t-test, part of GRAPHPAD Prism software ($P > 0.05$ ns, $P \leq 0.05$*, $P \leq 0.01$**, $P \leq 0.001$***).

2.9.10 Determination of the mitochondrial membrane potential using JC-1

The JC-1 dye undergoes a reversible change in fluorescence emission from green to orange as the mitochondrial membrane potential ($\Delta\Psi$) increases. This technique can give qualitative measurements, based on the shift in fluorescence emission, and quantitative measurements, based on the intensity of fluorescence emission. Cells with high $\Delta\Psi$ will form JC-1 aggregates and fluoresce red; those with low $\Delta\Psi$ will contain monomeric JC-1 and fluoresce green.

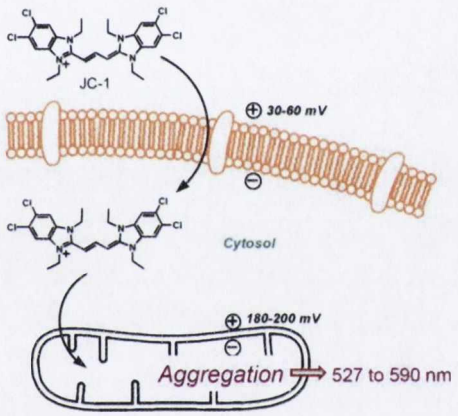

Figure 2.5: Scheme of the JC-1 assay taken from [103]

$3x10^5$ cells were seeded in 6-well plates (3ml total volume/well). Cells were incubated at 37°C overnight before treatment. The cells were treated with the compounds at different concentrations. After 2 and 4h incubation in the dark cells were harvested by scraping and adjusted to a total volume of 1 ml with prewarmed (37°C) fresh complete cell culture medium. As a positive control, cells were treated with 0.25mM of carbonyl cyanide *m*-(trifluoromethoxy) phenylhydrazone (FCCP), a depolarising/uncoupling compound, 15min before adding JC-1. Samples were then treated with 2.5µg/ml of JC-1 while vortexing followed by incubation for 20min in the dark at 37°C. Cells were then washed with PBS

and centrifugated for 5min at 300xg at room temperature. Cells were resuspend in 500µl PBS before CyAn analysis.

The 488nm laser was used to excite the monomeric JC-1 green fluorescence was detected in FL1 (Em: 530nm), the aggregate JC-1 orange/red fluorescence was detected FL2 (Em: 575nm) and the compounds were detected in FL4 (Em: 680).

Cell analysis was performed on the CyAn using appropriate gates counting 10,000 cells and using Summit software package. The standard compensations were performed using the depolarising-treated sample, the untreated control and by excluding the fluorescence of the compounds. The percentage of fluorescence within the cells was analysed using Flow Jo software. The ratio of red/green mean fluorescence values represent the mitochondrial $\Delta\Psi$ and were expressed as a percentage of the untreated control which is taken as 100%. Results were graphed as % $\Delta\Psi$ and analysed as the mean ± S.E.M in GRAPHPAD Prism software.

2.10 Protein quantification

The Pierce BCA Protein Assay is a detergent-compatible formulation based on bicinchoninic acid (BCA) for the colorimetric detection and quantification of total protein. This method combines the well-known reduction of cupric cation (Cu^{+2}) to cuprous cation (Cu^{+1}) by protein in alkaline medium (the biuret reaction) with the highly sensitive and selective colorimetric detection of the Cu^{+1} using a unique reagent containing BCA. The purple-coloured reaction product of this assay is formed by the chelation of two molecules of BCA with one cuprous ion. This water-soluble complex exhibits a strong absorbance at 562nm that is nearly linear with increasing protein concentrations over a broad working range (20-2,000µg/ml). The macromolecular structure of proteins, the number of peptide bonds and the presence of four particular amino acids (cysteine, cystine, tryptophan and tyrosine) are reported to be responsible for colour formation with BCA.

Protein samples were diluted 1 in 25/50 in distilled water. BCA Working Reagent (WR) (Pierce® BCA Protein Assay Kit) was prepared for the colorimetric detection and quantification of total protein.

200µl of BCA WR (50:1, Reagent A:B) was added to 20µl of diluted protein samples in triplicate and incubated at 37°C for 30 minutes. A series of dilutions of known

concentrations (0.0625mg/ml-2mg/ml) were prepared of the BSA protein and incubated with 200µl of BCA WR alongside the unknown(s) before the concentration of each unknown was determined based on a standard curve. The absorbance of all samples was read at 650nM.

2.11 Western blot analysis

Western blotting is an application where an electrical current is used to promote proteins (run on an SDS-PAGE denaturing gel) to transfer onto a charged membrane. The proteins can then be identified by probing with specific antibodies.

2.11.1 Sample preparation of whole cell lysates

To prepare samples for running on a gel, cells and tissues need to be lysed to release the proteins of interest. This solubilizes the proteins so they can migrate individually through a separating gel.

$0.25x10^6$ HeLa cells were seeded in T75 flasks. Adherent cells were incubated at 37°C overnight before being treated. The cells were treated with the compound and incubated for 24h before exposure to light to give light doses of 12.66 J/cm^2 or maintained in the dark. After 1h, adherent cells were trypsinised and harvested by centrifugation at 300xg for 5min and washed with 1ml of PBS. Proteins were put on ice to prevent proteolytic cleavage followed by centrifugation at 300xg for 5min. PARP sample buffer (1:20 dilution) was prepared fresh adding 50µl of 1M dithiothreitol (DTT) to 950µl of PARP buffer (62.5mM Tris/HCl (hydrogen chloride) pH 6.8, 6M urea, 10% (v/v) glycerol, 2% (w/v) SDS, 0.00125% bromophenol blue). Cell pellets were resuspended in 50-100µl (~depending on the number of cells and size of pellet) in PARP sample buffer followed by sonication with a Jencons ultrasonic processor for 11s to sheer the DNA. Then, the samples were heated in a pre-warmed heating block for 15min at 60°C. The lysates were incubated on ice until the gel was prepared. 20-30µg of each sample was added to the gel.

2.11.2 Sample preparation of the isolated mitochondrial and nuclear fractions

Mitochondrial and nuclear fractions were put on ice to prevent proteolytic cleavage. The BCA assay was used (as described above in Section 2.10) to measure the protein concentration of each fraction. Samples were prepared for SDS-PAGE, which is described below, by standardising protein concentration to 20µg/µl with 1x Laemmli buffer (60mM Tris-base (pH6.8), 4% SDS, 20% Glycerol) followed by sonication with an ultrasonic processor (Jencons) for 11s to sheer the membranes. Then, the samples were heated in a pre-warmed heating block for 2min at 100°C followed by addition of 1M DTT (1:20; final concentration 50mM) and bromophenol blue sample buffer (1:20) for visualisation to each sample. The lysates were incubated on ice until the gel was prepared.

2.11.3 Sodium dodecyl sulphate-polyacrylamide gel electrophoresis (SDS-PAGE)

SDS-PAGE was carried out on an 8% resolving gel and 5% stacking gel. The 8% resolving gel consisted of: distilled water (l4.6ml), Protogel™ Acrylamide Mix (2.7ml), 1.5M Tris pH 8.8 (2.5ml), 10% (w/v) SDS (100µl), 10% (w/v) Ammonium persulphate (APS) (100µl) and N,N,N',N',-tetramethylethylenediamine (TEMED) (6µl). The 5% stacking gel consisted of: distilled water (2.1ml), Protogel™ Acrylamide Mix (500 µl), 1M Tris pH 6.8 (380µl), 10% (w/v) SDS (30µl), 10% (w/v) APS (30µl) and TEMED (3µl). When the gel had polymerised, it was placed in an ATTO Electrophoresis Unit (Model AE6450) and the inner chamber was filled with 1x running buffer (25mM Tris, 192mM Glycine, 0.1% (w/v) SDS). The comb was removed and 5µl of pre-stained marker was added to 1 well.
The proteins were resolved through the stacking gel at 80V and 120mA for approximately 40min. Once the samples had been resolved past the stacking gel the current was increased to 110V for approximately 120min until the samples reached the bottom of the resolving gel.

2.11.4 Polyvinylidene difluoride (PVDF) wet transfer and Western blotting

Proteins resolved by SDS-PAGE were transferred onto a methanol activated PVDF membrane. The membrane (pore size 0.45µm) was cut to size and soaked in 100% methanol for 10 seconds and washed a couple of times in distilled water followed by

equilibration of the membrane along with 2 sponges and 6 pieces of Whatman filter paper in transfer buffer for 15min. The above components were placed in the following order into a transfer sandwich and clamped together ensuring there were no air bubbles.

Black side (bottom)

Filter Pad/Sponge

Filter Paper x3

Gel

PVDF membrane

Filter Paper x3

Filter Pad/Sponge

White side (top)

After which, the transfer sandwich was placed into a wet transfer BioRad transfer Blot Unit and filled with cold transfer buffer 1x (25mM Tris, 192mM Glycine, 10% (v/v) Methanol). Proteins were transferred onto the PVDF membrane for 1h at a current of 65V (169mA). The blot was then removed from the cassette and soaked in blocking solution (5% (w/v) Marvel Milk in 0.1% Tris-buffered saline (TBS) and Tween 20 (TBST) (500µl of Tween 20 in 500ml of 1x TBS) for 1h at room temperature. The membrane was washed twice for 3min in 1x TBS (10mM Tris, 150mM NaCl) and incubated with the primary antibody (1:500-1:1000 dilution in 5% blocking solution) overnight or for 2h at room temperature. The membrane was washed again three times for 5min in 1x TBST and incubated with the secondary antibody (anti-mouse, 1:2000-1:10,000 dilution in 5% blocking solution) for 1h at room temperature. The membrane was then washed three times for 10min in 1x TBST and again once for 5min in 1x TBS.

The membrane was added to reagents, HRP Substrate Peroxide solution and HRP Substrate Luminol Reagent, for 1min and developed by enhanced chemiluminescence (ECL) which detects the secondary antibody by means of HRP-catalysed oxidation of luminol to 3-aminophthalate and the release of light (chemiluminescence) under alkaline conditions. Results were recorded on Kodak X-Omat LS film and developed using an x-ray processor (Fuji).

2.11.5 Stripping blots and loading control re-probing

As an equal loading control the membrane was re-probed with β-actin. Chemicon 1x Re-Blot plus strong stripping buffer (5ml) was warmed up at 50°C and incubated with a membrane for 20min. The membrane was then washed in TBS and re-blocked in blocking solution (5% (w/v) Marvel Milk in 0.1% TBST). Anti-β-actin mouse monoclonal antibody (AbCAM, 1:5,000 dilution in 5% blocking solution) was incubated with the stripped membrane overnight at 4°C. Secondary antibody anti-mouse IgG-HRP (1:10,000 dilution in 5% blocking solution) was incubated with the blot for 1h at room temperature prior to wash (3 times per 10min in 1x TBST, and 1 time per 10min in 1x TBS) and ECL detection, as described in "PVDF wet transfer and Western blotting" section.

2.12 Fluorogenic caspase activation assay

Members of the ICE/CED-3 cysteine protease family have key roles in inflammation and mammalian apoptosis. The ICE family member caspase-3 (also known as CPP32, Yama, apopain) is activated early in apoptosis and appears to be involved in the proteolysis of several important molecules, including PARP. Activated caspase-3 cleaves PARP from 116kDa to an 85kDa residual fragment. The cleavage site in PARP is it from the C-terminal to Asp-216. The upstream sequence of the cleavage site, DEVD (Asp-Glu-Val-Asp), is utilized as a basis for the highly specific caspase-3 substrate, Ac-(N-acetyl)-DEVD-AMC (7-amino-4-methylcoumarin). Ac-DEVD-AMC is a synthetic tetrapeptide fluorogenic substrate for caspase-3 and contains the amino acid sequence of the PARP cleavage site at Asp-216. The tetrapeptide substrate can be used to identify and quantify caspase-3 activity in apoptotic cells. Caspase-3 cleaves the tetrapeptide between D and AMC, thus releasing the fluorogenic AMC, which can be quantified in a spectrofluorometer.

$0.325x10^6$ cells were seeded in T25 flasks (5ml total volume/flask). Adherent cells were incubated at 37°C overnight before treatment. Cells were treated with compound RE37 at 20μM for 24h before being exposed to light for 1h to give light doses of $12.66J/cm^2$, or kept in the dark. Cells were then incubated at different time points. The time points are

"time 0", which was immediately after light exposure, 30min, 1, 2, 4, 8 and 16h incubation.

At experimental endpoints, cells are captured by trypsinisation and centrifuged at 300xg for 5min. Cells were washed twice in ice cold PBS. The pellet was resuspended in 1x Harvesting Buffer (20mM Hepes (pH 7.5), 10% (w/v) Sucrose, 0.1% (w/v) CHAPS, 1% (v/v) Nonidet P40, 1mM Sodium EDTA (ethylenediaminetetraacetic acid)) supplemented with fresh 2mM DTT, 1mM PMSF, 1µg/ml Leupeptin and 1µg/ml Aprotinin. Cells were then lysed on ice for 10min, vortexed and incubated on ice for a further 10min. Lysates were centrifuged at 20,000xg for 20min at 4°C and supernatants were kept and stored at -20°C prior to analysis. The lysate protein concentration was determined by BCA assay as described in Section 2.10. 100µg of protein/sample was diluted to 50µl in 1x Harvesting Buffer in an Epppendorf tube followed by addition of 50µl of 2x Reaction Buffer (100mM Hepes, 10% (w/v) Sucrose, 0.1% (w/v) CHAPS and 1mM EDTA) supplemented with fresh 10mM DTT. 5µl of 1mM (20X) caspase specific substrate (50µM final substrate concentration) was incubated with lysates in the dark, at 37°C for 2h. Assay reaction mixtures were added to a 96-well plate and fluorescent intensity (FI) was read on a Spectramax Gemini fluorometric plate reader using a SoftMax Pro version 4.0 software package (Ex/Em: 380/460nm). Data was analysed by calculating fold induction of active caspase in drug and vehicle treated samples compared to treated samples maintained in the dark.

2.13 CytoTox 96® Non-Radioactive Cytotoxicity Assay

The CytoTox 96® Non-Radioactive Cytotoxicity Assay is a colorimetric assay which quantitatively measures lactate dehydrogenase (LDH), a stable cytosolic enzyme that is released upon cell lysis. Released LDH in culture supernatants is measured with a 30min coupled enzymatic assay, which results in the conversion of a tetrazolium salt (INT) into a red formazan product. The amount of colour formed is proportional to the number of lysed cells. The general chemical reactions of the CytoTox 96® Assay are as follows:

LDH

$$NAD+ + lactate \rightarrow pyruvate + NADH$$

Diaphorase

$$NADH + INT \rightarrow NAD+ + formazan\ (red)$$

$0.5x10^4$cells/well were seeded in 96-well plates (200 µl total volume/well). Cells were incubated at 37°C overnight before treatment with the compounds which was plated in triplicate and compared to dark-treated controls. Following 24h of treatment, the treated cells were either exposed to light for 1h to give a light dose of 12.66J/cm^2 or maintained in the dark. Following 23h of incubation an CytoTox 96® Assay, was performed: Lysis Solution (10X) was added in triplicate to cells not treated as positive control and incubated for 45–60min at 37°C; 50µl of supernatant was then transferred to an enzymatic assay plate; 50µl of Reconstituted Substrate Mix was added to each well of enzymatic assay plate followed by incubation for 30min at room temperature, protected from light; 50µl of Stop Solution was then added to each well. Absorption was measured using a microplate reader at 490nm.The LDH production was determined by subtracting the average absorbance values of the background culture medium from each group; the control lysed cells represented the LDH production/release. All data points were analysed using GRAPH PAD Prism software.

2.14 Comet assay

The Comet assay, also known as Single Cell Gel Electrophoresis assay, is an uncomplicated and sensitive technique for the detection of DNA damage at the level of the individual eukaryotic cell. The Comet assay should be prepared under dimmed or yellow light to prevent DNA damage from UV light. Moreover, all buffers have to be kept on ice to inhibit repair in unfixed cells and endogenous damage occurring during sample preparation.

$3x10^5$ cells/well HeLa cells were seeded in a 6-well plate (3ml/well) and incubated at 37°C overnight before being treated. Cells were then treated with 5µM of RE84 or 85 and incubated at 37°C for 24h before being exposed to light for 1h to give a light dose of 12.66J/cm^2 or maintained in the dark.

Cells were then trypsinised and resuspended in 20µl of PBS and 75µl of 0.5% low melting point agarose (LMPA) previously melted in microwave and cooled down at 37°C in a water bath to stabilize the temperature.

The slides, upon which the cells have to be placed, were prepared the day before use by dipping them in ethanol and burning them over a blue flame to remove the machine oil and dust. The slides were then dipped in normal melting point agarose (NMPA) up to one-third the frosted area. The underside of the slides was wiped to remove agarose and left to dry (either air dried or warmed at 50°C for quicker drying). The slides were then stored at room temperature until needed, avoiding high humidied conditions.

The cells-LMPA mix was placed on the slides previously prepared and covered with a coverslip. After the agarose layer hardened the coverslip was removed and further 75µl of LMPA was added to the slides and covered again with a coverslip. After the agarose layer hardened the coverslip was removed and the slides were then placed in pre-chilled lysis buffer (2.5M NaCl, 100mM EDTA, 10mM Tris, 1% (v/v) Triton X-100, pH10) for up to 2h at 4°C.

The slides were then placed side by side in a horizontal gel box which was previously filled with freshly made electrophoresis alkaline buffer (300mM NaOH (sodium hydroxide), 1mM EDTA, pH >13). The slides were let sit in the alkaline buffer for 20min to allow for unwinding of the DNA and for the expression of alkali-labile damage. The gel was run at 24 volts (~0.74 V/cm), current 300mA for 30min. The slides were then removed and the gel was rinsed twice, drop wise with neutralization buffer (0.4M Tris, pH 7.5) for at least 5min. The slides were then stained with PI (1:100 dilution) for 20min and then dipped in chilled distilled water to remove excess stain.

For visualization of DNA damage, observations were made of PI-stained DNA using a 40x objective on Olympus IX81 fluorescent microscope. The software Cell^P was used to collect images.

2.15 Isolation of mitochondria and nuclei from cultured cells

Each organelle has characteristics (size, shape and density for example) which make it different from other organelles within the same cell. If the cell is broken open in a gentle manner, each of its organelles can be subsequently isolated. The process of breaking open

cells is homogenization and the subsequent isolation of organelles is fractionation. Isolating the organelles requires the use of physical chemistry techniques, and those techniques can range from the use of simple sieves, gravity sedimentation or differential precipitation, to ultracentrifugation of fluorescent labelled organelles in computer generated density gradients.

2.15.1 Pierce® mitochondria isolation kit for cultured cells using Dounce homogenization

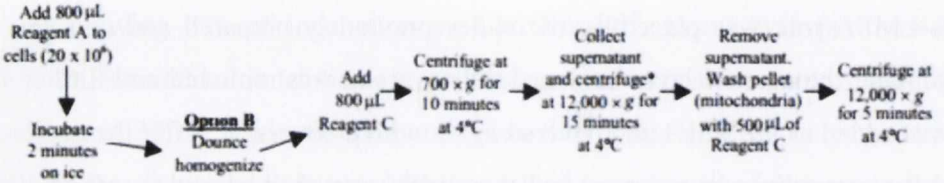

Figure 2.6: Procedure summary for the Pierce Mitochondria isolation Kit adapted from [104].

$1x10^7$ cells were seeded in T175 flasks (20ml total volume/flask). Cells were incubated at 37°C overnight before treatment. The cells were treated with the compounds at 3µM. After 4 and 24h incubation in the dark, cells were harvested by scraping, pelleted by centrifugation at 850xg for 5min and washed with pre-warmed PBS.

The pellet was resuspended in 800µl of Mitochondria Isolation Reagent A+1x protease inhibitor, vortexed at medium speed for 5s. and incubated on ice for 2min. Each sample was processed one at a time. The Dounce tissue grinder was pre-chilled on ice before use and after cells were homogenized on ice, 800µl of Mitochondria Isolation Reagent C+1x protease inhibitor was added to the lysed cells. The sample was then rinsed with 200µl of Mitochondria Isolation Reagent A and inverted several times to mix. The sample was then centrifuged at 700xg for 10min at 4°C. The supernatant was transferred to a new tube and centrifuged at 12,000xg for 15min at 4°C.

The supernatant represented the cytosolic fraction, which was transferred to a new tube while the pellet contained the isolated mitochondria. 500µl of Mitochondria Isolation Reagent C was added to the pellet and centrifuged at 12,000xg for 5min. The mitochondrial pellet was kept on ice before downstream processing in order not to compromise mitochondrial integrity.

2.15.2 Nuclei isolation from cultured cells using Dounce homogenization

$1x10^7$ cells were seeded in T175 flasks (20ml total volume/flask). Cells were incubated at 37°C overnight before treatment. The cells were treated with the compounds at 3µM. After 4 and 24h incubation in the dark, cells were harvested by scraping, pelleted by centrifugation at 850xg for 5min and washed with pre-warmed PBS. The pellets were resuspended in 1ml ice-cold STE buffer (250mM sucrose, 5mM Trizma base, 2mM EGTA + fresh 1x protease inhibitors, pH 7.4). Each sample was processed one at a time. The Dounce tissue grinder was pre-chilled on ice before use and after cells were homogenizated on ice, the cell homogenates were centrifuged in Eppendorf tubes at 800xg for 3 min at 4°C. The pellets represented the nuclear fraction plus other cell debris. The pellets were incubated with 100µl of Buffer B (20mM HEPES, 420mM NaCl, 1.5mM $MgCl_2$ (magnesium chloride), 0.2mM EDTA, 25% (v/v) glycerol + fresh 1x protease inhibitors pH 7.9) on ice for 30min. After incubation on ice, nuclear pellets were centrifuged at 12,000xg for 10min at 4°C. The supernatant represented an enriched nuclear fraction and the pellets were incubated again in Buffer B (20µl) for 15min on ice to ensure the nuclear fraction of all lysed cells was obtained. These pellets were centrifuged at 12,000xg for 10min at 4°C and the resulting supernatant combined with original supernatant. The final pellet represents intact cells and cellular debris.

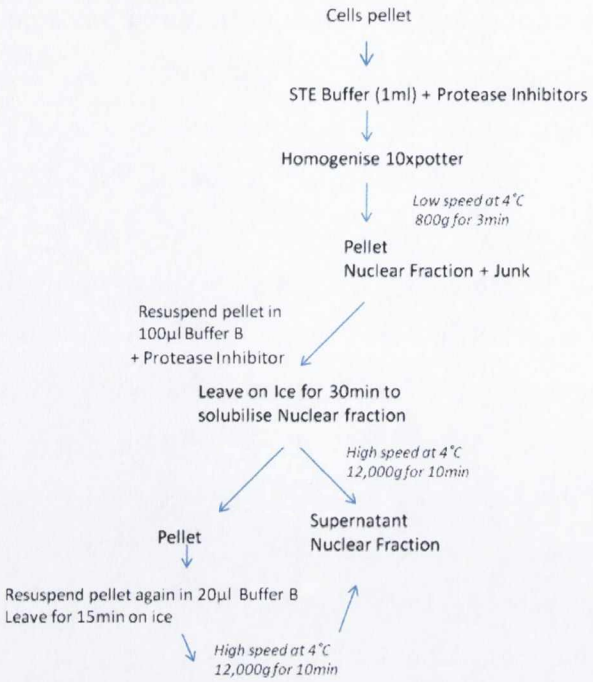

Figure 2.7: Procedure summary of the nuclei isolation protocol

2.15.3 Measurement of Ru(II) fluorescence in mitochondrial and nuclear fractions

The fluorescence of each fraction was measured at 635nm using a fluorescence spectrophotometer (Varian) (444nm laser; Ex/Em: 430/630nm) in 10mM phosphate buffer in PBS at pH7.4. The BCA assay was used (as described above in Section 2.10) to measure the protein concentration of each fraction and each fraction was normalised as fluorescence/µg of protein. Samples were prepared for SDS-PAGE, which is described in Section 2.11.2-4, by standardising protein concentration to 20µg/µl with 1x Laemmli buffer.

Chapter 3:

Investigation on organic pdppz derivative and on Ru(II) complexes based on a novel extended aromatic polypyridyl ligands as a DNA probe and photocleavage agents

Introduction

Taking into consideration previous studies of rigid 1,8-naphthalimide-diquat conjugates (within the Gunnlaugsson research group) which have been shown to bind DNA with high affinity, to have their emission efficiently quenched in the presence of DNA and to provide both electrostatic attraction to the helix and associating in the DNA groves [73], compound RE33 was investigated further. Studies performed by Robert B. P. Elmes, demonstrated that RE33 shows good water solubility and has a distinctive set of photophysical properties. DNA binding affinities of RE33 with stDNA (salmon testis DNA) showed a particular preference for $[poly(dGdC)]_2$ than for $[poly(dAdT)]_2$ [73].

In addition, further studies performed by Robert B. P. Elmes, show that RE33 is highly oxidising in its excited state whereby it undergoes a photoinduced electron transfer (PET) process in the presence of A and G sites on DNA [73]. Subsequently, studies on the interaction of RE33 with DNA, confirmed the perpendicular orientation of the pdppz portion on the compound relative to the DNA helix axis pointing towards intercalation as the most likely mode of interaction [73]. Furthermore, it was demonstrated that RE33 is an efficient DNA photocleavage agent, which has been shown using a plasmid DNA (pBR322 DNA) [73]. The excitation of the compound with and without DNA has been determined. The UV/Visible absorption, excitation and emission spectra of these compounds are shown in figure 3.2 and they have been recorded at pH 7.4 in 10mM phosphate buffer [73]. The emission of RE33 in aqueous solution was shown, by Robert B. P. Elmes, to have its excited state effectively quenched by 90% upon addition of stDNA [73]. Compounds containing diquat functionally are very well known oxidizing agents, and therefore the observed emission quenching is likely due to electron transfer from the DNA bases [73]. Quenching of this extent implies close association of the compound with the nucleotides, in a manner that allows for electron transfer from the bases to RE33 to take place [73].

With the aim to improve the DNA binding of the compound it was thought to add a metal centre to the structure, as in the last few decades, coordination complexes based on metal centres and polypyridyl ligand architectures have been developed as structure- and site-specific reversible DNA binding agents [105]. In particular, complexes based on Ru(II) centres have become of great interest due to their attractive photophysical properties, focusing on the use of these complexes in biological contexts.

The cellular uptake and target/localisation of the compound are very important from a therapeutic point of view in order to determine if the compounds are more suitable as imaging probes or as therapeutic agents. The cellular uptake and compartmentalization behaviours are usually related to their charge, size, substitution group and hydrophobicity/hydrophilicity. The complexes with positive charges can easily interact with and enter living cells. Many cationic Ru(II) complexes with two positive charges, can enter living cells [106]. On the other hand, the introduction of negative charges in the complex will reduce the cellular uptake ability of small molecules. The size of a molecule is critical to its application as therapeutic or diagnostic agent so the size of the heavy-metal complexes affects their intracellular uptake properties. Proteins in the cellular membrane act as channels and pump different molecules into and out of the cell maintaining the electric potential of the cell. A compound's localisation is very important because it is related to the limited migration of $^1O_2$ from the site of formation, sites of initial cell or tissue damage of photosensitization, and because it may be associated with cytotoxicity. In fact, cytotoxicity often originates with metabolism, survival and proliferation of cells and organisms or with non-specific binding to proteins and membranes [106]. For example, lipid and protein photooxidation in the cellular membrane generates the activation of the phospholypases from the membrane which leads to: changes in membrane permeability, reduced fluidity and inactivation of enzymatic systems and receptors [16] in fact complexes with high lipophilicity are usually highly cytotoxic. The non-specific binding may lead toxicity to normal cells [15]. In order to decrease the cytotoxicity, it is important to suppress non-specific interactions with extracellular substances such as proteins or non-specific binding to the cell surface. Peptide conjugation is widely used for improving both cellular and nuclear entry. Rhodium(III) 5,6-chrysenequinone diimine (chrysi) and Ru(II) dppz complexes, for example, were successfully delivered to the nucleus through covalent attachment to D-octa arginine [107].

The objective of the research presented in this Chapter will be the study of the uptake, localisation and investigation into cell death of RE33 and of a series of Ru(II) polypyridyl complexes, RE30, 34, 37, based on a novel extended, aromatic, polypyridyl ligand, pyrazino[2,3-h]dipyrido[3,2-a:2',3'-c]phenazine (pdppz). The structures of all the compounds are shown in figure 3.1. This pdppz ligand is based on the combination, in a single structure, of both dppz and TAP and is reported to insert between the base-pairs of B-form double-stranded DNA [108]. In order to increase the potency of the compounds,

further extension of the planar dppz structure would infer both increased DNA binding and photocleavage ability with possible formation of DNA photoadducts, as previously reported with Ru(II) complexes containing TAP [108]. What is more, pdppz displays varied and potentially useful photophysical properties in aqueous solution and it possesses multiple absorption bands which are expected to change upon interaction with DNA [73]. Moreover, complexes of this type show little or no photoluminescence at ambient temperature, however, upon addition of double helical DNA, intense photoluminescence is observed. This phenomena of the interaction of the complex with DNA was described by Barton *et al.* [91] and was called the 'light switch' effect, which is outlined in Section 1.4.1 of the first Chapter. Since dppz complexes all act as molecular light switches, showing minimal luminescence in aqueous solution and intense luminescence when bound to DNA, they have potential as a sensitive cellular probes [109]. In connection with that, the excitation of the compound with and without DNA has been determined. The UV/Visible absorption, excitation and emission spectra of these compounds are shown in figure 3.3 and they have been recorded at pH 7.4 in 10mM phosphate buffer [73]. Upon addition of stDNA, the intensity of fluorescence of RE30 and 34 in aqueous solution was shown, by Robert B. P. Elmes, to increase, until reaching a plateau followed by a subsequent decrease in emission [73]. Controversially, the emission of RE37 in aqueous solution was shown, by Robert B. P. Elmes, to have its excited state effectively quenched by 86% upon addition of stDNA [73]. Compounds RE30 and 34 after binding stDNA showed a 'light-switch' effect but RE37 did not.

Moreover, substituting the ancillary ligands on the dppz complex permits the variation in the overall complex charge, size and hydrophobicity.

With the aim to establish the effects of the variation of the ancilliary ligands around the Ru(II) centre and to provide a set of known photophysical properties that can be used to monitor the binding process, three different species have been synthesised. The first of them is RE30, which contains bpy around the Ru(II) centre; RE34, which contains phen and RE37 which contains TAP. These compounds have the potential to damage DNA through ROS production: as reported in previous publications, both $[Ru(bpy)_3]^{2+}$ and $[Ru(phen)_3]^{2+}$ cause photocleavage of DNA with $^1O_2$ sensitisation thought to be one of the main processes by which occurs [92]. Moreover, it was reported in previous literature that while bpy bound to DNA weakly through electrostatic interaction, phen interaction with DNA was much stronger [91]. TAP is an electron accepting ligand which confers to the

Ru(II) complex a strong oxidizing excited state on the complex, increasing the potential of the compound to bind DNA.

The nature of the binding interaction between the compound and the DNA is important because it affects the efficiency of any photoreactions that occur [110]. The design of sequence-specific DNA damaging agents is of great interest for the control of gene expression [110]. In relation to that, the pre-organised position of the complex in the DNA helix may lead to photoadduct formation and/or a reaction with the sugar moiety causing efficient DNA photocleavage. Several ruthenium compounds have been shown to inhibit DNA replication, possess mutagenic activity, induce SOS response (SOS response is a global response to DNA damage in which the cell cycle is arrested and DNA repair and mutagenesis are induced), bind to nuclear DNA and reduce RNA synthesis [111]. DNA interactions of antitumor ruthenium agents are of a great interest and several reviews have appeared that summarise anticancer effects of ruthenium complexes [111].

Fluorescence studies, performed by Robert B. P. Elmes, demonstrated that RE30, 34 and 37 showed striking emission modulation upon interaction with stDNA and the homopolymers $[poly(dGdC)]_2$ and $[poly(dAdT)]_2$ [73]. Moreover, they are capable of binding with high affinity to DNA, with strong evidence for an intercalatory mode of interaction [74]. It has been subsequently identified that both RE30 and 34 were unable to sensitise $^1O_2$ where RE37 was capable of $^1O_2$ production [73]. Studies on DNA photocleavage of pBR322 plasmid of RE30 and 34 showed negligible photocleavage while RE37 showed highly efficient cleavage [73].

Considering all of the above, the aim of the present study is to identify the potential of these compounds as spectroscopic probes for DNA or as possible DNA photocleavage agents for use in PDT.

Compounds which can be tolerated by cells, showing little or no cytotoxicity may be useful as imaging agents, whereas compounds which induce cytotoxicity when photoactivated may be useful in PDT.

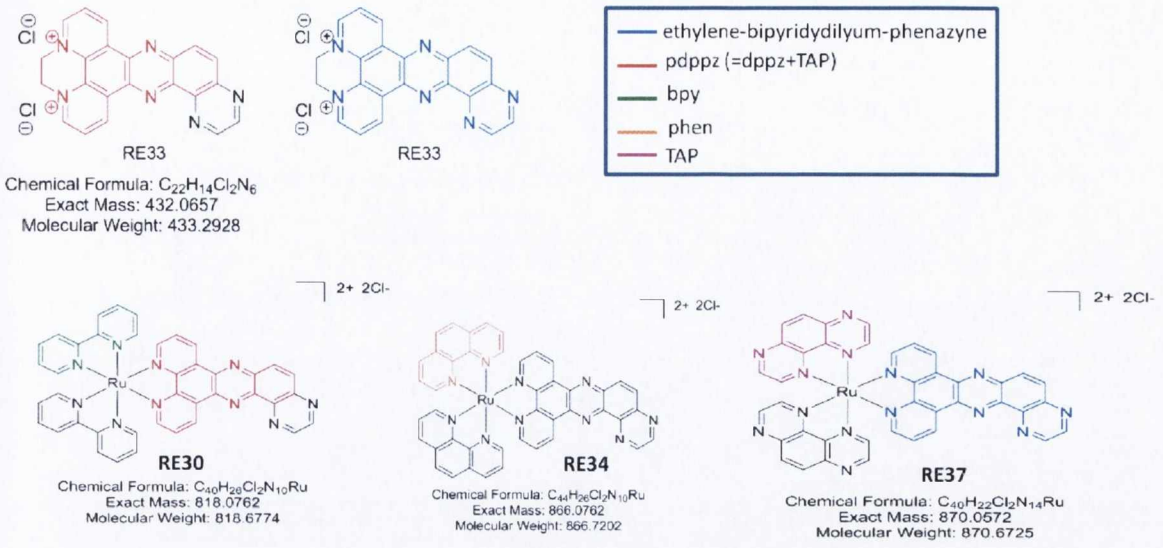

Figure 3.1: Structures, chemical formula, mass and molecular weight of the cationic derivative of pdppz RE33 and of the aromatic polypyridyl ligands around the metal centre of the Ru(II) metal compounds RE30, 34 and 37.

Results

3.1 RE33 and some Ru(II) compounds reduce cell viability in some malignant cell lines

In a preliminary screening experiment several cell lines were used in order to verify the efficacy of the compounds in different malignant cell lines (CRL, One 58, Mutu1, DG75 and HeLa). Cells were incubated with a range of concentrations (1, 10, 100μM) of RE33 and the Ru(II) polypyridyl metal compounds (RE30, 34 and 37) for 24h in the dark, and then for one half of the replicates the cells were illuminated (as described in Section 2.5 of the Materials and Methods) for 1h, and then all the cells incubated for a further 23h. An AB cell viability assay was performed with all the cells.

RE33 reduced cell viability at high concentrations (100μM) in all the tested cell lines and there was a difference in viability in mesothelioma and in Burkitt's lymphoma cell lines depending on illumination, but little difference in HeLa cells. The results are shown in figures 3.4.

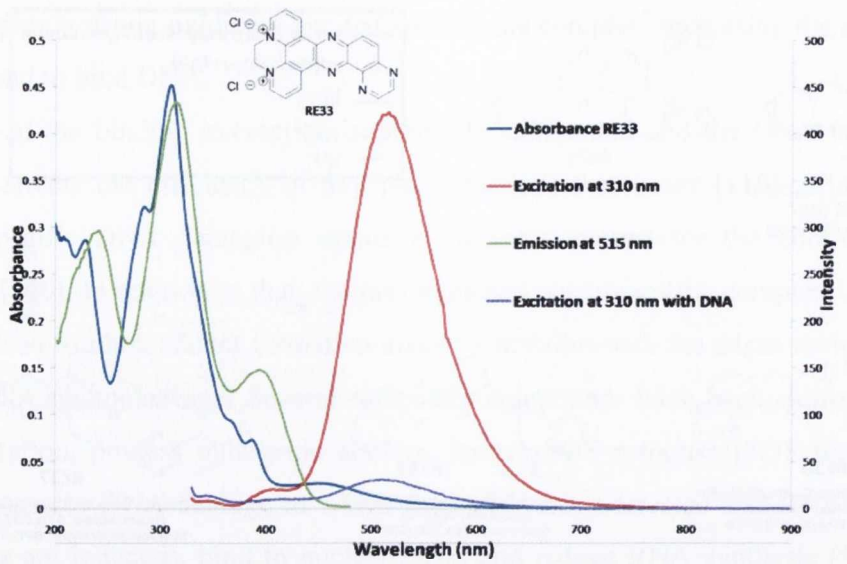

Figure 3.2: Structure and UV/Visible, excitation and emission spectra of RE33 compound (10μM) in 10mM phosphate buffer, pH7.4. Robert B.P Elmes performed this experiment.

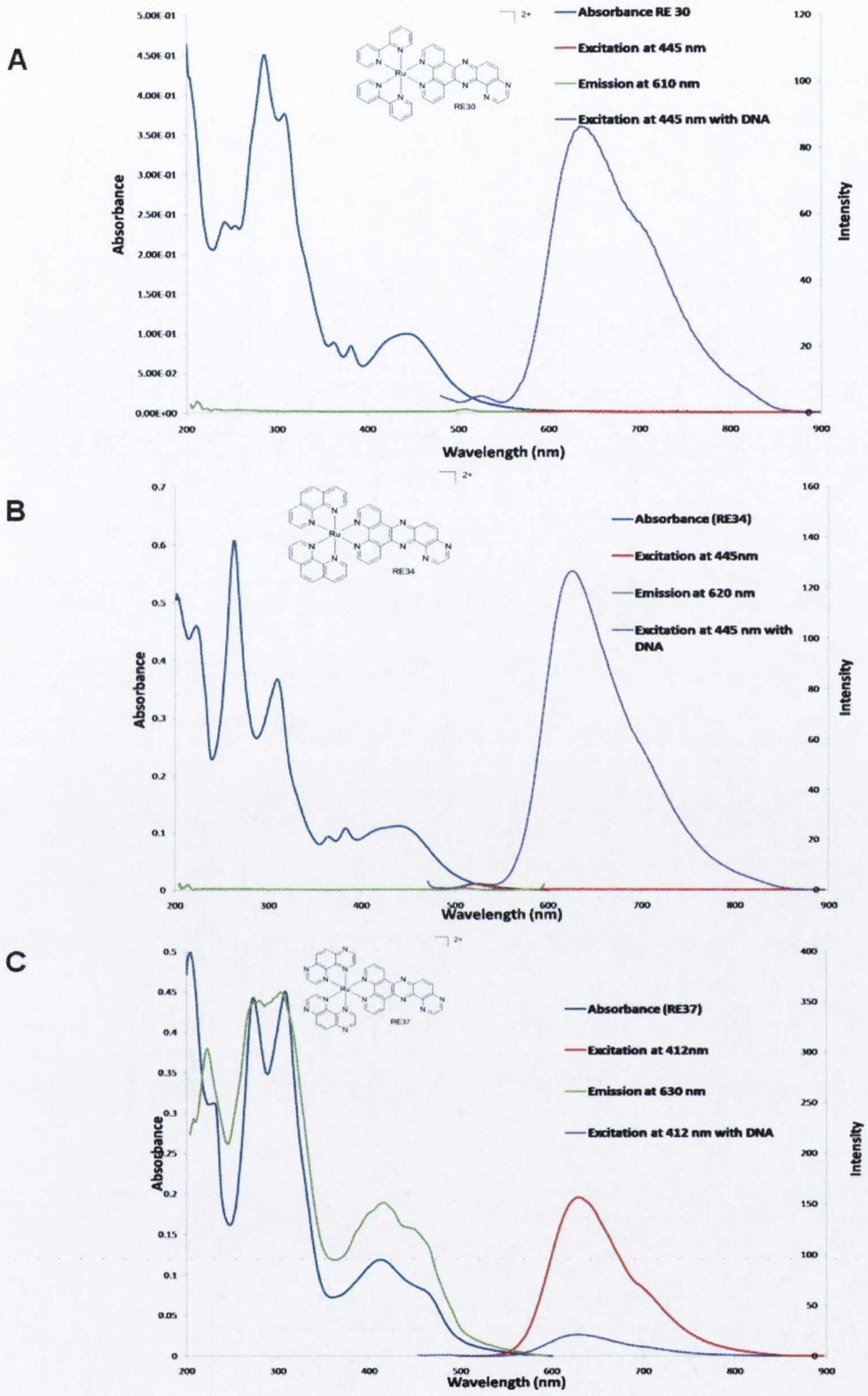

Figure 3.3: Structure and UV/Visible, excitation and emission spectra of RE30 (6.3μM) **(A)** in 10mM phosphate buffer, pH7.4; of RE34 (6.3μM) **(B)** in 10mM phosphate buffer, pH7.4 and of RE37 (6.3μM) **(C)** in 10mM phosphate buffer, pH7.4. Robert B.P Elmes performed this experiment.

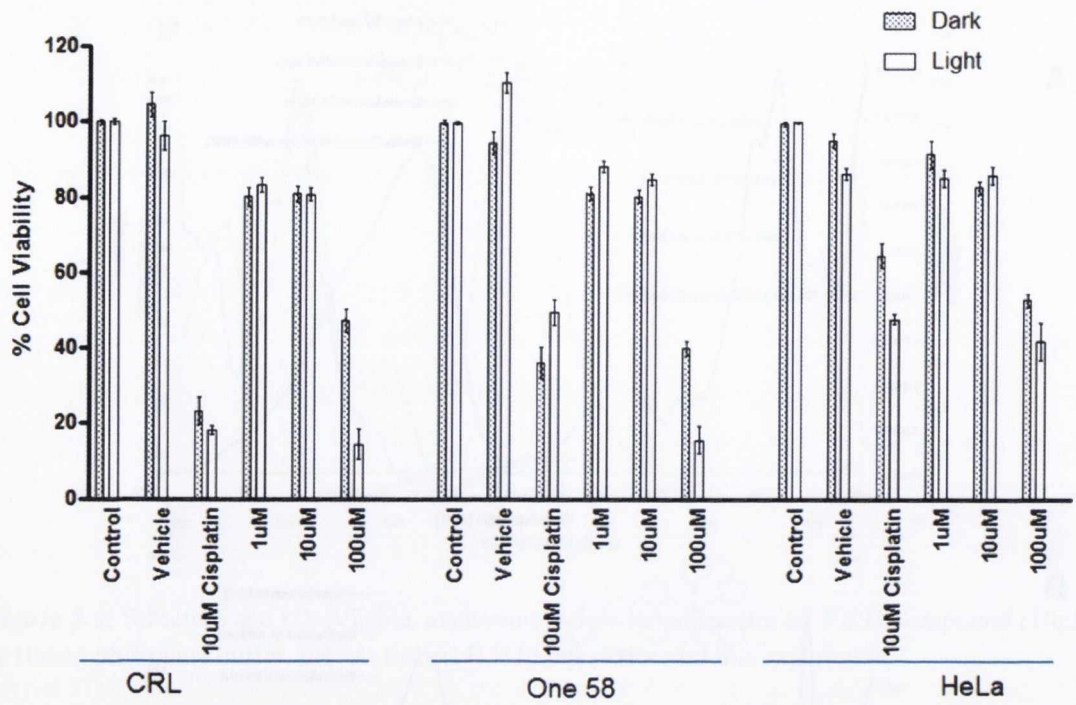

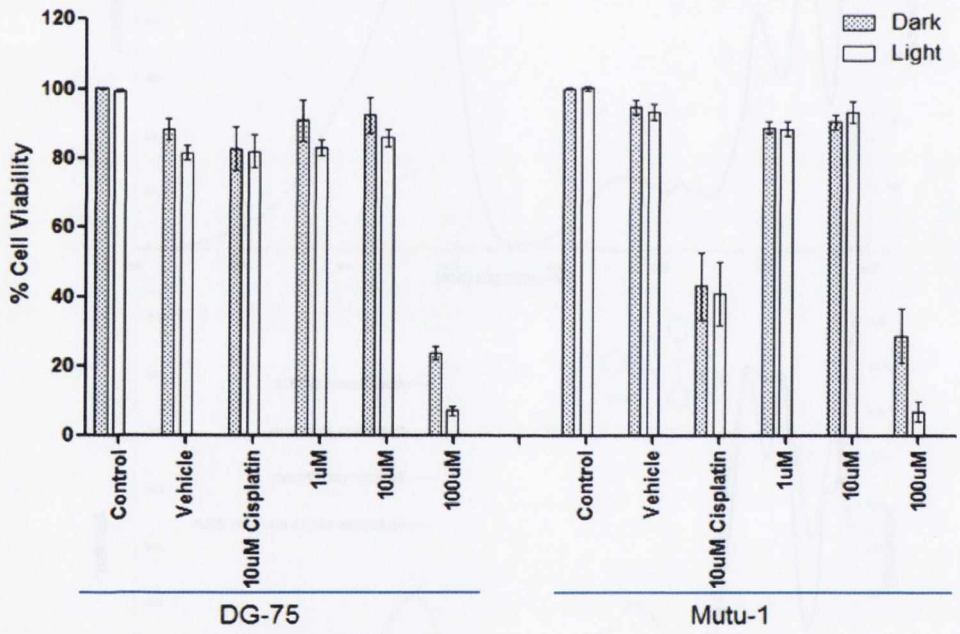

RE33 (100μM)		
Cell Lines	Dark (Mean±S.E.M.)	Light (Mean±S.E.M.)
HeLa	52.9±1.7	41.9±4.9
Mutu-1	24.9±7.3	7.6±2.9
DG-75	23.8±2.0	7.2±1.5
CRL	47.5±3.0	11.5±4.4
One 58	40.1±1.9	12.8±3.6

Figure 3.4: **The effect of RE33 on malignant cell lines with or without light exposure.**

$0.5x10^4$ CRL, HeLa and One 58 cells/well, $0.8x10^5$ Mutu-1 cells/well and $4x10^4$ DG-75 cells/well were seeded in 96-well plates (200 µl total volume/well). Adherent cells were incubated at 37°C overnight before treatment. RE33 concentrations (1, 10 and 100µM) were plated in triplicate and compared to dark-treated or positive controls (cisplatin at 10µM). Following 24h of treatment, the treated cells were either exposed to light for 1h to give a light dose of $12.66J/cm^2$ or maintained in the dark. Following 23h of incubation an AB assay was performed by adding 20µl of AB dye per well followed by 5-6h incubation at 37°C in the dark until the colour change occurred. The background fluorescence of media without cells plus AB was taken away from each group, and the control untreated cells represented 100% cell viability. The number of viable cells is expressed as a percentage of AB reduction for at least three independent experiments. Fluorescence was measured using a microplate reader (excitation 544nm, emission 590nm). Table of cell viability values is included on the graph.

RE30 and 34 reduced cell viability at high concentrations (100μM) in all the tested cell lines and there was no difference in viability whether cells were illuminated or not.
RE37 reduced cell viability at a high concentration but it reduced cell viability to a much greater extent when illuminated in four of the five cell lines tested. No light-induced reduction in cell viability was found in DG75 cell line. The results are shown in figures 3.5 and 3.6 and in the cell viability values in Table 3.1.

3.2 Concentration-dependence of light induced reduction in cell viability

In order to show concentration dependence of the light induced phenomenon with the compounds and to produce an IC_{50} value for decreased cell viability, RE33 and the Ru(II) compounds (RE30, 34 and 37) were screened with a range of concentrations. Cells were treated (1, 4, 7, 10, 40, 70, 100μM for RE30 and 34; 1, 4, 10, 25, 40, 50, 70, 75 and 100μM for RE33 and 37) and incubated for 24h in the dark, and then for one half of the replicates the cells were illuminated for 1h, and then all the cells incubated for further 23h. An AB cell viability assay was performed at all the cells.
Compound RE33 again induced a reduction in cell viability in most of the tested cell lines showing little difference between in light death or light independent viability. A more pronounced difference in viability in cells with or without illumination was shown with CRL and HeLa cell lines. The results are shown in figures 3.7 and 3.8.
Compounds RE30 and 34, again showed no effect on cell viability. Compound RE37 again showed an ability to reduce cell viability when illuminated, although the effectiveness varied in the different cell lines, with the most pronounced effect with CRL, HeLa and One 58, compared with DG75 and Mutu-1 cells. The compounds showed IC_{50} values for photo-induced reduction in cell viability of between 18-50μM. The results are shown in figure 3.9 to 3.13.

A

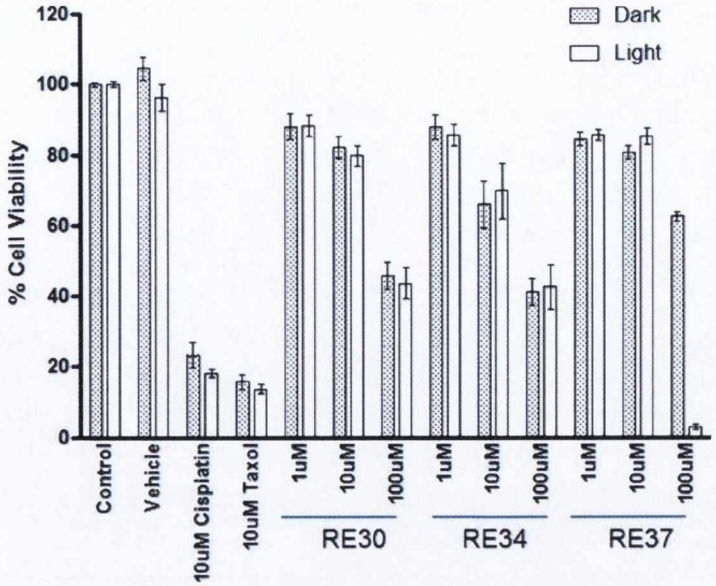
Dark
Light
% Cell Viability
120
100
80
60
40
20
0
Control
Vehicle
10uM Cisplatin
10uM Taxol
1uM
10uM
100uM
RE30
RE34
RE37

B

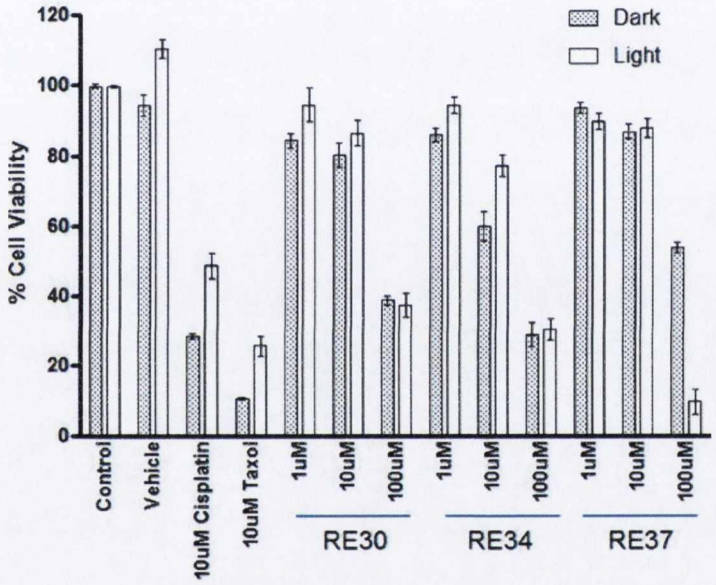
Dark
Light
% Cell Viability
120
100
80
60
40
20
0
Control
Vehicle
10uM Cisplatin
10uM Taxol
1uM
10uM
100uM
RE30
RE34
RE37

C

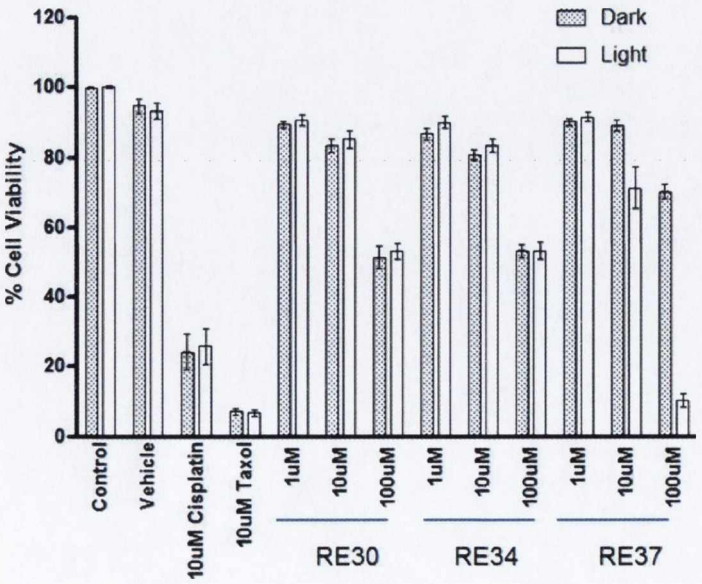
Dark
Light
% Cell Viability
120
100
80
60
40
20
0
Control
Vehicle
10uM Cisplatin
10uM Taxol
1uM
10uM
100uM
RE30
RE34
RE37

Figure 3.5: **Ru(II) compounds have different light dependent effects on cell viability.**

$0.5x10^4$ CRL **(A)** , One 58 **(B)** and $0.8x10^5$ Mutu-1 **(C)** cells/well were seeded in 96-well plates (200 µl total volume/well). Adherent cells were incubated at 37°C overnight before treatment. Each compound concentration (RE30, 34, 37 at 1, 10 and 100µM) was plated in triplicate and compared to dark-treated or positive controls (Cisplatin and Taxol either at 10µM). Following 24h of treatment, the treated cells were either exposed to light for 1h to give a light dose of $12.66J/cm^2$ or maintained in the dark. Following 23h of incubation an Alamar Blue assay was performed by adding 20µl of AB dye per well followed by 5-6h incubation at 37°C in the dark until the colour change occurred. The background fluorescence of media without cells plus AB was taken away from each group, and the control untreated cells represented 100% cell viability. The number of viable cells is expressed as a percentage of AB reduction for at least three independent experiments. Fluorescence was measured using a microplate reader (excitation 544nm, emission 590nm).

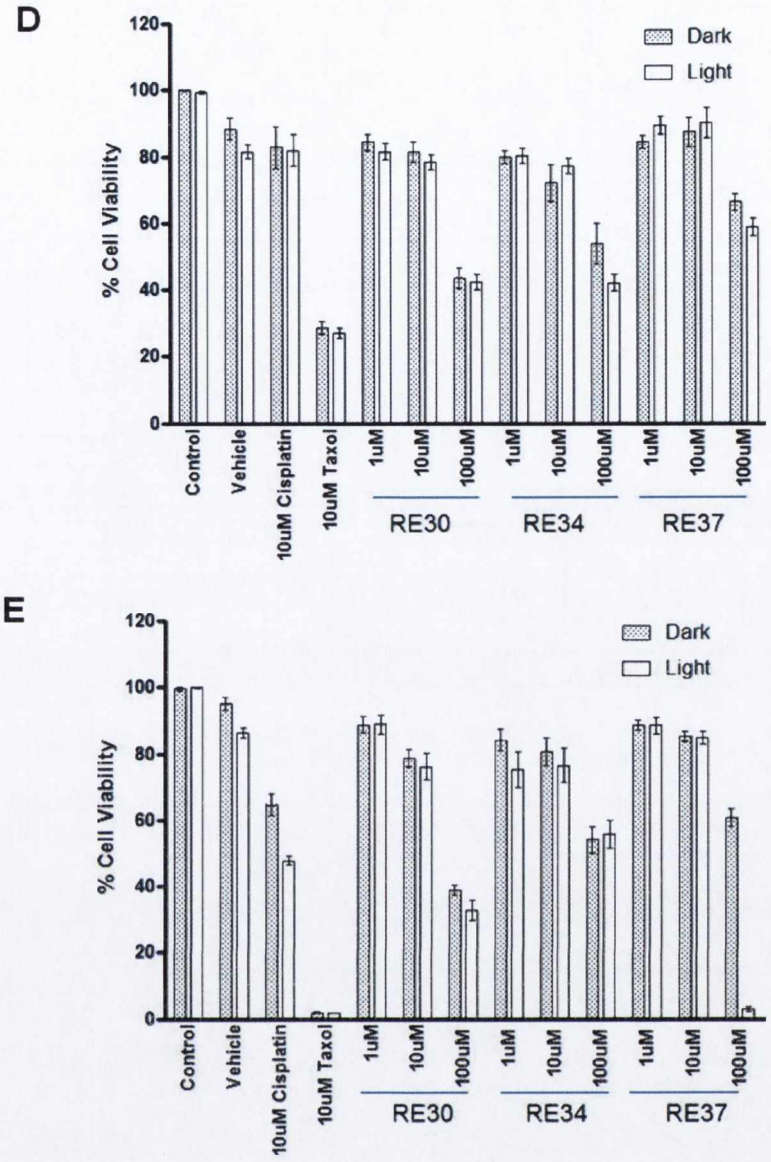

Figure 3.6: **Ru(II) compounds have different light dependent effects on cell viability.**

$4x10^4$ DG-75 **(D)** cells/well and $0.5x10^4$ HeLa **(E)** cells/well were seeded in 96-well plates (200 µl total volume/well). Adherent cells were incubated at 37°C overnight before treatment. Each compound concentration (RE30, 34, 37 at 1, 10 and 100µM) was plated in triplicate and compared to dark-treated or positive controls (Cisplatin and Taxol either at 10µM). Following 24h of treatment, the treated cells were either exposed to light for 1h to give a light dose of $12.66J/cm^2$ or maintained in the dark. Following 23h of incubation an AB assay was performed by adding 20µl of AB dye per well followed by 5-6h incubation at 37°C in the dark until colour change occurred. The background fluorescence of media without cells plus AB was taken away from each group, and the control untreated cells represented 100% cell viability. The number of viable cells is expressed as a percentage of AB reduction for at least three independent experiments. Fluorescence was measured using a microplate reader (excitation 544nm, emission 590nm).

CRL 5915		
Compounds	Dark (Mean±S.E.M.)	Light (Mean±S.E.M.)
30	45.8±3.9	43.7±4.3
34	41.2±3.8	42.7±6.3
37	62.5±1.4	3.0±0.7

One 58		
Compounds	Dark (Mean±S.E.M.)	Light (Mean±S.E.M.)
30	38.8±1.4	37.3±3.3
34	28.9±3.4	30.5±3.2
37	53.8±1.7	9.6±3.6

Mutu-1		
Compounds	Dark (Mean±S.E.M.)	Light (Mean±S.E.M.)
30	51.2±3.3	53.1±2.2
34	53.2±1.9	53.2±2.4
37	70.1±2.0	10.2±1.8

DG-75		
Compounds	Dark (Mean±S.E.M.)	Light (Mean±S.E.M.)
30	43.7±3.0	42.3±2.4
34	53.9±6.1	42.1±2.4
37	66.3±2.4	58.9±2.6

HeLa		
Compounds	Dark (Mean±S.E.M.)	Light (Mean±S.E.M.)
30	38.9±1.6	32.9±3.0
34	54.1±4.2	55.6±4.3
37	60.8±2.6	2.9±0.9

Table 3.1: **Table of cell viability.**

Mean±S.E.M. values for CRL, One 58, Mutu-1, DG-75 and HeLa treated with 100μM of compounds RE30, 34 and 37 with and without light exposure of at least three independent experiments.

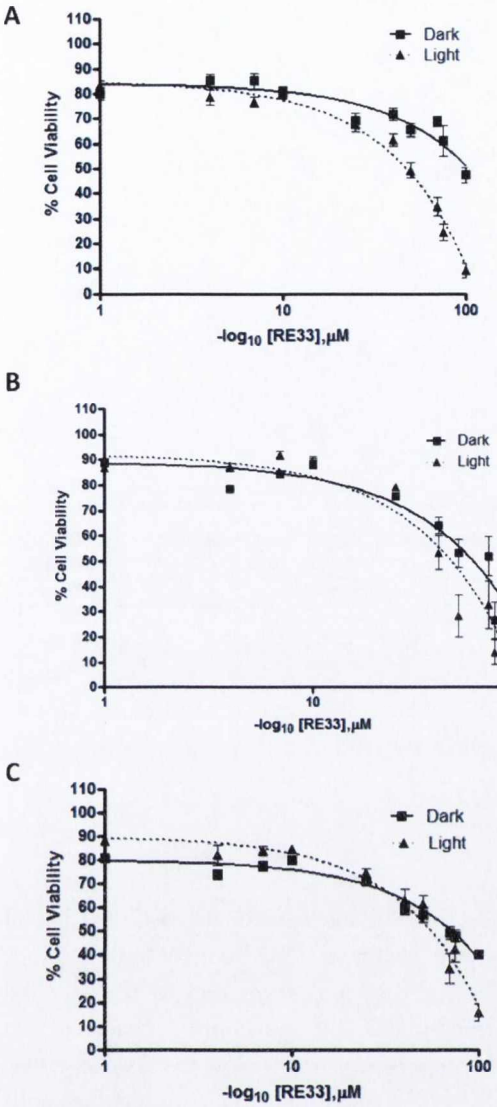

Cell lines		IC_{50} RE33 (µM)
CRL	Dark	95.0
	Light	38.6
Mutu-1	Dark	58.7
	Light	44.8
One 58	Dark	69.0
	Light	55.1

Figure 3.7: **The effect of RE33 on malignant cell lines with or without light exposure.**

$0.5x10^4$ CRL **(A)**, $0.8x10^5$ Mutu-1 **(B)** and $0.5x10^4$ One 58 **(C)** cells/well were seeded in 96-well plates (200 µl total volume/well). Cells were incubated at 37°C overnight before treatment. RE33 concentrations (1, 4, 7, 10, 25, 40, 50, 70, 75 and 100µM) were plated in triplicate and compared to dark-treated controls. Following 24h of treatment, the treated cells were either exposed to light for 1h to give a light dose of $12.66J/cm^2$ or maintained in the dark. Following 23h of incubation an AB assay was performed by adding 20µl of AB dye per well followed by 5-6h incubation at 37°C in the dark until the colour change occurred. The background fluorescence of media without cells plus AB was taken away from each group, and the control untreated cells represented 100% cell viability. The number of viable cells is expressed as a percentage of AB reduction of at least three independent experiments. Fluorescence was measured using a microplate reader (excitation 544nm, emission 590nm). The antiproliferative potency for each compound was determined by linear regression calculating an approximate IC_{50} ([Dose] when response is equal to 50% cell viability). All data points were analysed using GRAPH PAD Prism software. A table of IC_{50} values is included on the graph.

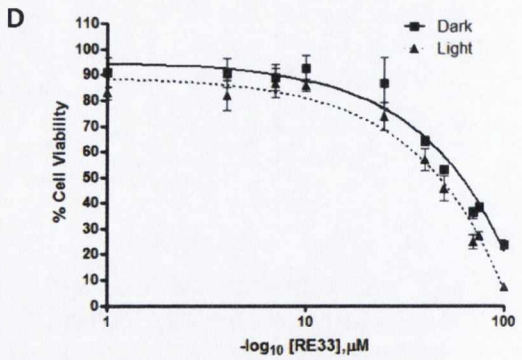

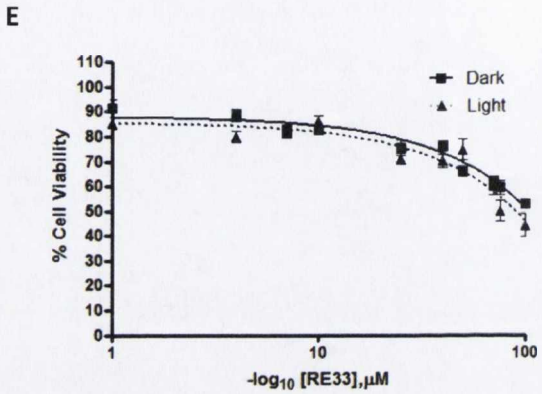

Cell lines		IC_{50} RE33 (µM)
DG-75	Dark	61.4
	Light	47.6
HeLa	Dark	ND
	Light	88.5

ND= not-determinable

Figure 3.8: **The effect of RE33 on malignant cell lines with or without light exposure.**

$4x10^4$ DG-75 **(D)** and $0.5x10^4$ HeLa **(E)** cells/well were seeded in 96-well plates (200 µl total volume/well). Cells were incubated at 37°C overnight before treatment. RE33 concentrations (1, 4, 7, 10, 25, 40, 50, 70, 75 and 100µM) were plated in triplicate and compared to dark-treated controls. Following 24h of treatment, the treated cells were either exposed to light for 1h to give a light dose of $12.66J/cm^2$ or maintained in the dark. Following 23h of incubation an AB assay was performed by adding 20µl of AB dye per well followed by 5-6h incubation at 37°C in the dark until the colour change occurred. The background fluorescence of media without cells plus AB was taken away from each group, and the control untreated cells represented 100% cell viability. The number of viable cells is expressed as a percentage of AB reduction of at least three independent experiments. Fluorescence was measured using a microplate reader (excitation 544nm, emission 590nm). The antiproliferative potency for each compound was determined by linear regression calculating an approximate IC_{50} ([Dose] when response is equal to 50% cell viability). All data points were analysed using GRAPH PAD Prism software. A table of IC_{50} values is included on the graph.

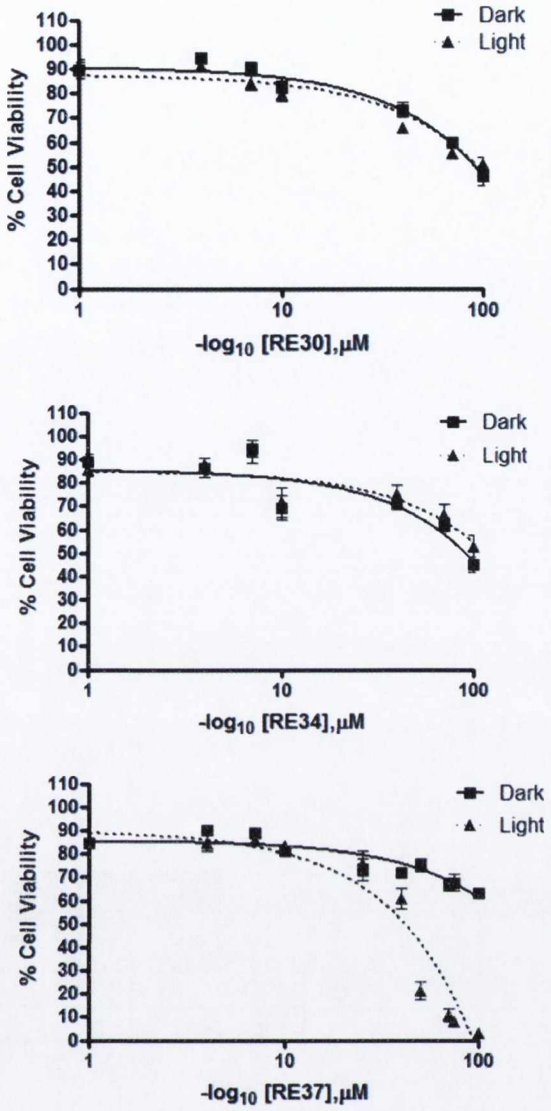

		IC_{50} (μM)		
		RE30	RE34	RE37
CRL	Dark	92.6	92.3	ND
	Light	91.2	73.1	42.3

ND= not-determinable

Figure 3.9: **The effect of Ru(II) compounds on CRL cells with or without light exposure.**

$0.5x10^4$ cells/well were seeded in 96-well plates (200 μl total volume/well). Cells were incubated at 37°C overnight before treatment. Each compound concentration (RE30 and 34 at 1, 4, 7, 10, 40, 70, 100μM and RE37 at 1, 4, 7, 10, 25, 40, 50, 70, 75 and 100μM) was plated in triplicate and compared to dark-treated controls. Following 24h of treatment, the treated cells were either exposed to light for 1h to give a light dose of $12.66J/cm^2$ or maintained in the dark. Following 23h of incubation an AB assay was performed by adding 20μl of AB dye per well followed by 5-6h incubation at 37°C in the dark until the colour change occurred. The background fluorescence of media without cells plus AB was taken away from each group, and the control untreated cells represented 100% cell viability. The number of viable cells is expressed as a percentage of AB reduction of at least three independent experiments. Fluorescence was measured using a microplate reader (excitation 544nm, emission 590nm). The antiproliferative potency for each compound was determined by linear regression calculating an approximate IC_{50} ([Dose] when response is equal to 50% cell viability). All data points were analysed using GRAP PAD Prism software. A table of IC_{50} values is included on the graph.

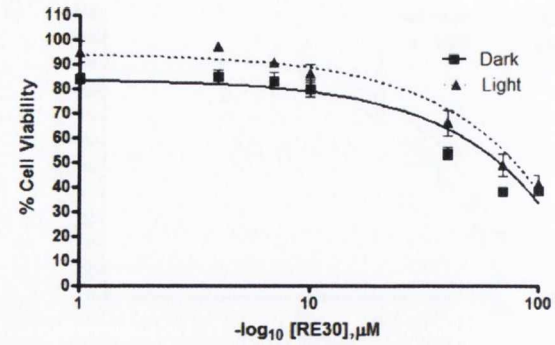

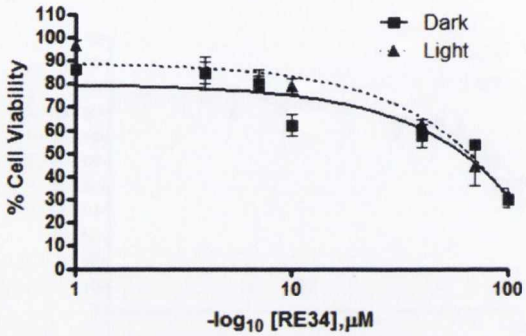

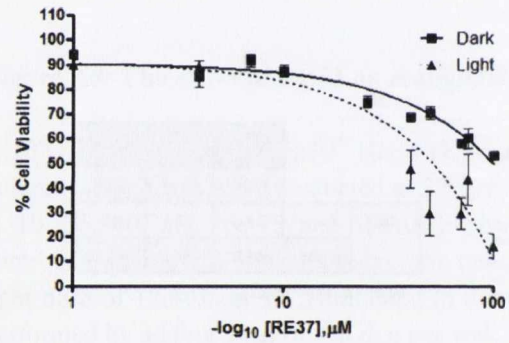

		IC_{50} (μM)		
		RE30	RE34	RE37
One 58	Dark	65.8	58.6	96.5
	Light	71.7	65.4	49.1

Figure 3.10: **The effect of Ru(II) compounds on One 58 cells with or without light exposure.**

$0.5x10^4$ cells/well were seeded in 96-well plates (200 μl total volume/well). Cells were incubated at 37°C overnight before treatment. Each compound concentration (RE30 and 34 at 1, 4, 7, 10, 40, 70 and 100μM and RE37 at 1, 4, 7, 10, 25, 40, 50, 70, 75 and 100μM) was plated in triplicate and compared to dark-treated controls. Following 24h of treatment, the treated cells were either exposed to light for 1h to give a light dose of $12.66J/cm^2$ or maintained in the dark. Following 23h of incubation an AB assay was performed by adding 20μl of AB dye per well followed by 5-6h incubation at 37°C in the dark until the colour change occurred. The background fluorescence of media without cells plus AB was taken away from each group, and the control untreated cells represented 100% cell viability. The number of viable cells is expressed as a percentage of AB reduction of at least three independent experiments. Fluorescence was measured using a microplate reader (excitation 544nm, emission 590nm). The antiproliferative potency for each compound was determined by linear regression calculating an approximate IC_{50}. ([Dose] when response is equal to 50% cell viability). All data points were analysed using GRAP PAD Prism software. A table of IC_{50} values is included on the graph.

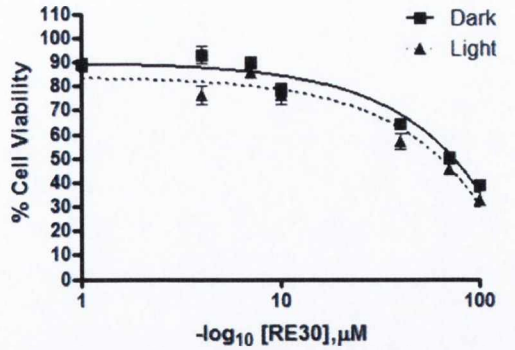

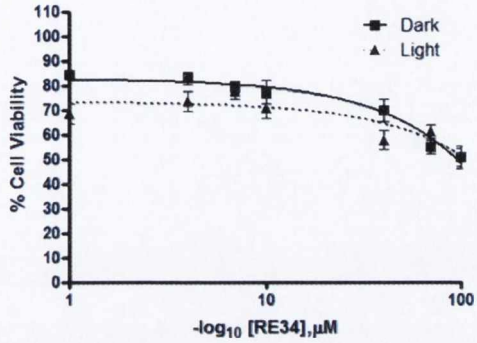

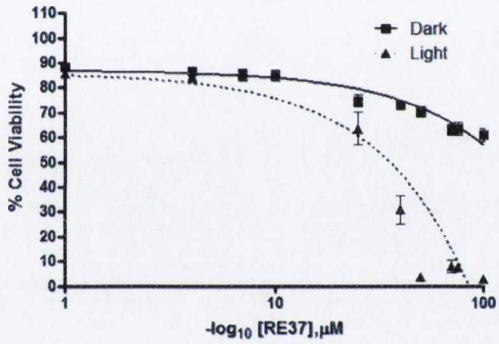

		IC_{50} (μM)		
		RE30	RE34	RE37
HeLa	Dark	69.2	ND	ND
	Light	61.2	ND	31.5

ND= not-determinable

Figure 3.11: **The effect of Ru(II) compounds on HeLa cells with or without light exposure.**

$0.5x10^4$ cells/well were seeded in 96-well plates (200 μl total volume/well). Cells were incubated at 37°C overnight before treatment. Each compound concentration (RE30 and 34 at 1, 4, 7, 10, 40, 70 and 100μM and RE37 at 1, 4, 7, 10, 25, 40, 50, 70, 75 and 100μM) was plated in triplicate and compared dark-treated controls. Following 24h of treatment, the treated cells were either exposed to light for 1h to give a light dose of $12.66J/cm^2$ or maintained in the dark. Following 23h of incubation an AB assay was performed by adding 20μl of AB dye per well followed by 5-6h incubation at 37°C in the dark until the colour change occurred. The background fluorescence of media without cells plus AB was taken away from each group, and the control untreated cells represented 100% cell viability. The number of viable cells is expressed as a percentage of AB reduction of at least three independent experiments. Fluorescence was measured using a microplate reader (excitation 544nm, emission 590nm). The antiproliferative potency for each compound was determined by linear regression calculating an approximate IC_{50} ([Dose] when response is equal to 50% cell viability). All data points were analysed using GRAP PAD Prism software. A table of IC_{50} values is included on the graph.

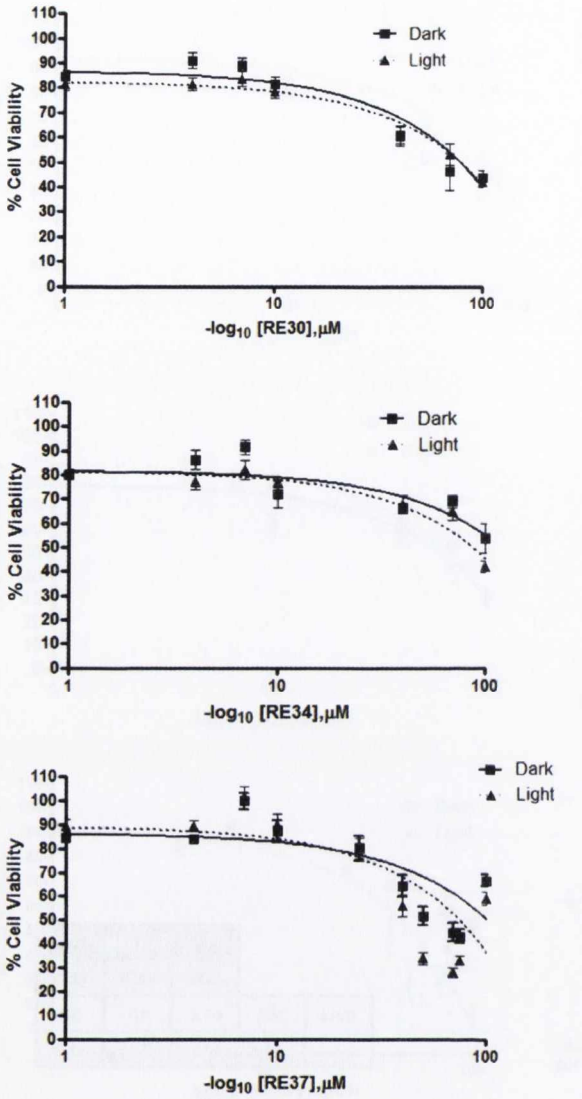

		IC_{50} (μM)		
		RE30	RE34	RE37
DG-75	Dark	74.0	ND	98.8
	Light	74.7	90	72.2

ND= not-determinable

Figure 3.12: **The effect of Ru(II) compounds on DG75 cells with or without light exposure.**

$4x10^4$ cells/well were seeded in 96-well plates (200 μl total volume/well). Cells were incubated at 37°C overnight before treatment. Each compound concentration (RE30 and 34 at 1, 4, 7, 10, 40, 70 and 100μM and RE37 at 1, 4, 7, 10, 25, 40, 50, 70, 75 and 100μM) was plated in triplicate and compared to dark-treated controls. Following 24h of treatment, the treated cells were either exposed to light for 1h to give a light dose of $12.66J/cm^2$ or maintained in the dark. Following 23h of incubation an AB assay was performed by adding 20μl of AB dye per well followed by 5-6h incubation at 37°C in the dark until the colour change occurred. The background fluorescence of media without cells plus AB was taken away from each group, and the control untreated cells represented 100% cell viability. The number of viable cells is expressed as a percentage of AB reduction of at least three independent experiments. Fluorescence was measured using a microplate reader (excitation 544nm, emission 590nm). The antiproliferative potency for each compound was determined by linear regression calculating an approximate IC_{50}. ([Dose] when response is equal to 50% cell viability). All data points were analysed using GRAP PAD Prism software. A table of IC_{50} values is included on the graph.

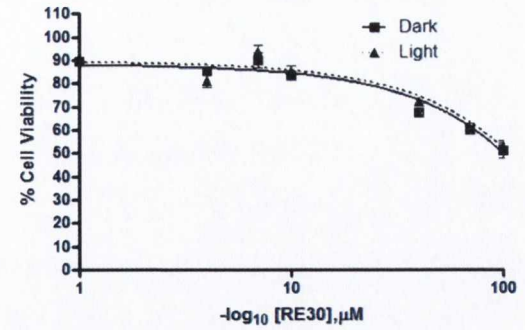

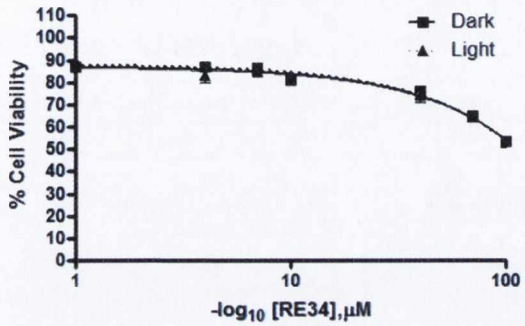

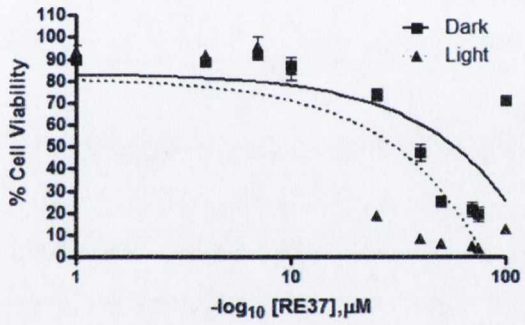

		IC_{50} (μM)		
		RE30	RE34	RE37
Mutu-1	Dark	ND	ND	55.7
	Light	ND	ND	30.6

ND= not-determinable

Figure 3.13: **The effect of Ru(II) compounds on Mutu-1 cells with or without light exposure.**

$0.8x10^5$ cells/well were seeded in 96-well plates (200 μl total volume/well). Cells were incubated at 37°C overnight before treatment. Each compound concentration (RE30 and 34 at 1, 4, 7, 10, 40, 70 and 100μM and RE37 at 1, 4, 7, 10, 25, 40, 50, 70, 75 and 100μM) was plated in triplicate and compared to dark-treated controls. Following 24h of treatment, the treated cells were either exposed to light for 1h to give a light dose of $12.66J/cm^2$ or maintained in the dark. Following 23h of incubation an AB assay was performed by adding 20μl of AB dye per well followed by 5-6h incubation at 37°C in the dark until the colour change occurred. The background fluorescence of media without cells plus AB was taken away from each group, and the control untreated cells represented 100% cell viability. The number of viable cells is expressed as a percentage of AB reduction of at least three independent experiments. Fluorescence was measured using a microplate reader (excitation 544nm, emission 590nm). The antiproliferative potency for each compound was determined by linear regression calculating an approximate IC_{50}. ([Dose] when response is equal to 50% cell viability). All data points were analysed using GRAP PAD Prism software. A table of IC_{50} values is included on the graph.

3.3 RE37 induces a change in the morphological appearance of the cells

In order to observe any cell morphology changes HeLa cells were incubated with 10 to 50μM of RE33, 30, 34 and 37 for 24h in the dark, and then for one half of the replicates the cells were illuminated for 1h, and them all the cells incubated for further 23h (figures 3.14 and 3.16). After cytospinning (described in section 2.6 of the Materials and Methods) the cells incubated with RE33, 30 and 34 and illuminated showed no difference in cell morphology when compared to cells which had not been illuminated, or cells without compound. On the other hand, the cells incubated with RE37 and illuminated appeared to show extensive membrane blebbing when compared to cells which had not been illuminated, or cells without compound. However, as the cytospin technique can alter the cytoskeleton structure of cells this was taken as a preliminary result which needed confirmation with further experiments.

3.4 Uptake of RE33 and the Ru(II) compounds into cells

Uptake experiments were performed to determine if the compounds were taken up by the cells in a time-dependent manner and to investigate any cell morphology effects of the compounds. HeLa cells were incubated for 4, 8 and 24h with RE33 at either 10 or 100μM or with 10μM of RE30 or 34. HeLa and CRL cells were incubated with 100μM RE37 prior to confocal microscopy. The ideal concentration used, to observe luminescence in confocal microscopy was determined by multiple experiments using different concentrations of the compounds.

In accordance with the excitation and emission spectra of the compounds, a 488nm laser was used in order to visualise the compounds while DAPI was used as a nuclear stain.

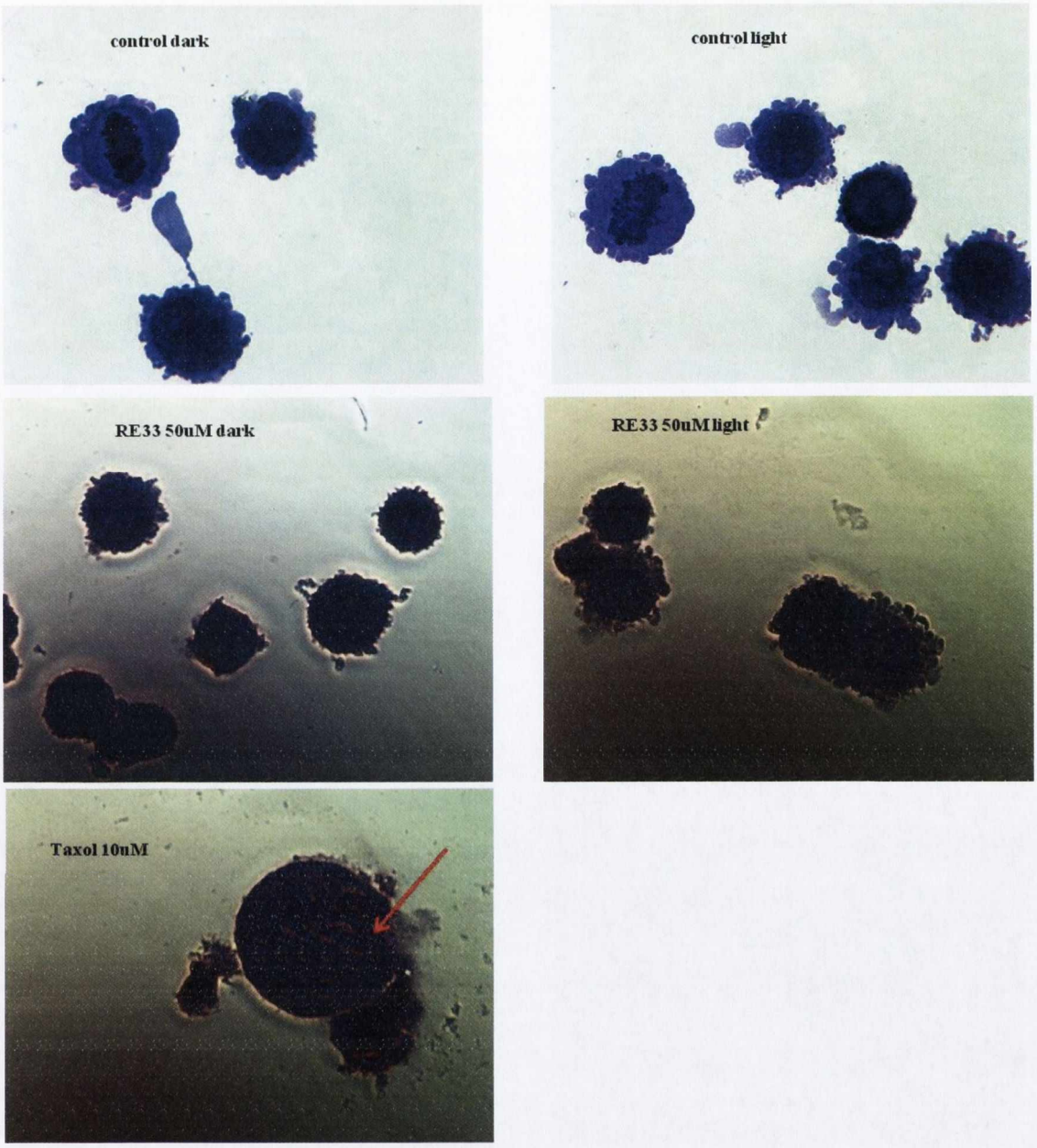

Figure 3.14: **Morphological appearance of HeLa cells after being treatment with RE33.**

Cells were seeded at a density of $0.25x10^6$ cells/ml, treated with RE33 for 24h and exposed to light for 1h to give light doses of $12.66J/cm^2$ or left in the dark. As a positive control, Taxol at 10μM was used. After incubation at 37°C for another 23h an aliquot of cells (150μl) were cytocentrifuged onto poly-l-lysine coated slides at 500xg for 2min using a Cytospin 3 (Shandon). The slides were removed and left to air-dry at room temperature for 2min. Staining was carried out using the RapiDiff kit containing solution A (100% methanol), solution B (Eosin Y) and solution C (methylene blue). The cells were fixed by dipping them ten times in solution A. The nucleus of the cells was stained pink by dipping the slide ten times in solution B and the cytoplasm was stained blue by dipping eight times in solution C. Excess dye was washed off with dH_2O. After allowing the slides to air dry cells were examined under a light microscope using 40x magnification. Results are representative of three independent experiments. The red arrow indicates DNA fragmentation.

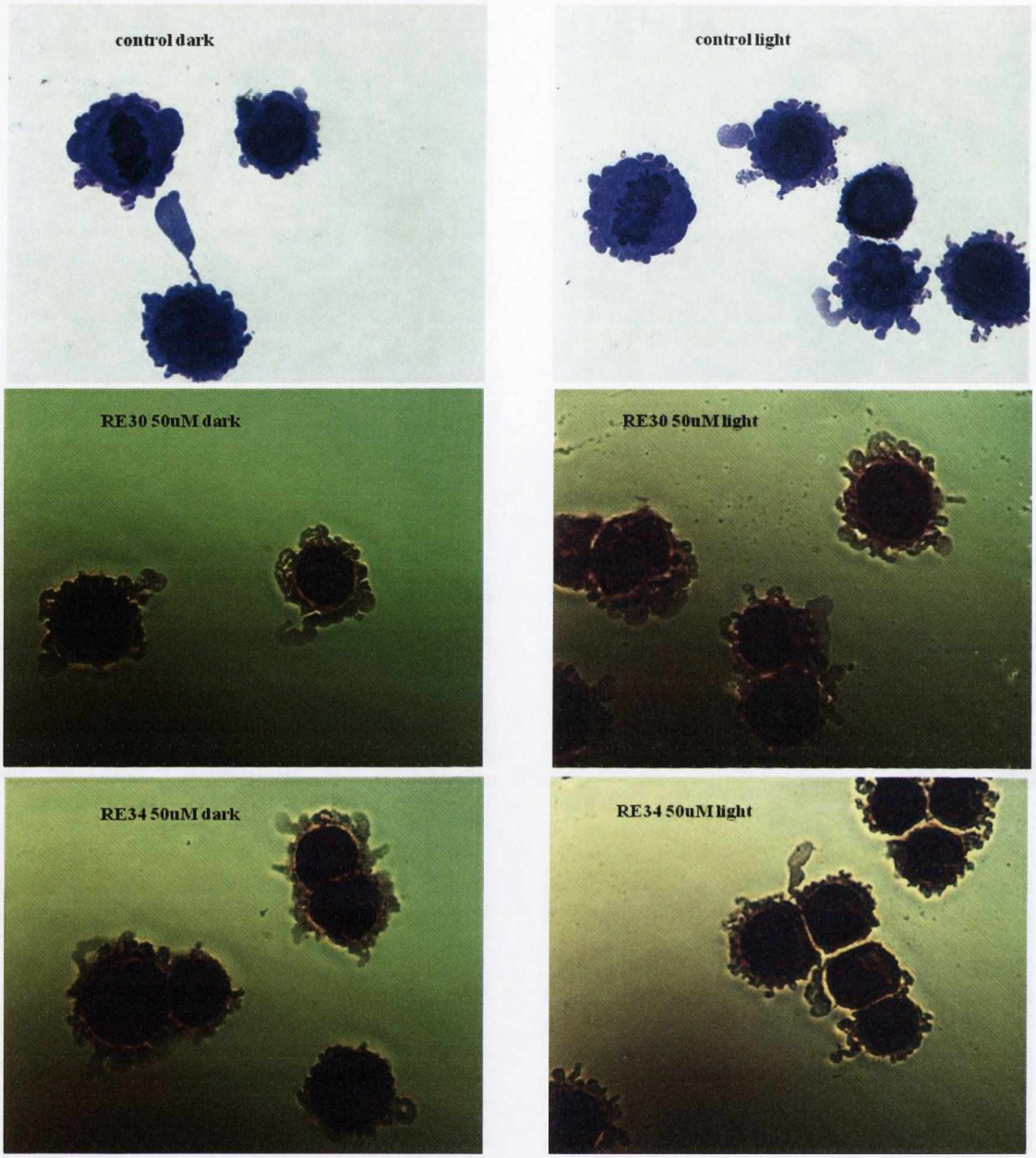

Figure 3.15: **Morphological appearance of HeLa cells after treatment with RE30 and 34.**

Cells were seeded at a density of $0.25x10^6$ cells/ml, treated with RE30, 34 for 24h and exposed to light for 1h to give a light dose of $12.66J/cm^2$ or maintained in the dark. As a positive control, Taxol at 10μM was used. After incubation at 37°C for another 23h an aliquot of cells (150μl) were cytocentrifuged onto poly-l-lysine coated slides at 500xg for 2min using a Cytospin 3 (Shandon). The slides were removed and left to air-dry at room temperature for 2min. Staining was carried out using the RapiDiff kit containing solution A (100% methanol), solution B (Eosin Y) and solution C (methylene blue). The cells were fixed by dipping them ten times in solution A. The nucleus of the cells was stained pink by dipping the slide ten times in solution B and the cytoplasm was stained blue by dipping eight times in solution C. Excess dye was washed off with dH_2O. After allowing the slides to air dry cells were examined under a light microscope using 40x magnification. Results are representative of three independent experiments.

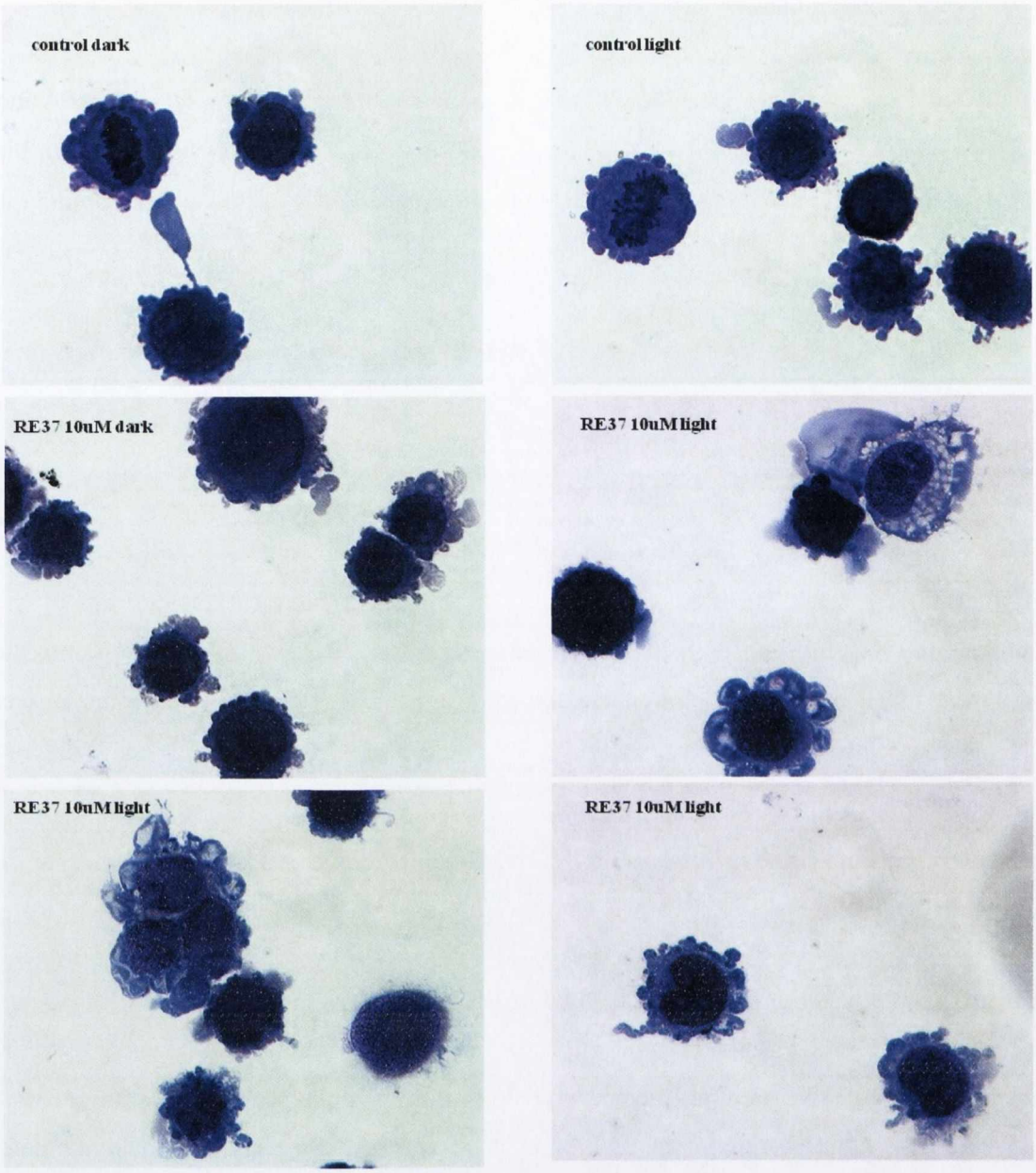

Figure 3.16: **Morphological appearance of HeLa cells after treatment with RE37.**

Cells were seeded at a density of $0.25x10^6$ cells/ml, treated with RE37 for 24h and exposed to light for 1h to give a light dose of $12.66J/cm^2$ or maintained in the dark. After incubation at 37°C for another 23h an aliquot of cells (150µl) were cytocentrifuged onto poly-l-lysine coated slides at 500xg for 2min using a Cytospin 3 (Shandon). The slides were removed and left to air-dry at room temperature for 2min. Staining was carried out using the RapiDiff kit containing solution A (100% methanol), solution B (Eosin Y) and solution C (methylene blue). The cells were fixed by dipping them ten times in solution A. The nucleus of the cells was stained pink by dipping the slide ten times in solution B and the cytoplasm was stained blue by dipping eight times in solution C. Excess dye was washed off with dH_2O. After allowing the slides to air dry cells were examined under a light microscope using 40x magnification. Results are representative of three independent experiments.

3.4.1 RE33 is taken up in HeLa cells

RE33 showed uptake into the cells with the compound visible in the cytoplasm after 4 and 8h. At longer time points, 24h, a peri-nuclear localisation of RE33 was observed with the nucleus appearing distorted as a 'bean-shaped' nucleus. In cells at longer time points the compound was more visible which is dependent on being in an appropriate molecular environment (figures 3.17 to 3.20).

3.4.2 RE30 and 34 showed uptake into HeLa cells and "light switch" increases in luminescence at long time point

RE30 and 34 showed uptake into HeLa cells with the compounds visible throughout the cytoplasm after 4 and 8h. At long time points, 24h, a peri-nuclear localisation of the compounds was observed with the nucleus appearing distorted. At long time points the compounds appeared more visible in the cells presumably due to the "light switch" effect that these compounds show, on binding DNA or indeed being in a non-polar environment [74] (figures 3.21 to 3.24).

3.4.3 RE37 showed uptake into cells

RE37 showed uptake into both HeLa and CRL cells (figure 3.25 to 3.28). CRL cells were tested with RE37 as second model. For HeLa cells the compound appeared in the cytoplasm at 4h, and then a peri-nuclear accumulation was observed at longer time points, 24h. In CRL cells the compound seemed in all areas of the cells even at short time points. The percentage of cells with RE37 visible in the cytoplasm, at the peri-nuclear region, in the nuclear region or the peri-nuclear localisation at the concave nucleus was expressed over the total amount of cells (approximately 100) per field of view (figure 3.29). While the bean-shaped nucleus is not likely to be due to the effects of the compounds, it is interesting how the compound clusters in that precise spot after 24h in HeLa cells and after 8 and 24h in CRL.

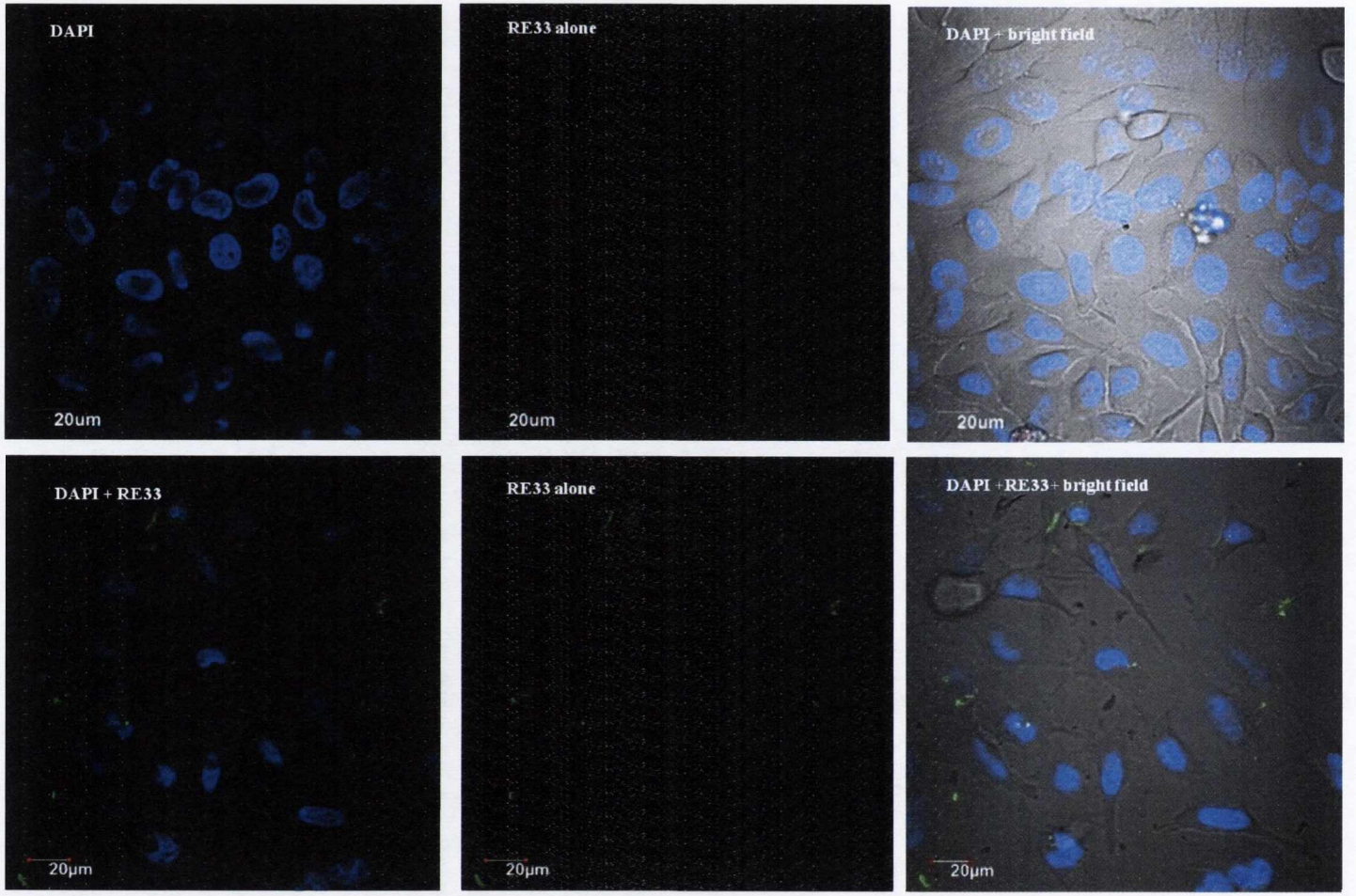
DAPI
20um
RE33 alone
20um
DAPI + bright field
20um
Untreated
DAPI + RE33
20µm
RE33 alone
20µm
DAPI +RE33+ bright field
20µm
4h

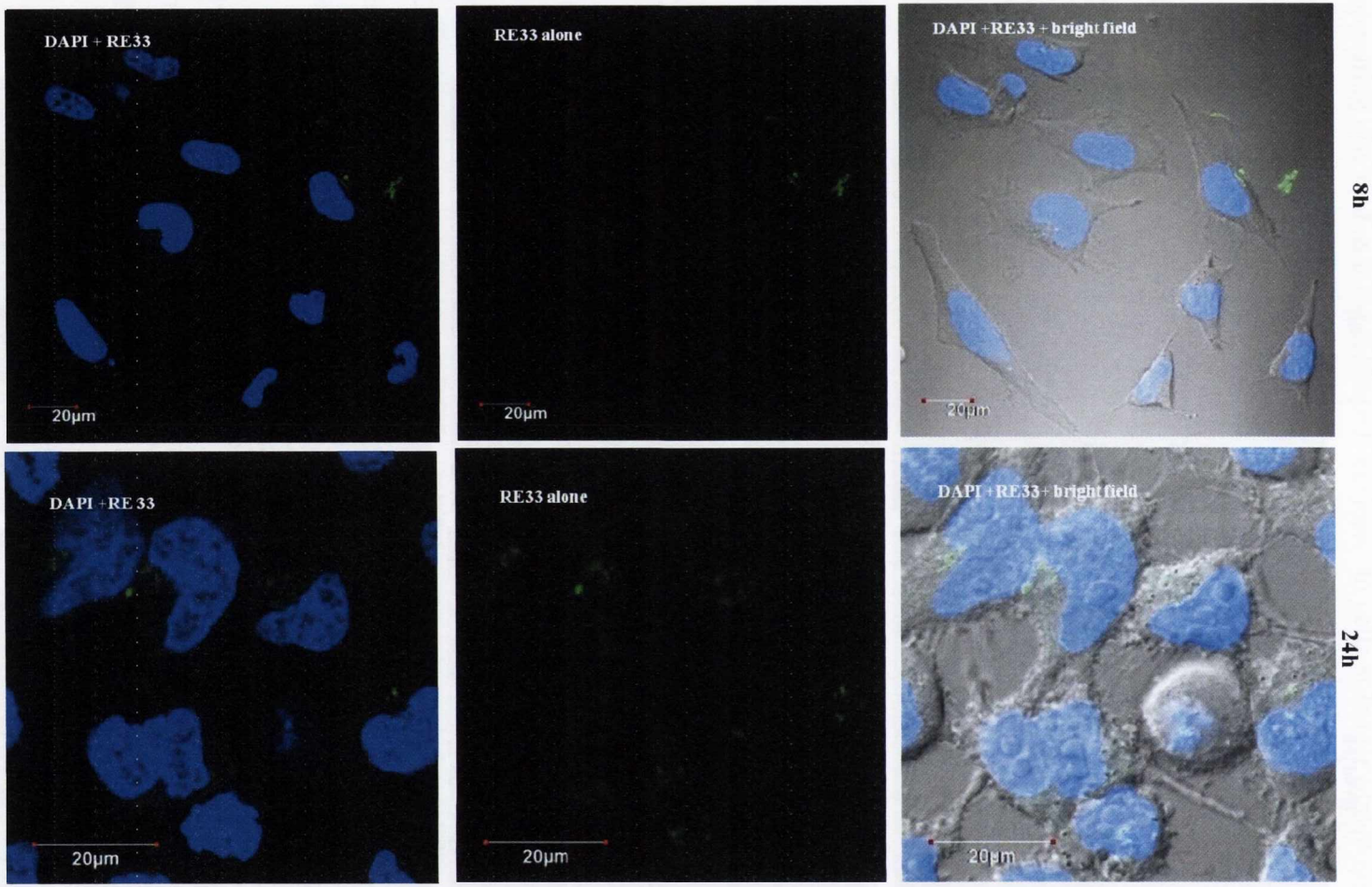
DAPI + RE33
20µm
RE33 alone
20µm
DAPI +RE33 + bright field
20µm
8h
DAPI +RE 33
20µm
RE33 alone
20µm
DAPI +RE33 + bright field
20µm
24h

Figure 3.17: **Time dependent localisation of RE33 in HeLa cells.**

$1x10^5$ cells/well were seeded in dish plates (Ø 22mm; 2ml total volume/well). Cells were incubated at 37°C overnight before treatment. The cells were then treated with 10μM of RE33 and incubated for 4, 8 and 24h. Cells were washed twice in PBS followed by the addition of fresh media and DAPI, followed by viewing using Olympus FV1000 confocal microscopy with a 60x oil immersion lens. After 4-8h the complex is non-specifically localised inside the cells. After 24h a peri-nuclerar clustering of the compound was observed. Image analysis was performed using FluoView Version 7.1 Software. RE33 was excited by a 488nm argon laser, emission 515nm and DAPI was excited by a 405 laser, emission 461nm. Results are representative of three independent experiments.

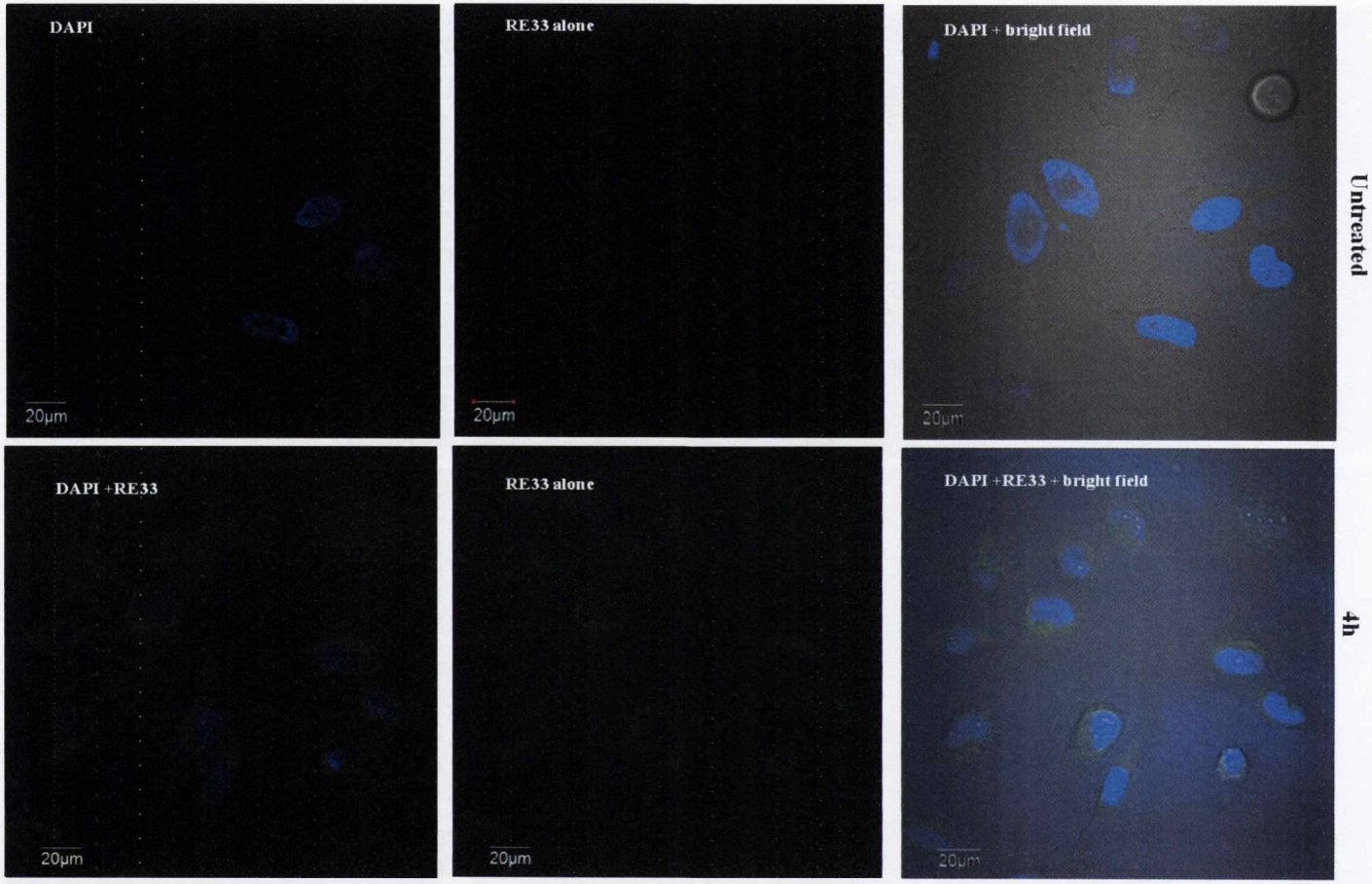
DAPI
RE33 alone
DAPI + bright field
Untreated
20μm
20μm
20μm
DAPI +RE33
RE33 alone
DAPI +RE33 + bright field
4h
20μm
20μm
20μm

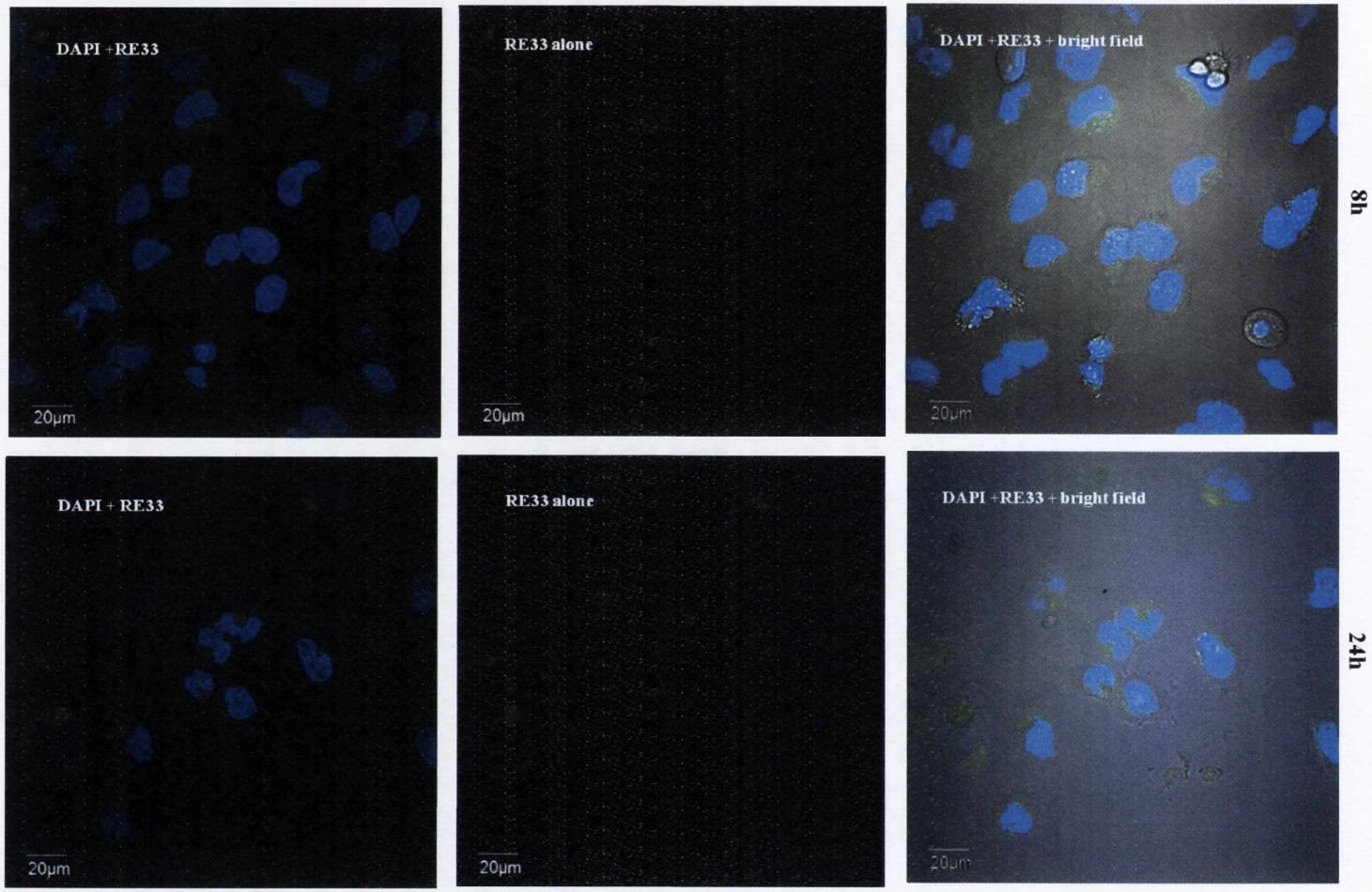
DAPI +RE33
20μm
RE33 alone
20μm
DAPI +RE33 + bright field
20μm
8h
DAPI + RE33
20μm
RE33 alone
20μm
DAPI +RE33 + bright field
20μm
24h

Figure 3.18: **Time dependent localisation of RE33 in HeLa cells.**

$1x10^5$ cells/well were seeded in dish plates (Ø 22mm; 2ml total volume/well). Cells were incubated at 37°C overnight before treatment. The cells were then treated with 100μM of RE33 and incubated for 4, 8 and 24h. Cells were washed twice in PBS followed by the addition of fresh media and DAPI, followed by viewing using Olympus FV1000 confocal microscopy with a 60x oil immersion lens. After 4-8h the complex is non-specifically localised inside the cells. After 24h a peri-nuclerar clustering of the compound was observed. Image analysis was performed using FluoView Version 7.1 Software. RE33 was excited by a 488nm argon laser, emission 525nm and DAPI was excited by a 405 diode laser, emission 461nm. Results are representative of three independent experiments.

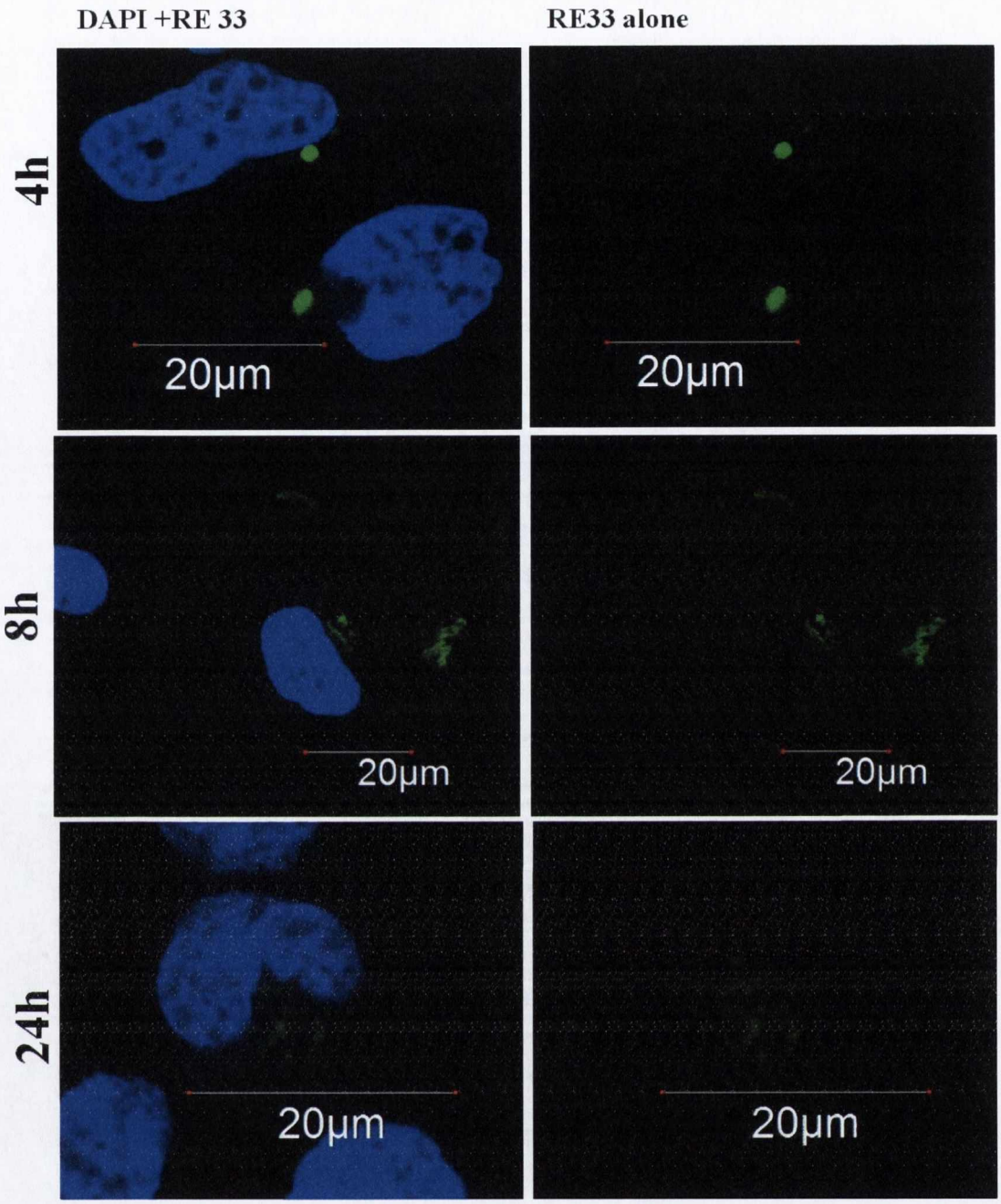

Figure 3.19: **Time dependent localisation of RE33 in HeLa cells.**

$1x10^5$ cells/well were seeded in dish plates (Ø 22mm; 2ml total volume/well). Cells were incubated at 37°C overnight before treatment. The cells were then treated with 10µM of RE33 and incubated for 4, 8 and 24h. Cells were washed twice in PBS followed by the addition of fresh media and DAPI, followed by viewing using Olympus FV1000 confocal microscopy with a 60x oil immersion lens. After 4-8h the complex is non-specifically localised inside the cells. After 24h a peri-nuclerar clustering of the compound was observed. Image analysis was performed using FluoView Version 7.1 Software. RE33 was excited by a 488nm argon laser, emission 515nm and DAPI was excited by a 405 laser, emission 461nm. Results are representative of three independent experiments.

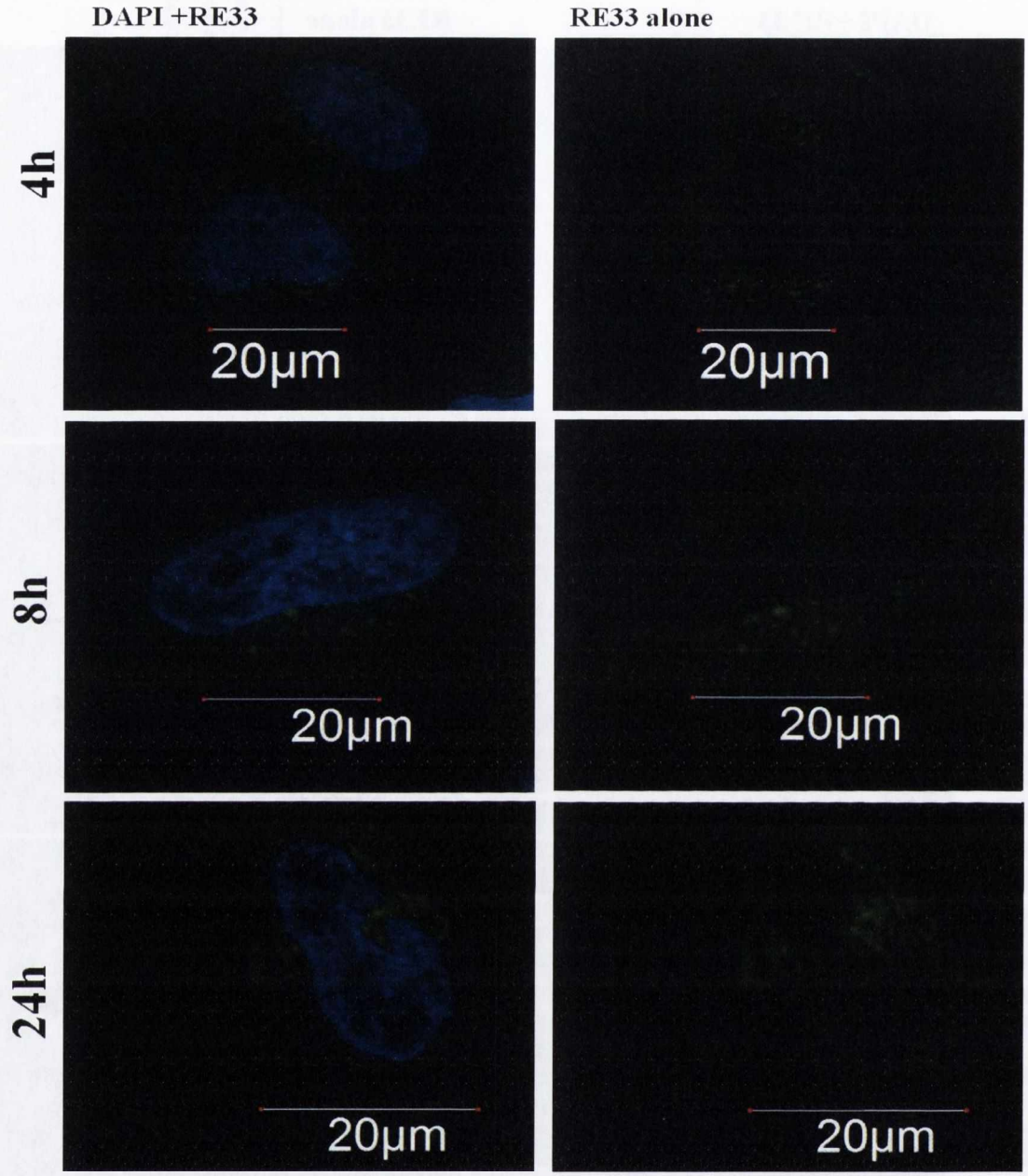

Figure 3.20: **Time dependent localisation of RE33 in HeLa cells.**

$1x10^5$ cells/well were seeded in dish plates (Ø 22mm; 2ml total volume/well). Cells were incubated at 37°C overnight before treatment. The cells were then treated with 100µM of RE33 and incubated for 4, 8 and 24h. Cells were washed twice in PBS followed by the addition of fresh media and DAPI, followed by viewing using Olympus FV1000 confocal microscopy with a 60x oil immersion lens. After 4-8h the complex is non-specifically localised inside the cells. After 24h a peri-nuclerar clustering of the compound was observed. Image analysis was performed using FluoView Version 7.1 Software. RE33 was excited by a 488nm argon laser, emission 515nm and DAPI was excited by a 405 laser, emission 461nm. Results are representative of three independent experiments.

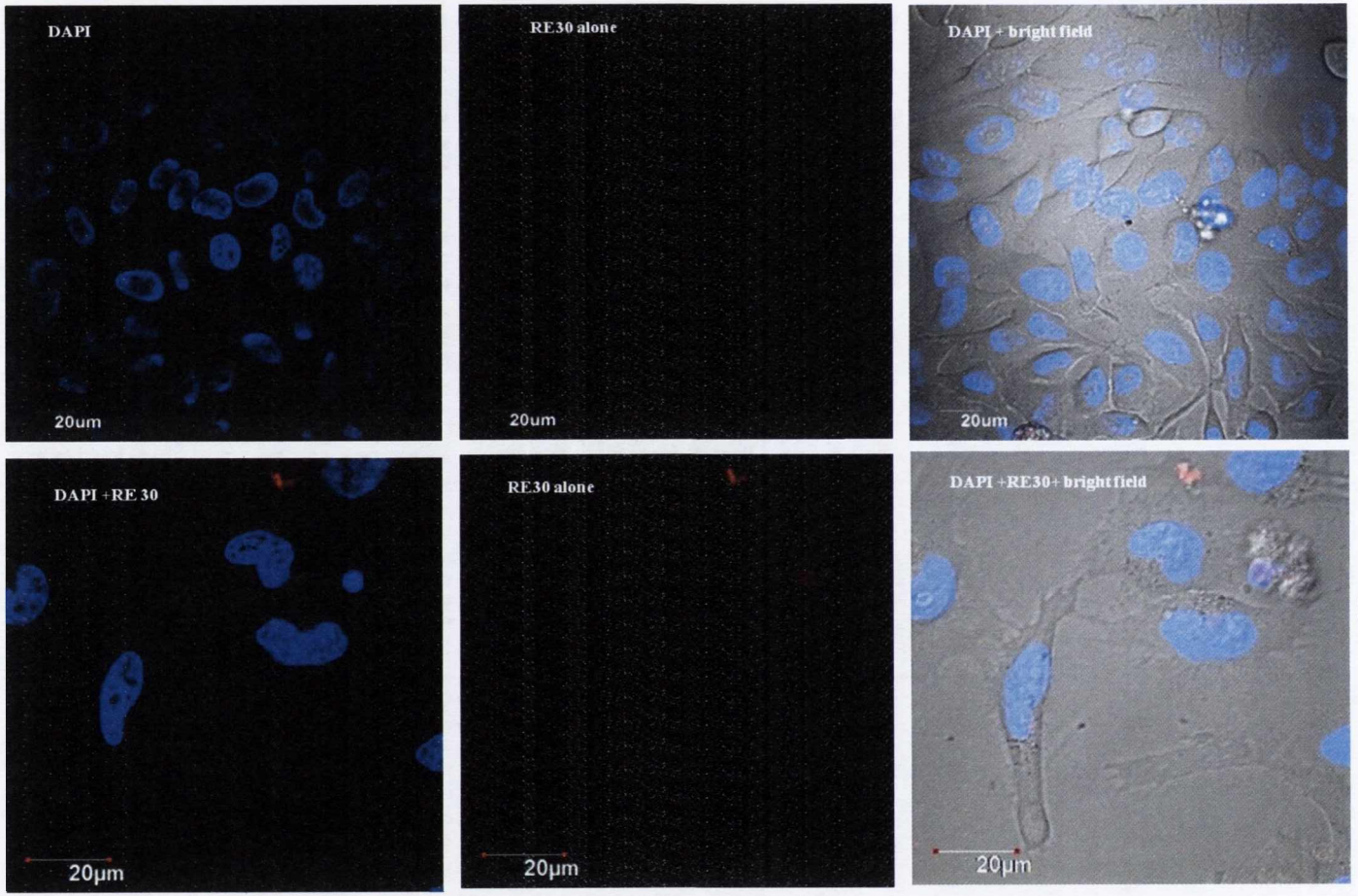
DAPI
20um
RE30 alone
20um
DAPI + bright field
20um
Untreated
DAPI +RE 30
20µm
RE30 alone
20µm
DAPI +RE30+ bright field
20µm
4h

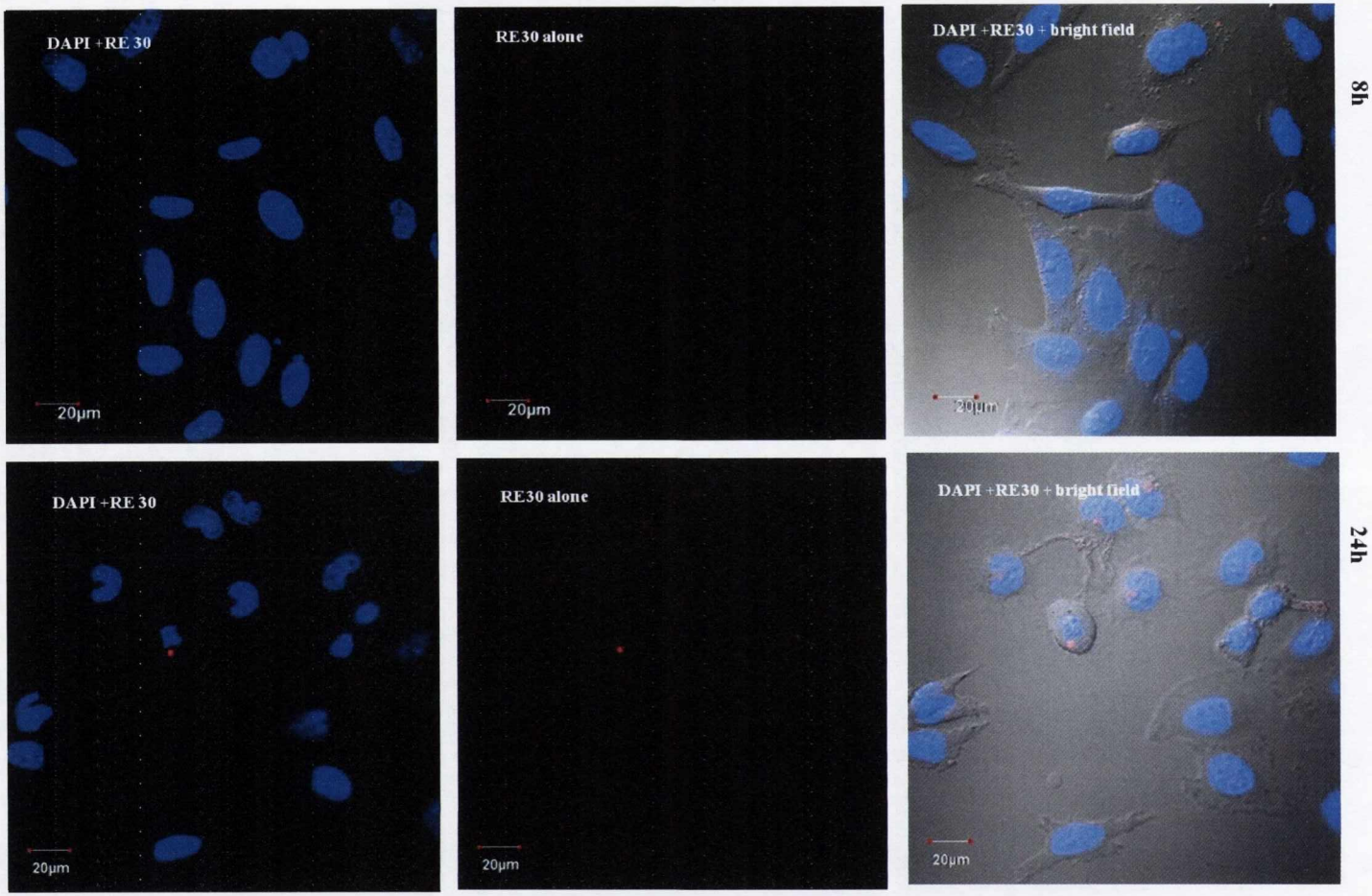
DAPI +RE 30
20µm
RE30 alone
20µm
DAPI +RE30 + bright field
20µm
8h
DAPI +RE 30
20µm
RE30 alone
20µm
DAPI +RE30 + bright field
20µm
24h

Figure 3.21: **Time dependent localisation of RE30 in HeLa cells.**

$1x10^5$ cells/well were seeded in dish plates (Ø 22mm; 2ml total volume/well). Cells were incubated at 37°C overnight before treatment. The cells were then treated with 10μM of RE30 and incubated for 4, 8 and 24h. Cells were washed twice in PBS followed by the addition of fresh media and DAPI, followed by viewing using Olympus FV1000 confocal microscopy with a 60x oil immersion lens. After 4-8h the complex is non-specifically localised inside the cells. After 24h a peri-nuclerar clustering of the compound was observed. Image analysis was performed using FluoView Version 7.1 Software. RE30 was excited by a 488nm argon laser, emission 620nm and DAPI was excited by a 405 laser, emission 461nm. Results are representative of three independent experiments.

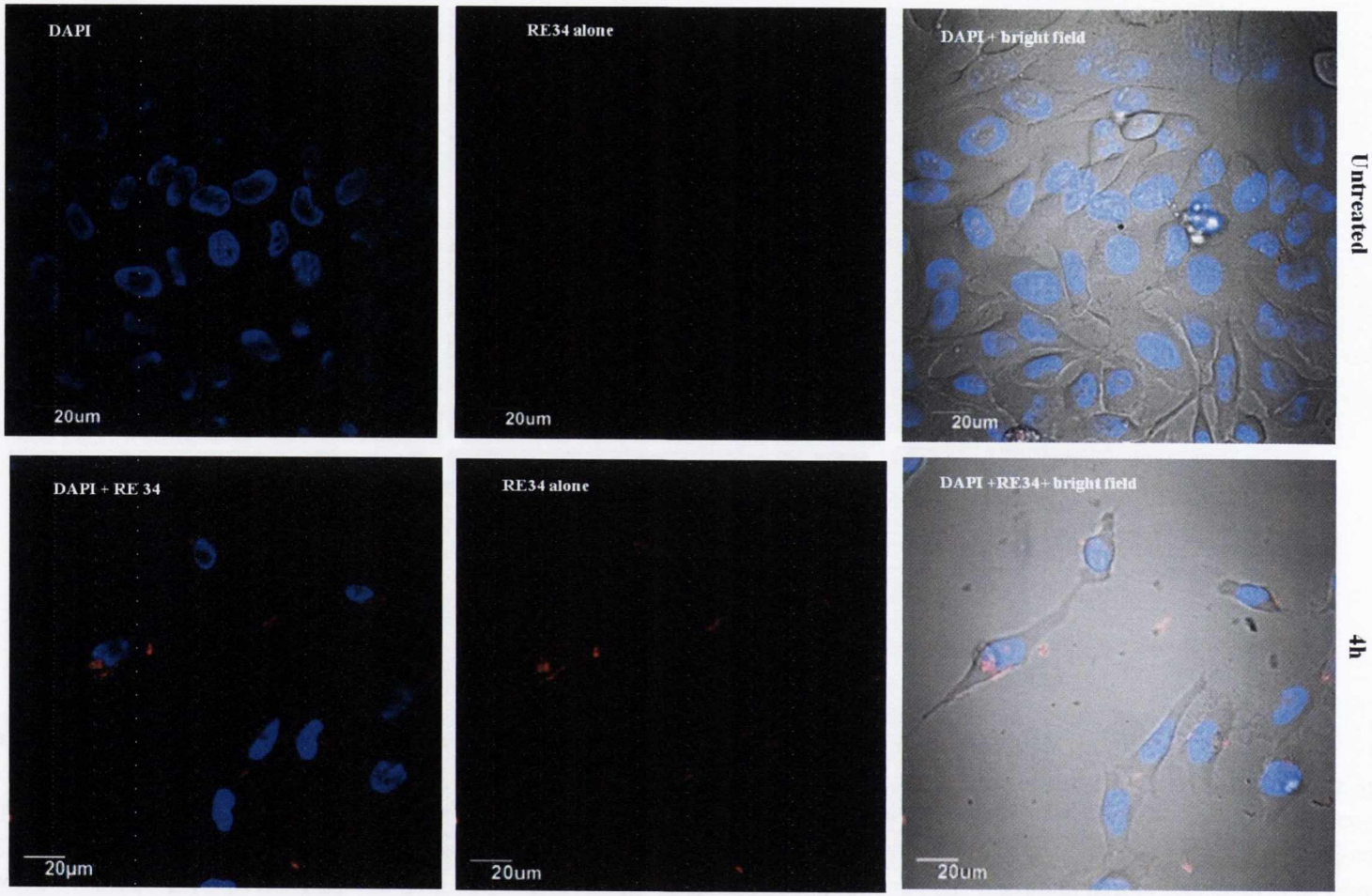
DAPI
20um
RE34 alone
20um
DAPI + bright field
20um
Untreated
DAPI + RE 34
20µm
RE34 alone
20um
DAPI +RE34+ bright field
20um
4h

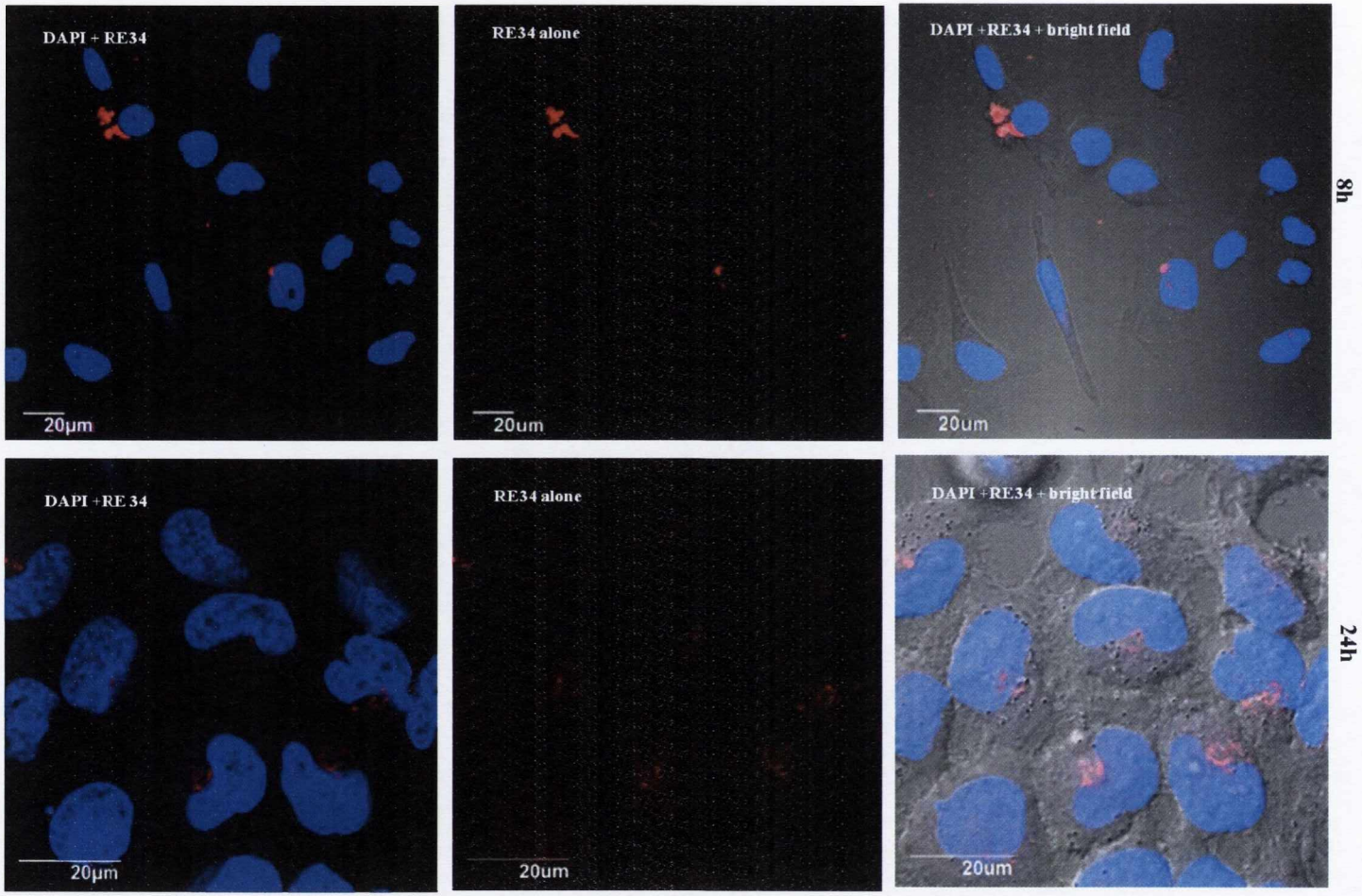
DAPI + RE34
20μm
RE34 alone
20um
DAPI +RE34 + bright field
20um
8h
DAPI +RE 34
20μm
RE34 alone
20um
DAPI +RE34 + bright field
20um
24h

Figure 3.22: **Time dependent localisation of RE34 in HeLa cells.**

$1x10^5$ cells/well were seeded in dish plates (Ø 22mm; 2ml total volume/well). Cells were incubated at 37°C overnight before treatment. The cells were then treated with 10μM of RE34 and incubated for 4, 8 and 24h. Cells were washed twice in PBS followed by the addition of fresh media and DAPI, followed by viewing using Olympus FV1000 confocal microscopy with a 60x oil immersion lens. After 4 and 8h the complex is non-specifically localised inside the cells. After 24h a peri-nuclerar clustering of the compound was observed. Image analysis was performed using FluoView Version 7.1 Software. RE34 was excited by a 488nm argon laser, emission 620nm and DAPI was excited by a 405 laser, emission 461nm. Results are representative of three independent experiments.

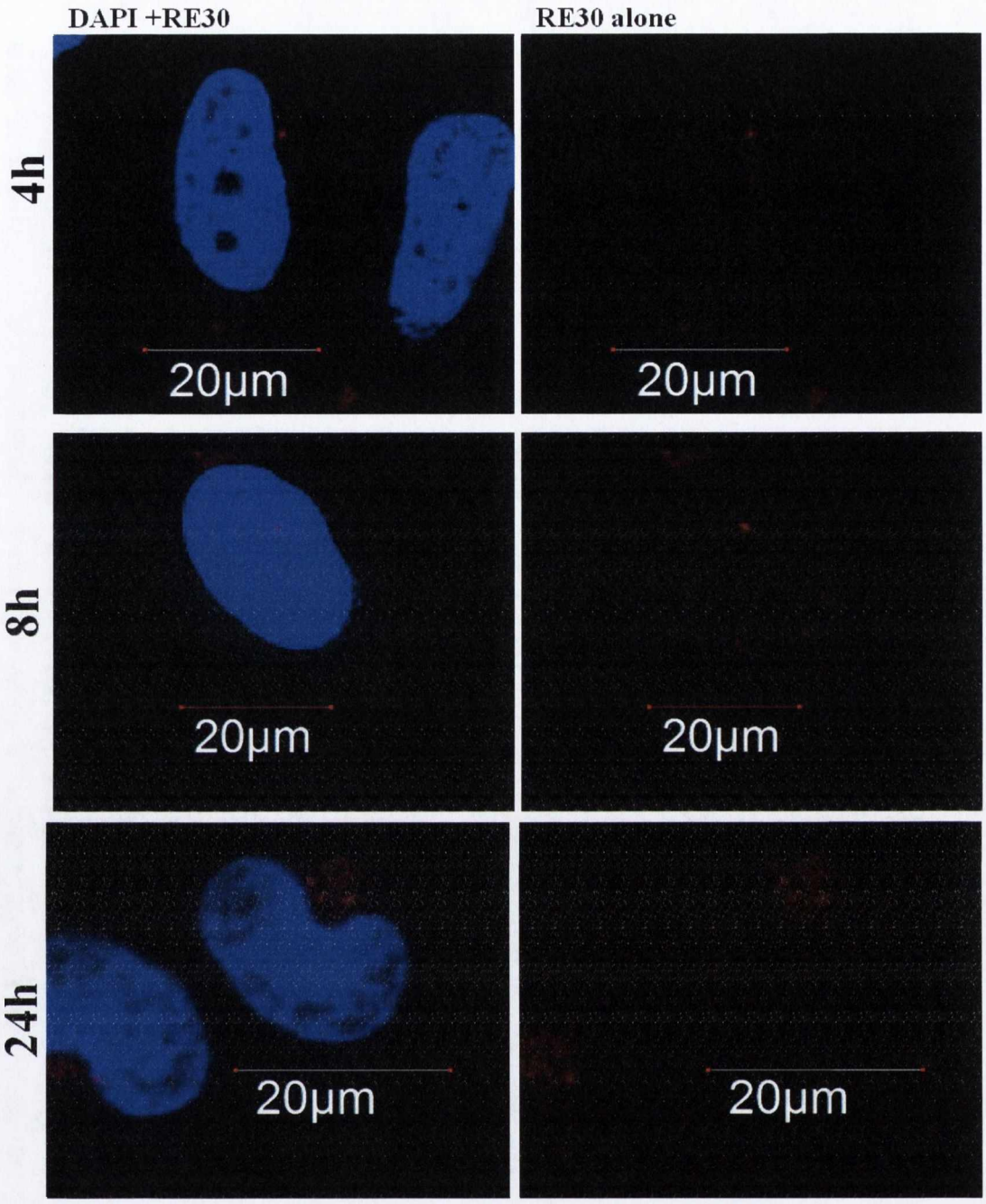

Figure 3.23: **Time dependent localisation of RE30 in HeLa cells.**

$1x10^5$ cells/well were seeded in dish plates (Ø 22mm; 2ml total volume/well). Cells were incubated at 37°C overnight before treatment. The cells were then treated with 10μM of RE30 and incubated for 4, 8 and 24h. Cells were washed twice in PBS followed by the addition of fresh media and DAPI, followed by viewing using Olympus FV1000 confocal microscopy with a 60x oil immersion lens. After 4-8h the complex is non-specifically localised inside the cells. After 24h a peri-nuclerar clustering of the compound was observed. Image analysis was performed using FluoView Version 7.1 Software. RE30 was excited by a 488nm argon laser, emission 620nm and DAPI was excited by a 405 laser, emission 461nm. Results are representative of three independent experiments.

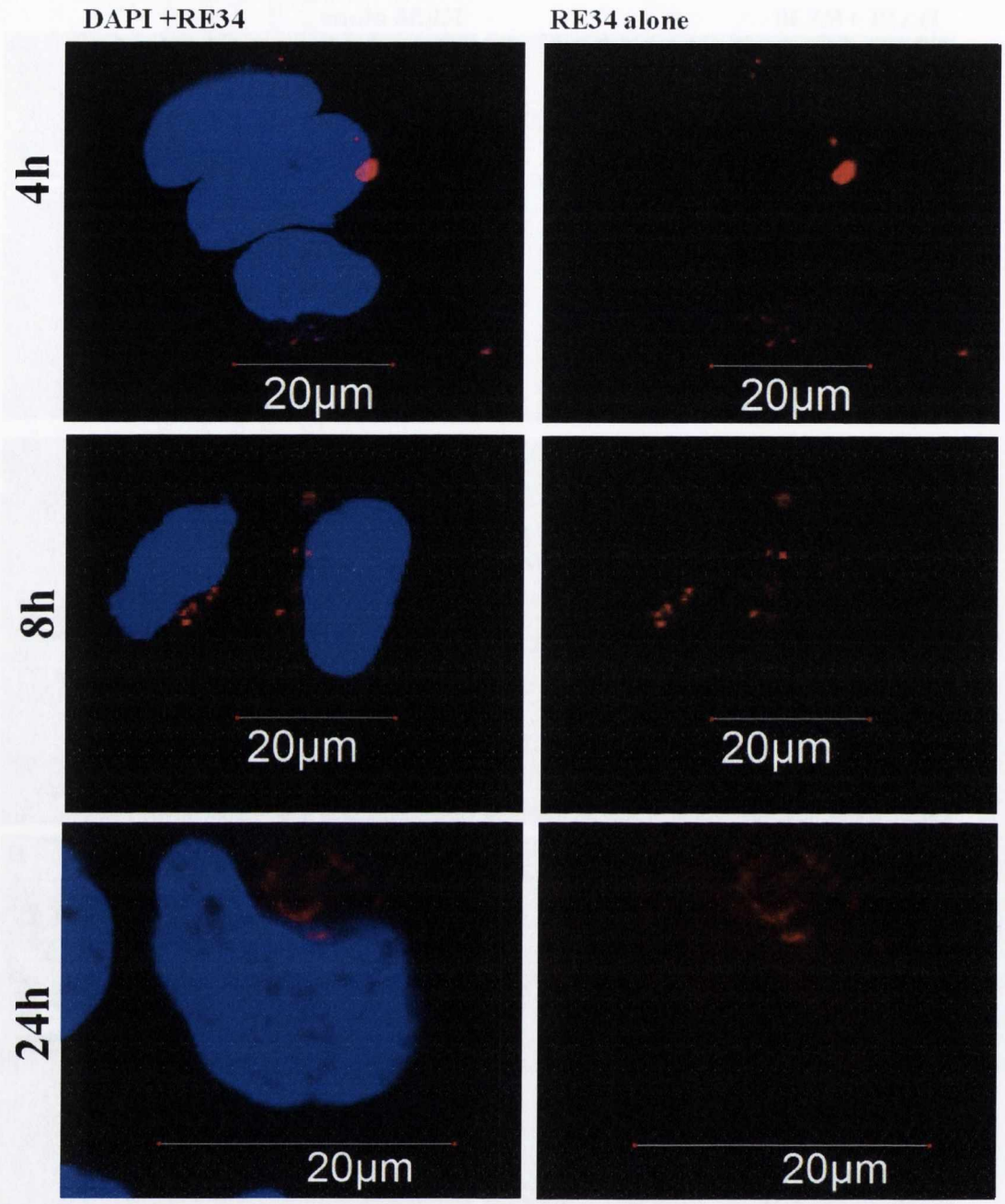

Figure 3.24: **Time dependent localisation of RE34 in HeLa cells.**

$1x10^5$ cells/well were seeded in dish plates (Ø 22mm; 2ml total volume/well). Cells were incubated at 37°C overnight before treatment. The cells were then treated with 10µM of RE34 and incubated for 4, 8 and 24h. Cells were washed twice in PBS followed by the addition of fresh media and DAPI, followed by viewing using Olympus FV1000 confocal microscopy with a 60x oil immersion lens. After 4 and 8h the complex is non-specifically localised inside the cells. After 24h a peri-nuclerar clustering of the compound was observed. Image analysis was performed using FluoView Version 7.1 Software. RE34 was excited by a 488nm argon laser, emission 620nm and DAPI was excited by a 405 laser, emission 461nm. Results are representative of three independent experiments.

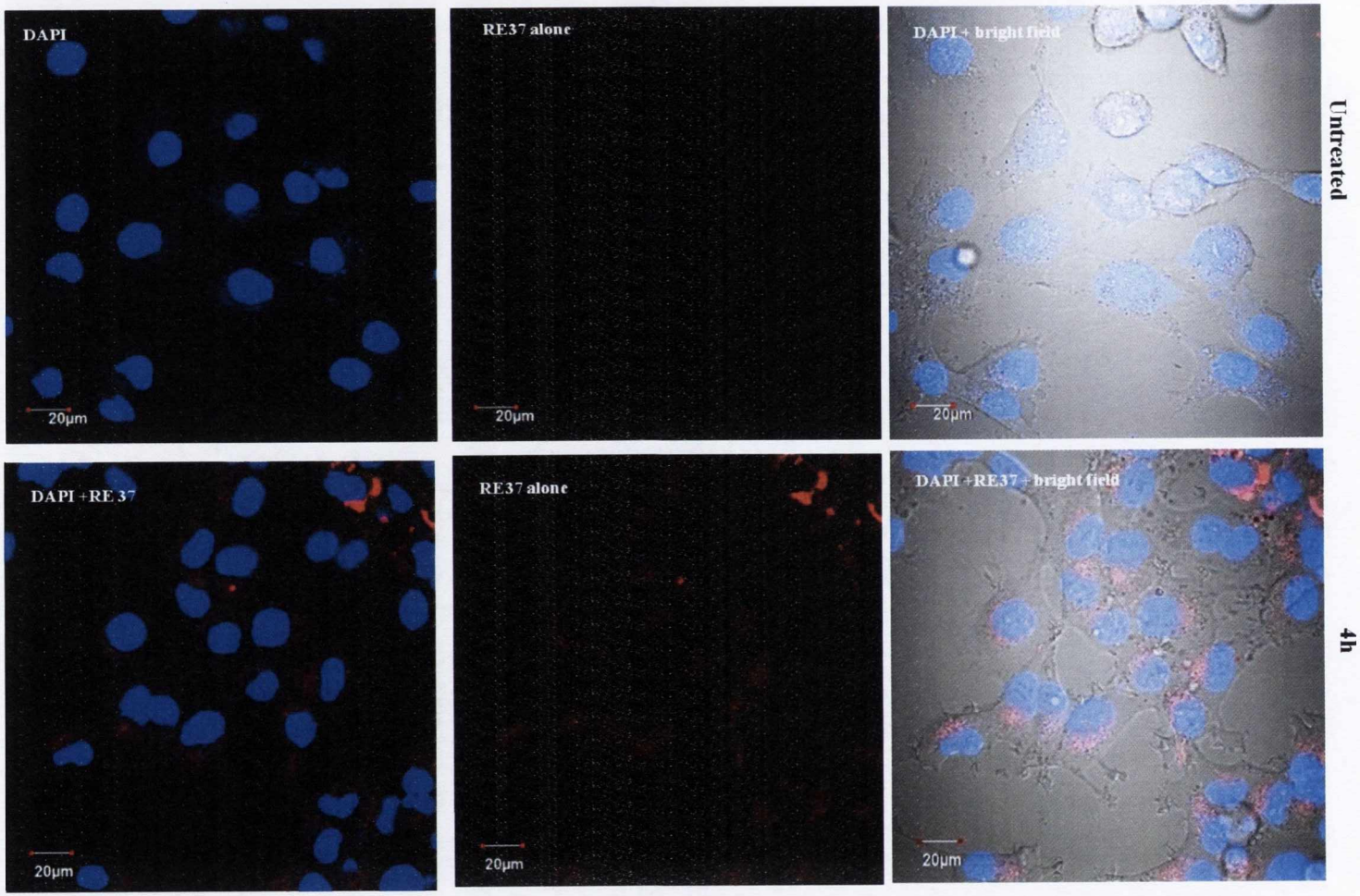
DAPI
RE37 alone
DAPI + bright field
Untreated
DAPI +RE 37
RE37 alone
DAPI +RE37 + bright field
4h
20µm

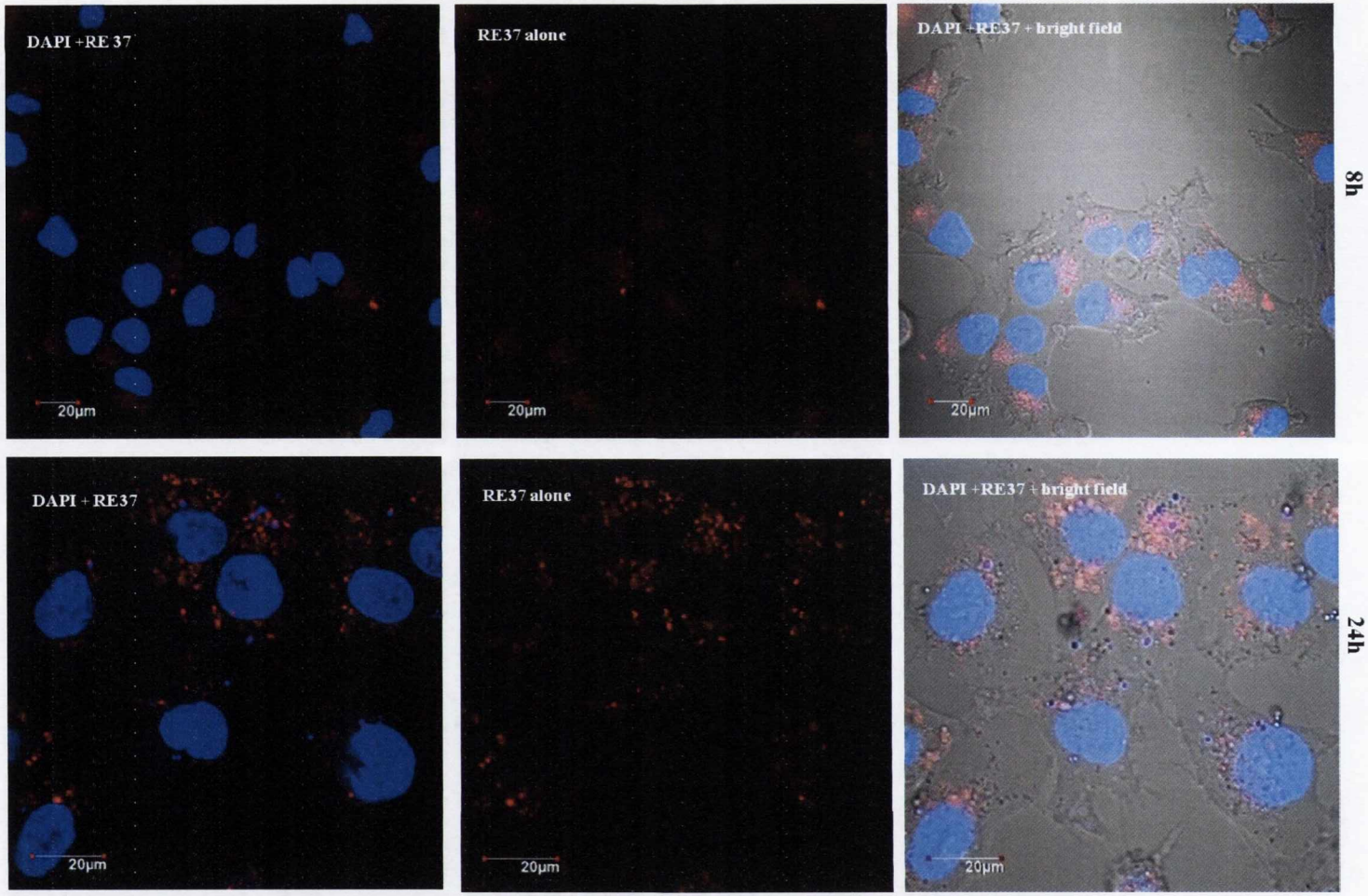
DAPI +RE 37
20µm
RE37 alone
20µm
DAPI +RE37 + bright field
20µm
8h
DAPI + RE37
20µm
RE37 alone
20µm
DAPI +RE37 + bright field
20µm
24h

Figure 3.25: **Time dependent localisation of RE37 in CRL cells.**

$1x10^5$ cells/well were seeded in dish plates (Ø 22mm; 2ml total volume/well). Cells were incubated at 37°C overnight before treatment. The cells were then treated with 100μM of RE37 and incubated for 4, 8 and 24h. Cells were washed twice in PBS followed by the addition of fresh media and DAPI, followed by viewing using Olympus FV1000 confocal microscopy with a 60x oil immersion lens. After 4h the complex is localised in the cytoplasm. After 8 and 24h a peri-nuclerar clustering of the compound was observed. Image analysis was performed using FluoView Version 7.1 Software. RE37 was excited by a 488nm argon laser, emission 620nm and DAPI was excited by a 405 laser, emission 461nm. Results are representative of three independent experiments.

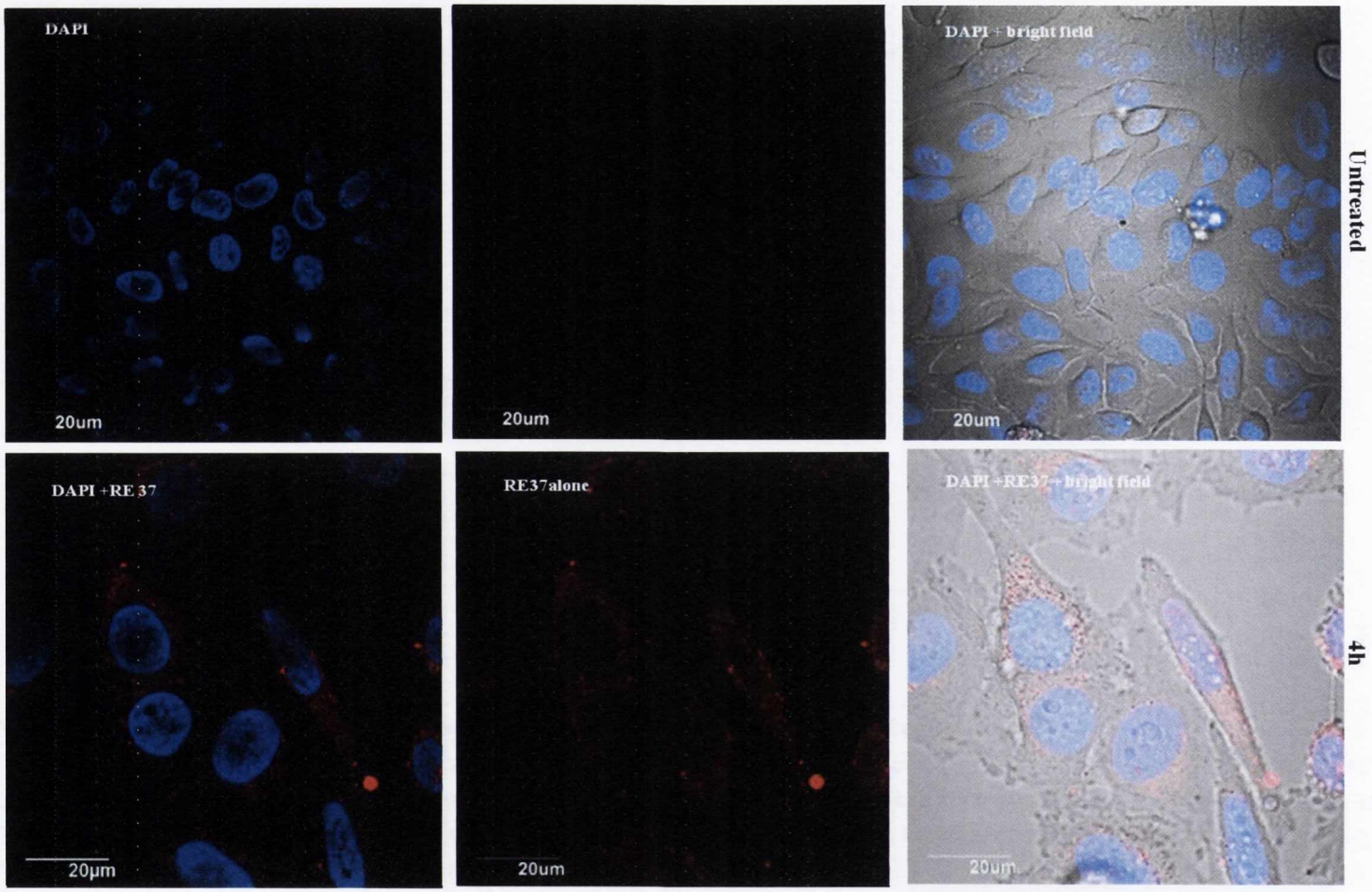
DAPI
20um
20um
DAPI + bright field
20um
Untreated
DAPI +RE 37
20μm
RE37alone
20um
DAPI +RE37+ bright field
20um
4h

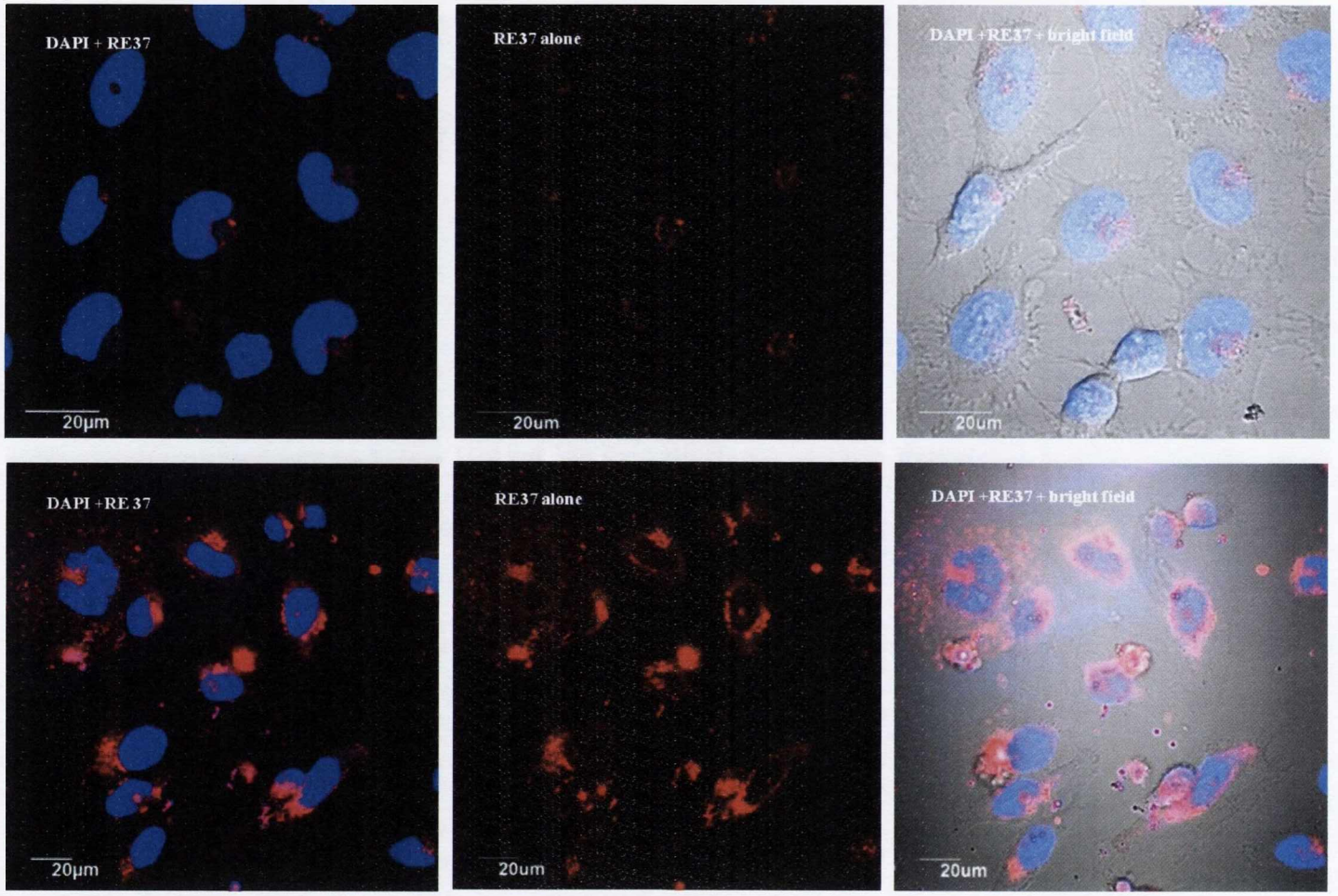
DAPI + RE37
20μm
RE37 alone
20um
DAPI +RE37 + bright field
20um
8h
DAPI +RE 37
20μm
RE37 alone
20um
DAPI +RE37 + bright field
20um
24h

Figure 3.26: **Time dependent localisation of RE37 in HeLa cells.**

$1x10^5$ cells/well were seeded in dish plates (Ø 22mm; 2ml total volume/well). Cells were incubated at 37°C overnight before treatment. The cells were then treated with 100μM of RE37 and incubated for 4, 8 and 24h. Cells were washed twice in PBS followed by the addition of fresh media and DAPI, followed by viewing using Olympus FV1000 confocal microscopy with a 60x oil immersion lens. After 4h the complex is localised in the cytoplasm. After 8 and 24h a peri-nuclerar clustering of the compound was observed. Image analysis was performed using FluoView Version 7.1 Software. RE37 was excited by a 488nm argon laser, emission 620nm and DAPI was excited by a 405 laser, emission 461nm. Results are representative of three independent experiments.

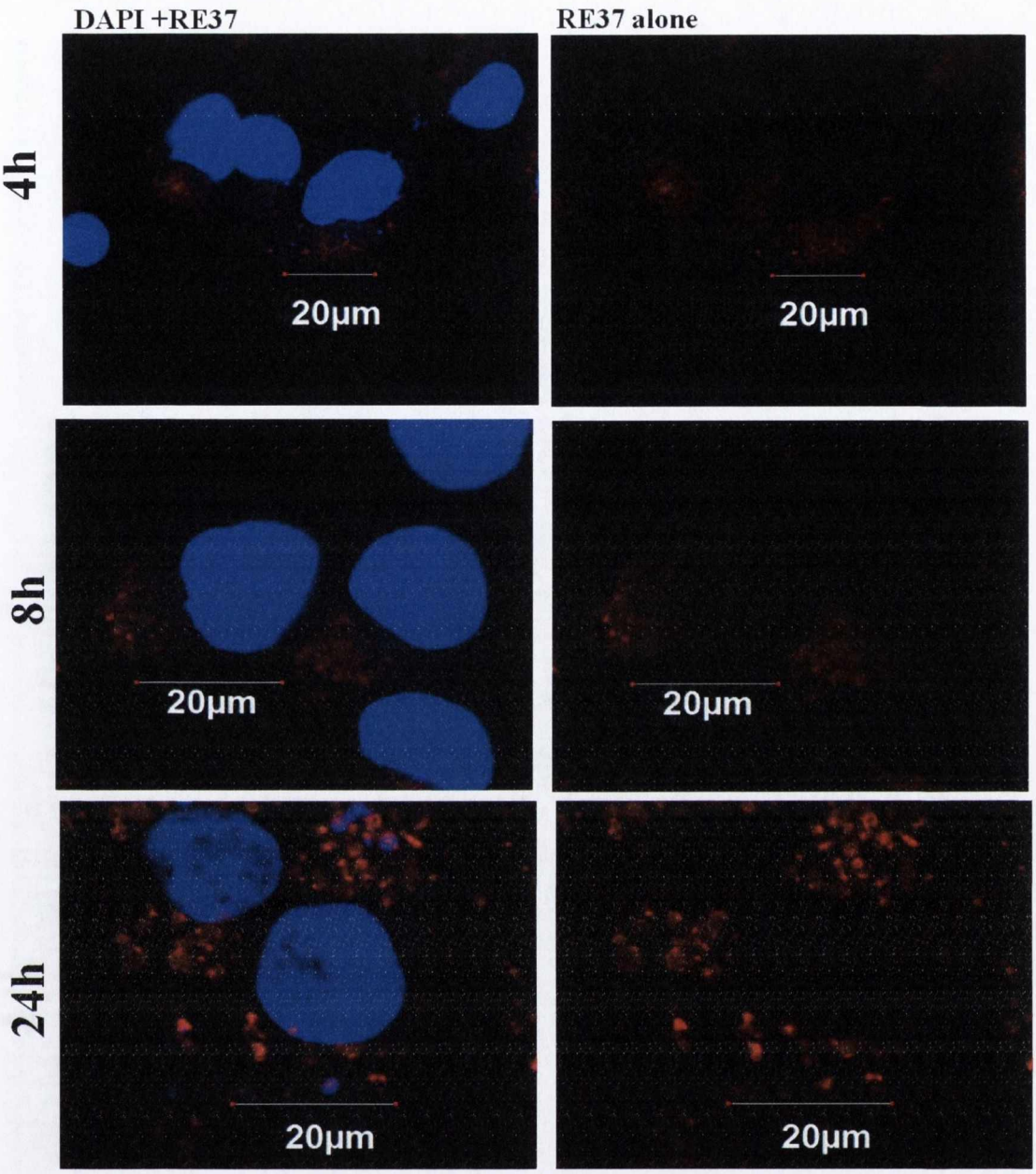

Figure 3.27: **Time dependent localisation of RE37 in CRL cells.**

$1x10^5$ cells/well were seeded in dish plates (Ø 22mm; 2ml total volume/well). Cells were incubated at 37°C overnight before treatment. The cells were then treated with 100µM of RE37 and incubated for 4, 8 and 24h. Cells were washed twice in PBS followed by the addition of fresh media and DAPI, followed by viewing using Olympus FV1000 confocal microscopy with a 60x oil immersion lens. After 4h the complex is localised in the cytoplasm. After 8 and 24h a peri-nuclerar clustering of the compound was observed. Image analysis was performed using FluoView Version 7.1 Software. RE37 was excited by a 488nm argon laser, emission 620nm and DAPI was excited by a 405 laser, emission 461nm. Results are representative of three independent experiments.

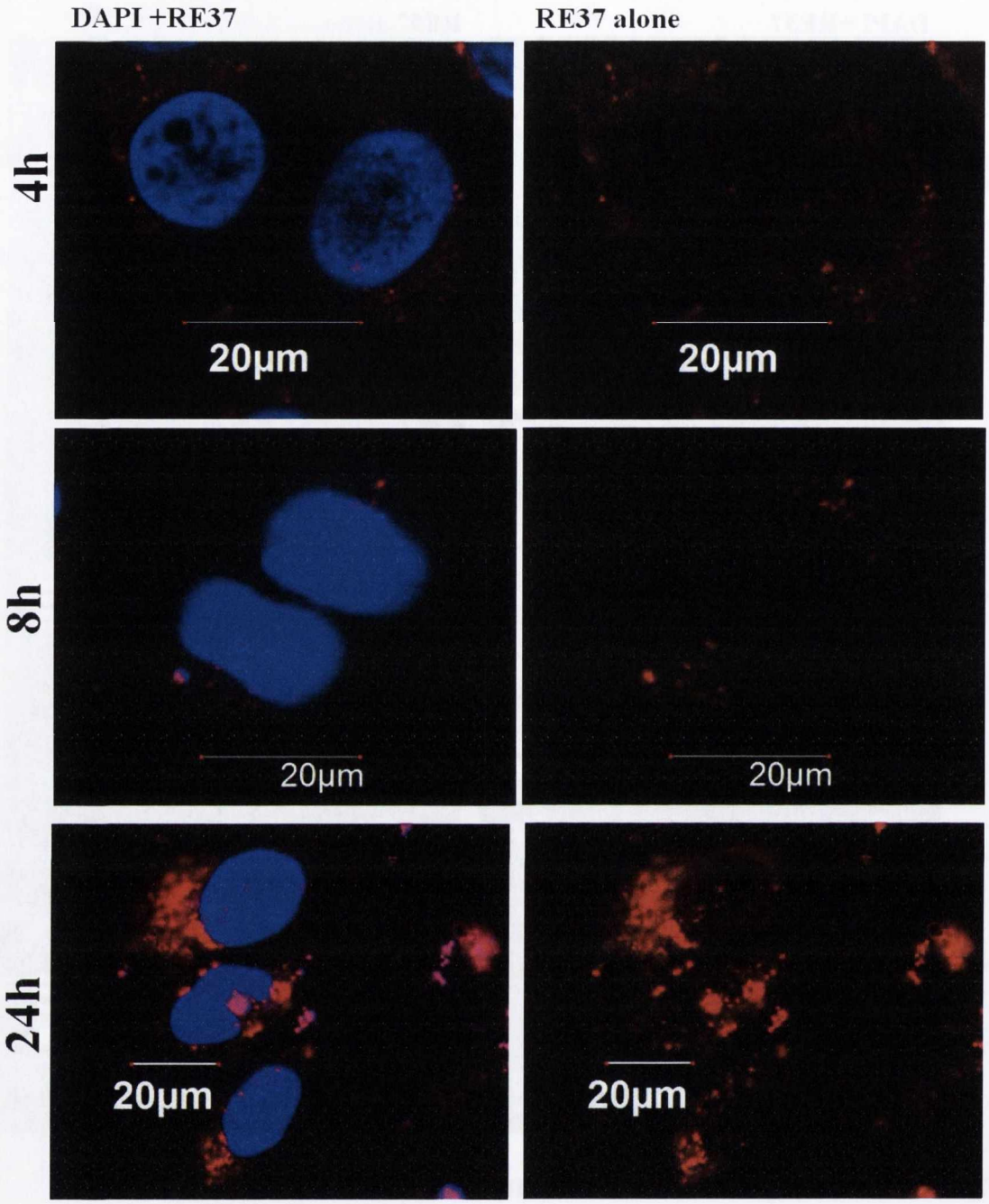

Figure 3.28: **Time dependent localisation of RE37 in HeLa cells.**

$1x10^5$ cells/well were seeded in dish plates (Ø 22mm; 2ml total volume/well). Cells were incubated at 37°C overnight before treatment. The cells were then treated with 100µM of RE37 and incubated for 4, 8 and 24h. Cells were washed twice in PBS followed by the addition of fresh media and DAPI, followed by viewing using Olympus FV1000 confocal microscopy with a 60x oil immersion lens. After 4h the complex is localised in the cytoplasm. After 8 and 24h a peri-nuclerar clustering of the compound was observed. Image analysis was performed using FluoView Version 7.1 Software. RE37 was excited by a 488nm argon laser, emission 620nm and DAPI was excited by a 405 laser, emission 461nm. Results are representative of three independent experiments.

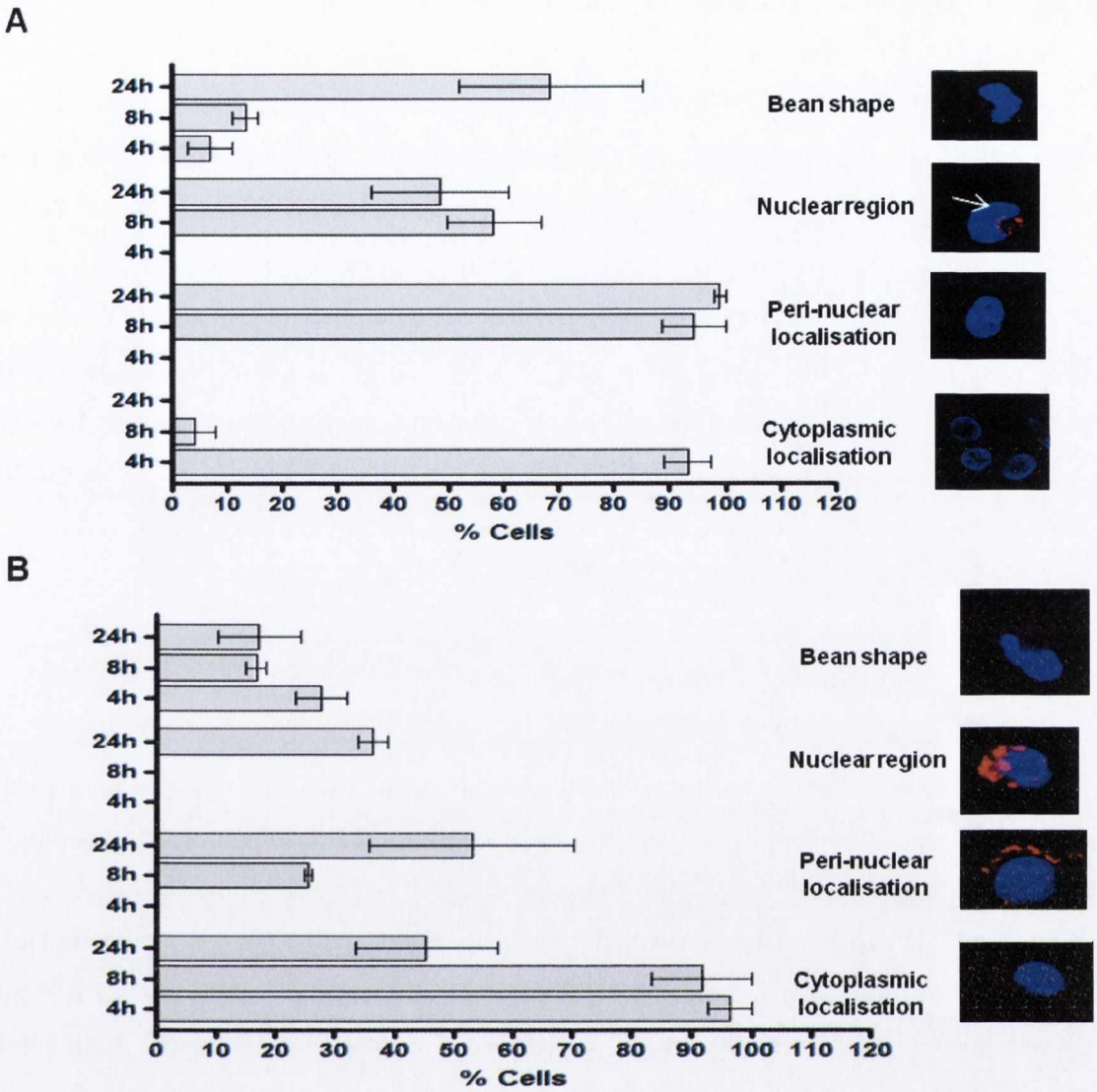

Figure 3.29: **Confocal studies of RE37 localization within cells.**

$1.7x10^5$ (cells/well) HeLa **(A)** and CRL **(B)** cells were seeded in glass bottom dish plates (Ø 22mm; 2ml total volume/well). Cells were incubated at 37°C overnight before treatment. The cells were then treated with 100μM of RE37 and incubated for 4, 8 and 24h. Cells were washed twice in PBS followed by the addition of fresh media before overnight Olympus FV1000 confocal microscopy with a 60x oil immersion lens. Image analysis was performed using FluoView Version 7.1 Software. The percentage of cells with fluorescence in the cytoplasm, in the peri-nuclear region, at the bean-shaped nucleus or in the nuclear region were expressed over the total number of cells (approximately 100) per field of view. RE37 was excited by a 488nm argon laser, emission 620nm and DAPI was excited by a 405 laser, emission 461nm. Results are representative of three independent experiments.

3.4.4 Live video of RE37 uptake in HeLa cells

Live videos were set up to collect more information about the localization of the compounds, but also to observe morphology changes, cell death and effects of any light irradiation (figures 3.30 and 3.31). HeLa cells were treated with 100μM of RE37 for 24h before capture with a live video. Over 12h overnight, images were taken every 10 min at 5% 488 laser intensity (laser was only switched on when the images were taken). Cell death was measured by counting damaged cells (cell shrinkage) as a percentage of total cells (approximately 100) per field of view. Cell death was more pronounced in the light irradiated samples. The videos are available in the DVD included in the back cover of the thesis.

3.5 RE33 and 37 induced cell death in HeLa cells

As previously described in Section 2.9 in the Materials and Methods, when apoptotic cells are stained with PI and analyzed with a flow cytometer, they display a broad hypodiploid (pre-G1) peak.

In order to investigate on the mechanism of cell death induced by the compounds in HeLa cells, apoptotic analysis was carried out. A range of different concentrations of RE33 and 37 were tested, from 5 to 100μM, and the cells were incubated for 48h in total (24h before light exposure followed by incubation for further 23h).

3.5.1 RE33 induces light-dependent apoptosis in HeLa cells at high concentrations

Apoptotic analysis was carried out in HeLa cells treated with RE33 because it was the only cell line where a small reduction in cell viability in non-illuminated cells was observed together with a greater reduction in cell viability when illuminated. The results showed an increase in light-dependent cell death with increasing concentrations of the compound between 40 and 100μM. A small degree of toxicity was found without light treatment (figure 3.32).

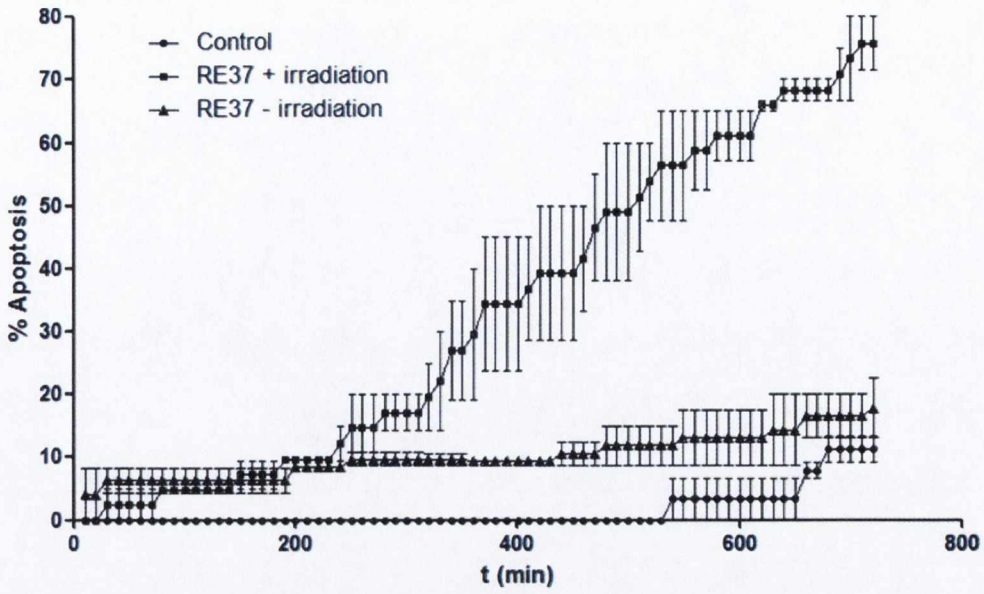

t(min)	Control	RE37 without irradiation	RE37 with Irradiation
	% HeLa cell death		
10	0	11.8±4.4	49.0±15.4
30	0	6.3±2.8	2.5±3.5
540	3.3±4.7	11.8±4.4	56.3±12.2
720	11.2±2.9	17.7±6.8	75.7±6.0

Figure 3.30: **Light-dependent cell death measured using life video capturing.**

$1.7x10^5$ (cells/well) HeLa cells were seeded in glass bottom dish plates (Ø 22mm; 2ml total volume/well). Cells were incubated at 37°C overnight before treatment. The cells were then treated with 100μM of RE37 and incubated for a further 24h. Cells were washed twice in PBS followed by the addition of fresh media before overnight Olympus FV1000 confocal microscopy with a 60x oil immersion lens. Cells irradiated were exposed for 30min at 5% 488nm laser intensity. The time point chosen represent the times where the major differences among treated and untreated cells with and without irradiation occurred. Image analysis was performed using FluoView Version 7.1 Software. The percentage of cell death was expressed over the total amount of cells (approximately 100) per field of view. During the 12h overnight, cells were incubated at 37°C, 5% CO_2 and images were taken every 10min at 5% 488nm laser intensity (laser was only on when the images were taken). RE37 was excited by a 488nm argon laser at 5% intensity, emission 620nm. Results are representative of three independent experiments.

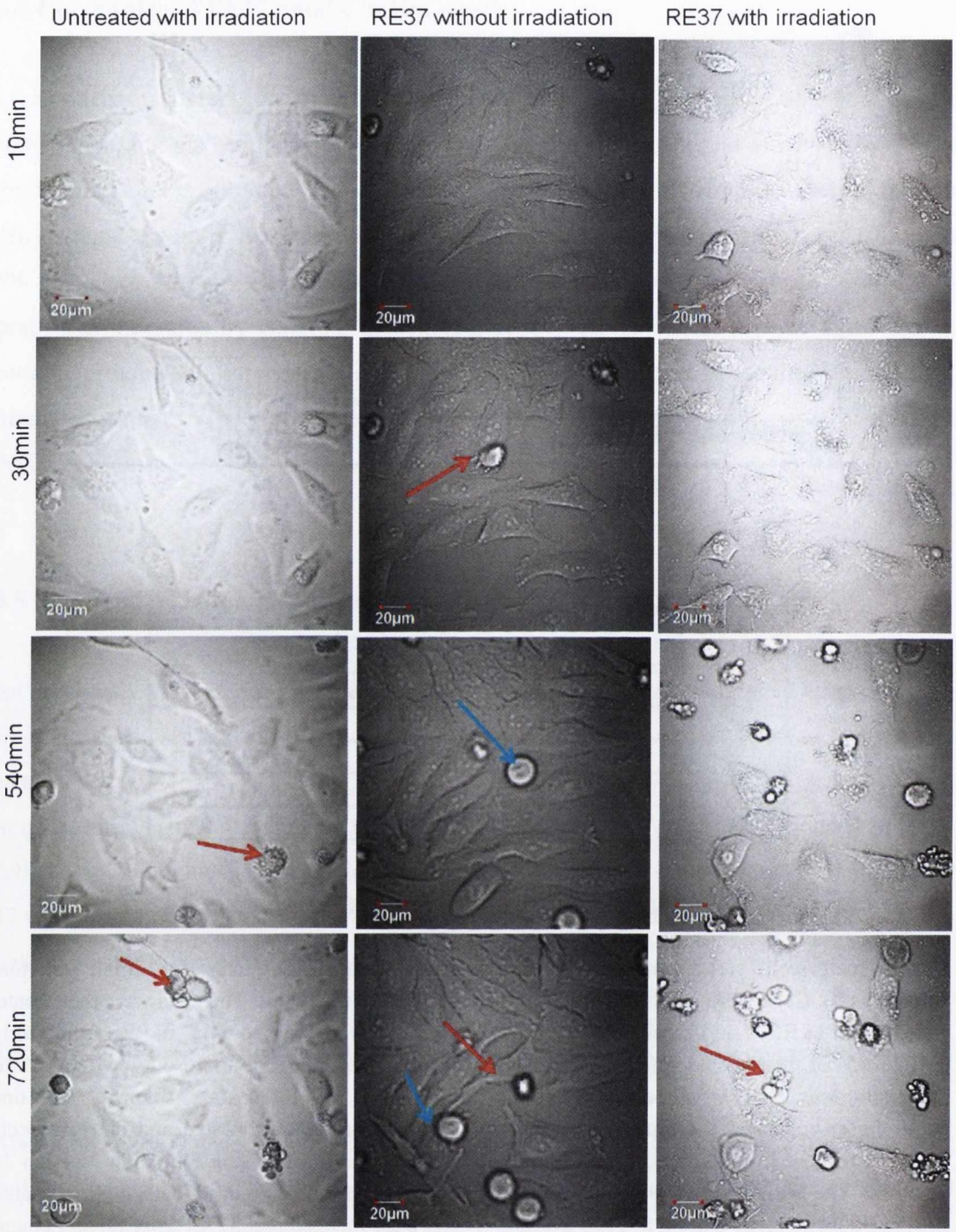
Untreated with irradiation
RE37 without irradiation
RE37 with irradiation
10min
30min
540min
720min
20μm

Figure 3.31: **Images of light-dependent cell death taken using live video capturing.**

$1x10^5$ HeLa cells/well were seeded in dish plates (Ø 22 mm; 2ml total volume/well). Cells were incubated at 37°C overnight before treatment. The cells were then treated with 100μM of RE37 and incubated for further 24h. Cells were washed twice in PBS followed by the addition of fresh media before viewing using Olympus FV1000 confocal microscopy with a 60x oil immersion lens. Cells irradiated were exposed for 30min at 5% laser intensity. The time point chosen represent the times where the major differences among treated and untreated cells with and without irradiation occurred. Image analysis was performed using FluoView Version 7.1 Software. Over 12h cells were at 37°C, 5% CO_2 and images were taken every 10min at 5% 488nm laser intensity (laser was only on when the images were taken). The percentage of cell death was analysed using grouped analyses row-means/totals in GRAPHPAD Prism software. Results are representative of three independent experiments. The red arrows indicate apoptotic bodies and the blue ones indicate cell division.

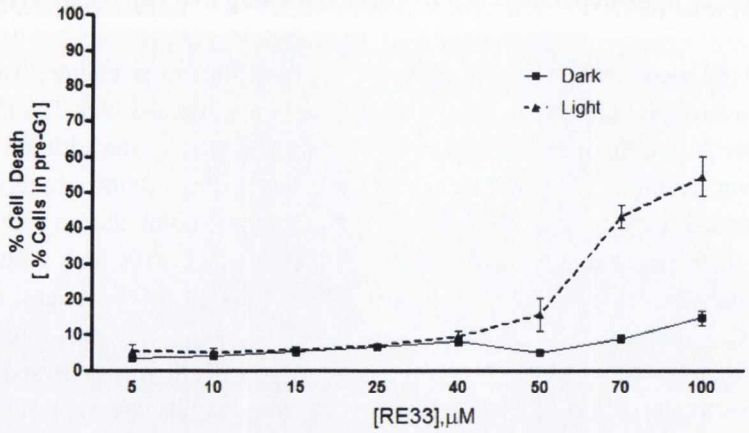

Figure 3.32: **Light-dependent toxicity of RE33 in HeLa cells.**

$0.25x10^6$ cells were seeded in T25 flasks (5ml total volume/well). Cells were incubated at 37°C overnight before treatment. The cells were treated with different concentrations of RE33 (5, 10, 15, 25, 40, 50, 70 and 100μM). After 24h incubation the treated cells were exposed to light for 1h to give light doses of $12.66J/cm^2$ or maintained in the dark. The percentage of cell death was compared with the treated cells in the dark. Following 23h of incubation the cells were fixed in ice cold 70% ethanol and PBS overnight at 4°C. After fixation, the cells were pelleted and resuspended in 300μl of PBS in FACS microtubes, 25μl of RNAse A (10mg/ml) and 75μl of PI (1mg/ml) were then added. The tubes were incubated at 37°C in the dark for 30min. Cell cycle analysis was performed using appropriate gates counting 10,000 cells and using CELLQUEST software package. Values are representative of at least three independent experiments.

3.5.2 RE37 induces apoptosis in a concentration-dependent manner

With the aim of establishing if the cell death observed with RE37 occurred via apoptosis, as suggested from the confocal studies, FACS analysis was carried out. The results showed an increase in cell death light treatment with increasing concentrations of the compound. Little or no toxicity was found without light treatment (figure 3.33A).
In figure 3.34, the graph shows the percentage of cell death in HeLa cells following treatment with all the different compounds discussed up until now (RE30, 34, 37 and 33) at a high concentration for comparison purposes.

3.5.3 RE37 induces apoptosis in a time-dependent manner

Having confirmed that the cells died via apoptosis, it was next important to understand how long the cells took to die after light exposure. In relation to that, 20μM of RE37 was chosen as the optimum concentration that led to 80% cell death. It was used for the set up of a time course experiment in order to understand how fast the cells die after light exposure. The results showed that cell death started during the light exposure with 20% of cell death immediately after light exposure. Cell death increased over a 24h period but only after light treatment (figure 3.33B).

3.6 The fluorescence of RE33 and 37 increases in cells in a time dependent manner

HeLa cells were incubated with 100μM of RE33 and 20μM of RE37 for different incubation times (2, 4, 8, 24 and 48h) and kept in the dark. For this experiment cells were treated with 20μM of RE37 instead then 100μM because it was chosen as the optimal concentration. RE37 at 100μM was the ideal concentration used to observe luminescence in confocal microscopy. Uptake in cells was quantified by flow cytometry measuring the compound fluorescence within cells and the difference in fluorescence over time. The results are shown in figures 3.35 and 3.36. The fluorescence of RE33 and 37 increases in cells in a time dependent manner. However, RE33 uptake appeared to reach a plateau at 24h. RE37 showed a greater fluorescence then RE33. The increase in fluorescence is dependent on being in an appropriate molecular environment.

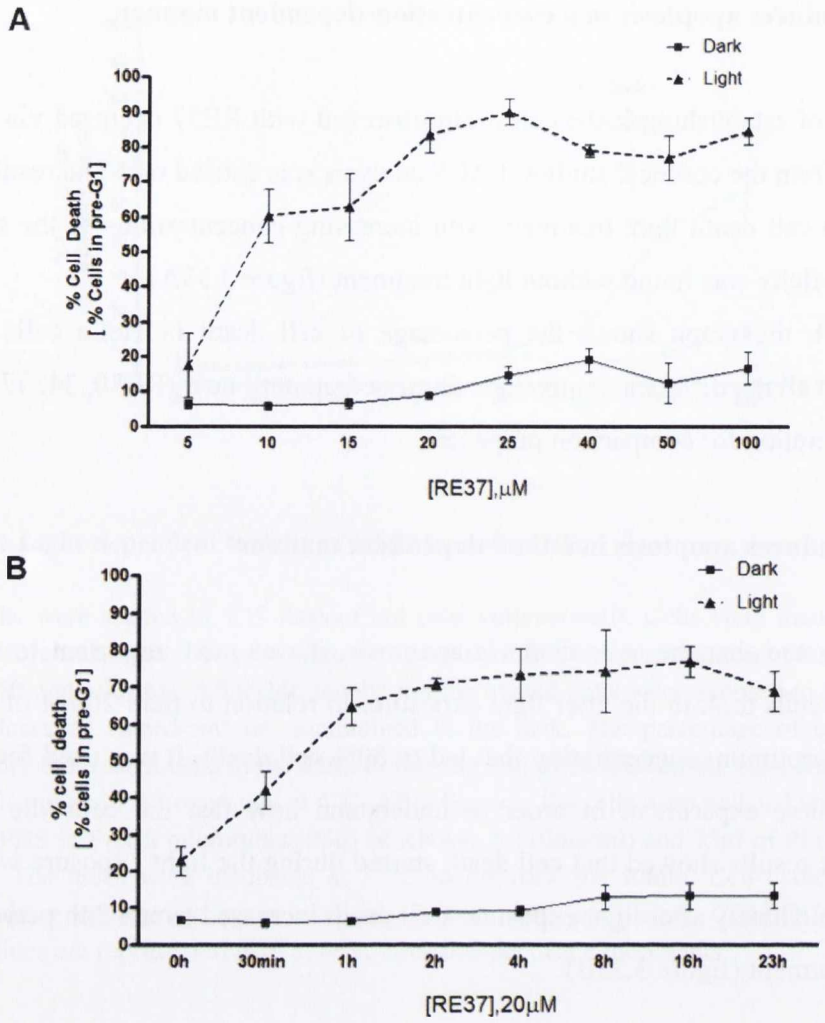

Figure 3.33: **RE37 induces programmed cell death in HeLa cells. (A) Concentration–dependence**

$1x10^5$ cells were seeded in 6-well plates (2.5ml total volume/well). Cells were incubated at 37°C overnight before treatment. The cells were treated with different concentrations of RE37 (5, 10, 15, 20, 25, 40, 50 and 100μM). After 24h incubation the treated cells were exposed to light for 1h to give light doses of $12.66J/cm^2$ or maintained in the dark. The percentage of cell death was compared with the treated cells in the dark. Following 23h of incubation the cells were fixed in ice cold 70% ethanol and PBS overnight at 4°C. After fixation, the cells were pelleted and resuspended in 300μl of PBS in FACS microtubes, 25μl of RNAse A (10mg/ml) and 75μl of PI (1mg/ml) were then added. The tubes were incubated at 37°C in the dark for 30min. Cell cycle analysis was performed using appropriate gates counting 10,000 cells and using CELLQUEST software package. **(B) Time-dependence** $1x10^5$ cells were seeded in 6-well plates. Cells were incubated at 37°C overnight before treatment. The cells were treated at 20μM with RE37. After 24h incubation the treated cells were exposed to light for 1h to give light doses of $12.66J/cm^2$ or maintained in the dark. The percentage of cell death was compared with the treated cells in the dark. After light exposure the percentage of cell death was analyzed at different time points (0h, 30min, 1, 2, 4, 8, 16 and 23h) followed by cells fixation as described in section A. Values are representative of at least three independent experiments.

A

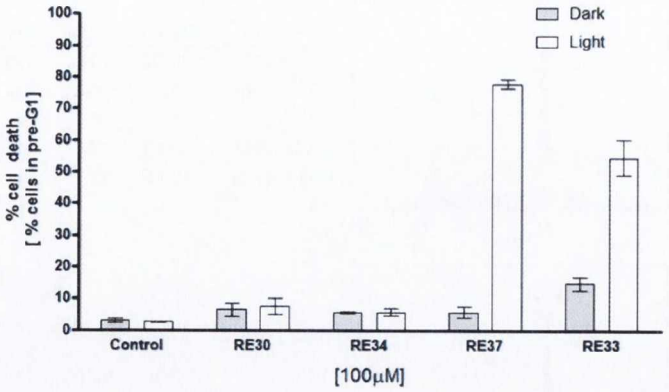

B

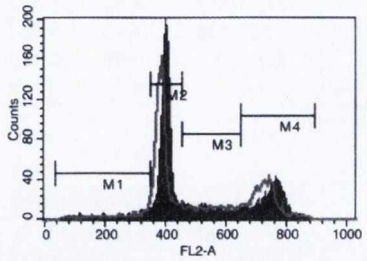

	Events	% Gated	% Total	Mean
	10000	100.00	100.00	495.13
M1	521	5.21	5.21	277.30
M2	5288	52.88	52.88	382.49
M3	1519	15.19	15.19	553.77
M4	2712	27.12	27.12	722.52

C

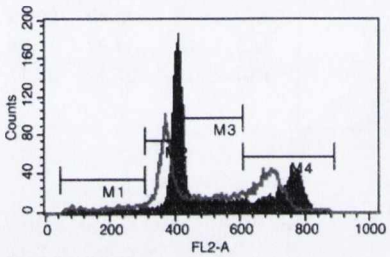

	Events	% Gated	% Total	Mean
	10000	100.00	100.00	493.10
M1	703	7.03	7.03	200.02
M2	3857	38.57	38.57	366.81
M3	2150	21.50	21.50	520.69
M4	3318	33.18	33.18	684.00

D

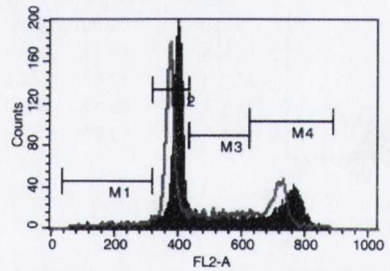

	Events	% Gated	% Total	Mean
	10000	100.00	100.00	476.96
M1	499	4.99	4.99	217.48
M2	5233	52.33	52.33	371.92
M3	1704	17.04	17.04	529.55
M4	2602	26.02	26.02	703.59

E

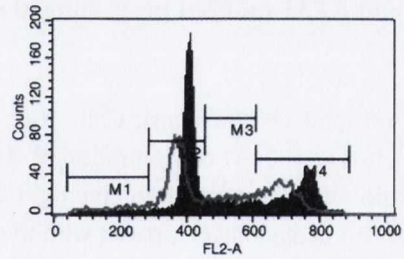

	Events	% Gated	% Total	Mean
	10000	100.00	100.00	477.22
M1	749	7.49	7.49	188.61
M2	4530	45.30	45.30	368.17
M3	1799	17.99	17.99	536.51
M4	2956	29.56	29.56	682.14

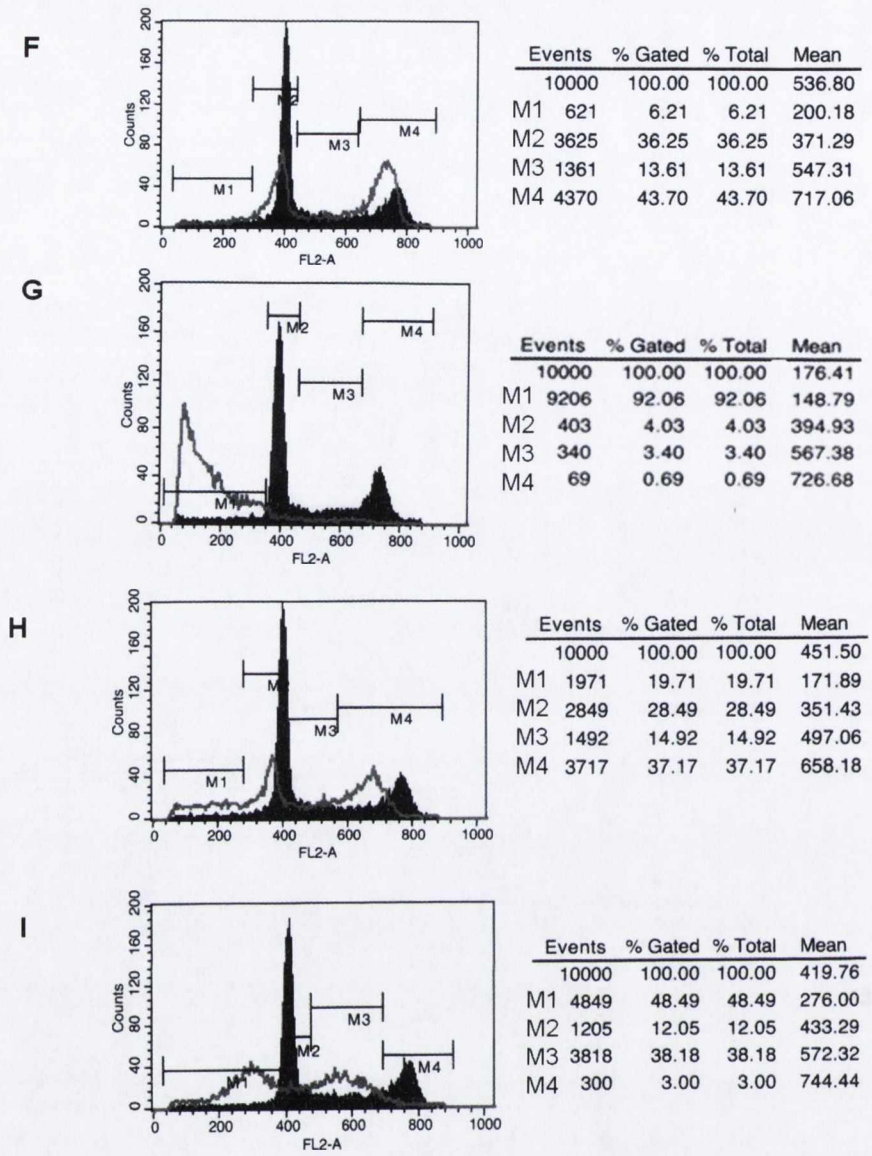

Figure 3.34: **Comparison of RE30, 34, 37 and RE33-induced programmed cell death in HeLa cells.**

$0.25x10^6$ cells were seeded in T25 flasks (5ml total volume/well). Cells were incubated at 37°C overnight before treatment. The cells were treated at 100μM concentration of RE30, 34, 33 and 37. After 24h incubation the treated cells were exposed to light for 1h to give light doses of $12.66J/cm^2$ or maintained in the dark. The percentage of cell death was compared with the treated cells in the dark. Following 23h of incubation the cells were fixed as described in Section 2.9.6. Cell cycle analysis was performed using appropriate gates counting 10,000 cells and using CELLQUEST software package. Values are representative of at least three independent experiments **(A)**. The figure also includes the gating data and the PI cell cycle profile of compounds RE30 in the dark **(B)** and in the light **(C)**, RE34 in the dark **(D)** and in the light **(E)**, RE37 in the dark **(F)** and in the light **(G)** and RE33 in the dark **(H)** and in the light **(I)**. In black is shown the untreated control and the grey line is the compounds cell cycle profile. The M1indicates the pre-G1, M2 the G1, M3 the S and M4 the G2/M phase.

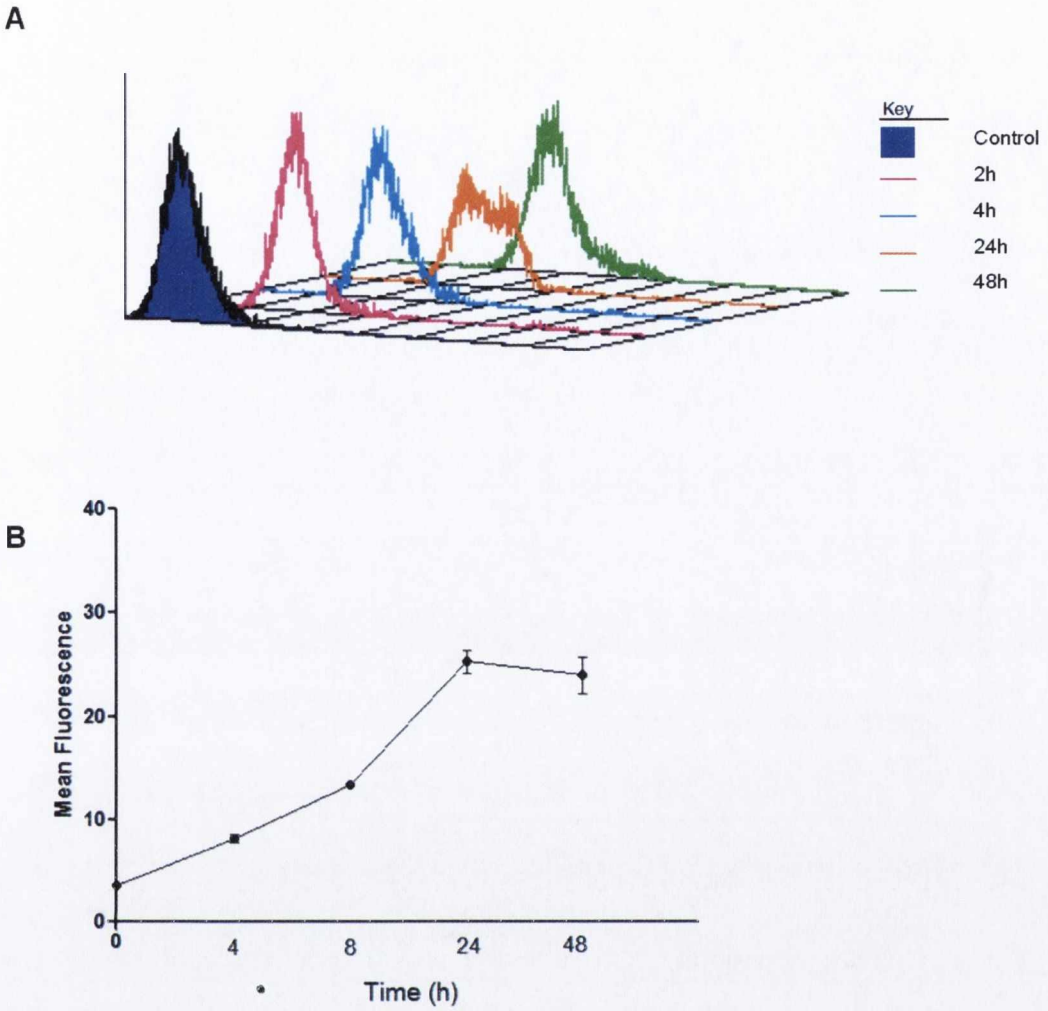

Figure 3.35: **Uptake of RE33 in HeLa cells.**

$0.25x10^6$ cells were seeded in T25 flasks (5ml total volume/well). Cells were incubated at 37°C overnight before treatment. The cells were treated with 100µM of RE33 and incubated in the dark at different time points. Cells were then harvested and washed in ice cold PBS followed by resuspension in ice cold PBS supplemented with 2% FBS in FACS microtubes. Cell analysis was performed using appropriate gates counting 10,000 cells and using CELLQUEST software package. The compound was excited by a 488nm argon laser, with emission observed at 515nm. A representative histogram of compound uptake **(A)**. The percentage of fluorescence within the cells is expressed as the mean ± S.E.M. and graphed using GRAPHPAD Prism software **(B)**. Values are representative of at three independent experiments.

A

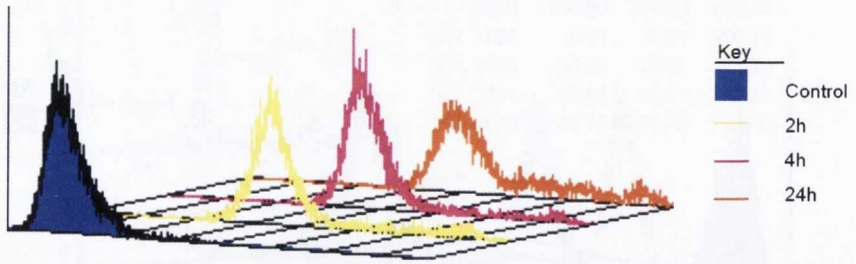

B

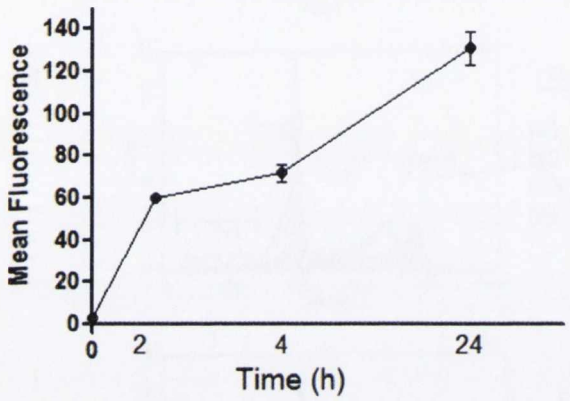

Figure 3.36: **Uptake of RE37 in HeLa cells.**

0.25x106 cells were seeded in T25 flasks (5ml total volume/well). Cells were incubated at 37°C overnight before treatment. The cells were treated with 100μM of RE37 and incubated in the dark at different time points. Cells were then harvested and washed in ice cold PBS followed by resuspension in ice cold PBS supplemented with 2% FBS in FACS microtubes. Cell analysis was performed using appropriate gates counting 10,000 cells and using CELLQUEST software package. The compound was excited by a 488nm argon laser, with emission observed at 630nm. A representative histogram of compound uptake (A). The percentage of fluorescence within the cells is expressed as the mean ± S.E.M. and graphed using GRAPHPAD Prism software (B). Values are representative of at three independent experiments.

3.7. RE37-induced apoptosis is caspase-dependent

It is important to provide further evidence for the apoptosis as the main mechanism of cell death. One approach is to establish the role, if any, of caspase involvement in compound-induced cell death by using a CI (Z-VAD-FMK) that irreversibly binds to the catalytic site of caspase proteases and can inhibit induction of caspase-dependent apoptosis. Cells were incubated with and without a pan-caspase inhibitor 4h prior incubation with RE37 for 24h before light exposure (as previously described). Extensive inhibition (>80%) of RE37 light induced cell death was found in the presence of this caspase inhibitor showing that caspases are involved in the process (figure 3.37A).

3.8 RE37 does not induce activation of caspase-3 in HeLa cells

With the aim to get more information about the mechanism of cell death, the activation of caspase-3, which is the main downstream caspase, was investigated. Cells were treated with RE37 (20μM) for 24h before being exposed to light followed by different incubation times ("time 0", 30min, 1, 2, 4, 8 and 16h), or kept in the dark. Caspase-3 activity was examined using a fluorogenic assay. RE37 did not appear to involve caspase-3 in the apoptotic process (figure 3.37B).

3.9 RE37 does not induce PARP cleavage in HeLa cells

In order to further confirm that RE37 (20μM) induced apoptosis in HeLa cells, the induction of PARP cleavage, which is a classical hallmark of apoptosis, was investigated. As an apoptotic positive control, nocodazole (10μM) was used. The cells were treated with the compound and incubated for 24h before exposure to light followed by an 1, 4 and 24h incubation, or maintained in the dark. PARP cleavage was examined by Western blot analysis. In HeLa cells, the cleaved form of PARP (85kDa) was detected in nocodazole treated lysates. In contrast, in RE37 treated lysates no PARP cleavage was observed. This result is consistent with the observed lack of casapse-3 activity, as PARP is usually, though not always, cleaved by caspase-3 (figure 3.38).

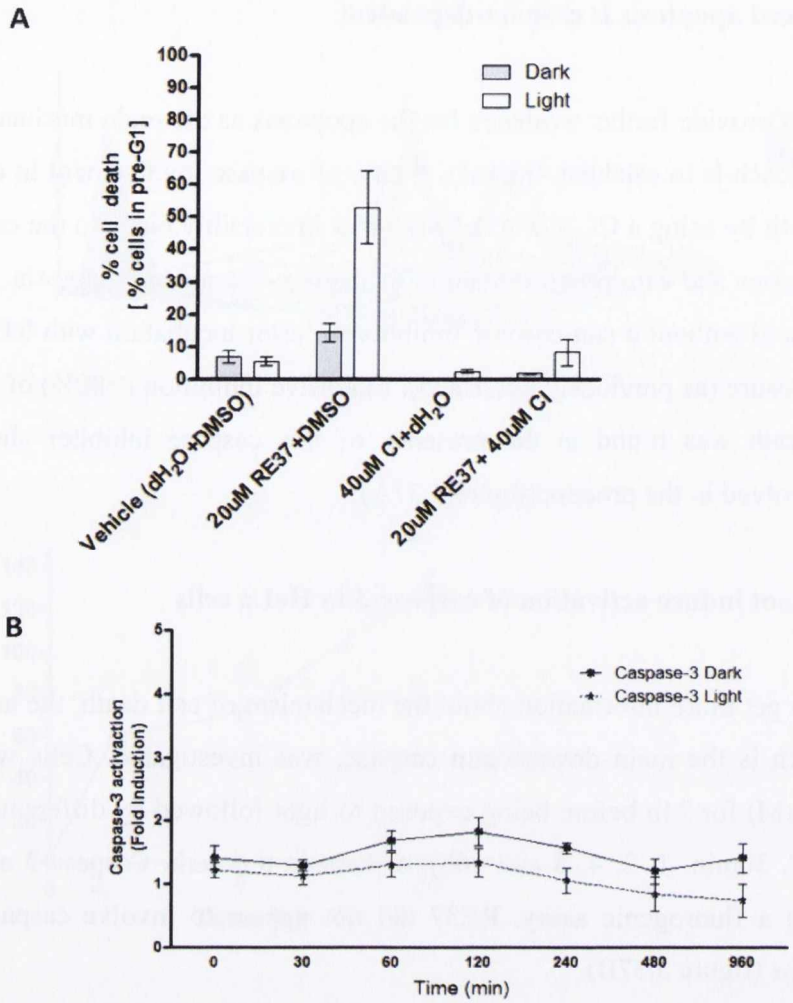

Figure 3.37: **Effect of RE37 on caspases in HeLa cells.**

Caspase-dependence (A) $1x10^5$ cells were seeded in 6-well plates and incubated at 37°C overnight. The cells were then treated with 40μM of CI followed by 20μM RE37 1h after and incubated for 24h before exposure to light for 1h to give light doses of 12.66J/cm^2. The percentage of cell death was compared with the treated cells in the dark and with the control cells treated only with CI. Following 4h of incubation the cells were fixed in ice cold 70% ethanol overnight at 4°C. After fixation, the cells were resuspended in 300μl of PBS in FACS microtubes, 25μl of RNAse A (10mg/ml) and 75μl of Propidium Iodide (1mg/ml) were then added. The tubes were incubated at 37°C in the dark for 30min. Cell cycle analysis was performed using appropriate gates counting 10,000 cells and using CELLQUEST software package.

Caspase-3 activity (B) $0.325x10^6$ cells were seeded in T25 flasks (5ml total volume/flask). Adherent cells were incubated at 37°C over night before treatment. Cells were treated with compound RE37 at 20μM for 24h before being exposed to light for 1h, to give light doses of 12.66J/cm^2, or kept in the dark. Cells were then incubated at different time points: "time 0", which was immediately after light exposure, 30min, 1, 2, 4, 8 and 16h incubation. At experimental endpoints, caspase-3 activation was determined as outlined in Section 2.12. Data was expressed as the mean ± S.E.M. and graphed using GRAPHPAD Prism software. Values are representative of three independent experiments.

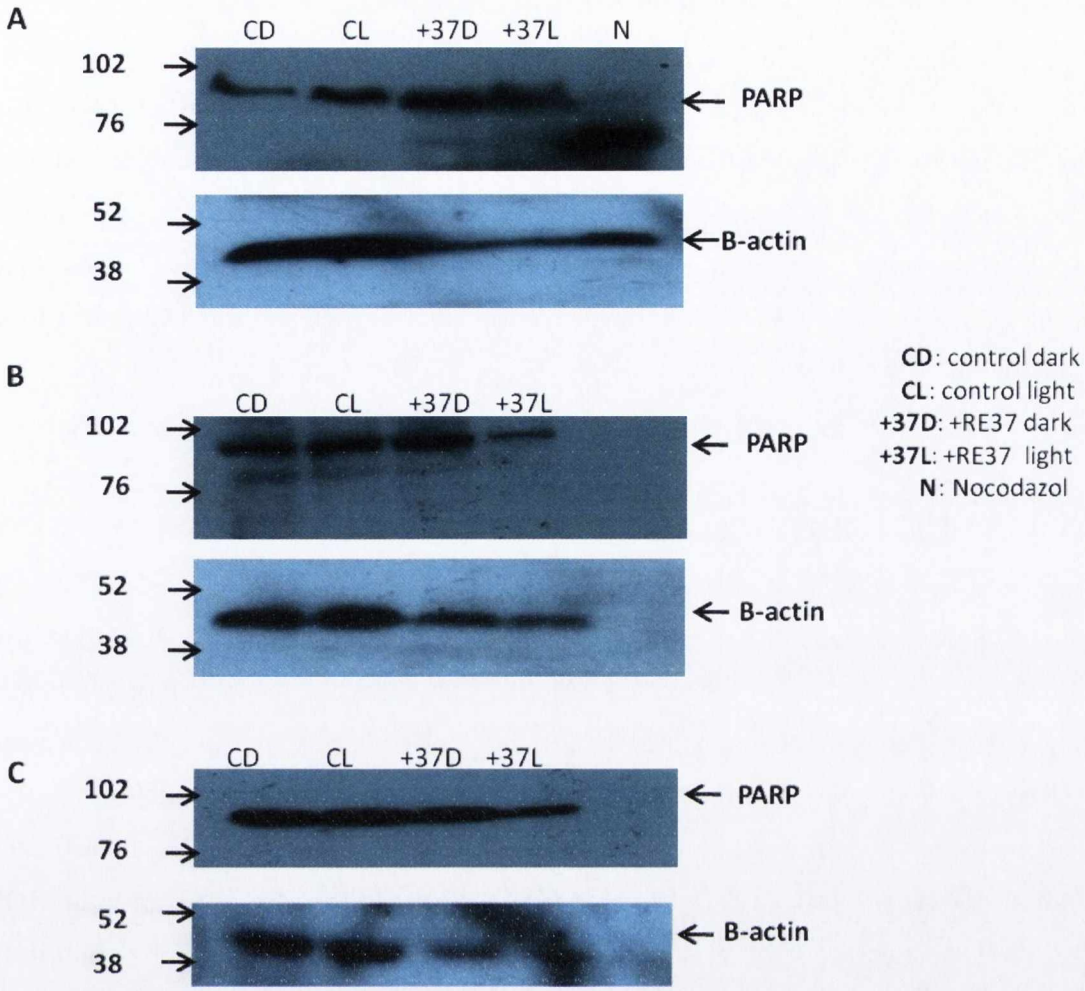

Figure 3.38: **RE37 did not induce PARP cleavage in HeLa cells.**

$1x10^6$ cells were plated in T75 flasks. Cells were incubated at 37°C overnight before being treated. The cells were treated with 20μM of RE37 and incubated for 24h before exposure to light for 1h to give light doses of $12.66J/cm^2$. Following a further 1h **(A)**, 4h **(B)** and 24h **(C)** cells were trypsinised and harvested by centrifugation. The pellet was then resuspended in PARP sample buffer (62.5mM Tris/HCl pH 6.8, 6M urea, 10% (v/v) glycerol, 2% (w/v) SDS, 0.00125% bromophenol blue) plus 1M DTT (1:20 dilution) followed by sonication with a ultrasonic processor Jencons for 11s to sheer the DNA. Then, the samples were heated in a pre-warmed heating block for 15min at 60°C. The lysates were incubated on ice until the gel was prepared. Western blot was performed as described in Materials and Methods Section. Blots were probed with anti-PARP antibody (116-85KDa) and re-probed with anti-β-actin (42KDa) as a loading control. Results are representative of three independent experiments.

3.10 RE37-induces apoptosis in a ROS dependent manner

The efficacy of photosensitization is directly related to the production of ROS. In order to establish any role for ROS in RE37 light-induced cell death, cells were incubated with N-Acetyl-L-Cysteine (NAC) (5mM) for 1h prior to RE37 incubation and light exposure as described previously. The results showed (figure 3.39A) that NAC reduced RE37 light dependent cell death by 67% showing that ROS is one of the causes involved in this form of cell death.

3.11. RE37 induces ROS production

In order to analyse the ability of RE37 to produce ROS and to quantify it, DCFH-DA dye (10μM) was used. The cells were treated with RE37 at 20μM and incubated for 24h before being exposed to light or maintained in the dark. After light exposure, the cells were incubated for further different time points. The results are shown in figures 3.39B.
Results showed a small increase in the intracellular ROS production in the light treated samples. However, analysis of the data (t-test) showed that the difference in ROS production between light treated and untreated sample is not significant ($P > 0.05$).

3.12 RE37 and 34 decrease mitochondrial membrane potential (MMP)

With the aim to analyse the effect that RE37 and 34 have on mitochondria, the variation of the mitochondrial membrane potential was investigated using JC1 dye. The cells were treated with RE37 at 20 and 100μM and with RE34 at100μM and incubated for 2 and 4h in the dark. The 100μM concentration was used in order to compare the results on MMP obtained by Suzanne Cloonan (for compound RE37) and Sandra Bright (for compound RE34) (of the Williams group), which are shown in figure 3.49B-C, using a different technique. Results showed RE37 (figure 3.40A) and 34 (figure 3.40B) to decrease the MMP in cells treated with either 20 or 100μM. Differences between the results may be due to the differences in the techniques.

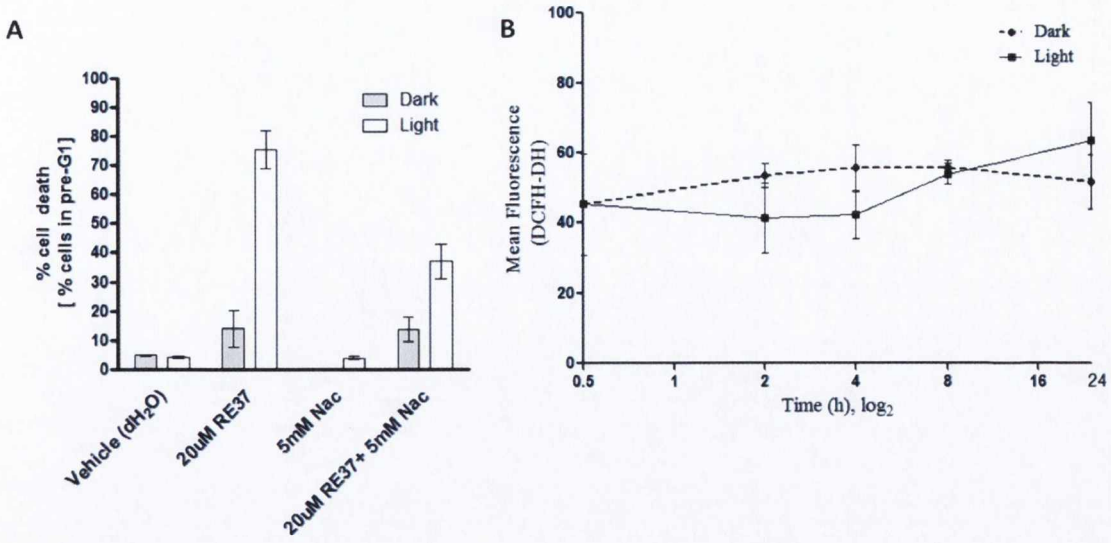

Figure 3.39: **ROS involvement in RE37-treated HeLa cells.**

ROS-dependence (A).1x10^5 cells were seeded in 6-well plates and incubated at 37°C overnight. The cells were then treated with 5mM Nac followed by 20μM RE37 1h after and incubated for 24h before exposure to light for 1h to give light doses of 12.66J/cm^2. The percentage of cell death was compared with the treated cells in the dark and with the control cells treated only with Nac. Following 23h of incubation the cells were fixed as described in Section 2.9.6. Cell cycle analysis was performed using appropriate gates counting 10,000 cells and using CELLQUEST software package. **ROS production (B)** 3x10^5 cells were seeded in T25 flascks (3ml total volume/well). Cells were incubated at 37°C overnight before treatment. The cells were treated with 20μM of RE37. Following 24h incubation the treated cells were exposed to light for 1h to give light doses of 12.66J/cm^2 or maintained in the dark for a further 2, 4, 8 and 24h. Cells were then washed with warm PBS and stained with DCFH-DA (10μM) and DRAQ-7 (1.5μM) as described in Section 2.9.10. The 488nm laser was used to excite the DCFH-DA and the 405nm laser was used to excite the DRAQ-7. DCFH-DA was detected in FL2 (Em: 575nm), the compound was detected in FL4 (Em: 680nm) and DRAQ-7 was detected in FL8 (Em: 665nm). Cell analysis was performed in the CyAn using appropriate gates counting 10,000 cells and using Summit software package. The necessary compensations were made to exclude the fluorescence of the compounds and the dead cells. The percentage of mean fluorescence within the cells was analysed using Flow Jo software, which generates histograms, and data was expressed as the mean ± S.E.M. and graphed using GRAPHPAD Prism software. The statistical analysis of the data was performed using unpaired t-test, part of GRAPHPAD Prism software ($P > 0.05$= ns).

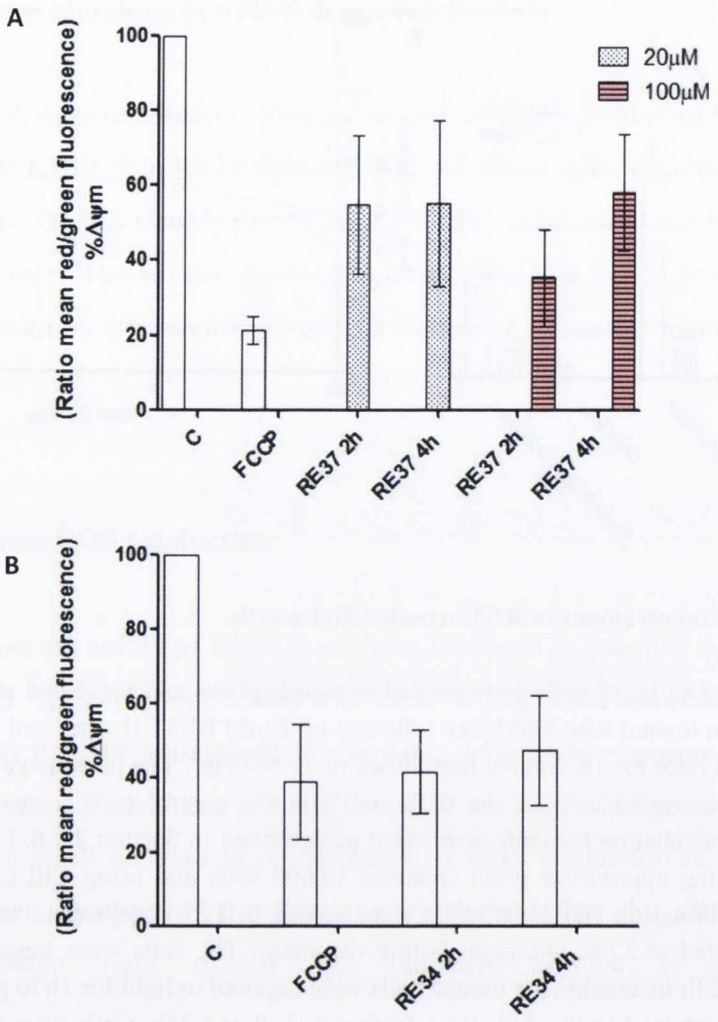

Figure 3.40: **RE37 and 34 decrease the mitochondrial membrane potential in HeLa cells.**

$3x10^5$ cells were seeded in 6-well plates (3ml total volume/well). Cells were incubated at 37°C overnight before treatment. The cells were treated with RE37 **(A)** at 20 and 100μM or with RE34 **(B)** at 100μM. After 2 and 4h incubation in the dark, cells were harvested by scraping and adjusted to a total volume of 1 ml with prewarmed complete cell culture medium. As a positive control, cells were treated with 0.25mM of FCCP. Samples were then treated with 2.5μg/ml of JC-1 followed by incubation for 20min in the dark at 37°C. Cells were then washed with PBS and centrifugated for 5min at 300xg at room temperature. Cells were resuspended in 500μl PBS before CyAn analysis. The 488nm laser was used to excite the monomeric JC-1 in green fluorescence which was detected in FL1 (Em: 530nm), the aggregate JC1 in orange/red fluorescence was detected FL2 (Em: 575nm) and the compounds were detected in FL4 (Em: 680). Cell analysis was performed in the CyAn using appropriate gates counting 10,000 cells and using Summit software package. The standard compensation was performed using the depolarising-treated sample, the untreated control and by excluding the fluorescence of the compounds. The percentage of fluorescence within the cells was analysed using Flow Jo software. The ratio red/green mean fluorescence ± S.E.M values represent the mitochondrial membrane potential and were expressed as a percentage of the untreated control which is taken as 100%, results were graphed using GRAPHPAD Prism software.

3.13 Effect of RE37 on the cytoskeleton

PDT has a strong effect on cell division, probably due to microtubule damage. In connection to that, investigation on the effect of RE37 on the cytoskeleton structure, such as actin and tubulin filaments was investigated.

HeLa cells were incubated with 100μM of RE37 for 24h in the dark and then samples were either illuminated for 1h and incubated for further 23h, or maintained in the dark. After being fixed, as described in Section 2.8.1, the cells were stained for visualisation with F-actin using an Alexa Fluor 488 Phalloidin probe (figures 3.41 and 3.43) or with a monoclonal anti-α-tubulin overnight followed by incubation with a secondary antibody anti-mouse Alexa 633 (figures 3.44 and 3.45). DAPI stain was utilised to stain the nucleus. The confocal microscopy images showed no change in the actin structure after light treatment but showed tubulin disruption after light treatment. Cell shrinkage was also evident in the cells treated with RE37 after light exposure.

3.14 RE37 is not toxic in the absence of illumination in HeLa cells

In this study we examined the effects of RE37 on HeLa cells without illumination over a 48-96h time frame using PI FACS analysis and confocal microscopy. Confocal microscopy demonstrated that over a total of 48 and 96h, RE37 (10μM) did not damage the cells (figure 3.46A). PI FACS analysis also showed that RE37 (10, 100μM) had no obvious apoptotic effect after 48h (figure3.46B).

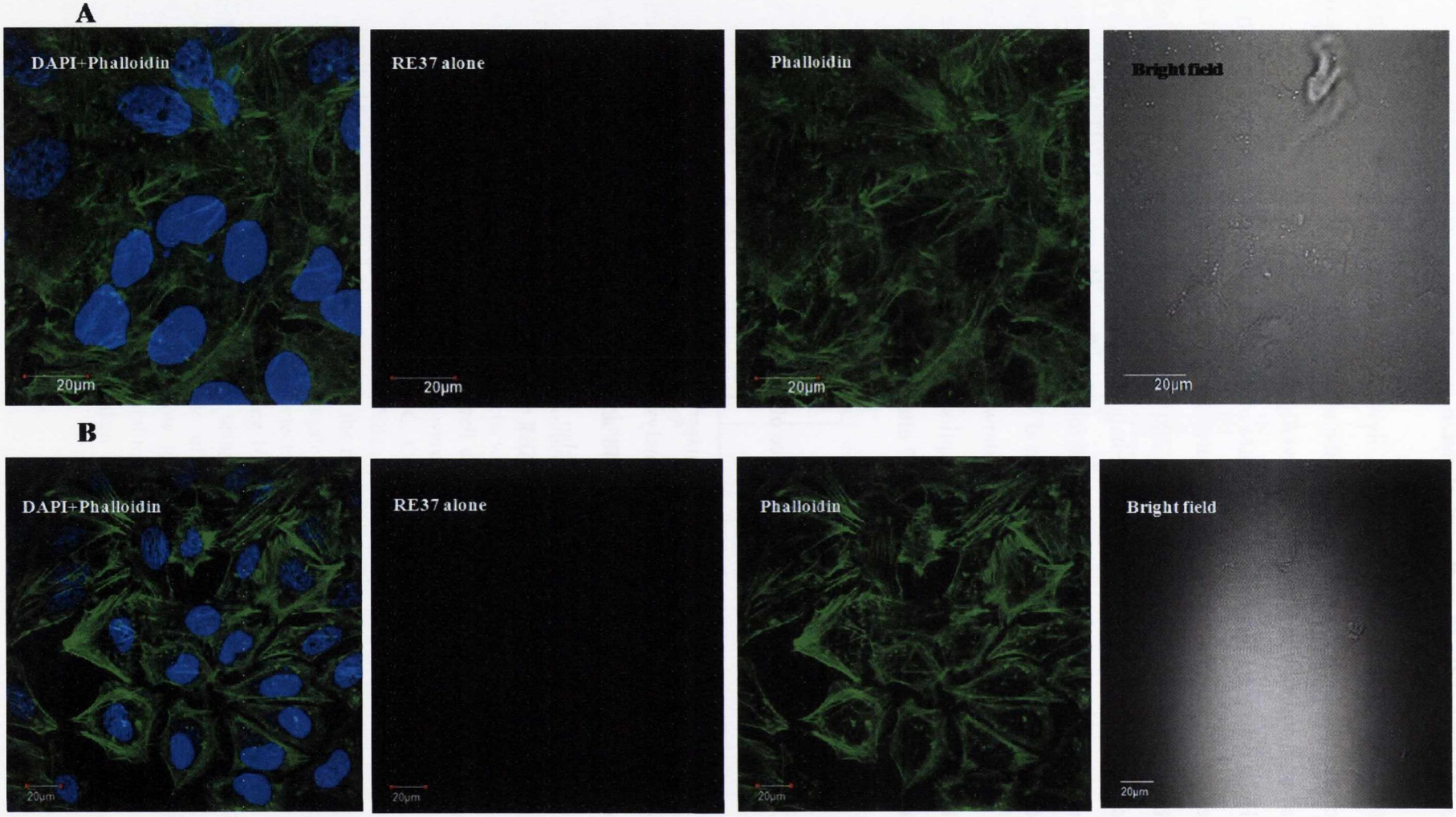
A
DAPI+Phalloidin
20μm
RE37 alone
20μm
Phalloidin
20μm
Bright field
20μm
B
DAPI+Phalloidin
20μm
RE37 alone
20μm
Phalloidin
20μm
Bright field
20μm

Figure 3.41: **Untreated HeLa cells stained with F-actin using Alexa Fluor 488 Phalloidin probe.**

$3x10^5$ cells/well were seeded on coverslips and placed inside a 6-well plate. Cells were incubated at 37°C overnight before adding the vehicle. Following 24h incubation the treated cells were maintained in the dark **(A)** or exposed to light for 1h to give light doses of $12.66J/cm^2$ **(B)**. Following a further 23h of incubation cells were washed twice with pre-warmed PBS, pH 7.4. Samples were fixed in 3% Paraformaldehyde solution in PBS for 10min at room temperature followed by two or more washes with PBS. Staining solution (0.2% Triton X-100 in PBS + phalloidin 488 (1/100 dilution) was added to the cells for 30min at room temperature followed by two or more washes with PBS. The cells on the coverslips were then transferred onto glass slides with DAPI gel added at room temperature and left overnight at room temperature before confocal microscopy. Image viewing using Olympus FV1000 confocal microscopy with a 60x oil immersion lens and analysed using the Imaris 3D software analyser (Bitplane). Image analysis was performed using FluoView Version 7.1 Software. Phalloidin was excited by a 488nm argon laser, emission 518nm and DAPI was excited by a 405 laser, emission 461nm. Results are representative of three independent experiments.

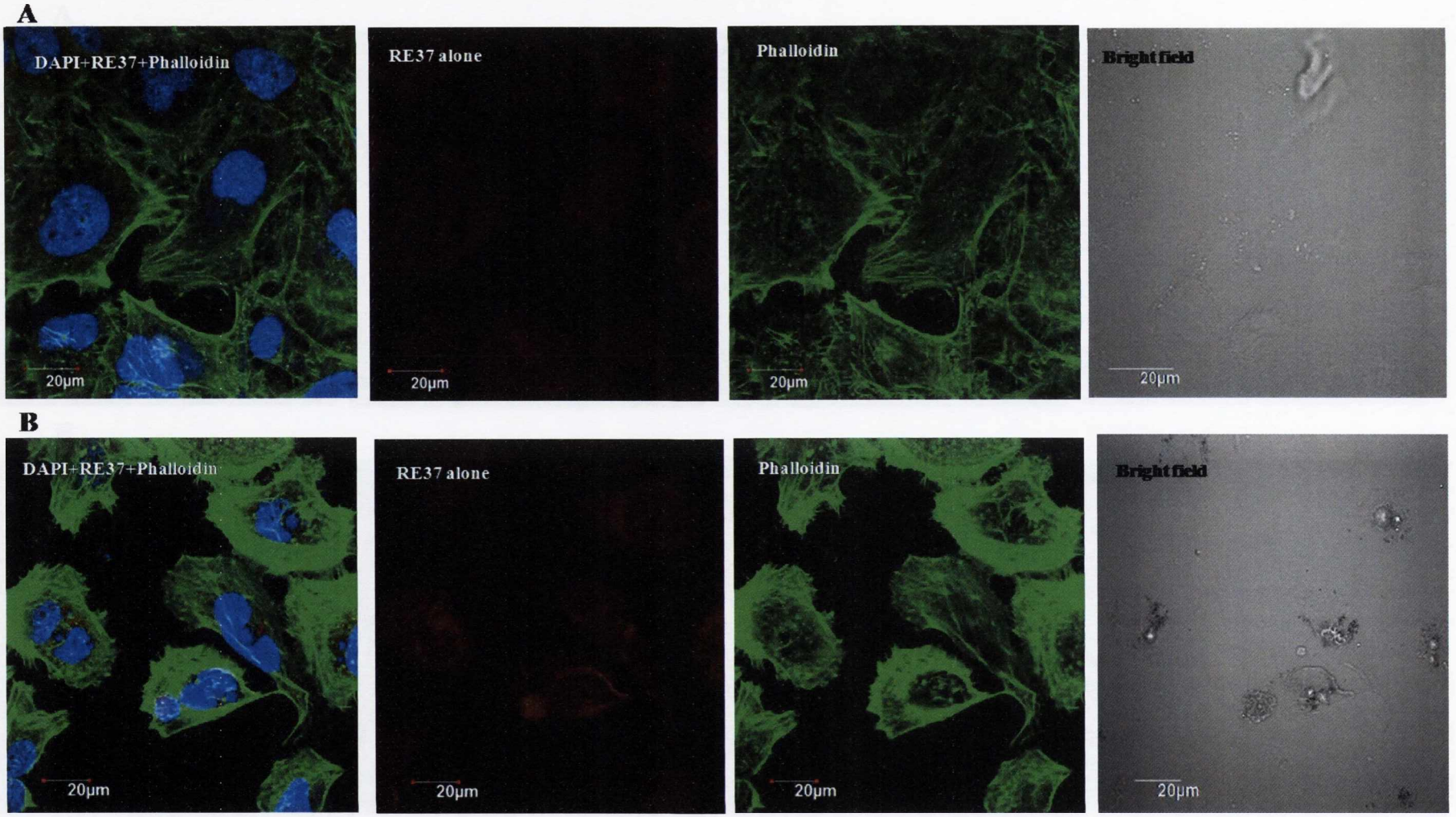
A
DAPI+RE37+Phalloidin
20μm
RE37 alone
20μm
Phalloidin
20μm
Bright field
20μm
B
DAPI+RE37+Phalloidin
20μm
RE37 alone
20μm
Phalloidin
20μm
Bright field
20μm

Figure 3.42: **Effect of RE37 on F-actin using Alexa Fluor 488 Phalloidin probe in HeLa cells.**

$3x10^5$ cells/well were seeded on coverslips and placed inside a 6-well plate. Cells were incubated at 37°C overnight before treatment with 100μM of RE37 and incubated for 24h. Following 24h incubation the treated cells were maintained in the dark **(A)** or exposed to light for 1h to give light doses of 12.66J/cm^2 **(B)**. Following a further 23h of incubation cells were washed twice with pre-warmed PBS, pH 7.4. Samples were fixed in 3% Paraformaldehyde solution in PBS for 10min at room temperature followed by two or more washes with PBS. Staining solution (0.2% Triton X-100 in PBS + phalloidin 488 (1/100 dilution) was added to the cells for 30min at room temperature followed by two or more washes with PBS. The cells on the coverslips were then transferred onto glass slides with DAPI gel added at room temperature and left overnight at room temperature before confocal microscopy. Image viewing using Olympus FV1000 confocal microscopy with a 60x oil immersion lens and analysed using the Imaris 3D software analyser (Bitplane). Image analysis was performed using FluoView Version 7.1 Software. RE37 and Phalloidin was excited by a 488nm argon laser, emission 612 and 518nm rispectively and DAPI was excited by a 405 laser, emission 461nm. Results are representative of three independent experiments.

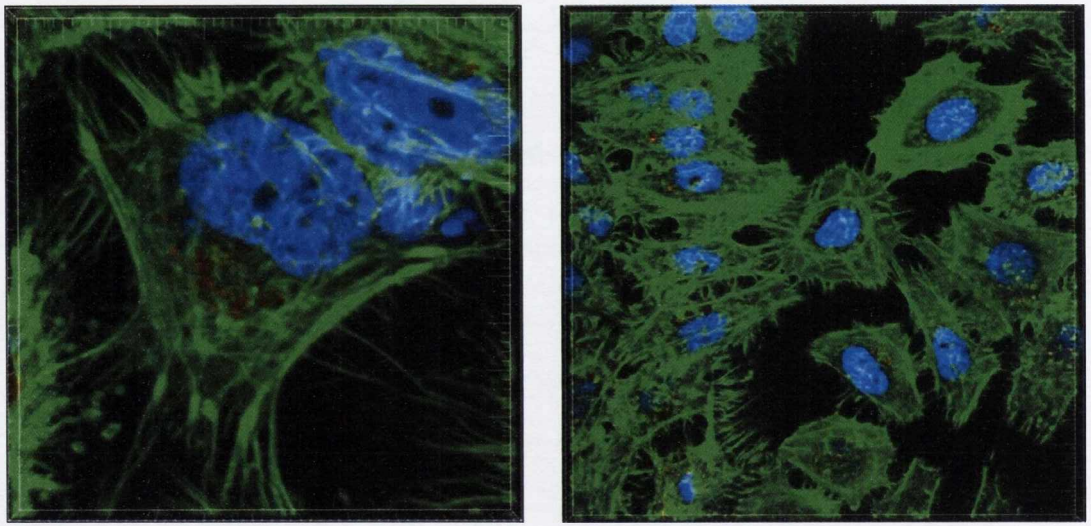

Figure 3.43: **3D images of the co-localisation study of RE37 with F-actin using Alexa Fluor 488 Phalloidin probe in HeLa cells.**

$3x10^5$ cells/well were seeded on coverslips and placed inside a 6-well plate. Cells were incubated at 37°C overnight before treatment. The cells were then treated with 100μM of RE37 and incubated for 24h. Following 24h incubation the treated cells were maintained in the dark. Following a further 23h of incubation cells were washed twice with pre-warmed PBS, pH 7.4. Samples were fixed in 3% Paraformaldehyde solution in PBS for 10min at room temperature followed by two or more washes with PBS. Staining solution (0.2% Triton X-100 in PBS + phalloidin 488 (1/100 dilution) was added to the cells for 30min at room temperature followed by two or more washes with PBS. The cells on the coverslips were then transferred onto glass slides with DAPI gel added at room temperature and left overnight at room temperature before confocal microscopy. Image viewing using Olympus FV1000 confocal microscopy with a 60x oil immersion lens. Image analysis was performed using FluoView Version 7.1 Software and analysed using the Imaris 3D software analyser (Bitplane). RE37 and Phalloidin were excited by a 488nm argon laser, emission 612 and 518nm rispectively and DAPI was excited by a 405 laser, emission 461nm. Results are representative of three independent experiments.

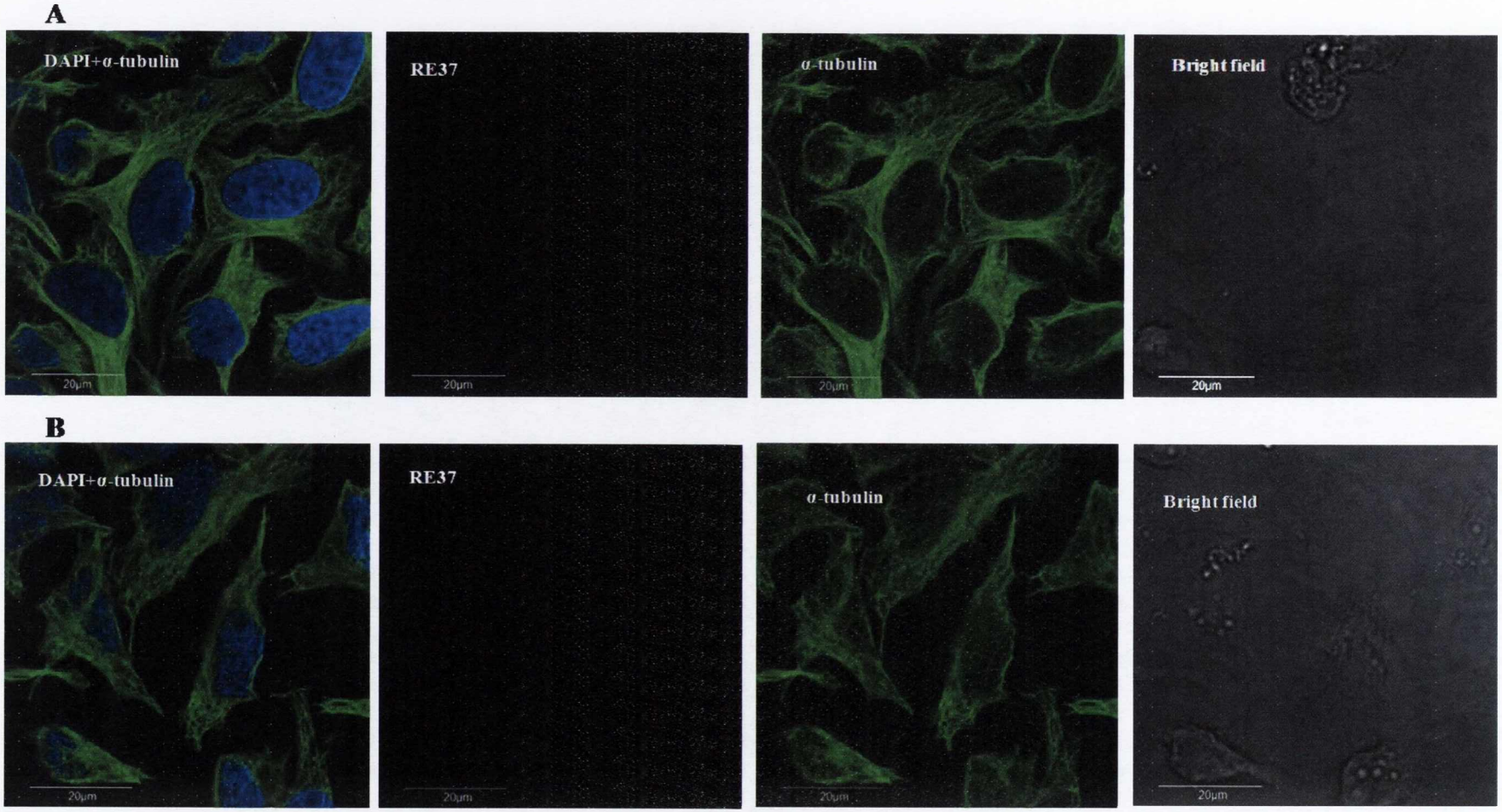
A
DAPI+α-tubulin
RE37
α-tubulin
Bright field
20μm
B
DAPI+α-tubulin
RE37
α-tubulin
Bright field
20μm

Figure 3.44: **Untreated HeLa cells stained with α-tubulin.**

$3x10^5$ cells/well were seeded on coverslips and placed inside a 6-well plate. Cells were incubated at 37°C overnight before the vehicle was added to untreated cells. Following 24h incubation the treated cells were maintained in the dark **(A)** or exposed to light for 1h to give light doses of $12.66J/cm^2$ **(B)** and then cells were washed twice with pre-warmed PBS, pH 7.4. Samples were fixed in 3% Paraformaldehyde solution in PBS for 10min at room temperature followed by two or more washes with PBS. Staining solution (2%BSA + 0.2% Triton X-100 in PBS) and monoclonal anti-α-tubulin (1/500 dilution) was added to the cells overnight at 4˚C. After two or more washes with PBS the cells on the coverslips were incubated with staining solution (2%BSA + 0.2% Triton X-100 in PBS) and anti-mouse Alexa 633 (1/1000 dilution) for 1h at room temperature and then transferred onto glass slides with DAPI gel added at room temperature and left overnight before confocal microscopy. Image viewing using Olympus FV1000 confocal microscopy with a 60x oil immersion lens and analysed using the Imaris 3D software analyser (Bitplane). Image analysis was performed using FluoView Version 7.1 Software. DAPI was excited by a 405 laser, emission 461nm and anti-mouse Alexa 633 was excited by a 633nm laser, emission 647nm . Results are representative of three independent experiments.

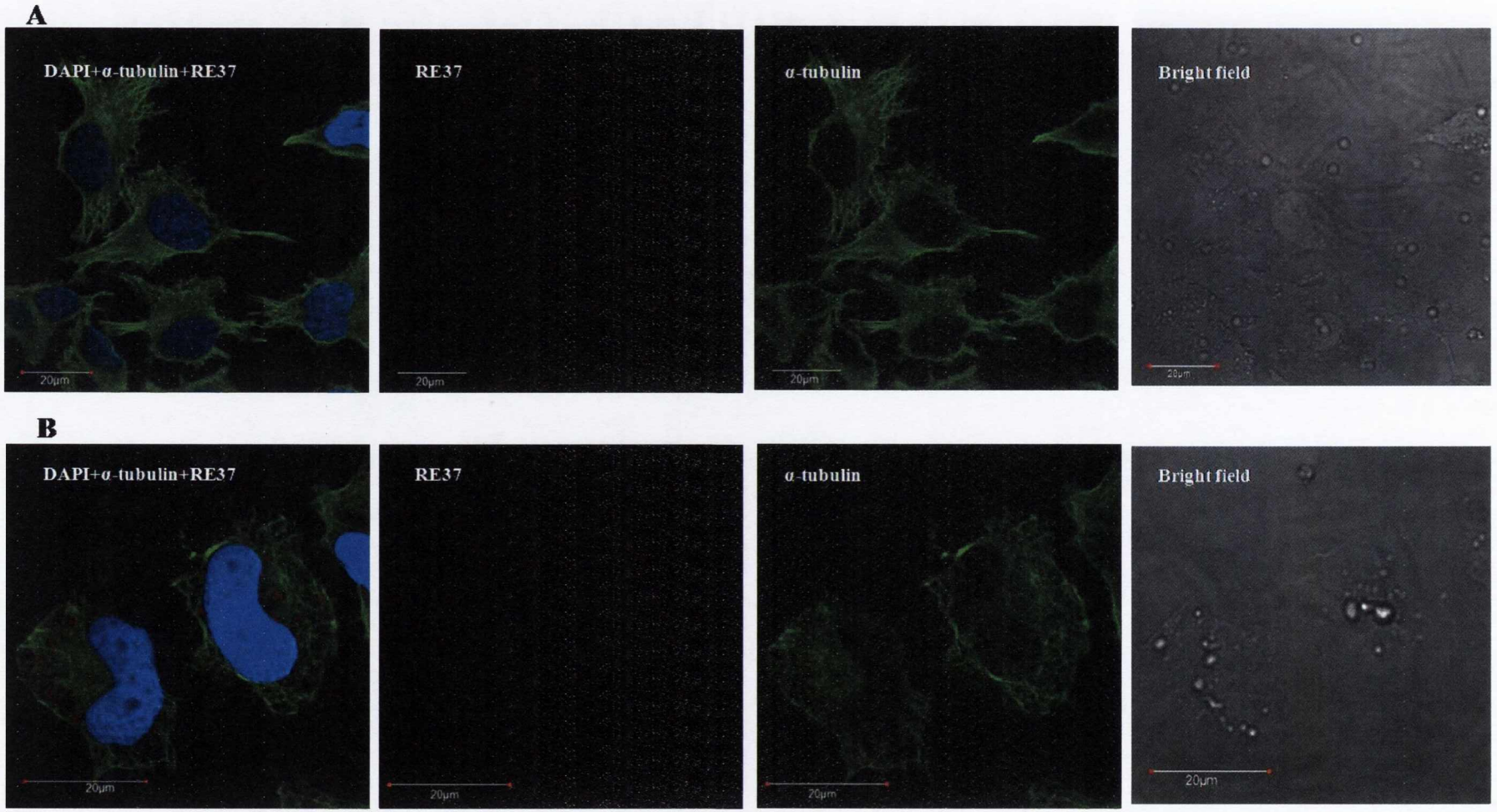
A
DAPI+α-tubulin+RE37
RE37
α-tubulin
Bright field
20μm
B
DAPI+α-tubulin+RE37
RE37
α-tubulin
Bright field
20μm

Figure 3.45: **Effect of RE37 on α-tubulin in HeLa cells.**

$3x10^5$ cell/well were seeded on coverslips and placed inside a 6-well plate. Cells were incubated at 37°C overnight before treatment with 100μM of RE37 and incubated for 24h. Following 24h incubation the treated cells were maintained in the dark **(A)** or exposed to light for 1h to give light doses of 12.66J/cm^2 **(B).** Following a further 23h of incubation cells were washed twice with pre-warmed PBS, pH 7.4. Samples were fixed in 3% Paraformaldehyde solution in PBS for 10min at room temperature followed by two or more washes with PBS. Staining solution (2%BSA + 0.2% Triton X-100 in PBS) + Monoclonal Anti-α-tubulin (1/500 dilution) was added to the cells overnight at 4°C. After two or more washes with PBS the cells on the coverslips were incubated with staining solution (2%BSA + 0.2% Triton X-100 in PBS) + Anti-Mouse Alexa 633 (1/1000 dilution) for 1h at room temperature and then transferred onto glass slides with DAPI gel added at room temperature and left overnight before confocal microscopy. Image viewing using Olympus FV1000 confocal microscopy with a 60x oil immersion lens and analysed using the Imaris 3D software analyser (Bitplane). Image analysis was performed using FluoView Version 7.1 Software. RE37 was excited by a 488nm argon laser, emission 612nm and DAPI was excited by a 405 laser, emission 461nm and Anti-Mouse Alexa 633 was excited by a 633nm laser, emission 647nm . Results are representative of three independent experiments.

A

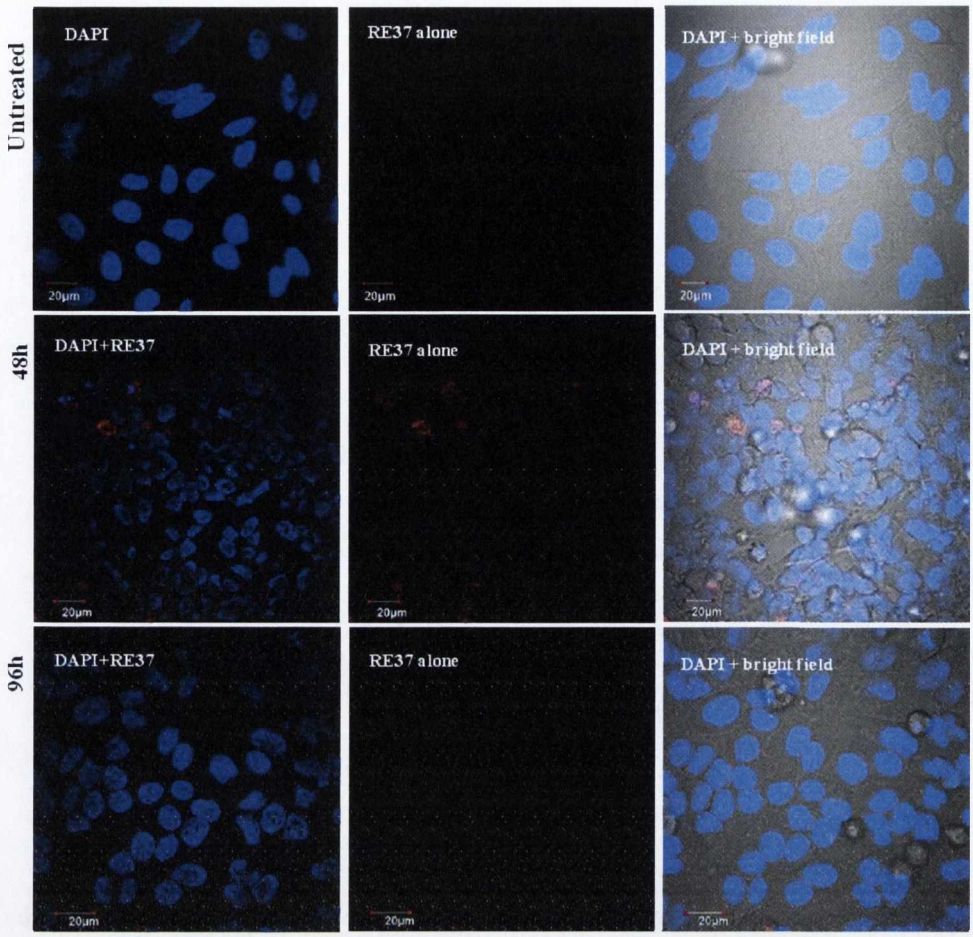
Untreated
DAPI
RE37 alone
DAPI + bright field
48h
DAPI+RE37
RE37 alone
DAPI + bright field
96h
DAPI+RE37
RE37 alone
DAPI + bright field
20µm

B

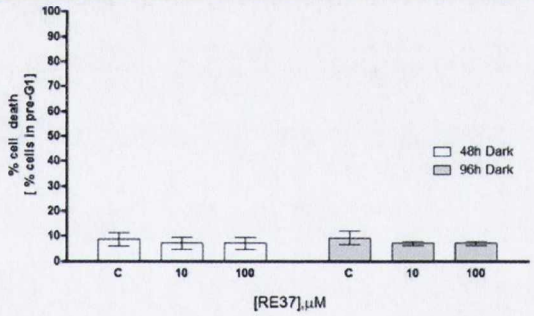
% cell death
[% cells in pre-G1]
48h Dark
96h Dark
C
10
100
C
10
100
[RE37],µM

Figure 3.46: **RE37 is not toxic in HeLa cells in the dark at either 48 or 96h.**

Confocal microscopy (A) . $1x10^5$ cells/well were seeded in dish plates (Ø 22mm; 2ml total volume/well). Cells were incubated at 37°C overnight before treatment. The cells were then treated with 10μM of RE37 for 24h, washed with PBS and resuspended in fresh media and incubated for a total of 48 and 96h. Cells were washed twice in PBS followed by the addition of fresh media and DAPI, followed by viewing using Olympus FV1000 confocal microscopy with a 60x oil immersion lens. Image analysis was performed using FluoView Version 7.1 Software. RE37 was excited by a 488nm argon laser, emission 620nm and DAPI was excited by a 405 laser, emission 461nm.
Flow cytometric (B). $0.25x10^6$ cells were seeded in T25 flasks (5ml total volume/well). Cells were incubated at 37°C overnight before treatment. The cells were treated with 10 and 100μM of RE37 for 24h. Cells were then washed twice in PBS followed by resuspension in warm fresh media. Cells were incubated for further 48 and 96h followed by fixation and FACS analysis using CELLQUEST software package. Results are representative of three independent experiments.

Discussion

The aim of this Chapter was to investigate whether the cationic derivative of pdppz (RE33) and the Ru(II) compounds with novel extended aromatic polypyridyl ligands (RE30, 34 and 37) could be taken up by cells, which would be a useful property for imaging, and whether they could induce light dependent cell death, a useful property for PDT. All the compounds tested were shown by confocal microscopy to rapidly enter the chosen cell lines (HeLa and CRL).

Various experiments were performed to characterise the uptake. Most of these experiments were performed in HeLa cells due to the more interesting localisation of the compound over 24h. It is also the case that HeLa cells have been the cell line of choice for many cell biology experiments on extracellular localisation, organelle trafficking, mitophagy, etc. suggesting HeLa cells to be a good model for our studies.

RE37 appeared in HeLa cells firstly in discrete 'packets' in the cytoplasm (4h); after 8h, a peri-nuclear localisation was observed. At a longer time point (24h) a peri-nuclear clustering of the compound, with the nucleus appearing distorted showing a 'bean-shape', was observed. On the other hand, RE37 in the CRL cell line, appeared visible throughout the cytoplasm of the cells at all time points.

The uptake profiles of HeLa cells treated with RE37 are consistent with an initial transport of Ru(II) compounds across the plasma membrane, followed by uptake into a cytoplasmic organelle, which then transports the compound to a new peri-nuclear localisation with the nucleus appearing distorted, Quantitative analysis of the uptake was performed to avoid any subjective misrepresentation of these effects (figure 3.29A).

For RE30 and 34, after 8h uptake, a discrete 'red spot' could be observed near the nucleus in cells, and at further uptake time points (24h), a clustering of the compounds to a peri-nuclear location was observed. In the case of shorter time points, discrete packets of luminescence were not observed in cytoplasm which may be due to a non-polar molecular environment. Moreover, it was observed that RE34 is more visible in cells than RE30.

RE33 appeared to enter HeLa cells at 4h and after 8h, a peri-nuclear localisation of RE33 could be observed to the distorted nucleus. At a longer uptake time point (24h), a peri-nuclear clustering of RE33 to the bean-shaped nucleus was observed.

Uptake experiments were also quantified by flow cytometry measuring the compound fluorescence in cells over time and results showed that RE33 and 37 increases in

fluorescence in the cells in a time-dependent manner. However, RE33 appeared to reach a plateau at 24h. Moreover, RE37 showed greater fluorescence then RE33. The increase in fluorescence is dependent on being in an appropriate molecular environment. In fact, it is possible that the compounds are in the cells but are dark and the precise location and indeed the range of uptake is not really known.

Various cell organelles could be postulated as targets for PDT therapy with different photosensitizers. Among them, plasma membranes, nuclei, mitochondria, golgi apparatus, lysosomes and cytoskeletal structures are susceptible to the photo-induced oxidative process [112].

Co-localisation using confocal microscopy and organelle markers for mitochondria, lysosomes and ER combined with the natural luminescence of RE37 was performed by Suzanne Cloonan who showed apparent co-localisation of RE37 with mitochondria and/or lysosomes (figures 3.47). Further experiments using transmission electron microscopy (T. E. M.) performed by Suzanne Cloonan showed a peri-nuclear clustering of mitochondria loaded with electron dense compound (figure 3.48).

These results suggested that RE37 (and possibly RE33, 30 and 34) were clearly taken up by mitochondria followed by peri-nuclear cluustering. This would not be surprising as the compounds are organic bases and therefore could enter mitochondria driven by the MMP. The effects of the compounds in mitochondria in part were determined using a JC1 assay and, results showed both RE37 and 34 to reduce the MMP without any recovery. It was shown that RE37 and RE34 decreased the MMP. Using an alternative assay ([^{3}H]TPMP ([^{3}H]triphenylmethylphosphonium) performed by Suzanne Cloonan and Sandra Bright (figure 3.49B)) a different result was observed for compound RE37 where the MMP appeared to recover after 4h incubation.

Overall, these results are constant with the peri-nuclear clustering of Ru(II) loaded mitochondria being due to a process similar, if not identical, to MMP depolarisation-induced mitophagy, a phenomena described by Sujeong Kim *et al.*[113], where gross insult of the mitochondria, results in peri-nuclear clustering as part of the mitophagic process. Cancer-derived cell lines, which show such an effect, are able to survive for a period of days without substantial mito-derived oxidative phosphorylation [113]. It is interesting that the Ru(II) loaded mitochondria seem to cluster to a peri-nuclear location to the distorted nucleus after 24h incubation.

It is hypothesised that this observation is consistent with damaged mitochondria being transported via microtubules to the microtubule organisation (MTOC) centre beside the nucleus. It may be that the mitochondria clustering results from physical forces between the MTOC, rough ER (RER) and nuclear membranes. Further studies may provide further evidence for these phenomena.

Initial microtubule disruption experiments performed by Suzanne Cloonan showed that intracellular transport of RE37 to the nuclear region was not dependent on the microtubule network with the microtubule inhibitors colchicine and nocodazole having no effect on nuclear edge localisation but accumulation in the cytoplasm was significantly reduced in the presence of these inhibitors (figure 3.50B).

Considering that PDT has a strong effect on cell division, probably due to microtubule damage, the effect of RE37 on the cytoskeletal structures was investigated with and without illumination demonstrating that RE37 uptake had no effects on the actin cytoskeleton after light treatment (figures 3.41 to 3.43) but a disruption of the tubulin filaments was observed after light treatment. In previous studies an alteration in the structure of the actin filament network after PDT in the presence of the fluorescent rhodamine phalloidin was shown [112].

Initially, it was thought that the phenomenon of the bean-shaped nucleus was a swollen nuclear envelope where the condensed nuclear material become separated from the nuclear membrane leading to the distorted shape as demonstrated in ultrastructural studies to the cell biology of Trypanosomatids (parasitic protozoans), which showed morphological alterations of parasites after different drug treatment such as mitochondria swelling with intra-mitochondrial vesicle formation, increased cytoplasmic vacuoles, and strong nuclear envelope dilatation [114]. However, TEM showed no alteration of the nuclear envelope (figure 3.48).

Further studies on cellular uptake performed by Suzanne Cloonan showed that RE37 entered HeLa cells in a temperature-dependent manner implying RE37 not to be membrane-permeable so it required active or facilitated uptake (figure 3.50A).

With the aim to investigate on the effect of these compounds with and without light treatment, cell viability studies were performed. Light dependent cell viability studies showed RE30 and 34 not to reduce cell viability in all the cell lines tested either with or without light treatment. RE33 instead reduced cell viability at high concentrations in some cell lines in a light-dependent manner showing little toxicity in the dark. RE37 showed an

ability to reduce cell viability in a light dependent manner, although the effectiveness varied with the different cell lines. The difference in potency of the compound after light exposure is likely to be correlated to the strong oxidizing excited state due to the electron accepting TAP ligand added to the Ru(II) complex, which is what differentiates RE37 from the other compounds. Moreover, cells treated with RE37 followed by light treatment showed a bigger degree of single strand DNA migration and damage compared to dark controls and compared to RE34 followed by light treatment as demonstrated by the single cell electrophoresis comet assay performed by Sandra Bright (figure 3.51). These results support previous data on DNA photocleavage of pBR322 plasmid performed by Robert B. P. Elmes demonstrating that RE37 can cleave DNA, which may be due to an indirect DNA-RE37 interaction.

Investigation of the mechanism of cell death using FACS analysis in HeLa cells treated with RE33 showed an increase in the percentage of cell death in cells with or without light treatment at high concentrations (70-100μM). However, after illumination the extent of cell death increased. RE37 induced apoptosis in a concentration and time dependent manner after light treatment. On the other hand, RE30 and 34 showed no cell death again either with or without light treatment. These experiments suggested RE37 to be more suitable for potential PDT therapy; instead RE30 and 34, which did not show any toxicity at all may be more suitable for cellular imaging.

Comparing RE33 to the Ru(II) compounds RE30, 34 and 37, these results showed RE33 to be unsuitable as a PDT agent due to the lack of difference in cell toxicity upon photoirradiation, together with toxicity in cells without light treatment if incubated at long time points.

Further investigation into the mechanism of cell death in HeLa cells showed RE37 to induce apoptosis in a caspase-dependent manner. In connection to that, investigation on the well-known target of caspase-protease, the PARP enzyme by Western blot analysis, showed no PARP cleavage in cells illuminated and non-illuminated despite that flow cytometry analysis showed a broad hypodiploid (pre-G1) peak. However, the apoptosis-positive control, Nocodazole, showed PARP cleavage. Furthermore, RE37 did not appear to involve caspase-3 in the apoptotic process which is the caspase involved in PARP cleavage. These results suggest that a different apoptotic pathway may occur probably due to the involvement of different processes in cells treated with PDT compounds such as

ROS production, which is a common response in cells treated with photosensitizers in PDT.

A different form of cell death has previously been described, called Type II programmed cell death (PCD) or autophagy , which has been observed in cancer cell lines from various tissues in response to a range of cancer therapies [115]. This form of cell death is a PARP-cleavage and caspase-independent form of cell death that occurs in cell lines that cannot die by normal apoptotic mechanism because of deficiency in Bcl2 proteins, for example Bax/Bac, or an absence of functional caspase-independent pathways, for example APAF-1. Moreover, some cell lines show diminished levels of stored intracellular calcium and display shortened rod-like mitochondria [115]. Autophagy can be caused by starvation, photogenes and toxins or during development and it is associated with the formation of large cytoplasmic autophagic vacuoles.

Considering that and the results obtained in HeLa cells treated with RE37, autophagy may be another PDT mechanism of cell death but further evidence is needed.

In relation to that, further investigation on the involvement of ROS production in apoptosis showed reduction in cell death in cells pre-treated with a ROS scavenger (Nac) and 20μM of RE37. Moreover, quantification of ROS production in HeLa cells treated with RE37 at the same concentration (20μM) resulted in a small production of intracellular ROS, statistical analysis of the data (t-test) showed that the difference in ROS production between light treated and untreated sample is not significant. However,in cells pre-treated with Nac and analysed by FACS, results showed that light dependent cell death was reduced from 75% to 36%. However, These results suggest that ROS production is not completely responsible for cell death but, contributed to it and the involvement of ROS, which are formed mostly in mitochondria, again confirmed the involvement of RE37 with this organelle.

The ability of a photosensitiser to enter a cell and not be toxic without light treatment is essential for any effective PDT agent. In this study we examined the effects of RE37 on HeLa cells non-illuminated over a 48-96h time frame using PI FACS analysis and confocal microscopy. Confocal microscopy demonstrated that after 48 and 96h, RE37 is not toxic to the cells kept in the dark (figure 3.46A). PI FACS analysis also showed that RE37 had no obvious apoptotic effect after 48h (figure3.46B). These results suggested that RE37 is tolerated by the cells when not illuminated.

In summary, RE33 appears not to be suitable as either a PDT agent or molecular probe due to the lack of difference in cell toxicity upon photoirradiation, the toxicity in cells without light treatment if incubated at long time points and due to the lack of intense luminescence within the cells. In contrast however, the ability of RE37 to induce cell death in a light dependent manner and to not be toxic in non-illuminated cells makes RE37 a good candidate in PDT. On the other hand, compounds RE30 and 34 present essential properties for fluorescence imaging application because they are non-toxic to the cells with no-phototoxicity. It is very important to keep in mind that the increase in fluorescence for this class of compounds is dependent on being in an appropriate molecular environment.

A

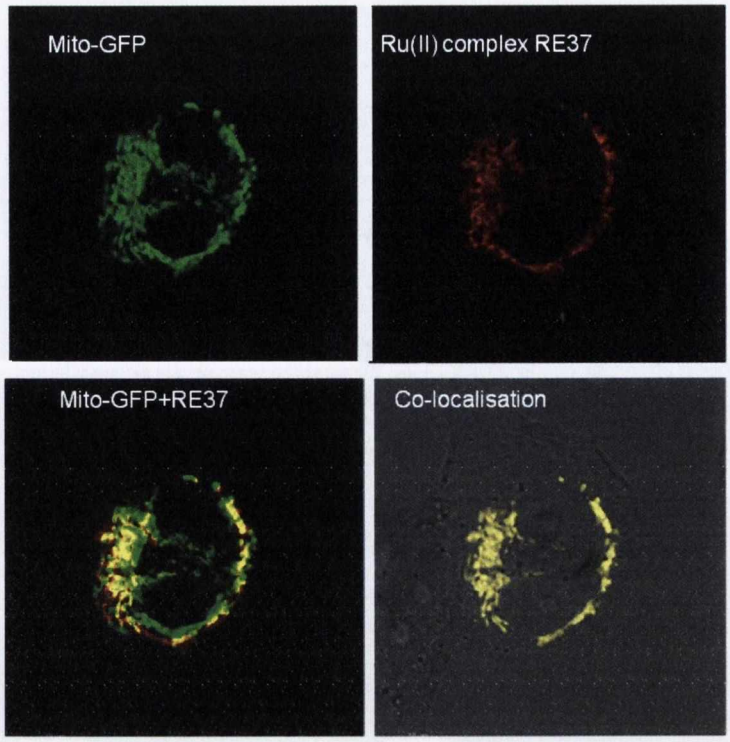
Mito-GFP
Ru(II) complex RE37
Mito-GFP+RE37
Co-localisation

B

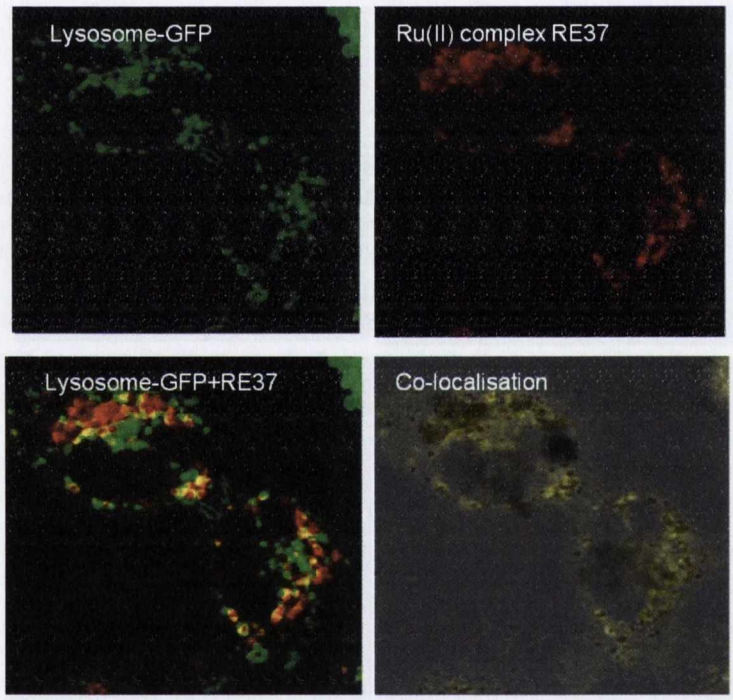
Lysosome-GFP
Ru(II) complex RE37
Lysosome-GFP+RE37
Co-localisation

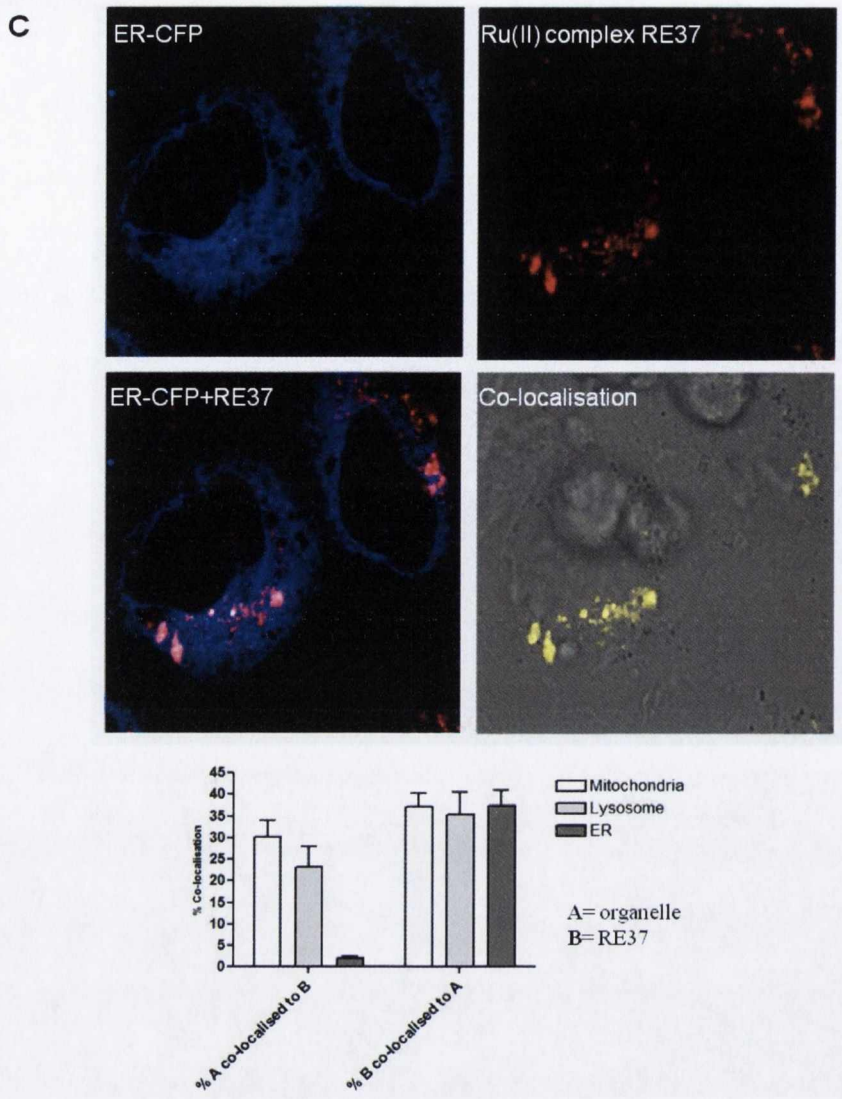

Figure 3.47: **Sub-cellular location of RE37.**

$0.3x10^5$ HeLa cells were seeded in dish plates (Ø 22mm; 2ml total volume/well), left for 24h, and transfected with an excitable (405nm)-GFP mitochondrial/lysosomal or CFP-tagged ER marker. After 24h, cells were treated with 5 (100μM) for 16h, washed twice with fresh media and analysed by live confocal microscopy using a Olympus FV1000 point scanning microscope with a 60x oil immersion lens with an NA (numerical aperture) of 1.42. The software used to collect images is FluoView Version 7.1 software. The sample was first excited with a 488nm laser diode and the emission of drug was monitored and captured at 600-700nm. The sample was then excited with a 405 nm laser diode (GFP) or a Green Helium-Neon laser (CFP) and the emission of the excitable marker was monitored and captured at 495-550nm (GFP) or 470-500nm (CFP). Both images were then overlaid and analysed using the Imaris 3D software analyser (Bitplane). Assessment of co-localisation of RE37 with, mitochondria **(A)**, endoplasmic reticulum **(B),** lysosomes **(C)** and of co-localisation of RE37 with, mitochondria, endoplasmic reticulum and lysosomes **(D)** (where A is the named organelle and B is RE37). Results are representative of three independent experiments. Suzanne Cloonan performed these experiments. The percentage of overlap expressed in the graph was calculated considerating the Pearson correlation coefficient analysed by Sandra Bright.

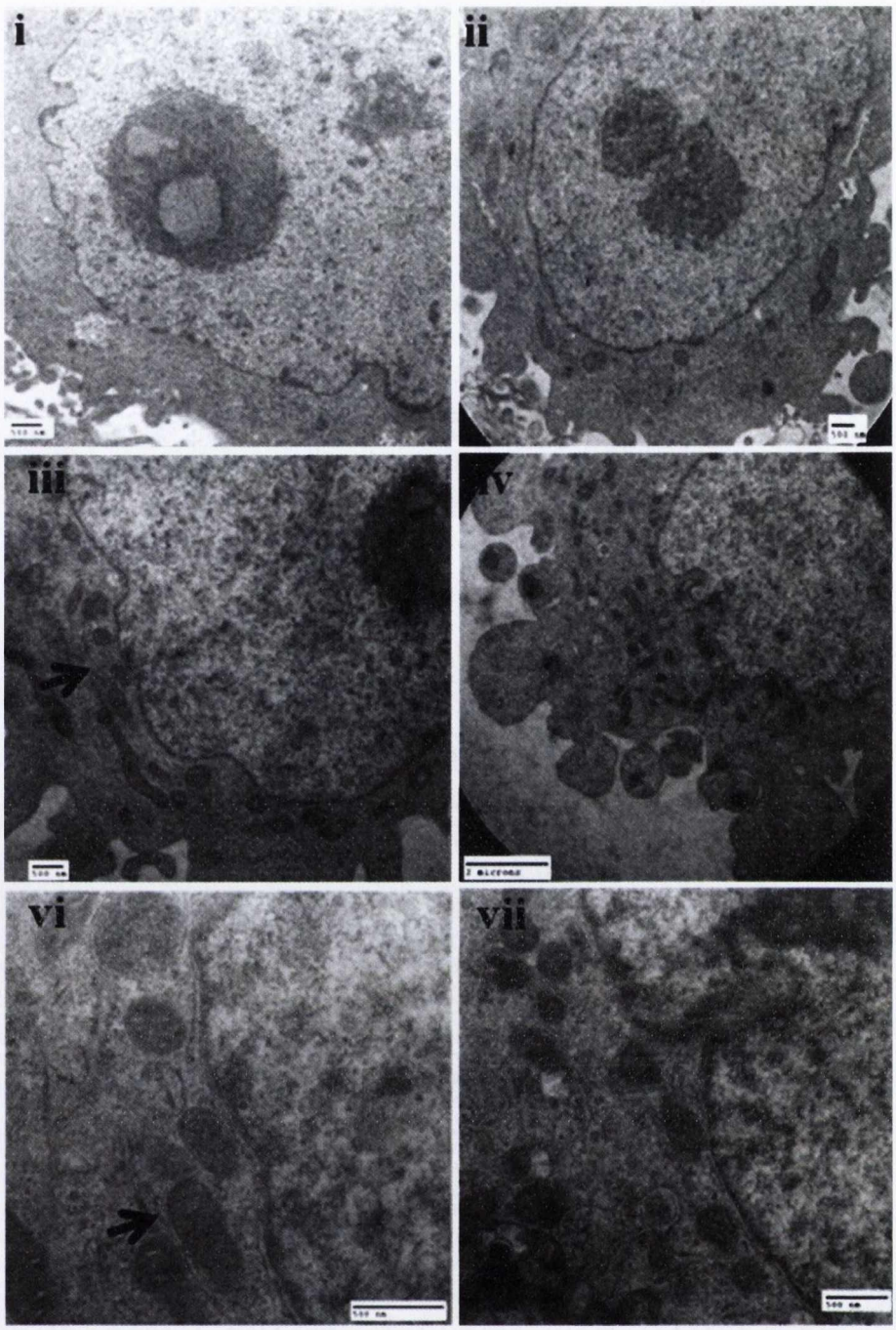

Figure 3.48: **The effect of RE37 on mitochondria.**

TEM of HeLa cells untreated **(A,i,ii)**, or treated with RE37 **(A, iii-vii)**. $1x10^6$ cells were plated in T75 flasks (10ml total volume/flask) and incubated at 37°C overnight before being treated. Cells were treated with 100μM of RE37for 24h, harvested and suspended in filtered PBS. After fixation with 16% paraformaldehyde, 25% glutaraldehyde and Hepes (pH7.5), cells were incubated at room temperature per 30min. Cells were then collected by centrifugation and washed with filtered PBS. The final pellet was resuspended in 500μl of PBS and passed on to CMA for TEM processing. Results are representative of three independent experiments. Suzanne Cloonan performed this experiment .

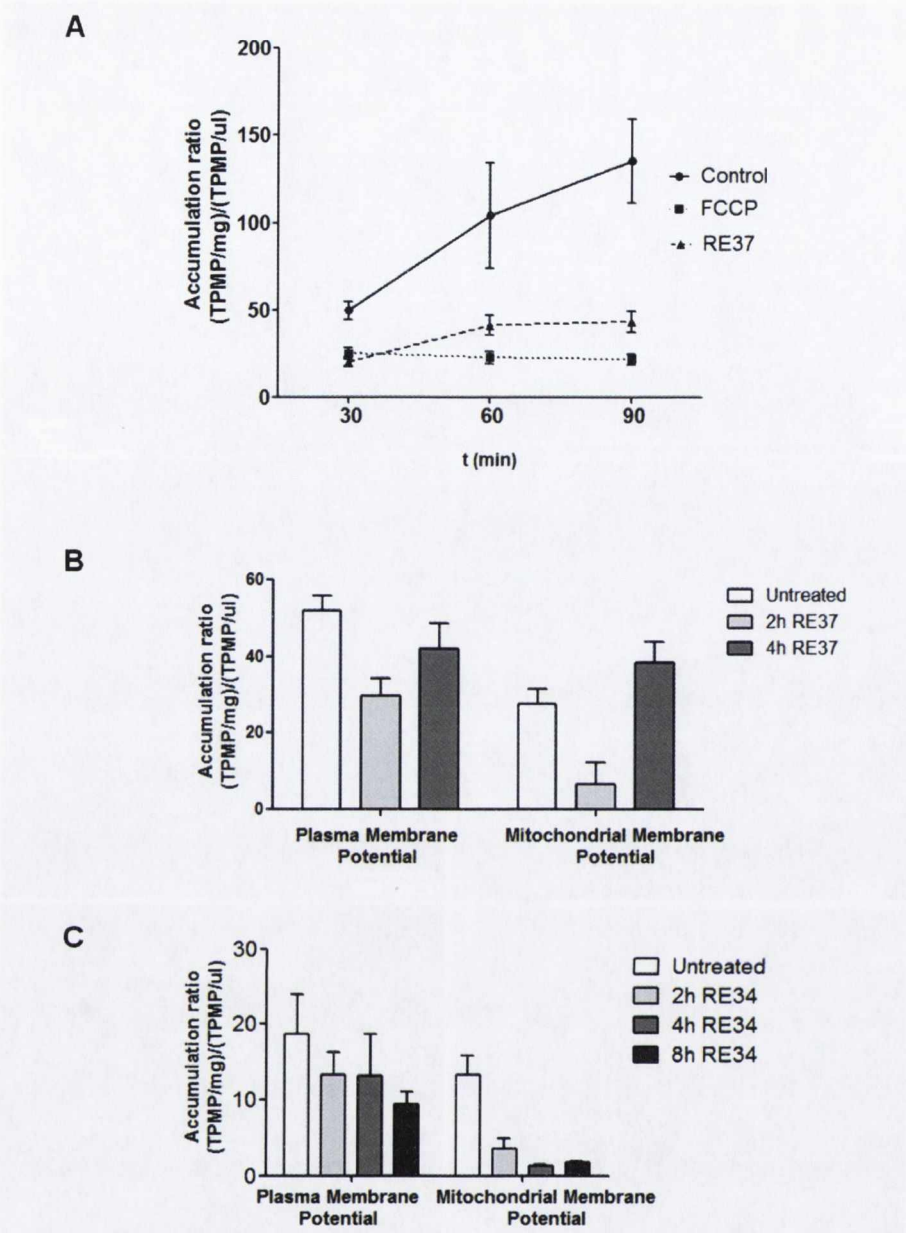

Figure 3.49: **The effect of RE37 and 34 on mitochondria.**

$1x10^7$ cells/well were seeded in T25 flasks (6ml total volume/flask). HeLa cells incubated for the required times with Ru(II) complexes followed by the addition of a final concentration of 5nM TPMP, 100nCi/ml [3H]TPMP and 5nM TPB for 90min with or without 1μM FCCP. After incubation, the cells were pelleted by centrifugation, 100μl of the supernatant was removed and the cell pellet resuspended in 100μl 20% Triton X-100. The radioactivity in the pellet and supernatant was quantitated using a liquid scintillation counter with appropriate quench corrections. Accumulation ratio = cpm/mg (pellet): cpm/μl (supernatant). Mitochondrial membrane potential = Accumulation ratio without FCCP – Accumulation ratio with FCCP. The effects of RE37 **(B, C)** and RE34 **(D)** on TPMP accumulation, a direct measure of mitochondrial membrane potential. Results are representative of three independent experiments. Suzanne Cloonan and Sandra Bright performed these experiments.

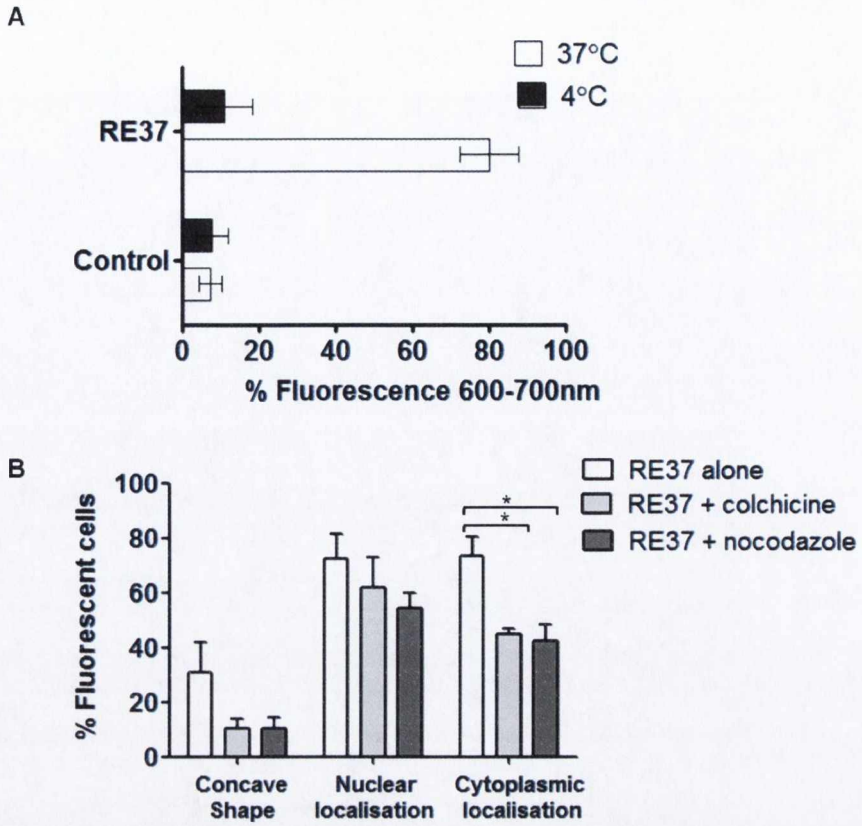

Figure 3.50: **Cellular Localisation and uptake of RE37 into HeLa cells.**

Temperature dependent uptake studies (A) $1x10^5$ cells/well were seeded in dish plates (Ø 22mm; 2ml total volume/well) and incubated at 37°C overnight. Cells were then incubated for 30min at 37°C or 4°C before being treated with 100μM of RE37 for 4h. Cells were washed twice in PBS followed by the addition of fresh media and DAPI, followed by viewing using Olympus FV1000 confocal microscopy with a 60x oil immersion lens. Image analysis was performed using FluoView Version 7.1 Software. RE37 was excited by a 488nm argon laser, emission 620nm and DAPI was exited by a 405 laser, emission 461nm. The percentage of cells with fluorescence at 600-700nm in the cytoplasm was expressed over the total amount of cells (approximately 100) per field of view.

Independent-intracellular microtubule network transport of RE37 to the nucleus. (B) $1x10^5$ cells/well were seeded in dish plates (Ø 22mm; 2ml total volume/well) and incubated at 37°C overnight. Cells were then pre-treated for 1h with 10μM of colchicine and nocodazol before being treated with 100μM of RE37 for 24h. Cells were washed twice in PBS followed by the addition of fresh media and DAPI, followed by viewing using Olympus FV1000 confocal microscopy with a 60x oil immersion lens. Image analysis was performed using Fluo View Version 7.1 Software. RE37 was excited by a 488nm argon laser, emission 620nm and DAPI was excited by a 405 laser, emission 461nm. The percentage of cells with fluorescence at 600-700nm in the cytoplasm was expressed over the total amount of cells (approximately 100) per field of view. Data was analysed with the software Prism GraphPad using a one-way ANOVA. For illustrative purposes the p values are presented as *, $p < 0.05$. Results are representative of three independent experiments. Suzanne Cloonan performed these experiments.

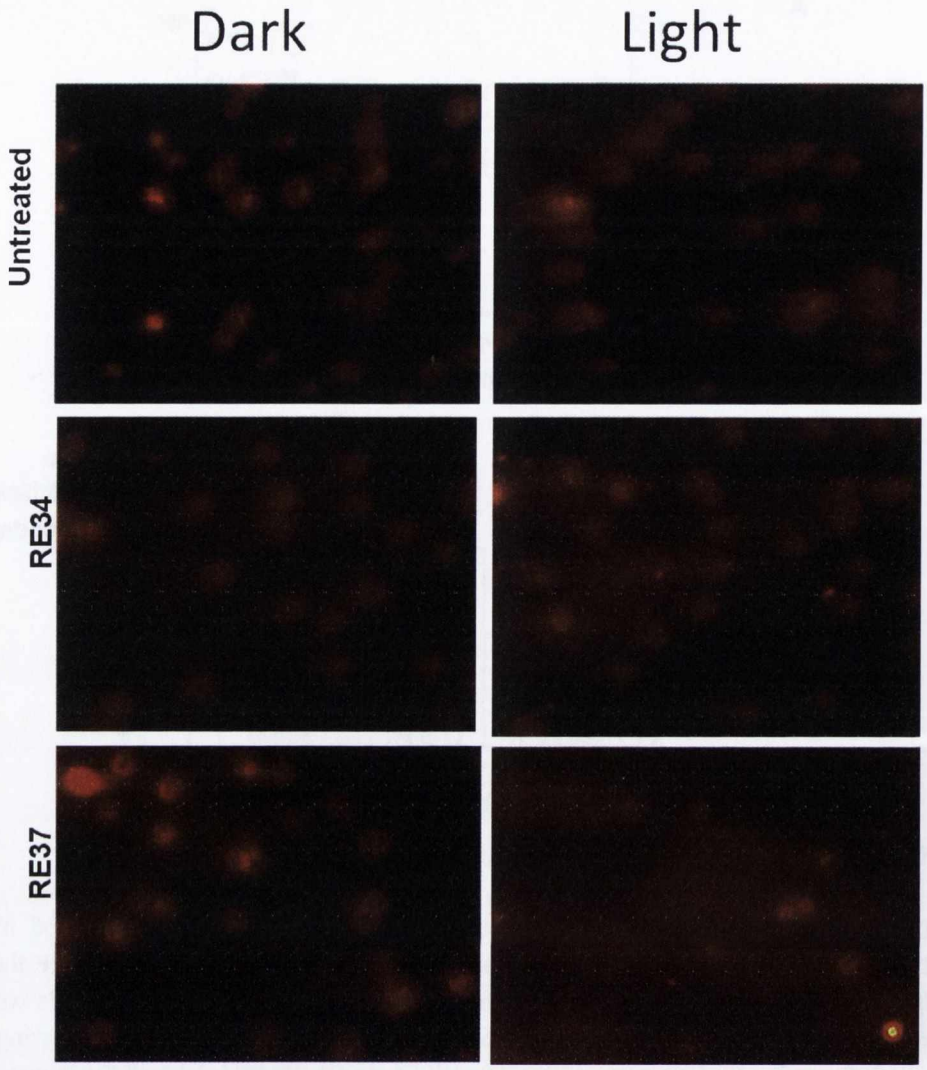

Figure 3.51: **RE37 light-induced intracellular DNA strand breakage in HeLa cells.**

$1x10^5$ cells/well were seeded in dish plates (Ø 22mm; 2ml total volume/well). Cells were treated with 20μM of RE37 for 24h + irradiation and incubated for a further 6h. Following which, cells were trypinised and resuspended in LMPA and added to slides pre-coated with NPA. Slides were then lysed (2.5M NaCl, 100mM EDTA, 10mM Tris, 1% (v/v) Triton X-100, pH 10) for 2h at -20°c and transferred to an alkaline buffer (300mM NaOH, 1mM EDTA, pH >13) for 20min to allow for unwinding of DNA and expression of alkali-labile damage. Slides were then subjected to electrophoresis at 24V, 300 mAmps for 30min. Samples were then neutralised in 0.4M Tris, pH 7.5 for 20min and stained with PI. Slides were viewed using an Olympus IX81 microscope with a 20x lens. The software Cell^P was used to collect images. Results are representative of three independent experiments. Sandra Bright performed these experiments.

Chapter 4

Investigation of 4-Amino 1,8-Naphthalimide Derived Tröger's Bases

Introduction

Continuing in the search for new Ru(II) based DNA binding motifs, Tröger's bases in combination with bimetallic Ru(II) complexes assembled by polypyridyl bridging ligands were used to synthesise compounds RE84 and 85 (figure 4.1), which have been isolated as a mixture of enantiomers.

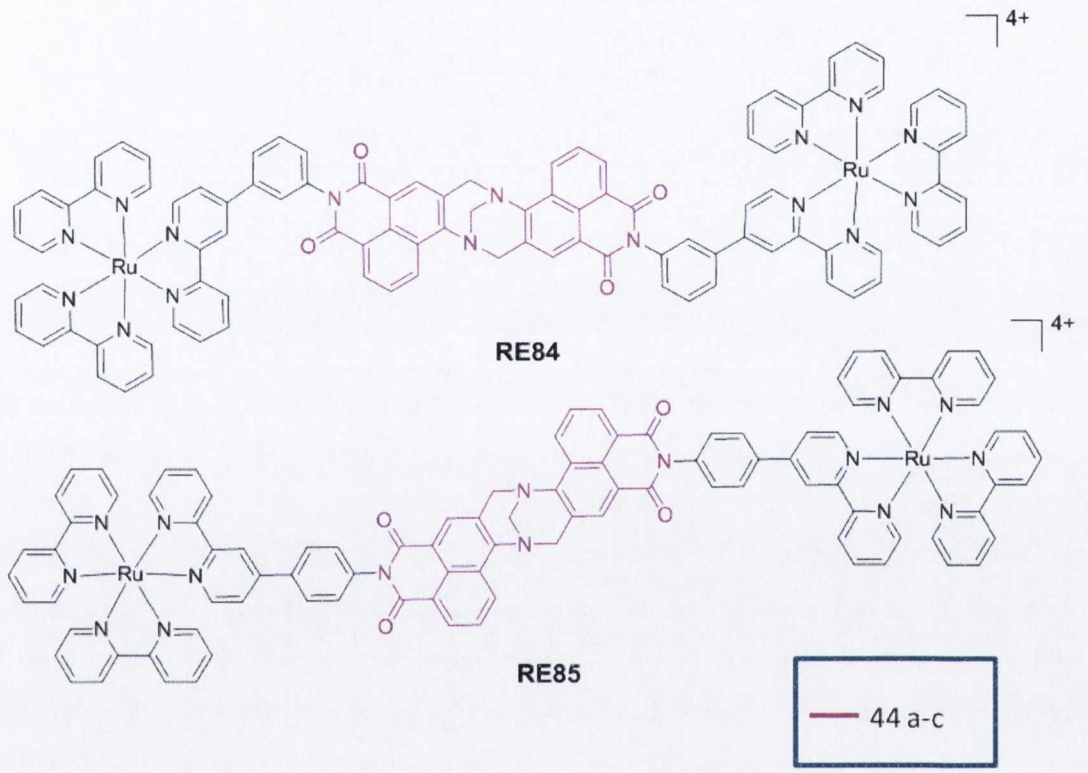

Figure 4.1: Structures of the bimetallic Ru(II)-1,8-naphthalimide containing Tröger's bases, RE84 and 85 and derivatives 44 a-c.

Previous examples in the literature include the development of a complex for DNA recognition from Yashima *et al.*[116], which reported the initial synthesis of a bis-(1, 10-phenanthroline) containing Tröger's base (figure 4.1A) and showed that a racemic mixture of this complex could interact with DNA. Moreover, it was demonstrated that the compound could cleave DNA when complexed with Cu(I) by conversion of a closed circular pUC18 plasmid to open circular DNA [116]. Another example of interest was the work of Kirsch De Mesmaekr *et al.*, who have exploited the available bipyridyl ligand binding sites of the racemic bis-(1, 10-phenanthroline) containing Tröger's base (figure 4.2A) from Yashima *et al.* by the synthesis of both mono (figure 4.2C) and bimetallic

(figure 4.2B) Ru(II) species [117, 118]. Further examples are the three stereoisomers of the Ru(II) complex bearing a chiral bis-phenanthroline Tröger's base analogue ($TBphen_2$), which have been isolated through crystallization and their interaction with DNA explored: results showed that the DNA binding affinity depends on the stereoisomer and it was seen to be mainly controlled by the absolute configuration of the metal centre of the complex as opposed to the chirality induced by the Tröger's base framework [118, 119].

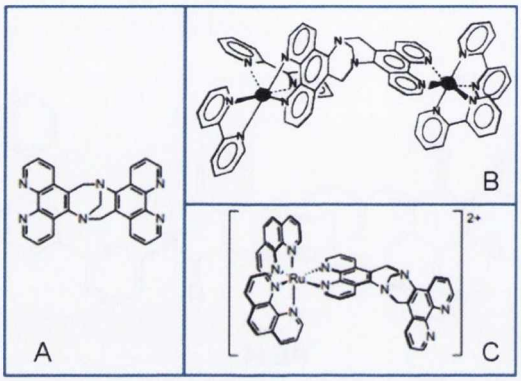

Figure 4.2: Structures of the racemic complex bis-(1, 10-phenanthroline) (A) and of both mono (C) and bimetallic (B) Ru(II) bipyridyl ligand binding sites of the racemic bis-(1, 10-phenanthroline) containing Tröger's base adapted from [116-119]

Of particular interest is the work of Veale *et al.*, in which Tröger's bases have been exploited as dual imaging-therapeutic agents where the organic derivatives bis-1,8-naphthalimide containing Tröger's base species (44 a-c) (figure 4.1) were also shown to selectively localise with the nucleus of K562 leukaemia cells [100, 120]. Moreover, derivatives 44 a-c exhibited other advantages such as the ability to bind DNA, showing concomitant changes in their ground and excited state properties. These species were also shown to induce apoptosis in K562 cells. Bimetallic Ru(II) complexes assembled by polypyridyl bridging ligands have also found numerous applications, most recently in DNA cellular imaging [99].

Considering all of the above, it was decided to modify the design of the 44 a-c to incorporate a bipyridyl portion that would allow the formation of bimetallic Ru(II)-1,8-naphthalimide compounds containing Tröger's bases, RE84 and 85. The UV/Visible absorption, excitation and emission spectra of these compounds, was determined without DNA by Robert B. P. Elmes, which have been recorded at pH 7.4 in 10mM phosphate buffer (figure 4.3) [73]. Upon binding of RE84 and 85 to stDNA the emission in aqueous

solution is initially seen to be quenched followed by a small increase (3-5%) leading to a plateau which corresponds to a situation where the compounds are fully bound to DNA [73]. The observed emission behaviour is most likely explained by a biphasic interaction upon addition of stDNA in relation to the hypochromic effect which is consistent with the existence of more than one site of binding [73]. In relation to that, a binding constant could not be determined accurately from the absorption or emission data due to the small magnitude of the changes and the observed biphasic behaviour of both RE84 and 85 [73].
DNA binding affinity revealed large stabilisation of the DNA helix upon interaction with both RE84 and 85, where RE84 was seen to be bound more strongly [73]. Furthermore, studies in the presence of varying ionic strengths suggested that, although electrostatic interactions play a role in the compounds ability to bind DNA , there are also other factors contributing to this interaction [73].
The objective of the research presented in this Chapter will be the study of cellular uptake and intra-cellular activity of the bimetallic Ru(II)-1,8-naphthalimide containing Tröger's bases, RE84 and 85, in HeLa cells.

Results

4.1 RE84 and 85 compounds reduce cell viability

HeLa cells were incubated with a range of concentrations (0.5, 0.7, 1, 1.5, 2, 3, 4, 5, 7.5, 10, 15μM) of the bimetallic Ru(II)-1,8-naphthalimide containing Tröger's bases (RE84 and 85) for 24h in the dark. Cells were then either illuminated (as described in Section 2.5 of the Materials and Methods) for 1h, or incubated for further 23h or samples were maintained in the dark. An AB cell viability assay was then performed. The results are shown in figure 4.4.
RE84 and 85 do not reduce cell viability in the dark up to a concentration of 10μM, whereas a photo-activation concentration-dependent reduction in cell viability was observed. The compounds showed IC_{50} values for photo-induced reduction in cell viability of between 1.33-4.33μM respectively.

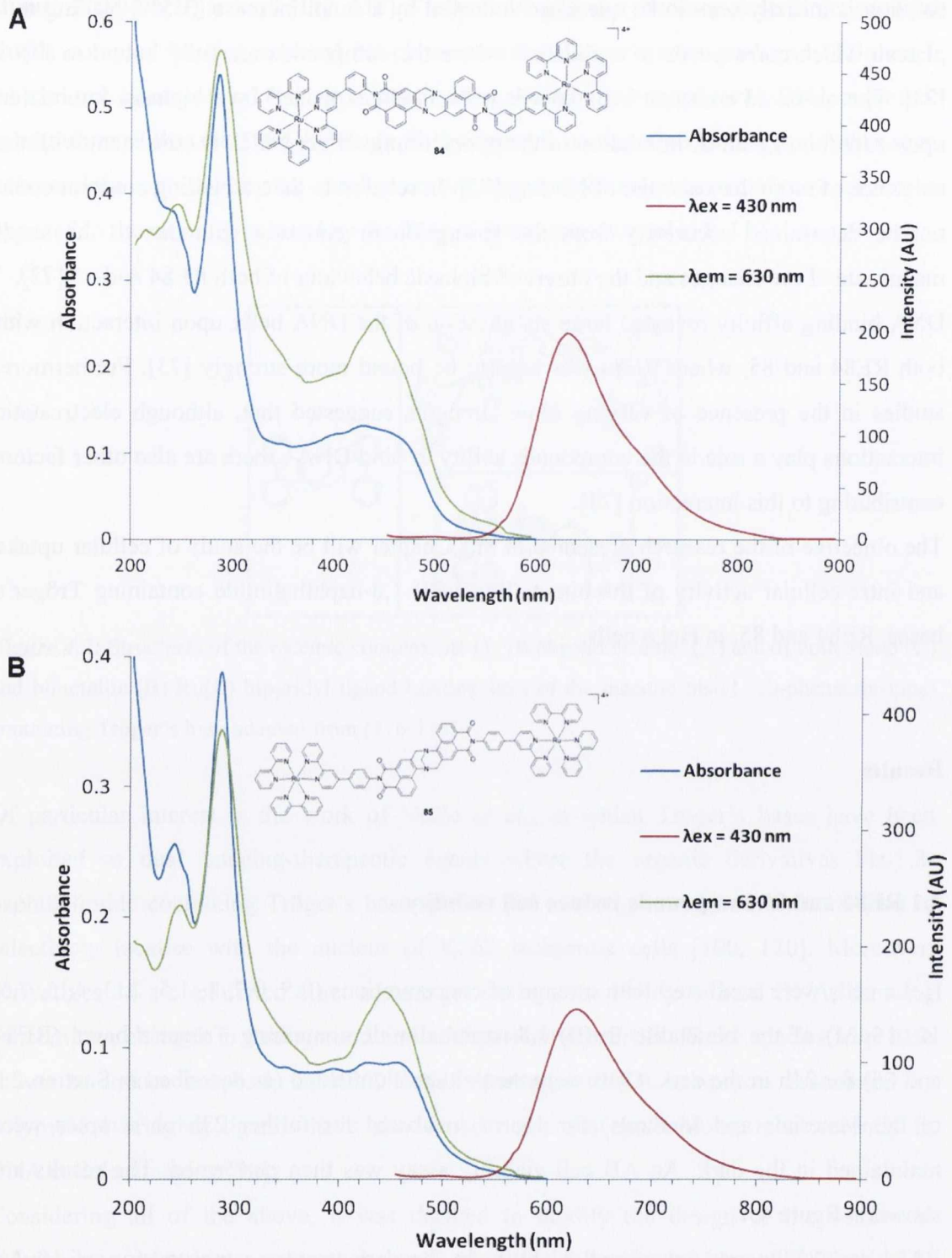

Figure 4.3: Structure and UV/Visible, excitation and emission spectra of RE84 (6.3μM) **(A)** and RE85 (10μM) **(B)** in 10mM phosphate buffer, pH7.4. Robert B.P Elmes performed these experiments.

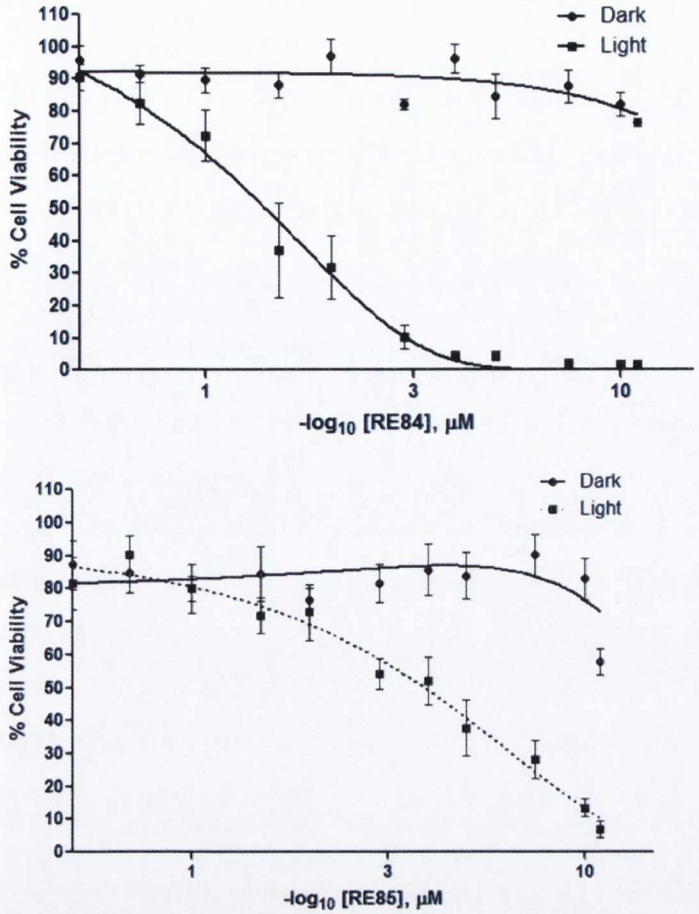

HeLa+RE84	IC_{50} (µM)
Dark	ND
Light	1.33

HeLa +RE 85	IC_{50} (µM)
Dark	ND
Light	4.23

ND= not-determinable

Figure 4.4: **The effect of RE84 and 85 on HeLa cells with or without light exposure.**

$0.5x10^4$ cells/well were seeded in 96-well plates (200 µl total volume/well). Cells were incubated at 37°C overnight before treatment. Each compound concentration (RE84 and 85 at 0.5, 0.7, 1, 1.5, 2, 3, 4, 5, 7.5, 10, 15µM) was plated in triplicate and compared to dark-treated controls. Following 24h of treatment, the treated cells were either exposed to light for 1h to give a light dose of $12.66J/cm^2$ or maintained in the dark. Following 23h of incubation an AB assay was performed by adding 20µl of AB dye per well followed by 5-6h incubation at 37°C in the dark until the colour change occurs. The background fluorescence of media without cells plus AB was taken away from each group, and the control untreated cells represented 100% cell viability. The number of viable cells is expressed as a percentage of AB reduction of at least three independent experiments. Fluorescence was measured using a microplate reader (excitation 544nm, emission 590nm). The antiproliferative potency of each compound was determined by non-linear regression (gaussian) calculating an approximate IC_{50} ([Dose] when response is equal to 50% cell viability). All data points were analysed using GRAPH PAD Prism software. ND – Not determined.

4.2 RE84 and 85 are taken up into HeLa cells

Uptake experiments were performed to determine if the compounds were taken up by the cells and to investigate any cell morphology effects of the compounds. HeLa cells were incubated with either 5 and 10μM RE84 and 85 for 2, 4, 8, 24h (figures 4.5 to 4.12).
The ideal concentration used, to observe luminescence in confocal microscopy was determined by multiple experiments using different concentrations of the compounds.
In accordance with the excitation and emission spectra of the compounds, a 488nm laser was used in order to visualise the compounds while DAPI was used as a nuclear stain.
RE84 and 85 (at either 5 or 10μM) showed uptake (2h) into HeLa cells and at all time points (2-24h), a peri-nuclear location of the compounds was observed. At the longest time point (24h), the peri-nuclear clustering of the compounds to a bean-shaped nucleus was shown. Cells incubated with 10μM RE84 and 85 under the confocal laser showed extensive membrane swelling when compared to the untreated cells. This occurs also in cells treated at 5μM if exposed to the confocal laser for too long. These results suggested that the compounds are activated quickly by the confocal laser depending on the concentration of the compounds.

4.3 RE84 and 85 show florescence in cells at short time points

HeLa cells were incubated with 5μM of RE84 and 85 and kept in the dark at different incubation times (5, 15, 30, 60, 120, 240, 480 and 1440min). Uptake in cells was quantified by flow cytometry measuring the compound fluoresence within cells and the difference in fluoresence overtime. The results are shown in figures 4.13 and 4.14.
Results showed fluorescence in cells treated with RE84 and 85 within 5min, showing an increase in fluorescence in a time-dependent manner. It was observed that the mean fluoresence of RE84 was higher than compound RE85 at the same concentration. The increase in fluorescence is dependent on being in an appropriate molecular environment.


DAPI
20µm
RE84 alone
20µm
DAPI + bright field
20µm
Untreated

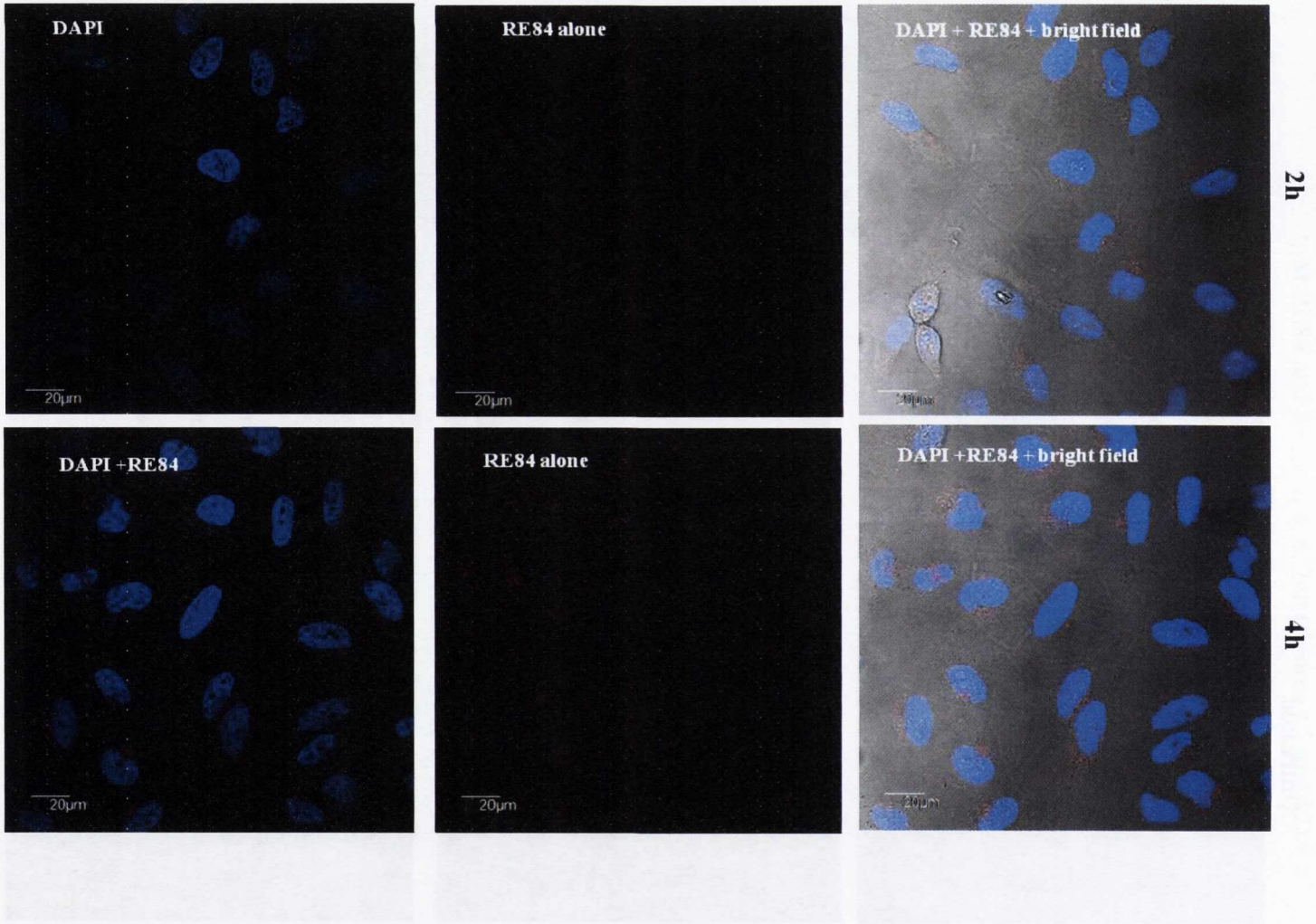
DAPI
RE84 alone
DAPI + RE84 + bright field
2h
DAPI +RE84
RE84 alone
DAPI +RE84 + bright field
4h
20µm

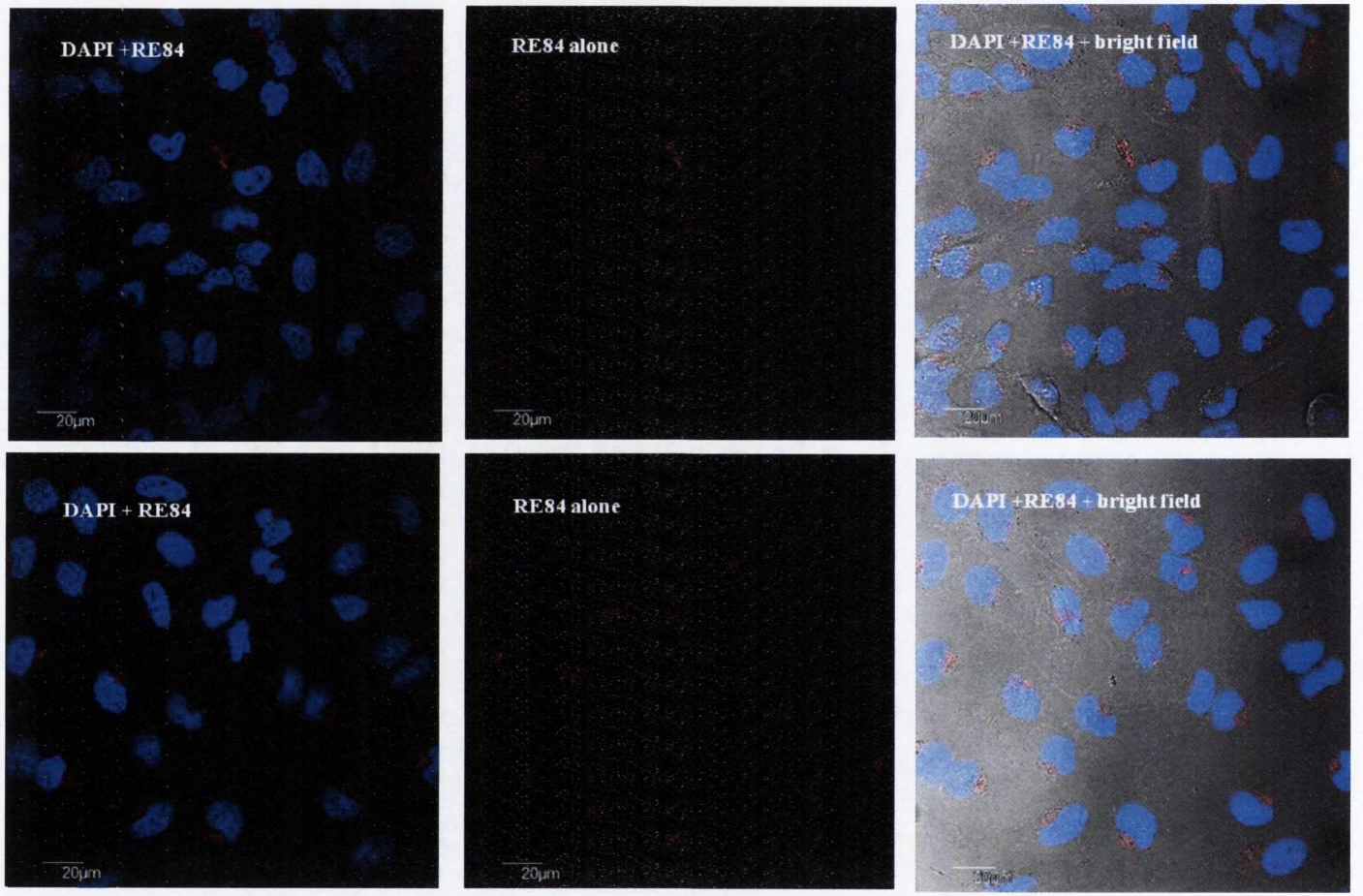
DAPI +RE84
20µm
RE84 alone
20µm
DAPI +RE84 + bright field
20µm
8h
DAPI + RE84
20µm
RE84 alone
20µm
DAPI +RE84 + bright field
24h

Figure 4.5: **Time dependent localisation of RE84 in HeLa cells.**

$1x10^5$ cells/well were seeded in dish plates (Ø 22mm; 2ml total volume/well). Cells were incubated at 37°C overnight before treatment. The cells were then treated with 5μM of RE84 and incubated for 2, 4, 8 and 24h. Cells were washed twice in PBS followed by the addition of fresh media and DAPI, followed by viewing using Olympus FV1000 confocal microscopy with a 60x oil immersion lens. The complex is localised either in the cytoplasm or to the edge of the nucleus. Image analysis was performed using FluoView Version 7.1 Software. RE84 was excited by a 488nm argon laser, emission 620nm and DAPI was excited by a 405 diode laser, emission 461nm. Results are representative of three independent experiments.

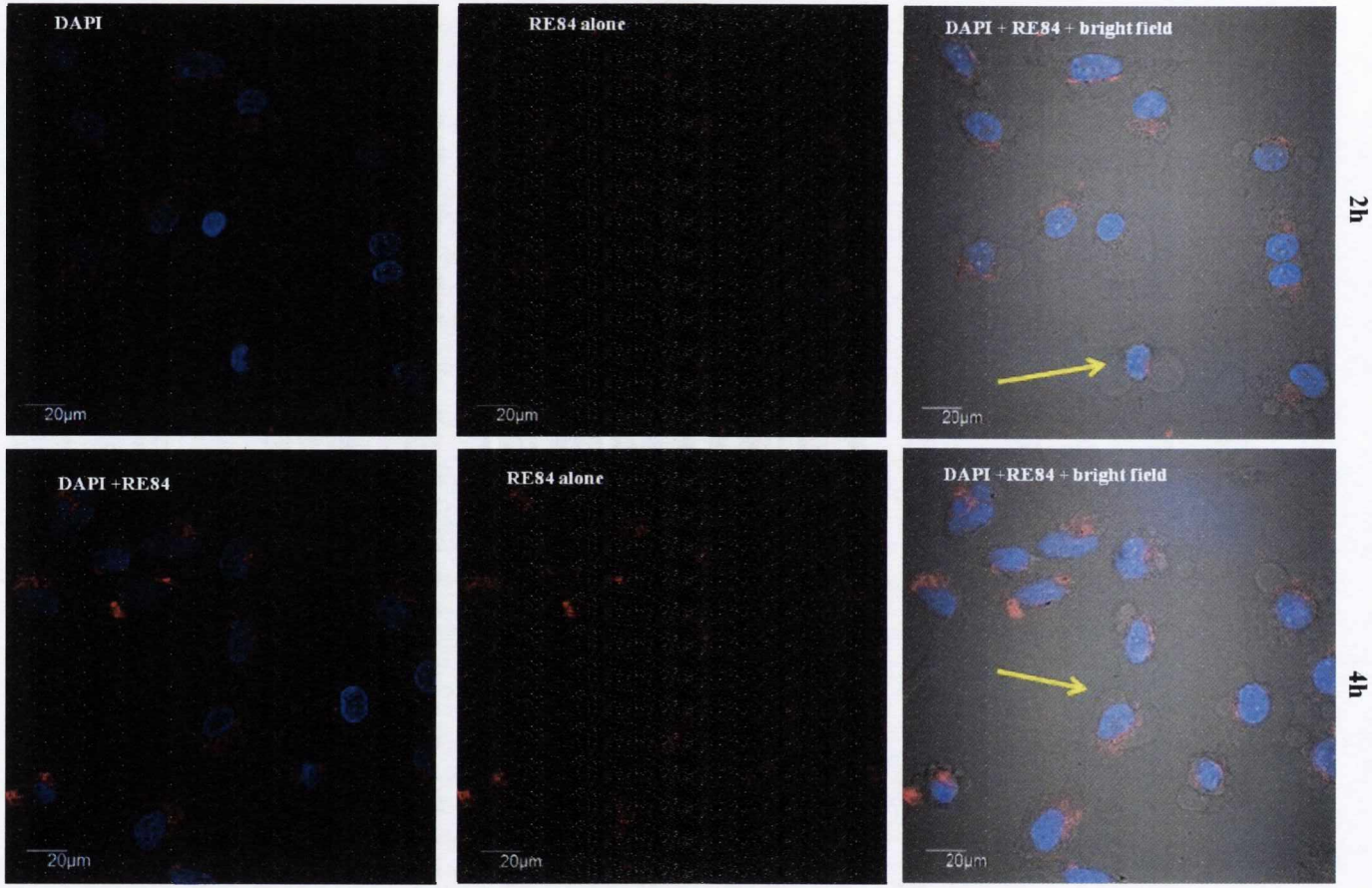
DAPI
RE84 alone
DAPI + RE84 + bright field
2h
DAPI +RE84
RE84 alone
DAPI +RE84 + bright field
4h
20µm

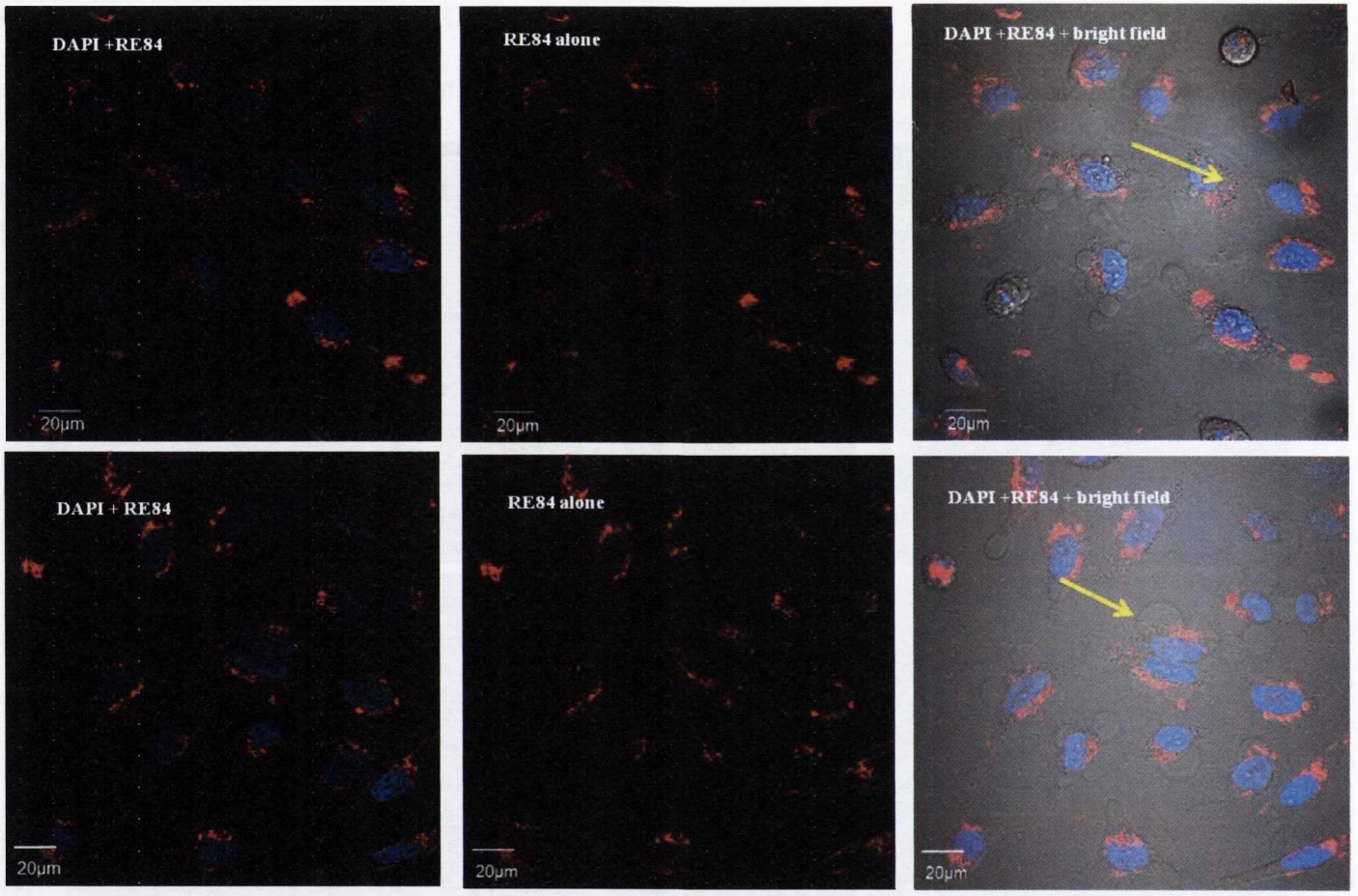
DAPI +RE84
20μm
RE84 alone
20μm
DAPI +RE84 + bright field
20μm
8h
DAPI + RE84
20μm
RE84 alone
20μm
DAPI +RE84 + bright field
20μm
24h

Figure 4.6: **Time dependent localisation of RE84 in HeLa cells.**

$1x10^5$ cells/well were seeded in dish plates (Ø 22mm; 2ml total volume/well). Cells were incubated at 37°C overnight before treatment. The cells were then treated with 10μM of RE84 and incubated for 2, 4, 8 and 24h. Cells were washed twice in PBS followed by the addition of fresh media and DAPI, followed by viewing using Olympus FV1000 confocal microscopy with a 60x oil immersion lens. The complex is localised either in the cytoplasm or to the edge of the nucleus. Image analysis was performed using FluoView Version 7.1 Software. RE84 was excited by a 488nm argon laser, emission 620nm and DAPI was excited by a 405 diode laser, emission 461nm. Results are representative of three independent experiments. The arrows in yellow indicate cell swelling.

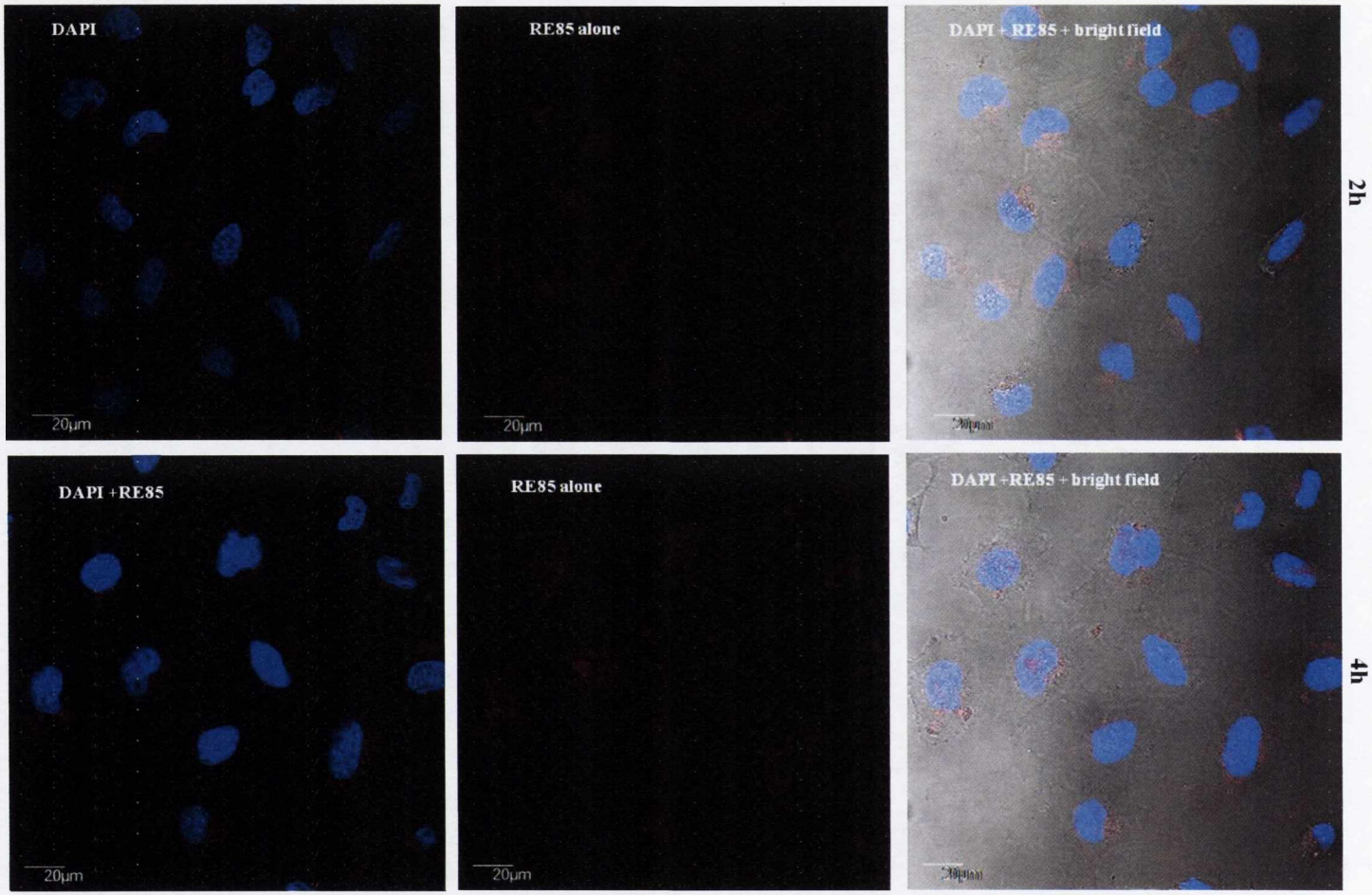
DAPI
20µm
RE85 alone
20µm
DAPI + RE85 + bright field
2h
DAPI +RE85
20µm
RE85 alone
20µm
DAPI +RE85 + bright field
4h

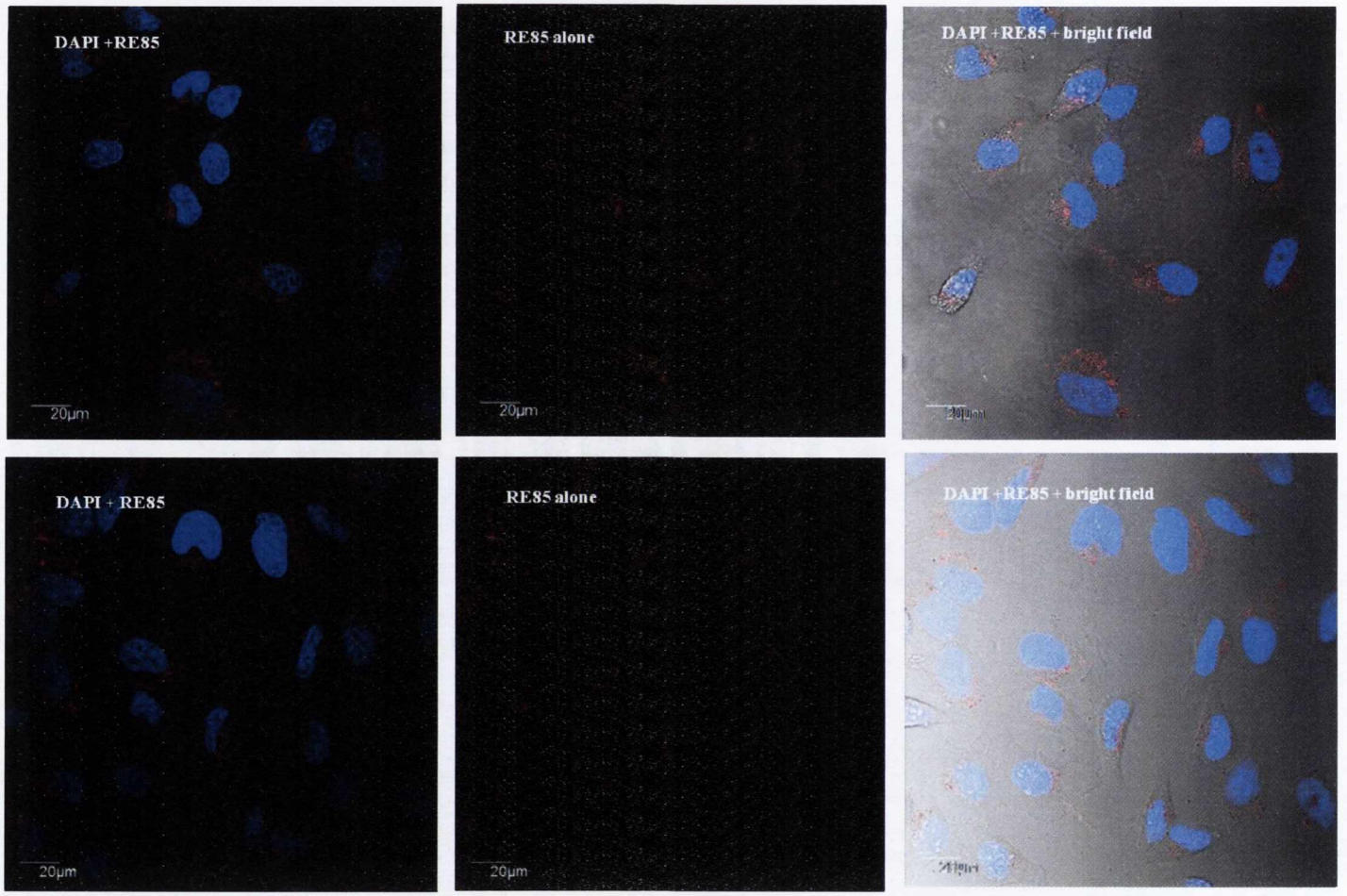
DAPI +RE85
20μm
RE85 alone
20μm
DAPI +RE85 + bright field
8h
DAPI + RE85
20μm
RE85 alone
20μm
DAPI +RE85 + bright field
24h

Figure 4.7: **Time dependent localisation of RE85 in HeLa cells.**

$1x10^5$ cells/well were seeded in dish plates (Ø 22mm; 2ml total volume/well). Cells were incubated at 37°C overnight before treatment. The cells were then treated with 5μM of RE85 and incubated for 2, 4, 8 and 24h. Cells were washed twice in PBS followed by the addition of fresh media and DAPI, followed by viewing using Olympus FV1000 confocal microscopy with a 60x oil immersion lens. The complex is localised either in the cytoplasm or to the edge of the nucleus. Image analysis was performed using FluoView Version 7.1 Software. RE85 was excited by a 488nm argon laser, emission 620nm and DAPI was excited by a 405 diode laser, emission 461nm. Results are representative of three independent experiments.

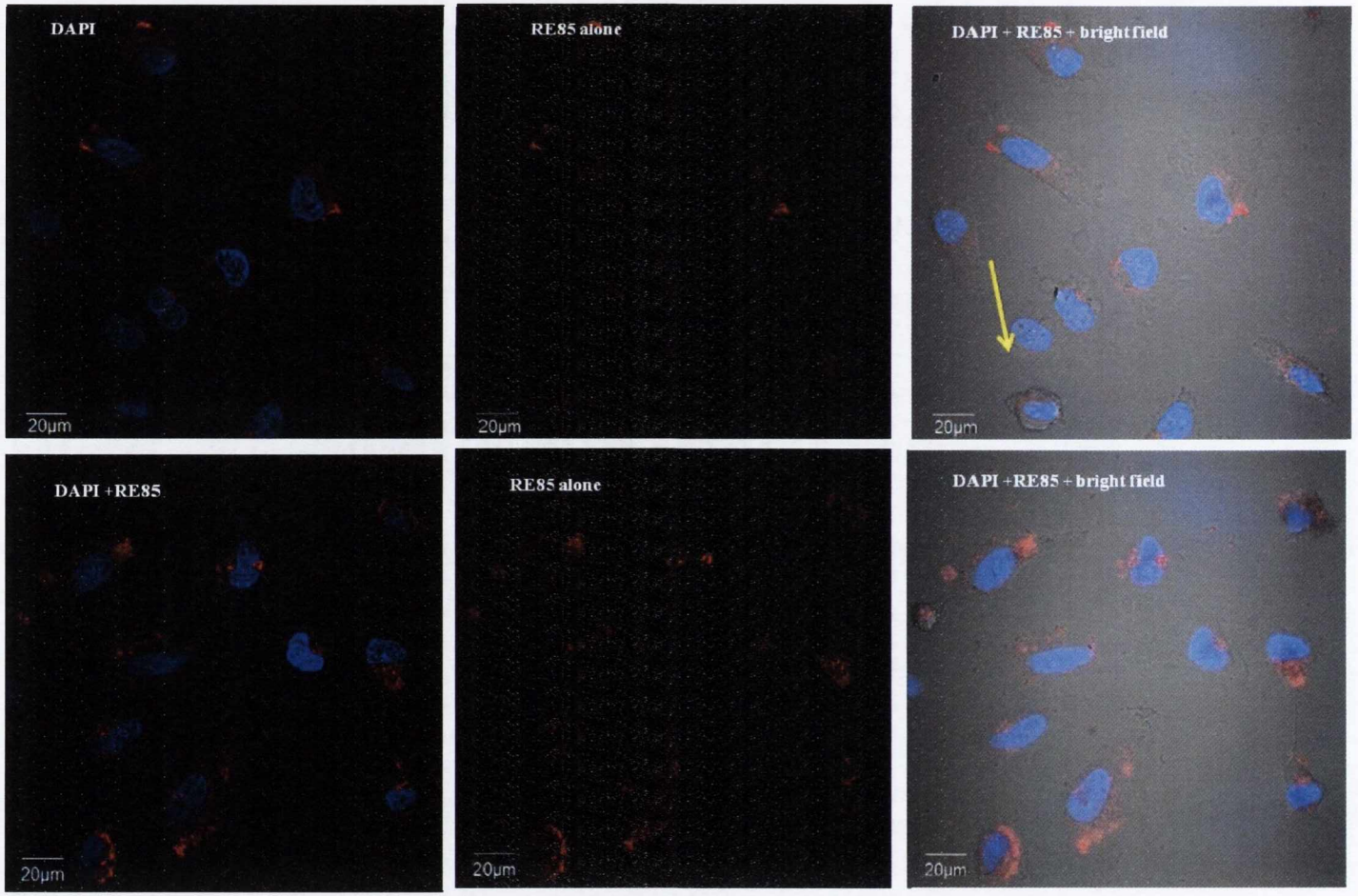
DAPI
20μm
RE85 alone
20μm
DAPI + RE85 + bright field
20μm
2h
DAPI +RE85
20μm
RE85 alone
20μm
DAPI +RE85 + bright field
20μm
4h

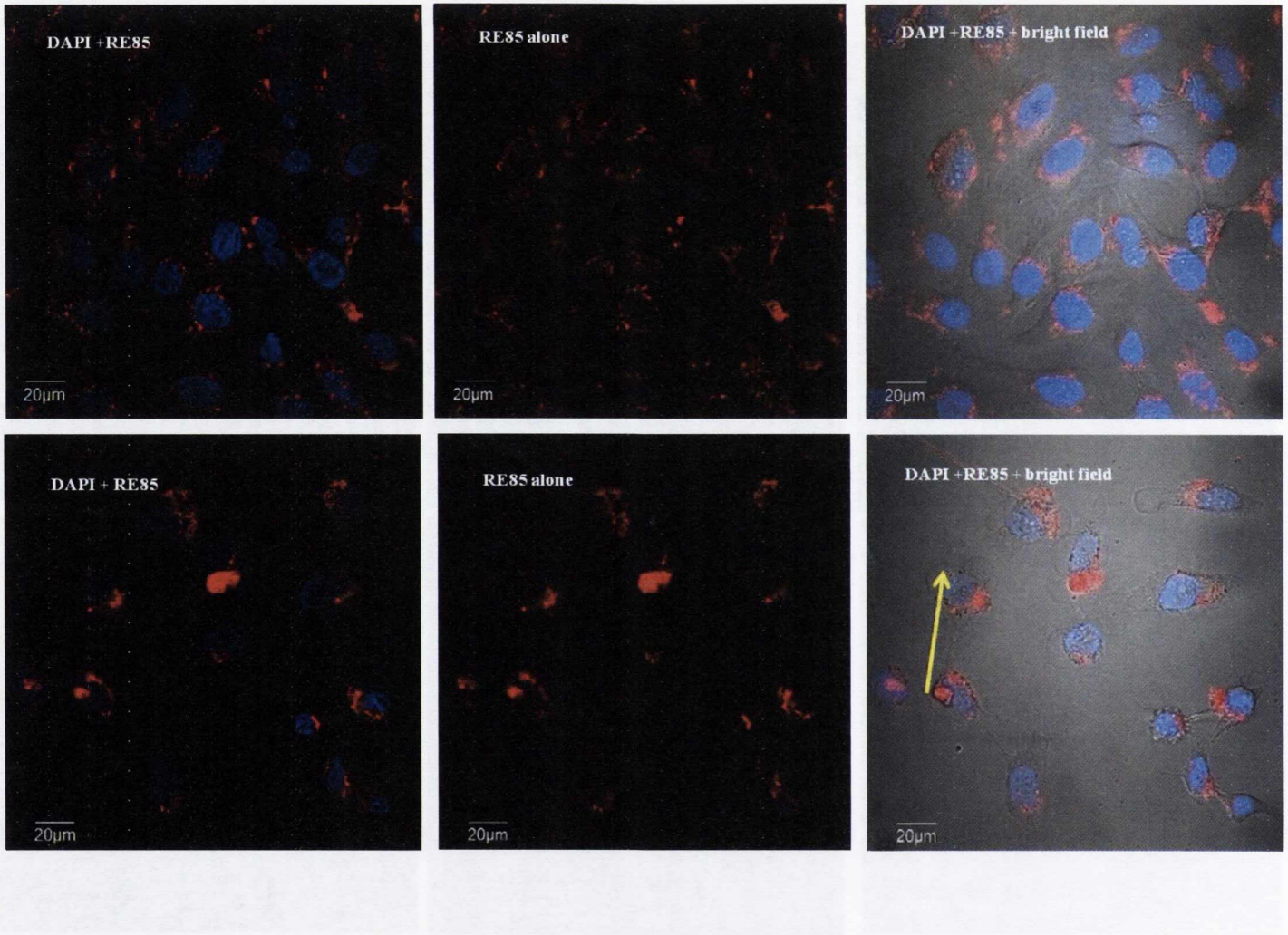
DAPI +RE85
20µm
RE85 alone
20µm
DAPI +RE85 + bright field
20µm
8h
DAPI + RE85
20µm
RE85 alone
20µm
DAPI +RE85 + bright field
20µm
24h

Figure 4.8: **Time dependent localisation of RE85 in HeLa cells.**

$1x10^5$ cells/well were seeded in dish plates (Ø 22mm; 2ml total volume/well). Cells were incubated at 37°C overnight before treatment. The cells were then treated with 10μM of RE85 and incubated for 2, 4, 8 and 24h. Cells were washed twice in PBS followed by the addition of fresh media and DAPI, followed by viewing using Olympus FV1000 confocal microscopy with a 60x oil immersion lens. The complex is localised either in the cytoplasm or to the edge of the nucleus. Image analysis was performed using FluoView Version 7.1 Software. RE85 was excited by a 488nm argon laser, emission 620nm and DAPI was excited by a 405 diode laser, emission 461nm. Results are representative of three independent experiments. The arrows in yellow indicate cell swelling.

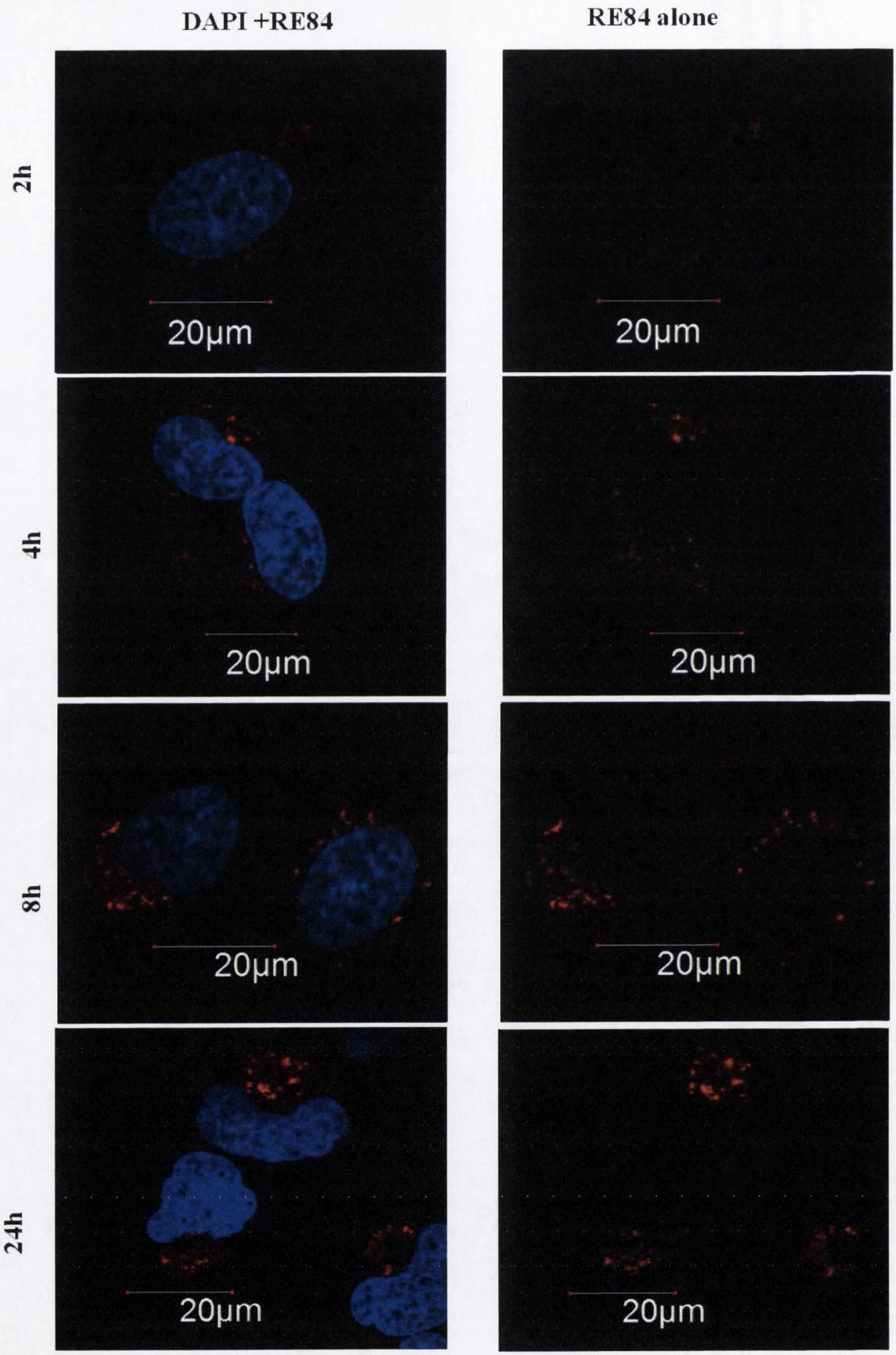
DAPI +RE84
RE84 alone
2h
4h
8h
24h
20μm
20μm
20μm
20μm
20μm
20μm
20μm
20μm

Figure 4.9: **Time dependent localisation of RE84 in HeLa cells.**

$1x10^5$ cells/well were seeded in dish plates (Ø 22mm; 2ml total volume/well). Cells were incubated at 37°C overnight before treatment. The cells were then treated with 5μM of RE84 and incubated for 2, 4, 8 and 24h. Cells were washed twice in PBS followed by the addition of fresh media and DAPI, followed by viewing using Olympus FV1000 confocal microscopy with a 60x oil immersion lens. The complex is localised either in the cytoplasm or to the peri-nuclear region. Image analysis was performed using FluoView Version 7.1 Software. RE84 was excited by a 488nm argon laser, emission 620nm and DAPI was excited by a 405 diode laser, emission 461nm. Results are representative of three independent experiments.

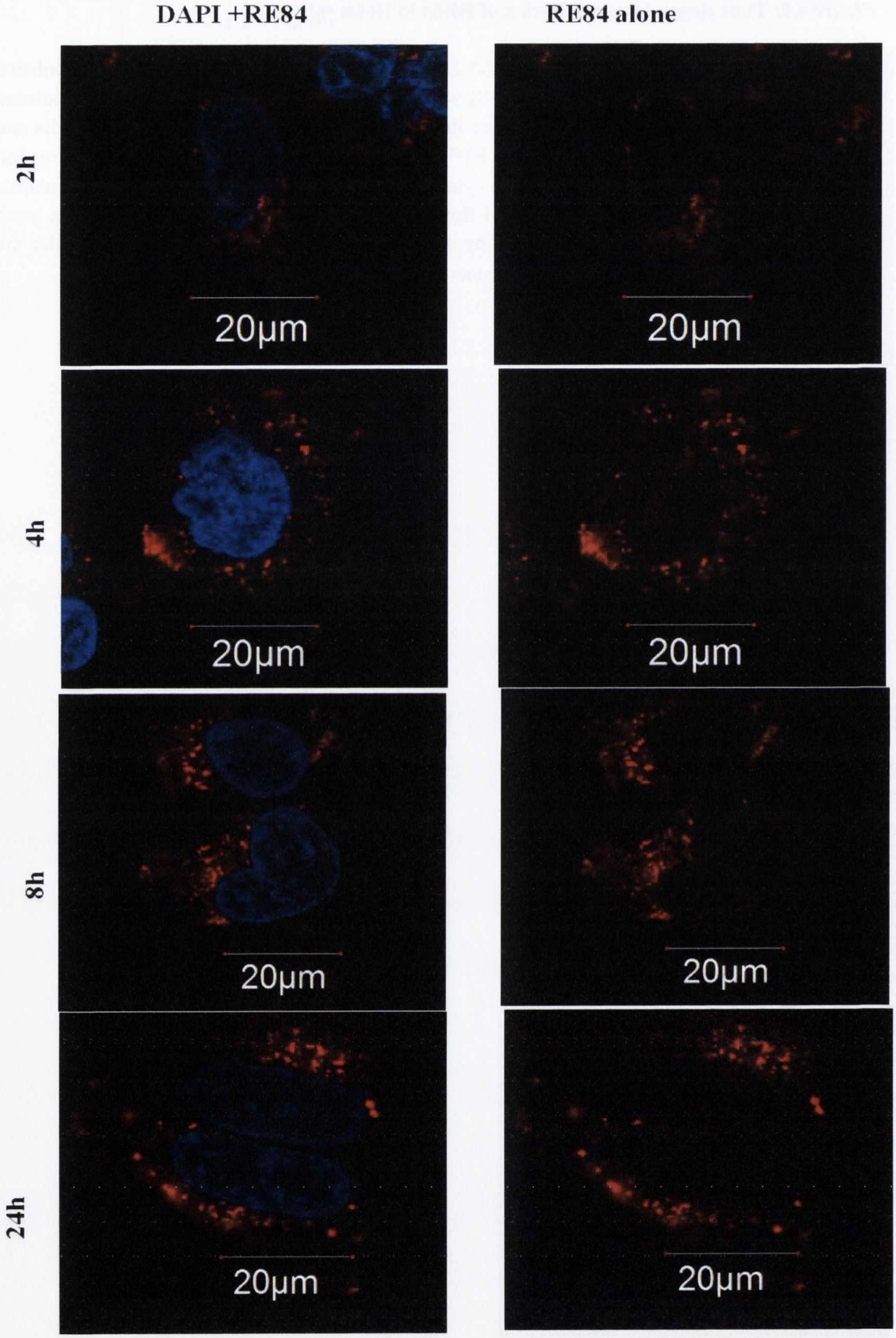
DAPI +RE84
RE84 alone
2h
4h
8h
24h
20µm
20µm
20µm
20µm
20µm
20µm
20µm
20µm

Figure 4.10: **Time dependent localisation of RE84 in HeLa cells.**

$1x10^5$ cells/well were seeded in dish plates (Ø 22mm; 2ml total volume/well). Cells were incubated at 37°C overnight before treatment. The cells were then treated with 10μM of RE84 and incubated for 2, 4, 8 and 24h. Cells were washed twice in PBS followed by the addition of fresh media and DAPI, followed by viewing using Olympus FV1000 confocal microscopy with a 60x oil immersion lens. The complex is localised either in the cytoplasm or to the peri-nuclear region. Image analysis was performed using FluoView Version 7.1 Software. RE84 was excited by a 488nm argon laser, emission 620nm and DAPI was excited by a 405 diode laser, emission 461nm. Results are representative of three independent experiments.

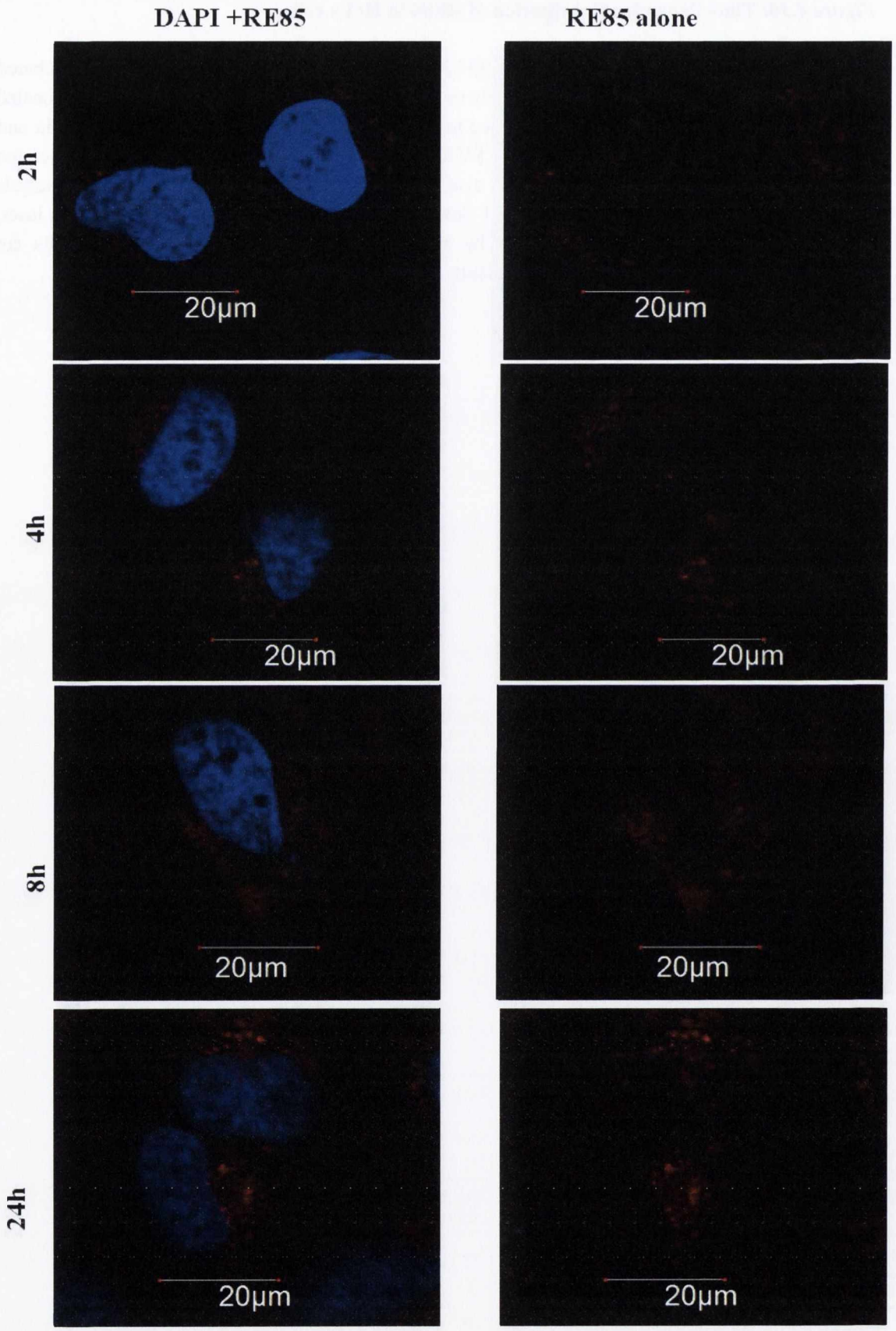
DAPI +RE85
RE85 alone
2h
4h
8h
24h
20μm

Figure 4.11: **Time dependent localisation of RE85 in HeLa cells.**

$1x10^5$ cells/well were seeded in dish plates (Ø 22mm; 2ml total volume/well). Cells were incubated at 37°C overnight before treatment. The cells were then treated with 5μM of RE85 and incubated for 2, 4, 8 and 24h. Cells were washed twice in PBS followed by the addition of fresh media and DAPI, followed by viewing using Olympus FV1000 confocal microscopy with a 60x oil immersion lens. The complex is localised either in the cytoplasm or to the peri-nuclear region. Image analysis was performed using FluoView Version 7.1 Software. RE85 was excited by a 488nm argon laser, emission 620nm and DAPI was excited by a 405 diode laser, emission 461nm. Results are representative of three independent experiments.

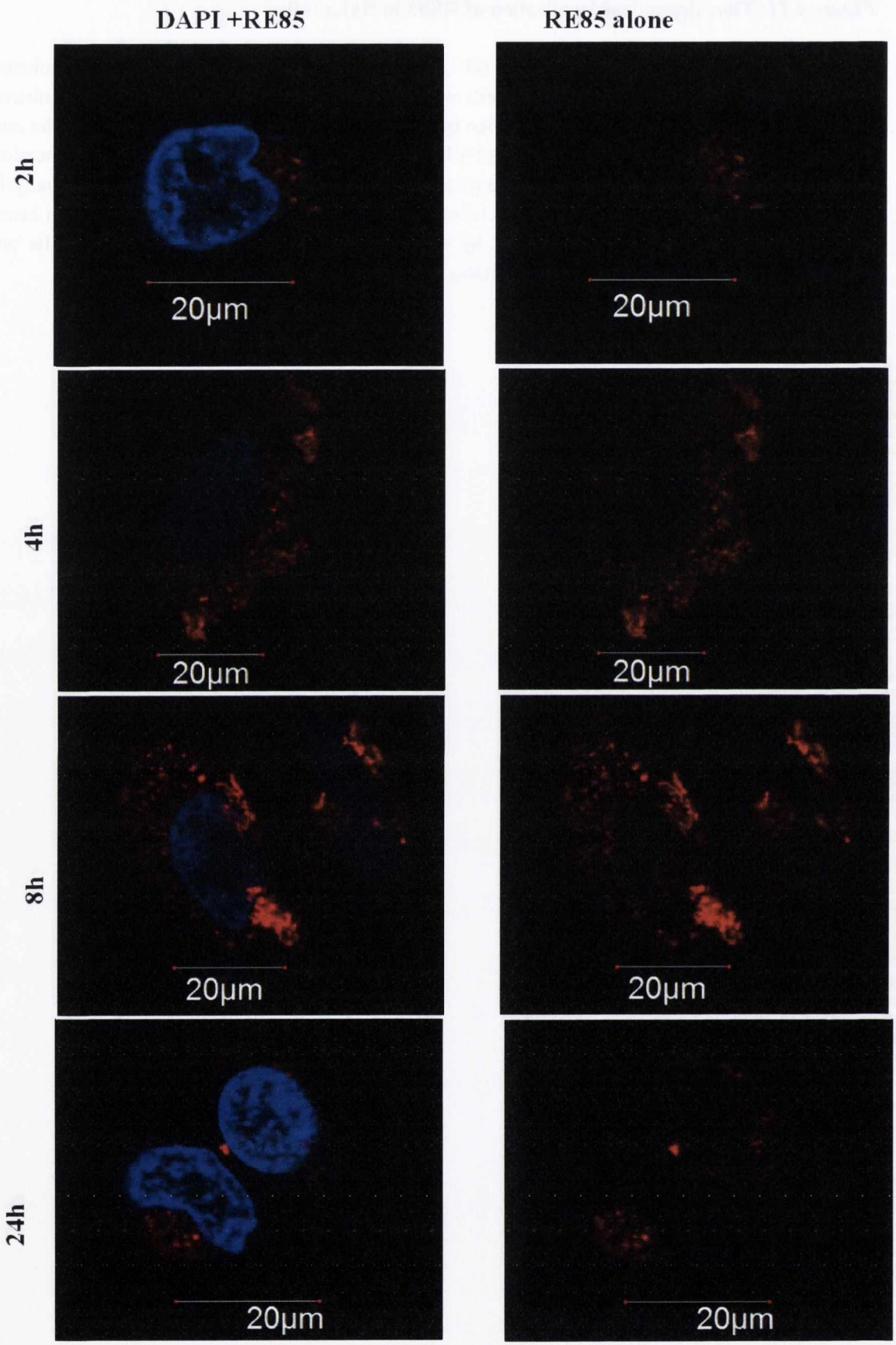
DAPI +RE85
RE85 alone
2h
4h
8h
24h
20μm

Figure 4.12: **Time dependent localisation of RE85 in HeLa cells.**

$1x10^5$ cells/well were seeded in dish plates (Ø 22mm; 2ml total volume/well). Cells were incubated at 37°C overnight before treatment. The cells were then treated with 10μM of RE85 and incubated for 2, 4, 8 and 24h. Cells were washed twice in PBS followed by the addition of fresh media and DAPI, followed by viewing using Olympus FV1000 confocal microscopy with a 60x oil immersion lens. The complex is localised either in the cytoplasm or to the peri-nuclear region. Image analysis was performed using FluoView Version 7.1 Software. RE85 was excited by a 488nm argon laser, emission 620nm and DAPI was excited by a 405 diode laser, emission 461nm. Results are representative of three independent experiments.

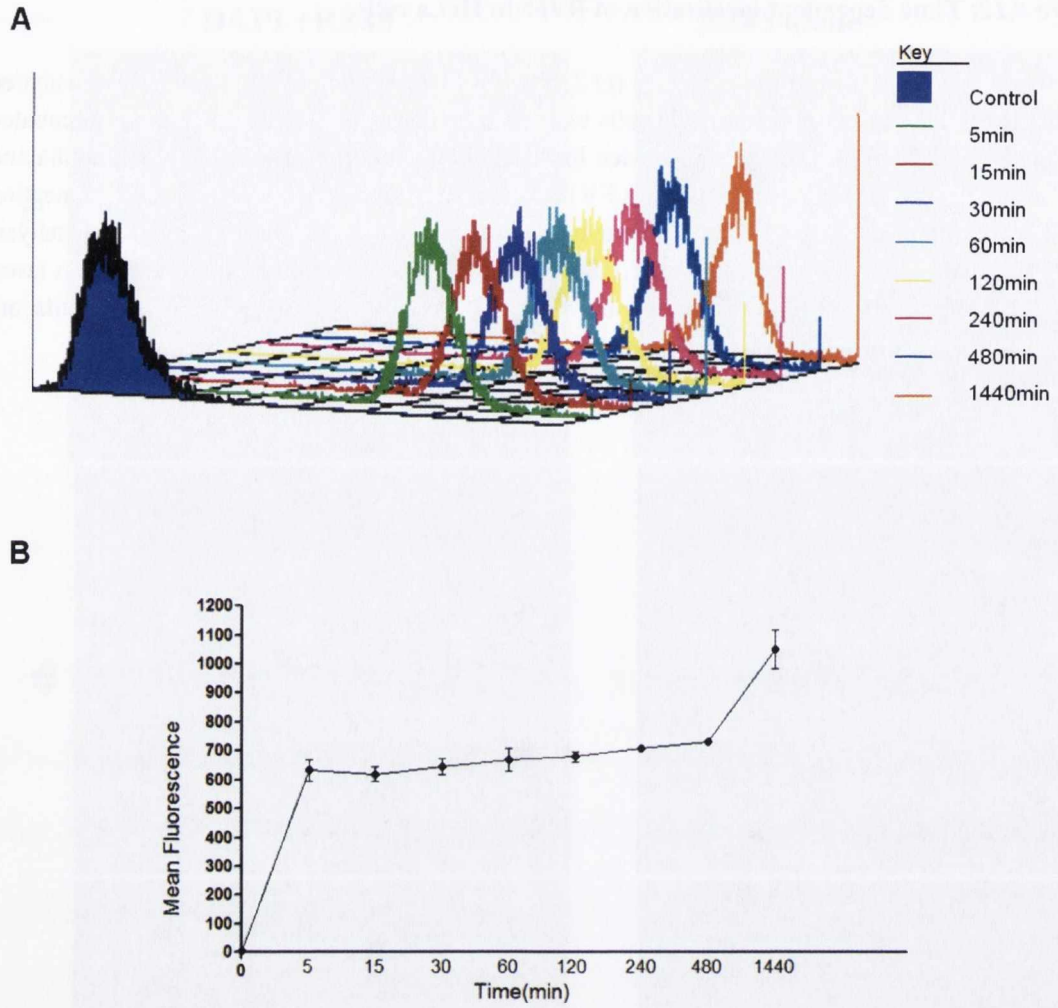

Figure 4.13: **Uptake of RE84 in HeLa cells.**

$0.25x10^6$ cells were seeded in T25 flasks (5ml total volume/well). Cells were incubated at 37°C overnight before treatment. The cells were treated with 5μM of RE84 and 85 and incubated in the dark at different time points. Cells were then harvested and washed in ice cold PBS followed by resuspention in ice cold PBS supplemented with 2% FBS in FACS microtubes. Cell analysis was performed using appropriate gates counting 10,000 cells and using CELLQUEST software package. The compounds were excited by a 488nm argon laser, with emission observed at 630nm. A representative histogram of compound uptake **(A)**. The percentage of fluorescence within the cells is expressed as the mean ± S.E.M. and graphed using GRAPHPAD Prism software. Values are representative of three independent experiments **(B)**.

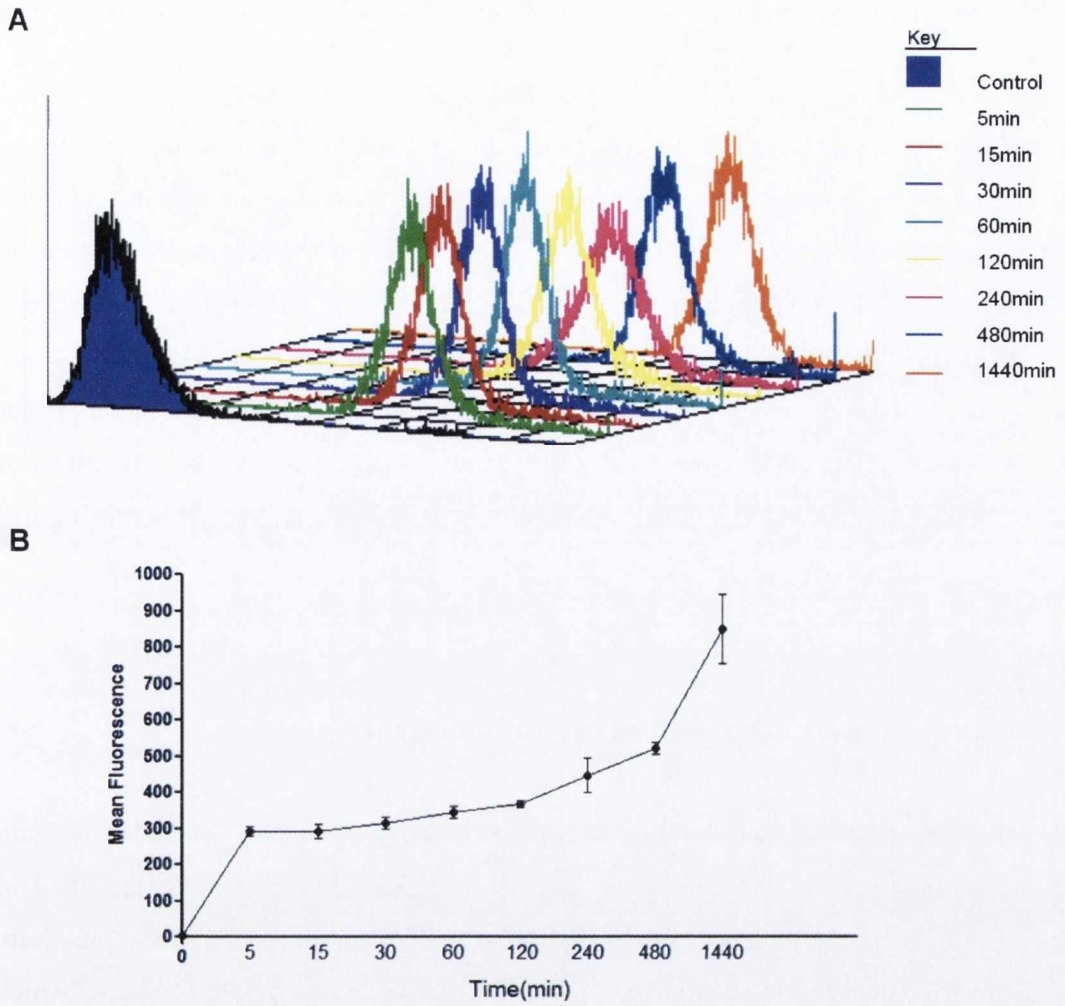

Figure 4.14: **Uptake of RE85 in HeLa cells.**

$0.25x10^6$ cells were seeded in T25 flasks (5ml total volume/well). Cells were incubated at 37°C overnight before treatment. The cells were treated with 5μM of RE84 and 85 and incubated in the dark at different time points. Cells were then harvested and washed in ice cold PBS followed by resuspention in ice cold PBS supplemented with 2% FBS in FACS microtubes. Cell analysis was performed using appropriate gates counting 10,000 cells and using CELLQUEST software package. The compounds were excited by a 488nm argon laser, with emission observed at 630nm. A representative histogram of compound uptake **(A)**. The percentage of fluorescence within the cells is expressed as the mean ± S.E.M. and graphed using GRAPHPAD Prism software. Values are representative of three independent experiments **(B).**

4.4 RE84 and 85 induce a low level of apoptosis in HeLa cells with an increase in S phase

In order to investigate the mechanism of cell death, a range of different concentrations of RE84 and 85 were tested, from 0.5 to 40μM. Cells were incubated for 48h in total (24h before light exposure followed by incubation for further 23h). The results showed an increase in cell death from 10 to 40μM whether cells were illuminated or not but, cell death increased somewhat when cells are illuminated (figures 4.15A and 4.17A). Moreover, the results showed an increase in the S phase of the cell cycle to a much greater extent in non illuminated cells from 10 to 15μM (figures 4.16A and 4.18B). The effect of RE84 and 85 on the G1 and G2/M cell cycle phases in HeLa cells are graphed in figures 4.15 to 4.18.

4.5. RE84 and 85 release LDH in a light dependent manner

HeLa cells were incubated with a range of concentrations (0.5, 1, 2, 3, 5 and 10μM) with compounds RE84 and 85 for 24h. Cells were then either illuminated (as described in Section 2.5 of the Materials and Methods) for 1h or maintained in the dark. Samples were then subjected to a CytoTox 96® Non-Radioactive Cytotoxicity Assay which quantitatively measures lactate dehydrogenase (LDH), a stable cytosolic enzyme that is released upon cell lysis/necrosis. The results are shown in figure 4.19.

Results showed a small increasing release of LDH with increasing concentration of the compounds. Comparing the samples with and without light treatment, results suggested an increase in LDH production in cells when illuminated, again suggesting the compounds are toxic when activated by the light.

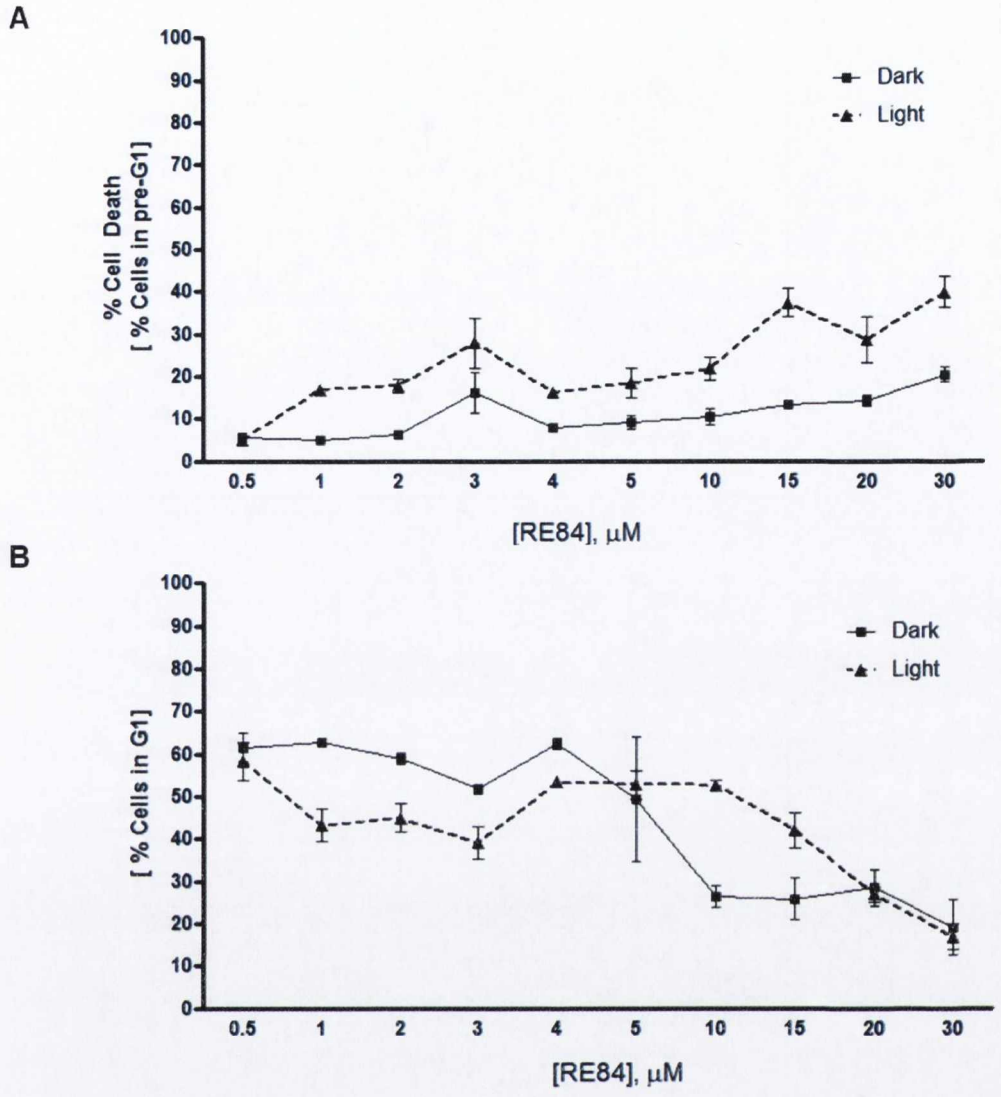

Figure 4.15: **The effect of RE84 on the cell cycle phases in HeLa cells.**

$0.25x10^6$ cells were seeded in T25 flasks (5ml total volume/well). Cells were incubated at 37°C overnight before treatment. The cells were treated with different concentrations of RE84 (0.5, 1, 2, 4, 5, 10, 15, 20 and 30µM). After 24h incubation the treated cells were exposed to light for 1h to give light doses of $12.66J/cm^2$ or maintained in the dark. Following 23h of incubation the cells were fixed in ice cold 70% ethanol and PBS overnight at 4°C. After fixation, the cells were pelleted and resuspended in 300µl of PBS in FACS microtubes, 25µl of RNAse A (10mg/ml) and 75µl of PI (1mg/ml) were then added. The tubes were incubated at 37°C in the dark for 30min. Cell cycle analysis was performed using appropriate gates counting 10,000 cells and using CELLQUEST software package. The percentage of cell in pre-G1 **(A)** and in G1 **(B)** phase were compared with the treated cells in the dark respectively. Values are representative of at least three independent experiments.

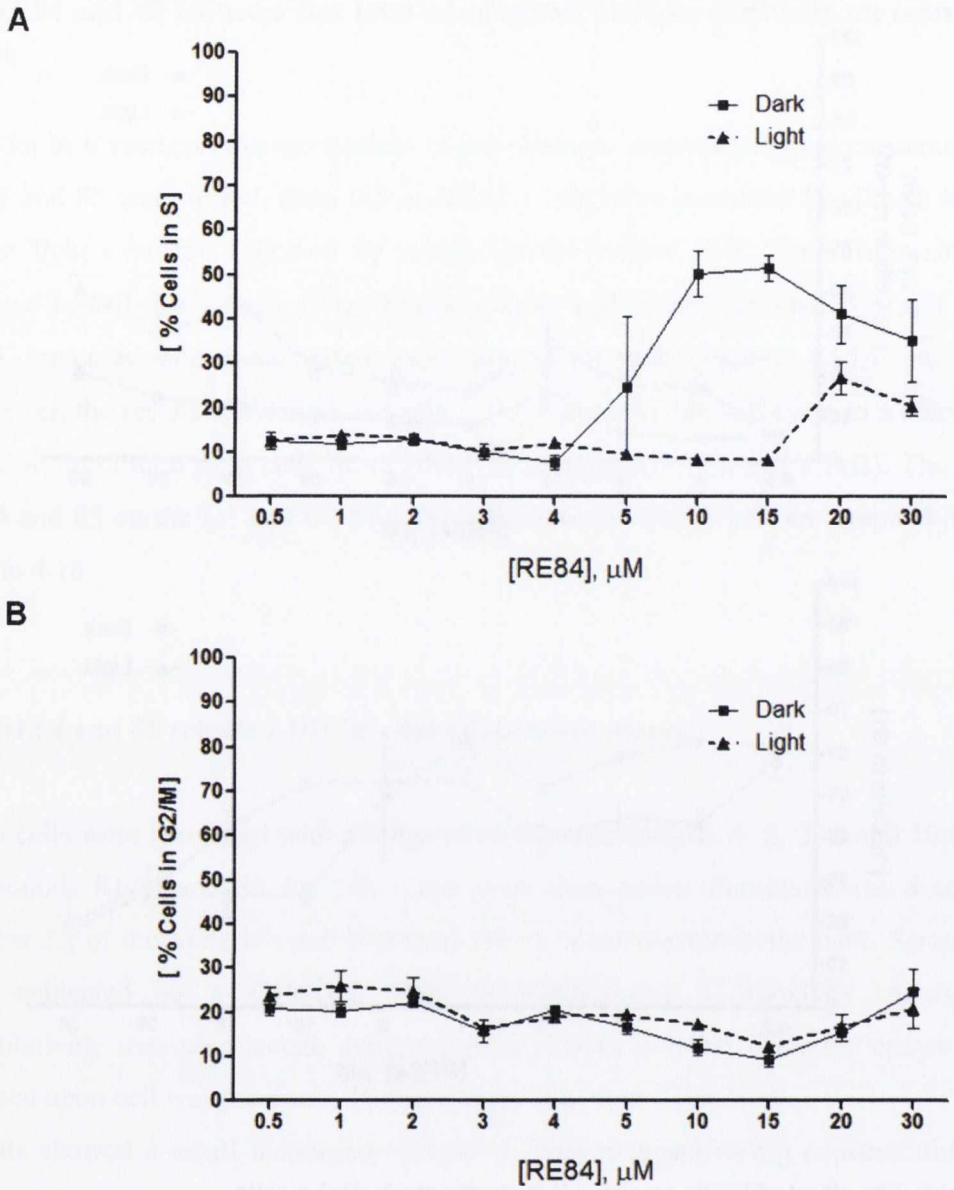

Figure 4.16: **The effect of RE84 on the cell cycle phases in HeLa cells.**

$0.25x10^6$ cells were seeded in T25 flasks (5ml total volume/well). Cells were incubated at 37°C overnight before treatment. The cells were treated with different concentrations of RE84 (0.5, 1, 2, 4, 5, 10, 15, 20 and 30μM). After 24h incubation the treated cells were exposed to light for 1h to give light doses of $12.66J/cm^2$ or maintained in the dark. Following 23h of incubation the cells were fixed in ice cold 70% ethanol and PBS overnight at 4°C. After fixation, the cells were pelleted and resuspended in 300μl of PBS in FACS microtubes, 25μl of RNAse A (10mg/ml) and 75μl of PI (1mg/ml) were then added. The tubes were incubated at 37°C in the dark for 30min. Cell cycle analysis was performed using appropriate gates counting 10,000 cells and using CELLQUEST software package. The percentage of cell in S **(A)** and in G2/M **(B)** phase were compared with the treated cells in the dark respectively. Values are representative of at least three independent experiments.

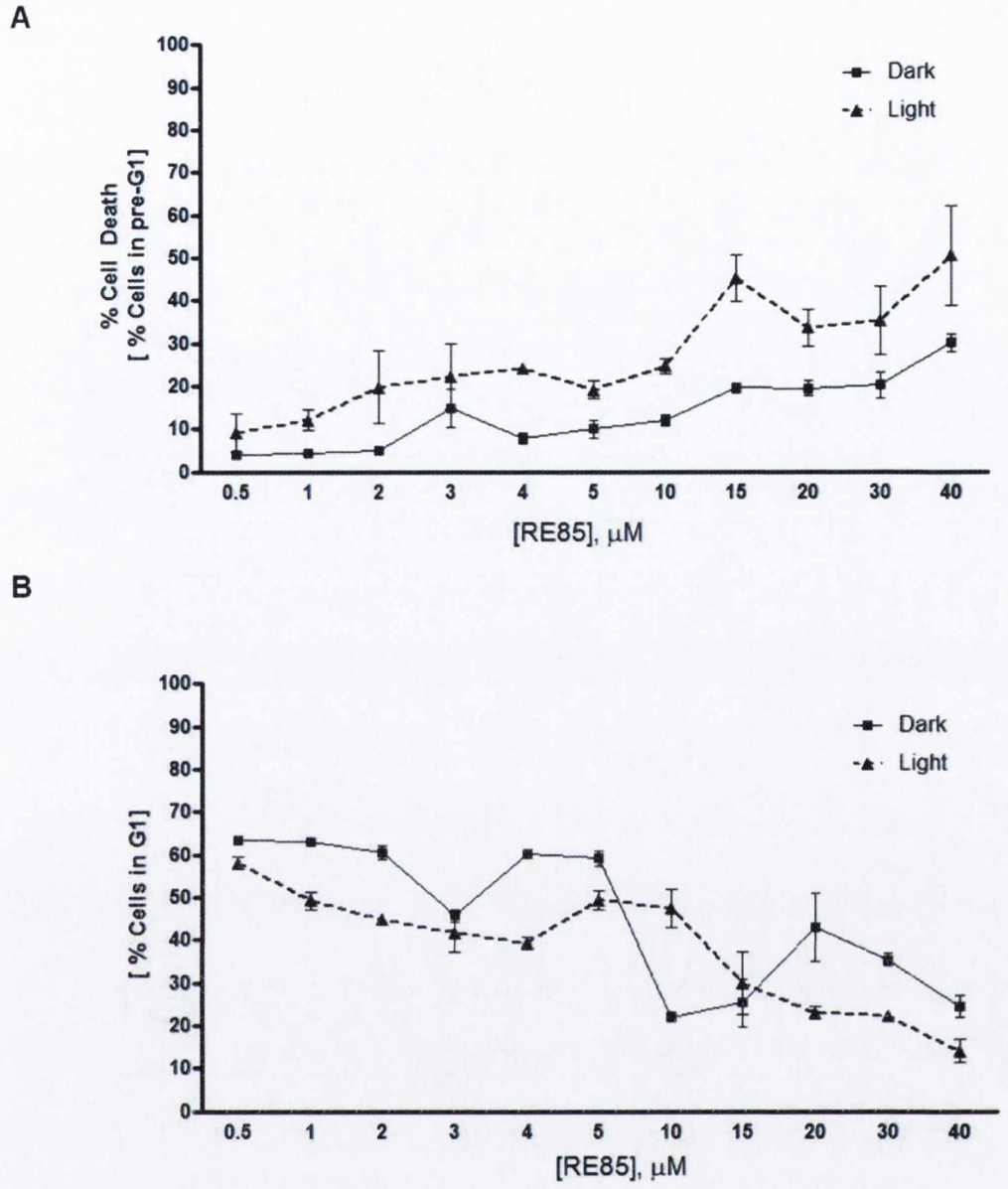

Figure 4.17: **The effect of RE85 on the cell cycle phases in HeLa cells.**

$0.25x10^6$ cells were seeded in T25 flasks (5ml total volume/well). Cells were incubated at 37°C overnight before treatment. The cells were treated with different concentrations of RE85 (0.5, 1, 2, 4, 5, 10, 15, 20, 30 and 40μM). After 24h incubation the treated cells were exposed to light for 1h to give light doses of $12.66J/cm^2$ or maintained in the dark. Following 23h of incubation the cells were fixed in ice cold 70% ethanol and PBS overnight at 4°C. After fixation, the cells were pelleted and resuspended in 300μl of PBS in FACS microtubes, 25μl of RNAse A (10mg/ml) and 75μl of PI (1mg/ml) were then added. The tubes were incubated at 37°C in the dark for 30 minutes. Cell cycle analysis was performed using appropriate gates counting 10,000 cells and using CELLQUEST software package. The percentage of cell in pre-G1 **(A)** and in G1 **(B)** phase were compared with the treated cells in the dark respectively. Values are representative of at least three independent experiments.

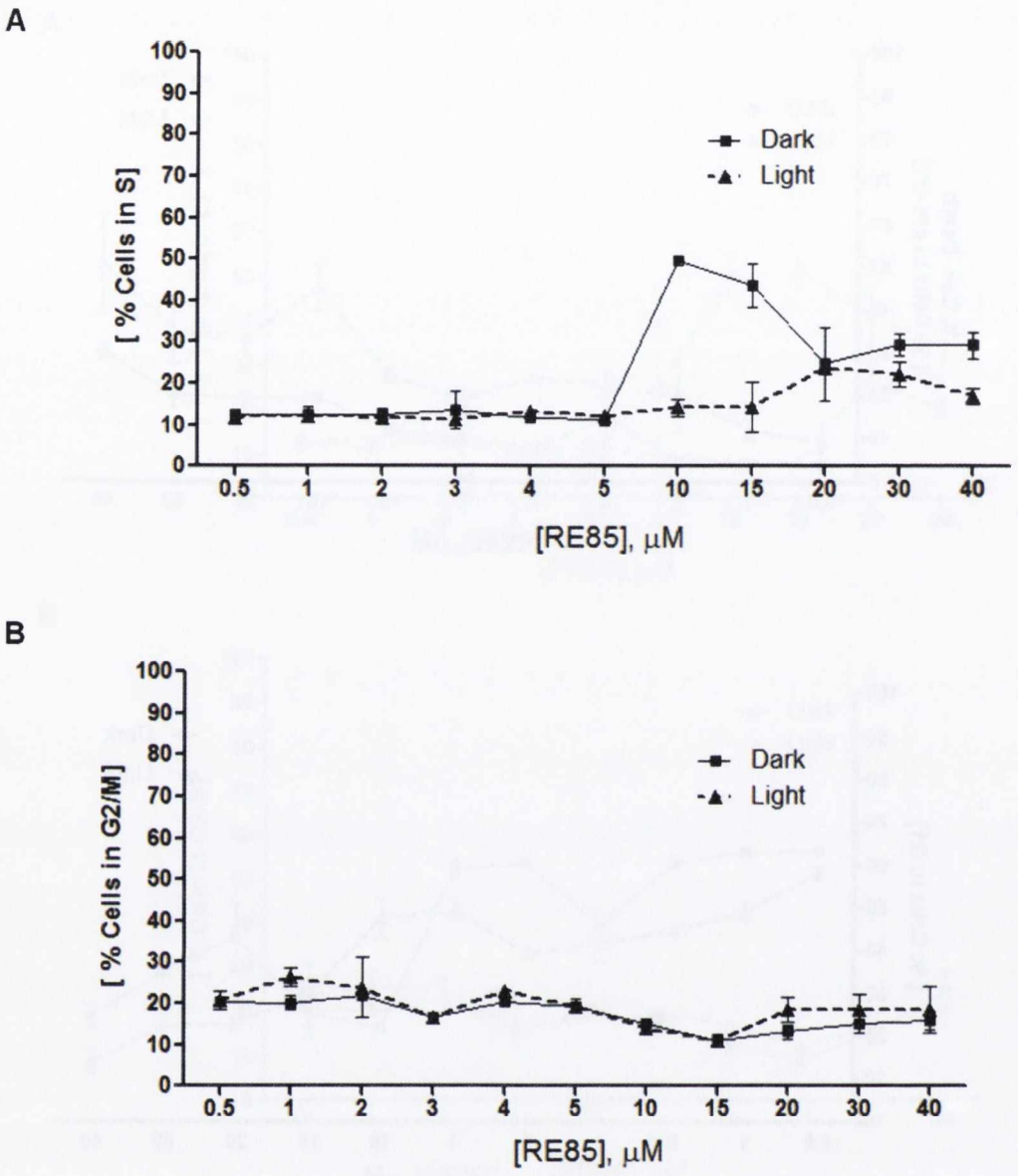

Figure 4.18: **The effect of RE85 on the cell cycle phases in HeLa cells.**

$0.25x10^6$ cells were seeded in T25 flasks (5ml total volume/well). Cells were incubated at 37°C overnight before treatment. The cells were treated with different concentrations of RE85 (0.5, 1, 2, 4, 5, 10, 15, 20, 30 and 40µM). After 24h incubation the treated cells were exposed to light for 1h to give light doses of $12.66J/cm^2$ or maintained in the dark. Following 23h of incubation the cells were fixed in ice cold 70% ethanol and PBS overnight at 4°C. After fixation, the cells were pelleted and resuspended in 300µl of PBS in FACS microtubes, 25µl of RNAse A (10mg/ml) and 75µl of PI (1mg/ml) were then added. The tubes were incubated at 37°C in the dark for 30min. Cell cycle analysis was performed using appropriate gates counting 10,000 cells and using CELLQUEST software package. The percentage of cell in S **(A)** and in G2/M **(B)** phase were compared with the treated cells in the dark respectively. Values are representative of at least three independent experiments.

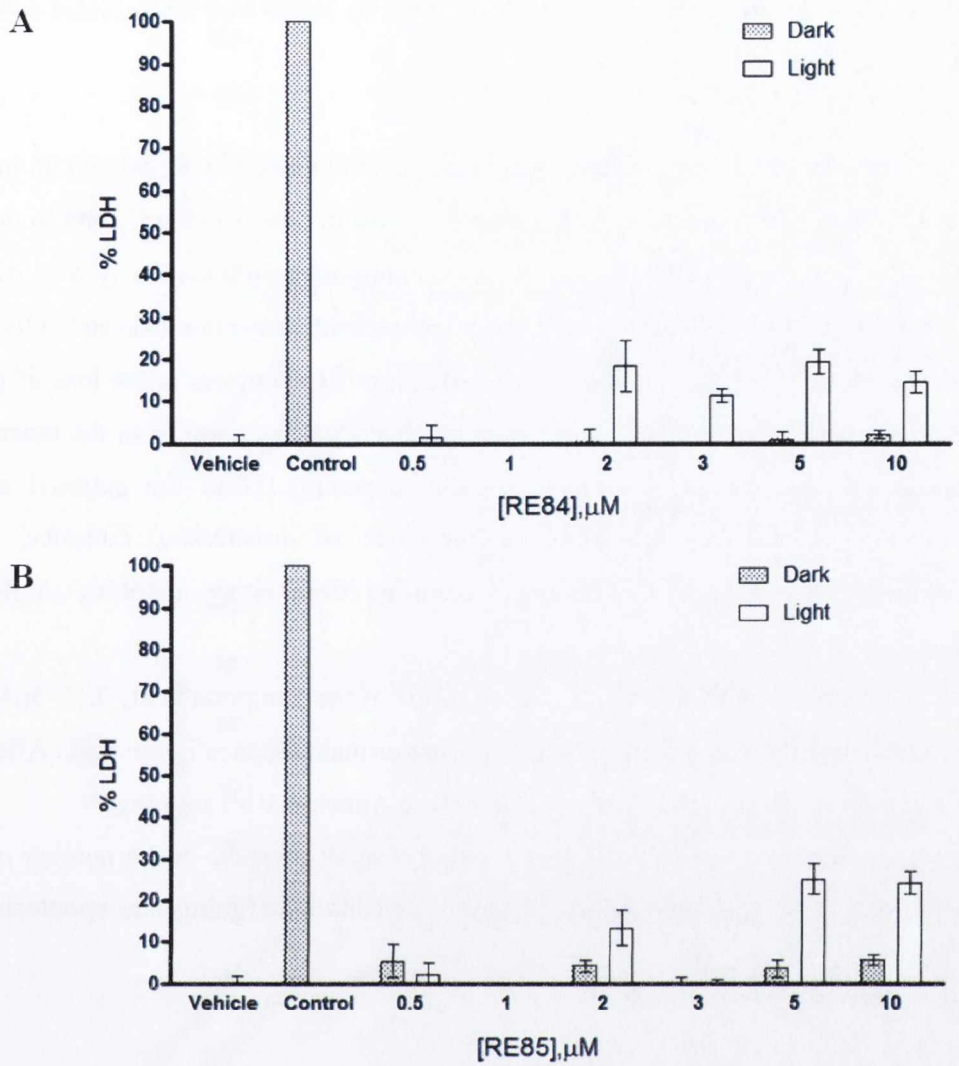

Figure 4.19: **The cytotoxicity effect of RE84 and 85 on HeLa cells with or without light exposure.**

$0.5x10^4$ cells/well were seeded in 96-well plates (200 µl total volume/well). Cells were incubated at 37°C overnight before treatment. RE84 **(A)** and RE85 **(B)** concentrations (0.5, 1, 2, 3, 5 and 10µM) were plated in triplicate and compared to dark-treated controls. Following 24h of treatment, the treated cells were either exposed to light for 1h to give a light dose of $12.66J/cm^2$ or maintained in the dark. Following 23h of incubation a CytoTox 96® Assay, which quantitatively measures LDH, was performed as described in Section 2.13. The LDH production was determined by subtracting the average of absorbance values of the culture medium background from each group and, the control lysed cells represented the 100% LDH production. Absorbance was measured using a microplate reader at 490nm. All data points were analysed using GRAPH PAD Prism software. Results are representative of three independent experiments.

4.6 Investigation on the form of cell death induced by RE84 and 85 in HeLa cells with or without light exposure.

With the aim to further investigate the form of cell death induced by RE84 and 85 in HeLa cells, FITC conjugated Annexin V /PI staining was used in order to identify and to quantify apoptotic cells on a single-cell basis by FACS. Staining cells simultaneously with Annexin V (FITC) and PI allows the discrimination of intact cells in early apoptosis and cells in late apoptosis or necrotic cells. One of the earliest features of apoptosis is the loss of plasma membrane asymmetry which leads to the membrane-PS translocation from the inner to the outer leaflet of the plasma membrane, thereby exposing PS to the external cellular environment. PS translocation precedes the loss of membrane integrity, which accompanies the later stages of cell death resulting from either apoptotic or necrotic processes.

The cells were treated with different concentrations of the compounds (1, 2, 3, 5μM) and incubated for 24h followed by either light exposure or maintainance in the dark. After light exposure cells were incubated for further 23h before Annexin V/PI staining.

Results are shown in figure 4.20. Results showed a small increase in the number of cells undergoing early apoptosis and a larger number of cells undergoing late apoptosis upon light activation of RE84 and 85.

4.7 Live video of RE84 uptake in HeLa cells.

Live videos were set up to collect more information about morphology changes, cell death and effects of any light irradiation following treatment with RE84. HeLa cells were treated with 1 and 3μM of RE84 for 30min before capture with a live video. Over 12h, images of cells were taken every 10 min at 5% 488 laser intensity (laser was only switched on when the images were taken). Cell death was measured by counting damaged cells (cell shrinkage) as a percentage of total cells (approximately 100) per field of view (figure 4.21). Representative images at 10, 60, 120 and 240min are illustrated (figure 4.22) showing cell death which appeared as apoptotic bodies for both of the concentrations but at the higher concentration (3μM) cell swelling is more pronounced. The videos are available in the DVD included in the back cover of the thesis.

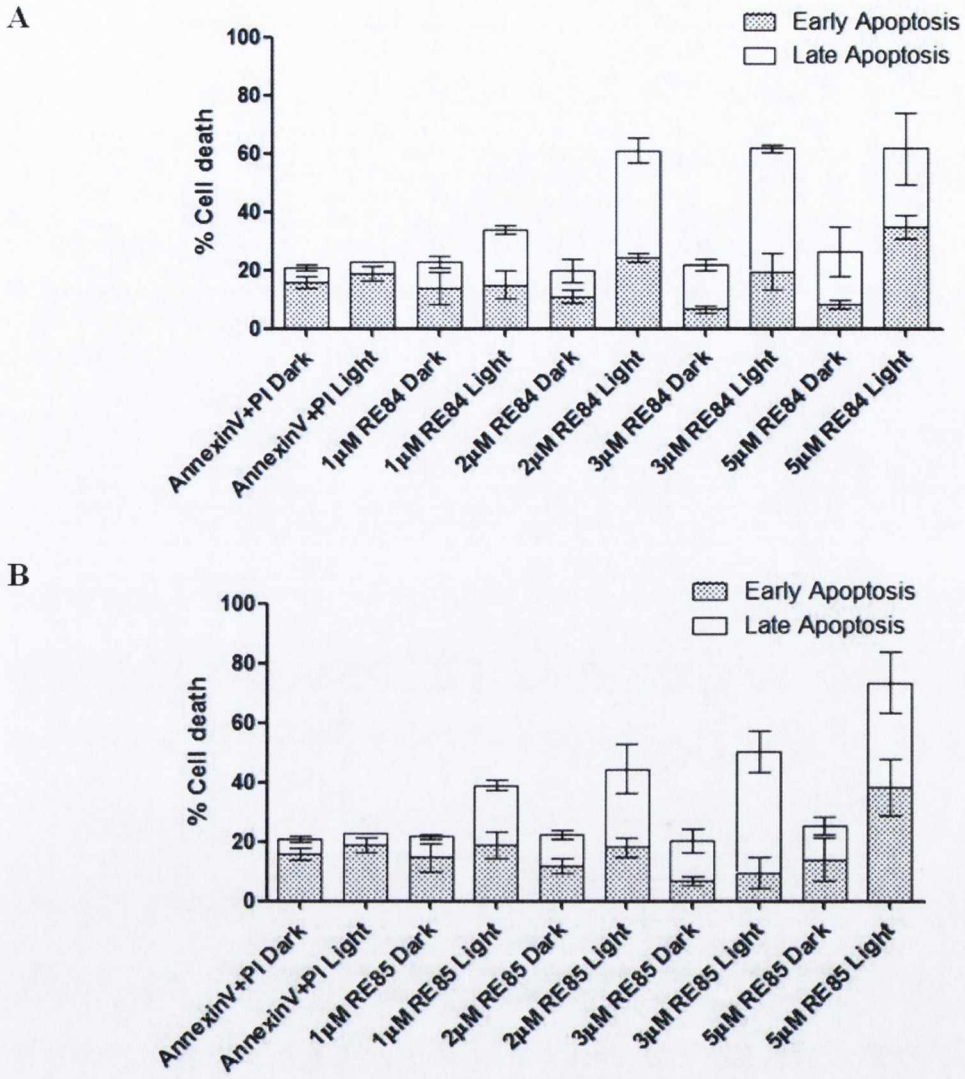

Figure 4.20 : **Investigation into the form of cell death induced by RE84 and 85 in HeLa cells with or without light exposure.**

$1x10^5$ HeLa cells were seeded in T25 flasks (5ml total volume/flask). Adherent cells were incubated at 37°C overnight before treatment. The cells were treated with different concentrations of the compounds and incubated for 24h followed by either light exposure for 1h to give light doses of 12.66 J/cm^2 or maintained in the dark. After light exposure cells were incubated for a further 23h before Annexin V/PI staining, which was performed as described in Section 2.9.8. The 488nm laser was used to excite the FITC conjugated Annexin V and the PI: FITC Annexin V was detected in FL1 (emission: 530nm), PI was detected in FL2 (emission: 575nm) and the compounds were detected in FL4 (emission 680). Cell analysis was performed in the CyAn using appropriate gates counting 10,000 cells and using Summit software package. The standard compensation was performed using the untreated control, cells stained only with Annexin V or PI, cells stained with both Annexin V/PI and by excluding the fluorescence of the compounds. The percentage of fluorescence into the cells was analysed using Flow Jo software. The percentage of cell death within the cells is expressed as the mean ± S.E.M. and graphed using GRAPHPAD Prism software. Results are representative of three independent experiments.

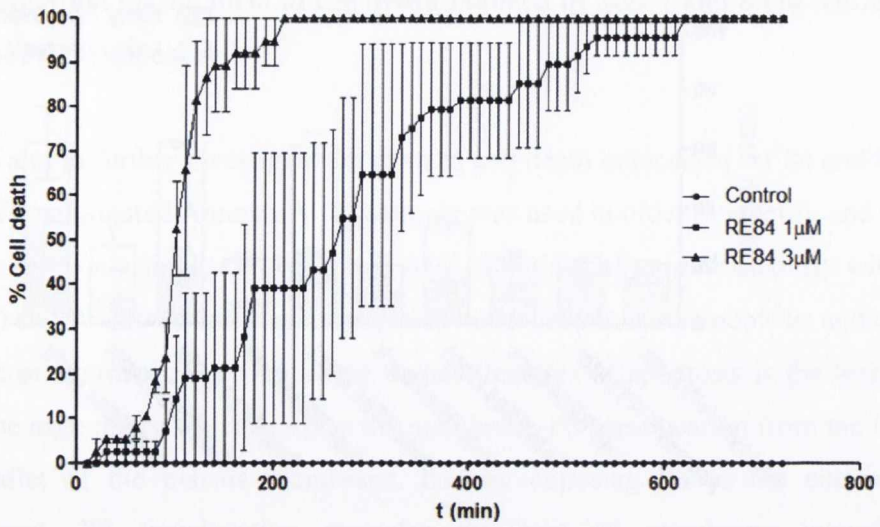

t(min)	Control	RE84 1μM	RE84 3μM
	% HeLa cell death		
10	0	0	0
60	0	2.3±2.3	7.8±2.6
120	0	19.4±19.4	81.5±13.1
240	0	43.26±28.8	100.0±0

Figure 4.21: **Light-dependent cell death measured using life video capturing.**

$2x10^5$ (cells/well) HeLa cells were seeded in glass bottom dish plates (Ø 22mm; 2ml total volume/well). Cells were incubated at 37°C overnight before treatment. The cells were then treated with 1 and 3μM of RE84 and incubated for 30min before overnight Olympus FV1000 confocal microscopy with a 60x oil immersion lens. Image analysis was performed using FluoView Version 7.1 Software. The percentage of cell death was expressed over the total amount of cells (approximately 100) per field of view. During the 12h overnight video, cells were incubated at 37°C, 5% CO_2 and images were taken every 10min at 4% laser intensity (laser was only on when the images were taken). RE84 was excited by a 488nm argon laser at 4% intensity, emission 620nm. Results are representative of three independent experiments.

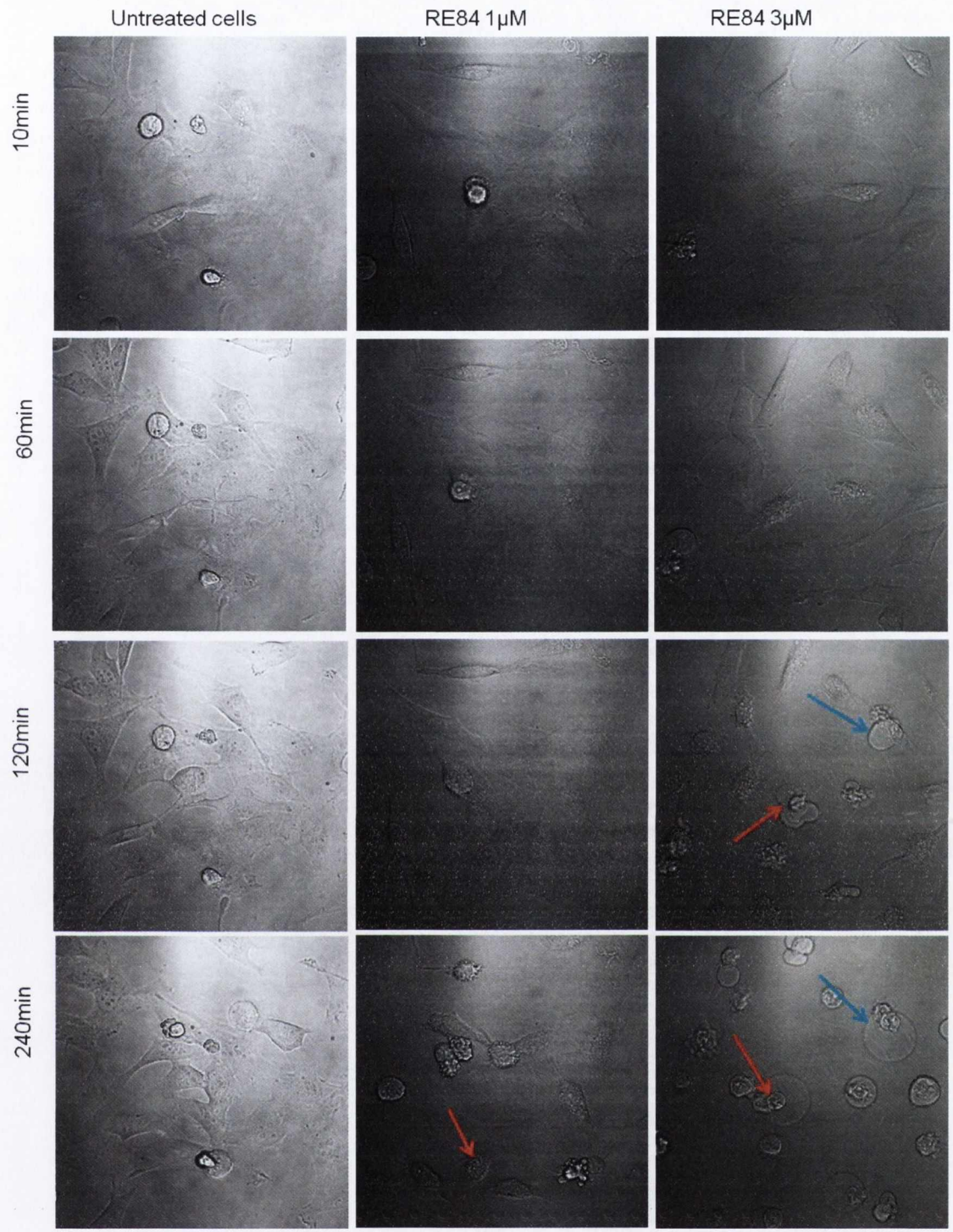
Untreated cells
RE84 1µM
RE84 3µM
10min
60min
120min
240min

Figure 4.22: **Light-dependent cell death measured using life video capturing.**

$2x10^5$ (cells/well) HeLa cells were seeded in glass bottom dish plates (Ø 22mm; 2ml total volume/well). Cells were incubated at 37°C overnight before treatment. The cells were then treated with 1 and 3μM of RE84 and incubated for 30min before overnight Olympus FV1000 confocal microscopy with a 60x oil immersion lens. Image analysis was performed using FluoView Version 7.1 Software. The percentage of cell death was expressed over the total amount of cells (approximately 100) per field of view. During the 12h overnight video, cells were incubated at 37°C, 5% CO_2 and images were taken every 10min at 4% laser intensity (laser was only on when the images were taken). RE84 was excited by a 488nm argon laser at 4% intensity, emission 620nm. Results are representative of three independent experiments. The blue arrows indicates cell swelling and the red once indicate cell death.

4.8 RE84 and 85 are tolerated by the cells

In order to see if RE84 and 85 are tolerated by the cells when not illuminated, HeLa cells were incubated with 5μM for 24h in the dark and fixed as described in Section 2.8.1. Cells were fixed because the confocal laser in live images activates the compounds very fast compromising cell integrity.

After being fixed, the cells were stained with DAPI to stain the nucleus and visualised using confocal microscopy. The results are shown in figures 4.23.

The confocal microscopy images showed no change in the morphological appearance of the cells suggesting that the presence of the compound is not toxic to the cells.

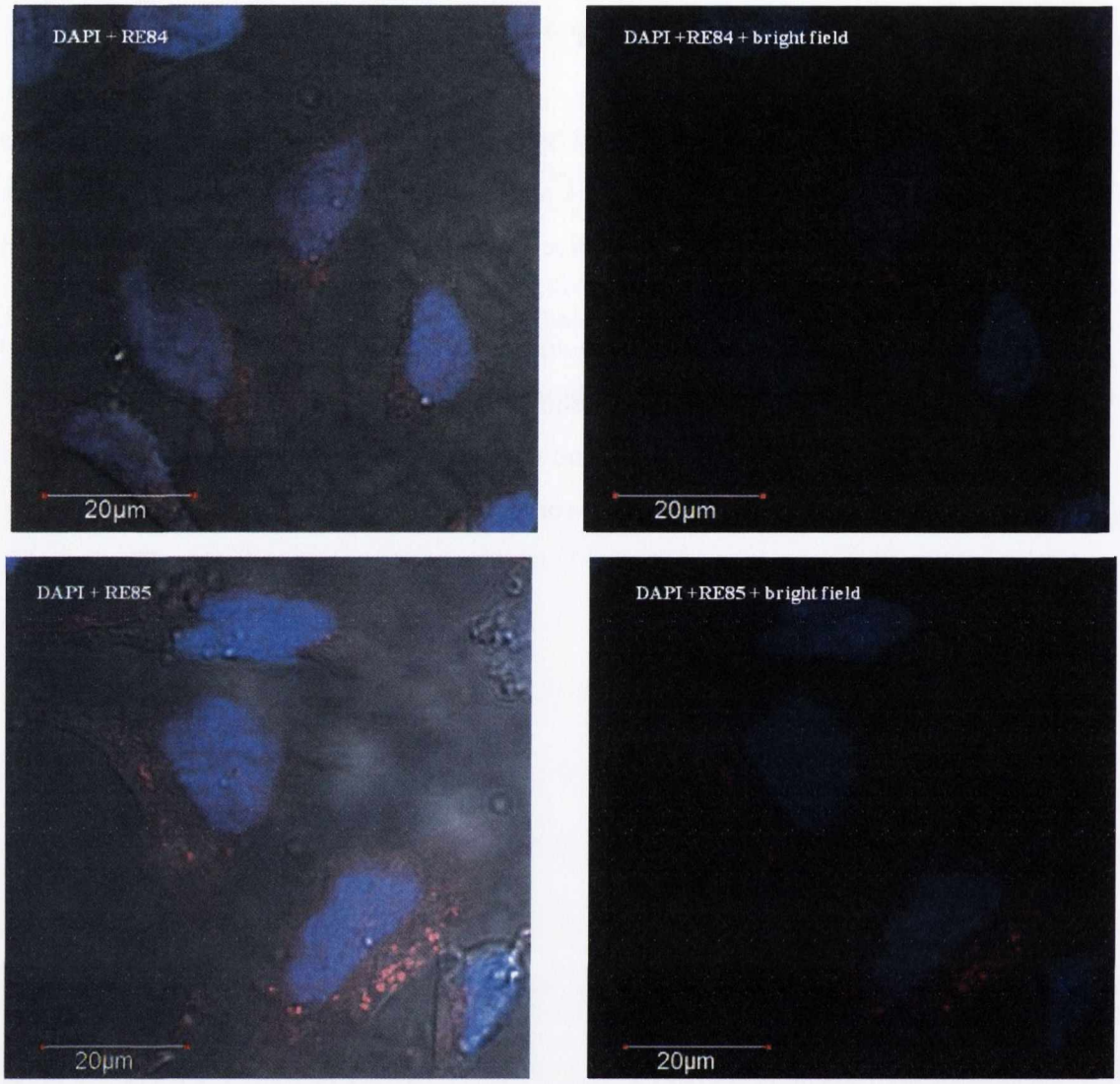

Figure 4.23: **RE84 and 85 are tolerated by the cells.**

$3x10^5$ cell/well were seeded on coverslips and placed inside a 6-well plate. Cells were incubated at 37°C overnight before treatment with 5µM of RE84 and 85 and incubated for 48h. Cells were washed twice with pre-warmed PBS, pH 7.4. Samples were fixed in 3% Paraformaldehyde solution in PBS for 10min at room temperature followed by two or more washes with PBS and then transferred onto glass slides with DAPI gel added at room temperature and left overnight before confocal microscopy. Image viewing using Olympus FV1000 confocal microscopy with a 60x oil immersion lens and analysed using the Imaris 3D software analyser (Bitplane). Image analysis was performed using FluoView Version 7.1 Software. Compounds were excited by a 488nm argon laser, emission 612nm and DAPI was excited by a 405 laser. Results are representative of three independent experiments.

Discussion

The aim of this Chapter was to investigate whether the two novel bimetallic Ru(II)-1,8-naphthalimide compounds containing Tröger's bases species, RE84 and 85, were taken up by cells and if they could induce light dependent cell death, which determines whether the compounds are suitable for cellular imaging or therapeutics for PDT. These complexes are potentially capable of binding DNA and compounds that form chemical bonds with DNA molecules represent several important classes of anticancer compounds [121].

The compounds were tested in HeLa cells to be consistent in comparing the results with the other compounds RE30, 34, 37 and RE33.

In order to characterize the uptake of these compounds, confocal microscopy studies were performed at different time points. Results showed RE84 and 85 were taken up into the cells at 2h. For all time points (2-24h) a peri-nuclear localization of the compounds was observed and following longer incubation times the compounds were more visible. Moreover, RE84 and 85 appeared very luminescent in the cells at lower concentrations than the previous compounds (RE30, 34, 37 and 33) making them very good compounds for localization studies. However, it is important to consider that the apparent increase in visibility of these compounds compared to RE37 may be attributed to factors such as uptake efficiency and quantum yields aswell an increase in luminescence.

It has been observed that cells treated with these compounds cannot be visualised for too long under the confocal microscope because the confocal laser activated the compounds and cells started dying rapidly depending on the concentration of the compound used. This is the reason why some cytotoxicity was observed in the cells treated at 10μM concentration, with cell swelling evident after only 2h of incubation. This occurred in cells treated at 5μM concentration too if visualised for a longer time under the microscope.

In contrast to the previous compounds, this result suggested that RE84 and 85 are more potent compared to RE37 when illuminated.

Similarly to the localization of compound RE37, confocal images suggested RE84 and 85 to be localised in the mitochondria even though the compounds where synthesised to target DNA.

The uptake of the compounds in cells was confirmed investigating the cellular uptake of the compounds using flow cytometry which showed fluorescence in cells within 5min with

RE84 being more fluorescent then 85 but, again it is important to consider that the luminescence of the compounds is dependent upon many factors as mentioned above.

Light-dependent cell viability assays showed RE84 and 85 reduced cell viability to a greater extent when illuminated. These results suggest RE84 and 85 as potentially suitable PDT agents due to the greater difference in cell toxicity upon photoillumination and to the absence of toxicity in cells without light treatment. Moreover, these results demonstrated that the cells can tolerate the compounds and that no change in the morphological appearance of the cells in the dark occurred as shown in figure 4.24. Comparing these compounds with RE37, RE84 and 85 showed a reduction in cell viability in a light dependent manner at lower concentrations then RE37. This is considered advantageous from a clinical point of view in terms of reducing the accumulation of the compound in the tissue and in terms of reducing the time of recovery/elimination of the compound from the tissue, which is related to the reduction of any potential side effects.

With the aim to investigate the mechanism of cell death in HeLa cells treated with compounds RE84 and 85, apoptotic analysis was conducted using flow cytometry. Increasing the concentration (4 to 40μM) of both RE84 and RE85, results displayed a small hypodiploid (pre-G1) peak in cells with and without being illuminated. However, the extent of apoptosis in illuminated cells increased compared to cells that were not illuminated (figures 4.15A and 4.17 A). However, the number of apoptotic cells found during photoirradiation was lower than expected considering the large reduction in viability observed with the AB results (figure 4.4), which thus suggests another form of cell death may be taking place.

Furthermore, in cells treated with either RE84 or 85, an increase in the S phase population of cells non-illuminated was observed at high concentrations (10 to 15μM). As the compounds do not localise within the nucleus, this S-phase delay is likely to be due to a downstream effect after the localization of the compounds in mitochondria.

There can be many different causes that can lead to an increase in S phase population of cells. The mechanisms that underlie the inhibition of DNA replication by carcinogen-induced DNA damage are not thoroughly understood and both, passive and active mechanisms are thought to contribute to the overall inhibition: direct blockage of the replication apparatus by a bulky template lesion represents a passive mechanism of inhibition of the replication; in contrast, an active process requires the generation of some type of stress signals, its transduction to sites away from the primary lesion and inhibition

of DNA synthesis even in replication units that did not incur any direct damage [122]. For example many cytotoxic anticancer agents damage DNA directly, interfering with DNA metabolism or chromosome segregation, which are particularly toxic in dividing cells [123]. Alternatively, compounds that form chemical bonds with DNA, which represent several important classes of anticancer compounds synthesized and tested for anticancer activity that are in clinical use, appear to inhibit cell division and stimulate apoptosis caused by the formation of DNA adducts [121]. Etoposide-induced cell cycle delay and arrest-dependent modulation of topoisomerase II enzyme, which inhibition prevent the relaxation of the supercoiled DNA blocking DNA transcription and replication, in lung cancer cells [124].

However, this experiment together with the confocal microscopy and cell viability assay studies, demonstrate that the effect of these compounds in cells at high concentrations may be relevant because the difference in cell toxicity upon illumination occurs at lower concentrations (1-5μM) than the S phase arrest.

In connection to these results, another assay (AnnexinV/PI) to identify the form of cell death induced by these compounds was performed and results showed cell death in a light dependent manner with both AnnexinV and PI positive cells.

This assay does not distinguish between cells that have undergone apoptotic death versus those that have died as a result of a necrotic pathway because they will also stain with both AnnexinV and PI, but the cytotoxicity assay, which quantitatively measures lactate dehydrogenase (LDH), suggested cells not to be necrotic implying that apoptosis occurs.

Cellular swelling has also been shown in the confocal images, which is one of the responses in necrotic cells, at high concentrations of the compounds which is in contrast with the LDH release/production experiment but, this can be related to the difference in the light source used (the xenon lamp and the confocal lasers) because PDT effect may be enhanced by appropriate manipulation of the illumination process [1]. The LDH release results may suggest that compounds are simply being anti-proliferative in cells but, the cell viability and the AnnexinV/PI results, exclude this hypothesis.

In summary, the cellular uptake of RE84 and 85 into the cells is related to their solubility in water and growth media and their highly positive charge, which means that these compounds can easily interact with and enter living cells. In comparison with the compounds RE30, 34 and 37, the uptake and the high fluorescence of RE84 and 85 showed into the cells facilitate the visualisation of the compounds which was advantageous for

investigating on the uptake and co-localisation/dynamic with cellular organelles such us mitochondria. Furthermore, an AB assay showed compounds RE84 and 85 to be tolerated by the cells without light treatment and to reduce cell viability in a light-dependent manner at a greater extent and a lower concentration then compound RE37. This suggests RE84 and 85 to be potentially suitable as PDT agents owing to the difference in cell toxicity with and without light treatment and not to be suitable as imaging agents due to the rapid activation of the compounds under the confocal light. In PDT the biological efficacy of the photosensitizer is associated with its localisation [1, 72]. In connection with that, investigating on the localization of the compounds in order to understand more their mechanism of action inside the cells is important. Moreover, taking into consideration the results obtained in the co-localisation studies of RE37, which is localized in the mitochondria, and considering the similarity in the localization studies using confocal microscopy of RE84 and 85 with RE37, results suggest future investigation on the interaction of RE84 and 85 with mitochondria and nucleus. In fact, even if RE84 and 85 derived from the structure of the organic compounds 44 a-c, which have been showed to bind DNA in cells, and even if bimetallic Ru(II) complexes assembled by polypyridyl bridging ligands have also found numerous applications in DNA cellular imaging, RE84 and 85 may be not localized in the nucleus. It is at the moment not understood which difference in the structure makes the compounds bind preferentially nuclear DNA or mitochondria. Furthermore, investigation on the effect of these compounds in mitochondria is suggested considering that the therapeutic effect in PDT is mediated by the generation of ROS, which the vast majority of it is produced by mitochondria. Taking into account the promising results obtained in this Chapter, further investigation on the localization and effects of RE84 and 85 on mitochondria and DNA is needed.

Chapter 5

Investigation on the mechanism of action of compounds RE84 and 85 in HeLa cells

Introduction

The localisation and the mechanism of action of compounds RE84 and 85 inside the cells, is of great interest for our group. The historical development of the understanding of the mechanism of action of PDT agents at the cellular level has been dealt with in numerous papers in which it is stated that cationic sensitizers localize in both the nucleus and mitochondria: lipophilic ones tend to bind to membrane structures, and water-soluble drugs are often found in lysosomes [1]. Aside from the lipid/water partition coefficient, other factors are also important, such as molecular weight and charge distribution. In some cases light exposure leads to a relocalization of the sensitizers [1]. The mechanism of action is clearly linked to the intracellular localization of the sensitizers because the lifetime of the main active photoproduct being short in cells reduces the $^1O_2$ diffusion from the site of production [1].

Moreover, PDT has a strong effect on cell division, which is mainly due to microtubule damage [1]. For example, studies on the photosensitizing effects of zinc(II)-phthalocyanine (ZnPc) on the cytoskeleton of HeLa cells showed a variable photodamage to microtubules, actin microfilaments and intermediate filaments of keratin, as well as on α-actinin, which was dependent on treatment conditions inducing deep alterations on interphase and mitotic microtubules [1250].

Under certain conditions this kind of damage may contribute significantly to PDT induced cell death [1].

Apoptosis is a popular field of cancer research and this form of cell death has also been demonstrated for PDT [1]. A common thread running through many reports relates to the appearance of mitochondrial photodamage [1]. For example, Kessel *et al.,* have proposed that mitochondrial damage may be an important step in PDT-induced apoptosis and that the mechanism of PDT-induced cell death initially appeared to have the characteristics of necrosis, but an apoptotic mechanism has been implicated in examples of phototoxicity: the apoptotic program is part of the genetic apparatus of the cell, such that some signals lead to a series of events, resulting in DNA and cellular fragmentation with these fragments engulfed by adjoining cells and inflammatory effects, which are the result from morphological changes in necrotic cells (membrane breakage, release of lysosomes), do not occur [126].

It has been described in previous literature that the ability of cytochrome c to 'trigger' apoptosis by its own release into the cytoplasm together with additional factors. Kessel *et al.,* proposed that apoptosis was initiated before the MMP was abolished suggesting that a mitochondrial modification secondary to initiation of apoptosis, leads to a decrease in the membrane potential [1, 126]. Release of other mitochondrial proteins has also been implicated in the initiation of apoptosis although the role of these products is not yet clear. For example, Bcl-2 a protein which can impair or prevent the apoptotic response to many stimuli is located in mitochondrial membranes and can prevent loss of cytochrome c. Moreover, cell lines which overexpress bcl-2 demonstrate PDT-resistance and substantial mitochondrial alterations were observed in a cell line selected for PDT resistance [126]. Mitochondrial modification after the initiation of apoptosis is suggested by the finding that protease activity associated with apoptosis can alter the ability of cytochrome c to function in the electron-transport chain indicating that loss of the MMP occurs as a result of photodynamic action rather than as a consequence of the apoptotic program [126]. The latter reflects inactivation of a membrane transport system, indicative of substantial membrane alterations. These results, along with previous reports, suggested that a delayed or absent apoptotic response is correlated with membrane photodamage, perhaps affecting membrane-associated signalling systems [126].

Mitochondrial damage in PDT has an effect on the cytoskeleton-based transportation system and mitochondrial morphology. Mitochondria need to be strategically localised at particular subcellular sites for providing energy supply and for participating in intracellular signalling [57], for example local interactions between adjacent mitochondria allow for the spreading of apoptosis. The distribution of mitochondria to strategic sites is likely to be established by a cytoskeleton-based transportation system (microfilaments, microtubules, and intermediate filaments) [57]. In fact, for the binding of cytoskeletal elements, docking proteins have been identified on mitochondria [57]. It has also been proposed that a bidirectional coupling between mitochondria motility and morphology, whereby the dynein-dynactin complex contributes to the mitochondrial targeting of Drp1, promotes mitochondrial fission to make possible anterograde transport of the mitochondria by kinesis family motors [57].

Dynactin is a multisubunit protein complex in eukaryotic cells required as an activator of cytoplasmic dynein, which is a motor protein also called molecular motor or motor molecule in cells that converts the chemical energy contained in ATP into the mechanical

energy of movement and which regulates the subcellular distribution of mitochondria by controlling the recruitment of the fission factor [127, 182]. Dynactin acts as an adapter between dynein and the cargo and enhances the movement of dynein by increasing its processivity [128].

It has been also reported (for example with Photofrin), that PDT results in a decrease in the intracellular ATP concentration [126]. Since mitochondria represent the cellular source of ATP, mitochondrial photodamage would be expected to affect ATP levels [126, 129]. Apoptosis generally requires the participation of ATP and can be initiated by a fall in cellular ATP levels, although a more substantial loss of ATP can lead to a necrotic outcome. However, Kessel concluded that the delay or absence of apoptosis after membrane photodamage is not related to ATP depletion, but it may result from leakage of other necessary cytosolic components or additional sites of membrane photodamage which inactivate proteases or other apoptotic factors [126].

In summary these results suggest that mitochondrial photodamage can directly initiate apoptosis by leading to loss of products into the cytoplasm which serves to initiate a late step in the apoptotic program without intermediate signal-transduction pathways but, the role of the release of other mitochondrial proteins that has been implicated in the initiation of apoptosis is not yet clear [126].

What is important for an efficient biological response in PDT is the localization of the photosensitizer, as said above, and the illumination process.

Selectivity of PDT effects may also be enhanced by appropriate manipulation of the illumination process by varying the timing of the illumination since photosensitizer distribution is dependent on the time after delivery. In relation to that, there appears to be a threshold for PDT effects: at low doses of light and/or photosensitizer tissue damage seems repairable [1]. Moreover, the source must generate light at a wavelength, or over a wavelength range, that matches the activation spectrum of the photosensitizer. While most photosensitizers can be activated over a wide range of wavelengths, it is clearly best to activate the drug at its maximum absorption, since this will generate the greatest concentration of toxic photoproducts such as $^1O_2$ [1].

The photosensitizers of greatest interest in PDT bind to various cytoplasmic membranes but are not found in the nucleus and do not bind to DNA [60]. Nevertheless, some DNA damage is produced that can lead to mutagenesis, the extent of which is dependent on the photosensitizer, the cellular repair properties and the target gene. The initial oxidative

reactions lead to damage to organelles in which the dye is bound, culminating in cell death and destruction of the tumour or abnormal tissue [60]. PDT also triggers the activation of several signal transduction pathways in the treated cells; some of these are stress responses aimed at cell protection, while others are likely to contribute to the cell death process and apoptosis is a common mechanism of cell death after PDT both *in vitro* and *in vivo* [60].

Even if the vast majority of published cell studies have demonstrated that cellular phototoxicity is likely caused by the generation of reactive singlet oxygen by photosensitizers associated with organelles such as the lysosomes and mitochondria, studies have demonstrated that in cells treated with several different photosensitizers, the interphase nucleus was the most sensitive target site, followed by the perinuclear cytoplasm, and finally the peripheral cytoplasm [130]. There are also several studies that demonstrate a PDT effect on DNA, chromosomes and the mitotic spindle [130]. However, it is not clear whether these effects are due to generation of singlet oxygen elsewhere in the cell, or directly at the nuclear/mitotic spindle site [130].

Verteporfin has been reported as an example of a photosensitizer which induces apoptosis after mitochondrial photodamadge (figure 5.1). It has been described that immediately after PDT, an increase in mitochondrial cytochrome c and apoptosis-inducing factor (AIF) levels were detected in the cytosol in primary human aortic SMCs and that cytosolic levels of the pro-apoptotic Bcl-2 family member Bax decrease reciprocally throughout this period, but this change did not occur before cytochrome c release. Caspase-9 and caspase-3 activity was also visible after cytochrome c release followed by caspase-6, -7 and -8 [131]. The AIF is a bifunctional pro-apoptotic mitochondrial protein with both an electron acceptor/donor (oxidoreductase) function and an apoptogenic function. It has been shown in certain cell types to be released from mitochondria whereupon it translocates to nuclei and stimulates chromatin condensation and DNA fragmentation. However, this study underlined that individual cell types respond differently to PDT and may use distinct biochemical pathways to achieve apoptotic cell death [131]. As such, it was of interest to our group to determine the effects of RE84 and RE85 on the cytoskeleton, mitochondria and nuclei.

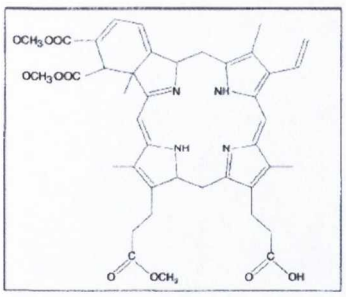

Figure 5.1: Chemical structure of verteporfin adapted from [129].

Results

5.1 RE84 and 85 induce intracellular ROS production in a light dependent manner

In order to confirm the potential of these compounds to produce ROS and to quantify it, DCFH-DA dye (10μM) was used. The cells were treated with RE84 and 85 at different concentrations (1, 3 and 5μM) with and without pre-treatment for 1h with Nac (5mM) and incubated for 24h before being exposed to light or maintained in the dark. The results are shown in figures 5.2 and 5.3.

Results showed an increase in ROS production in a light dependent manner with increasing concentrations of the compounds. Moreover, the addition of Nac reduced the light dependent ROS production, but only in cells treated with RE84.

5.2 RE84 and 85 decrease mitochondrial membrane potential

With the aim to analyse the effect that RE84 and 85 have on mitochondria, the variation of the mitochondrial membrane potential was investigated using JC-1 dye. The cells were treated with RE84 and 85 at 3μM and incubated for 2 and 4h in the dark.

The results are shown in figures 5.4. Results showed a decrease in the mitochondrial membrane potential in a time dependent manner. RE84, decreased the mitochondrial membrane potential to a greater extent than RE85.

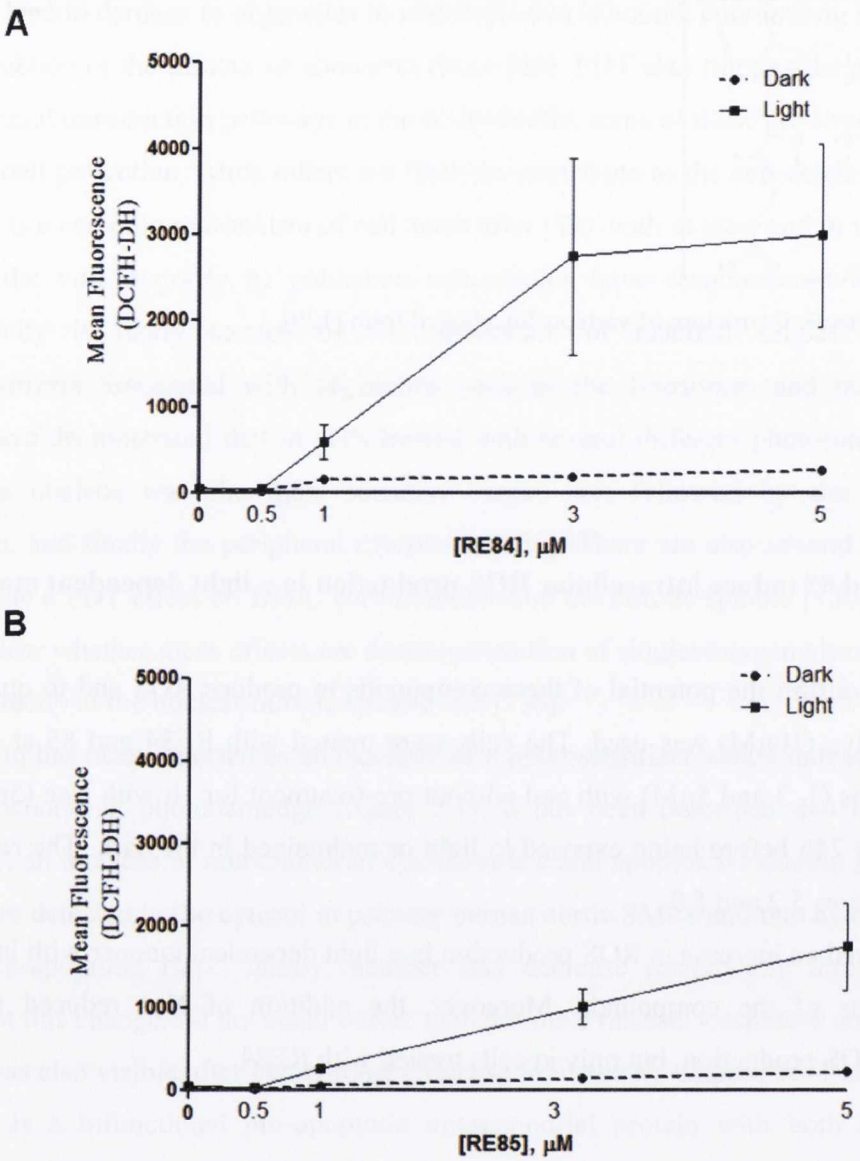

Figure 5.2: **RE84 and 85 induce ROS production in HeLa cells.**

$3x10^5$ cells were seeded in 6-well plates (3ml total volume/well). Cells were incubated at 37°C overnight before treatment. The cells were treated with 0.5, 1, 3 and 5µM of RE84 **(A)** and 85 **(B)**. Following 24h incubation the treated cells were exposed to light for 1h to give light doses of $12.66J/cm^2$ or maintained in the dark. Cells were then washed with warm PBS and stained with DCFH-DA (10µM) and DRAQ7 (1.5µM) as described in Section 2.9.10. The 488nm laser was used to excite the DCFH-DA and the 405nm laser was used to excite the DRAQ-7. DCFH-DA was detected in FL2 (Em: 575nm) and the compounds were detected in FL4 (Em: 680nm). Cell analysis was performed on the CyAn using appropriate gates counting 10,000 cells and using Summit software package. The necessary compensations were made to exclude the fluorescence of the compounds and the dead cells. The percentage of mean fluorescence within the cells was analysed using Flow Jo software, which generates histograms, and data was expressed as the mean ± S.E.M. and graphed using GRAPHPAD Prism software.

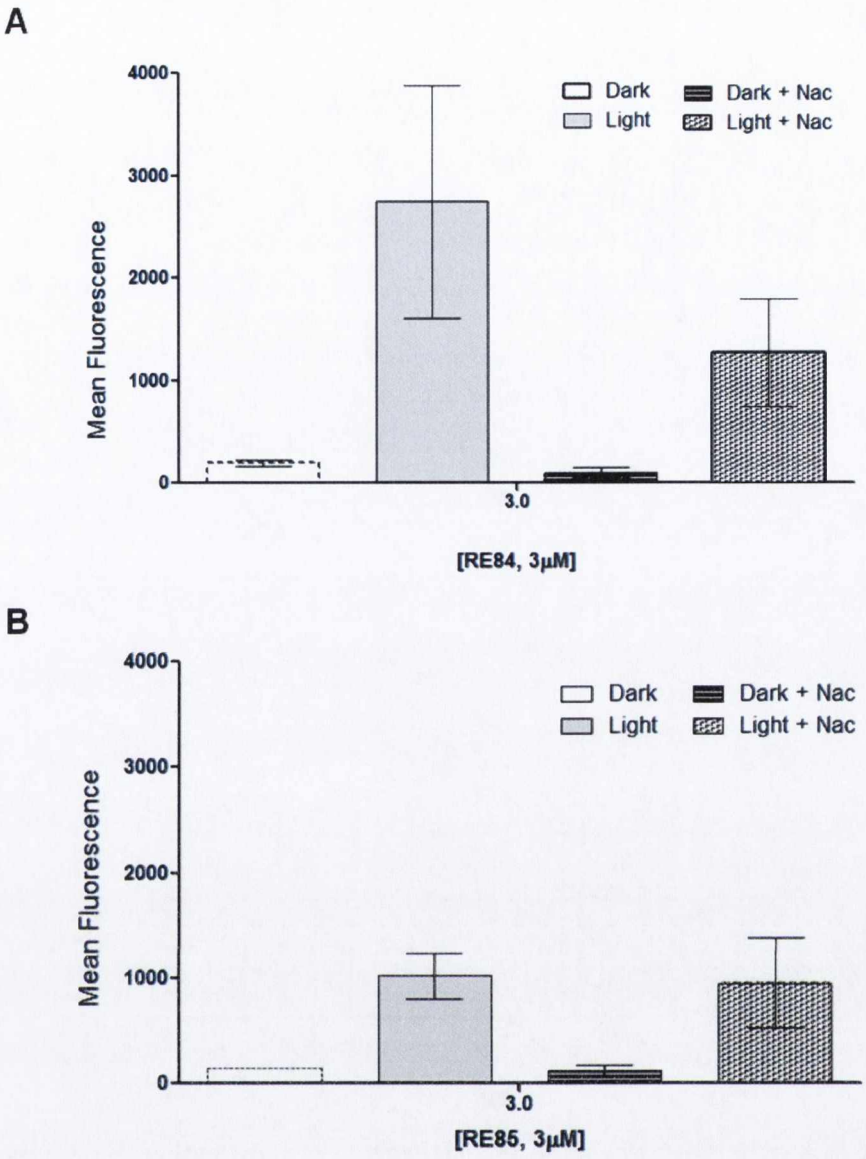

Figure 5.3: **RE84 and 85 induce ROS production in HeLa cells.**

$3x10^5$ cells were seeded in 6-well plates (3ml total volume/well). Cells were incubated at 37°C overnight before treatment. The cells were pre-treated with 5mM of Nac for 1h followed by treatment with 3μM of RE84 **(A)** and RE85 **(B)**. Following 24h incubation the treated cells were exposed to light for 1h to give light doses of $12.66J/cm^2$ or maintained in the dark. Cells were then washed with warm PBS and stained with DCFH-DA (10μM) and DRAQ7 (1.5μM) as described in Section 2.9.10. The 488nm laser was used to excite the DCFH-DA and the 405nm laser was used to excite the DRAQ-7. DCFH-DA was detected in FL2 (Em: 575nm) and the compounds were detected in FL4 (Em: 680nm). Cell analysis was performed in the CyAn using appropriate gates counting 10,000 cells and using Summit software package. The necessary compensations were made to exclude the fluorescence of the compounds and the dead cells. The percentage of mean fluorescence within the cells was analysed using Flow Jo software, which generates histograms, and data was expressed as the mean ± S.E.M. and graphed using GRAPHPAD Prism software. Results were then compared with cells without pre-treatment with Nac.

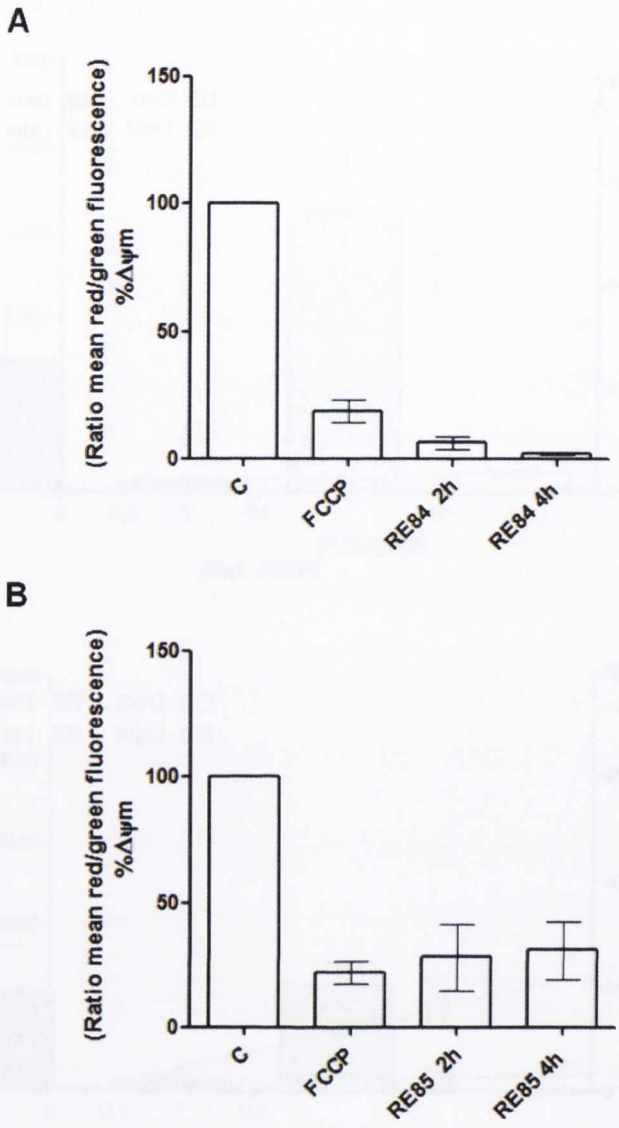

Figure 5.4: **RE84 and 85 reduce the mitochondrial membrane potential in HeLa cells.**

$3x10^5$ cells were seeded in 6-well plates (3ml total volume/well). Cells were incubated at 37°C overnight before treatment. The cells were treated with RE84 **(A)** and 85 **(B)** at 3μM. After 2 and 4h incubation in the dark cells were harvested by scraping and adjusted to a total volume of 1 ml with prewarmed fresh complete cell culture medium. Cells were then stained with JC-1 as described in Section 2.9.11. As a positive control, cells were treated with 0.25mM of FCCP.
The 488nm laser was used to excite the monomeric JC-1, green fluorescence, was detected in FL1 (Em: 530nm), the aggregate JC-1, orange/red fluorescence, was detected FL2 (Em: 575nm) and the compounds were detected in FL4 (Em: 680). Cell analysis was performed on the CyAn using appropriate gates counting 10,000 cells and using Summit software package. The standard compensations were performed using the depolarising-treated sample, the untreated control and by excluding the fluorescence of the compounds. The percentage of fluorescence within the cells was analysed using Flow Jo software. The ratio of red/green mean fluorescence ± S.E.M values represent the mitochondrial membrane potential and were expressed as a percentage of the untreated control which is taken as 100%, results were graphed using GRAPHPAD Prism software.

5.3 RE84 dramatically and rapidly affects the mitochondrial morphology when illuminated

Confocal experiments were performed to investigate any effect of the compounds on mitochondrial morphology. As a preliminary experiment, HeLaDsRed transfected cells were incubated for 2h with 5μM of RE84 and viewed using confocal microscopy before mitochondrial movement/effect experiments were performed. The results are shown in figures 5.5 to 5.7.

Results showed RE84 to have a dramatic effect on the mitochondria a few minutes after a short laser irradiation, which consisted of rounding and/or swelling of the mitochondria. It was observed that cells irradiated with the 488nm laser together with the 543nm laser accelerated mitochondrial rounding. Moreover, the use of the mercury bulb (white-green region) in the confocal made this process even more dramatic. The mitochondrial-morphology change after light exposure suggested mitochondria photodamage which can potentially lead to cell death. The mitochondria morphology of the untreated cells did not change after light exposure to either 543nm+mercury bulb or 488nm+mercury bulb laser as shown in figure 5.5. The videos are available in the DVD included in the back cover of the thesis.

5.4 RE84 affects the mitochondria in a dramatic manner

In order to study the effects of RE84 on mitochondria, HeLaDsRed cells were treated with different concentrations of the compound (1, 3, 5μM). Moreover, cells were exposed to laser light at different wavelengths (543 and 488nm) to visualise any differential effects of the compound on the mitochondria/cell.

This study was performed using spinning disk confocal microscopy because it is the better technique of choice for investigation of dynamics in living cells. The results are shown in figures 5.8 and 5.10.

Results showed that the form of cell death depends on the concentration of the compound and the form of light source used. The 488nm laser, which is the wavelength that maximally activates the compound, accelerated the cell death. Moreover, low concentrations of the compound led to apoptotic bodies while at high concentrations cell death appeared to have the characteristics of necrosis.

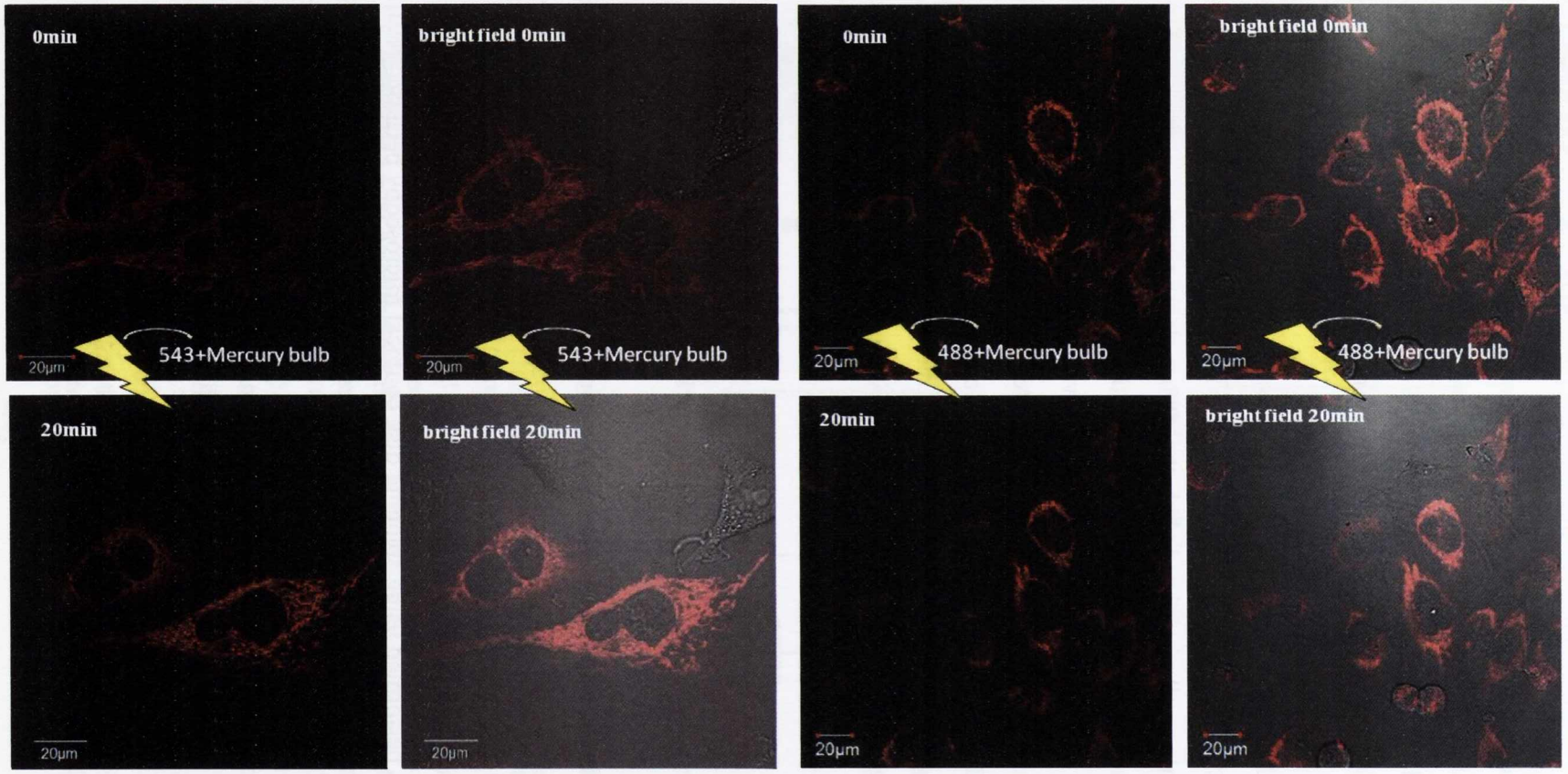
0min
bright field 0min
0min
bright field 0min
20μm
543+Mercury bulb
20μm
543+Mercury bulb
20μm
488+Mercury bulb
20μm
488+Mercury bulb
20min
bright field 20min
20min
bright field 20min
20μm
20μm
20μm
20μm

Figure 5.5: **Untreated HeLa-DsRed cells excited with a 543 or 488nm laser and mercury bulb.**

$1x10^5$ cells/well were seeded in dish plates (Ø 22mm; 2ml total volume/well). Cells were incubated at 37°C overnight before being analysed. Cells were washed twice in PBS followed by the addition of fresh media followed by viewing using Olympus FV1000 confocal microscopy with a 60x oil immersion lens. Image analysis was performed using FluoView Version 7.1 Software. DsRed was excited by a 543nm argon laser, emission 583nm. Results are representative of three independent experiments. The orange arrow indicates the linear mitochondria.

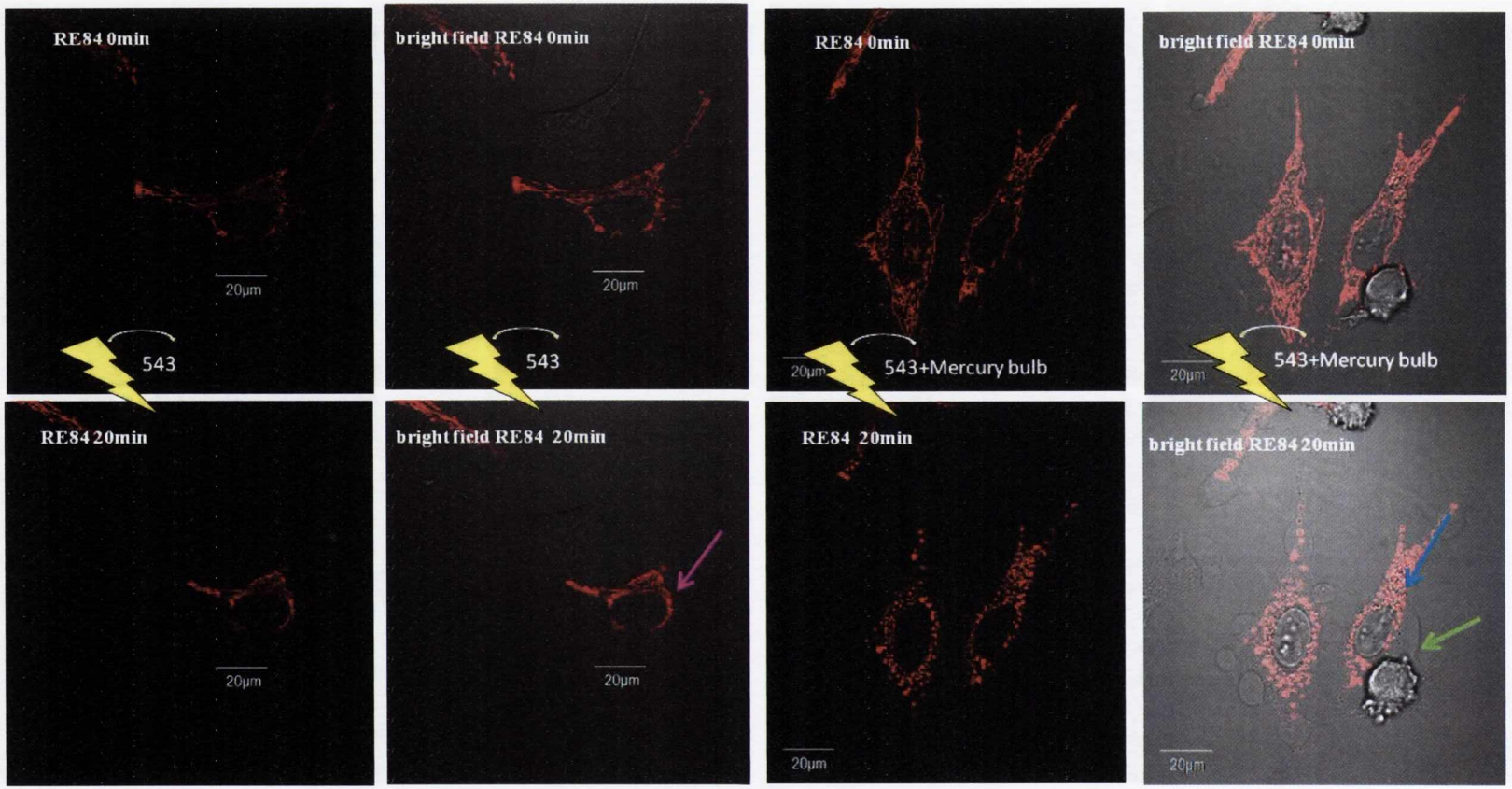
RE84 0min
20μm
543
bright field RE84 0min
20μm
543
RE84 0min
20μm
543+Mercury bulb
bright field RE84 0min
20μm
543+Mercury bulb
RE84 20min
20μm
bright field RE84 20min
20μm
RE84 20min
20μm
bright field RE84 20min
20μm

Figure 5.6: **Effect of RE84 on mitochondria after activation of the compound with a 543nm laser±mercury bulb.**

$1x10^5$ cells/well were seeded in dish plates (Ø 22mm; 2ml total volume/well). Cells were incubated at 37°C overnight before treatment. The cells were then treated with 5μM of RE84 for 2h before viewing using Olympus FV1000 confocal microscopy with a 60x oil immersion lens. Image analysis was performed using FluoView Version 7.1 Software. DsRed was excited by a 543nm argon laser, emission 583nm. Results are representative of three independent experiments. The orange arrow indicates the linear mitochondria, the blue one indicates the round mitochondria, the green one indicates the cell swelling and the pink one indicates cell shrinkage.

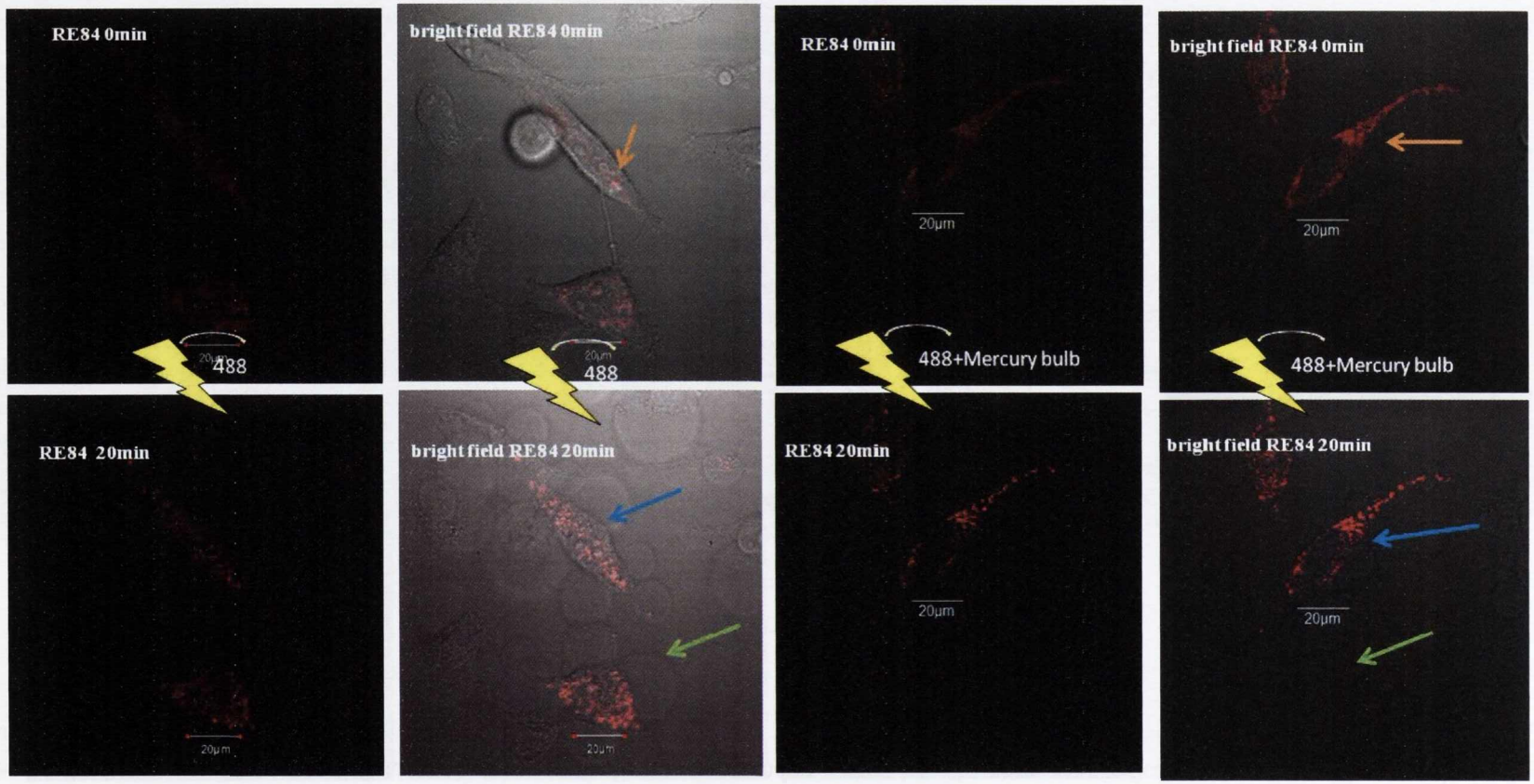
RE84 0min
488
bright field RE84 0min
488
RE84 0min
20μm
488+Mercury bulb
bright field RE84 0min
20μm
488+Mercury bulb
RE84 20min
20μm
bright field RE84 20min
20μm
RE84 20min
20μm
bright field RE84 20min
20μm

Figure 5.7: **Effect of RE84 on mitochondria after activation of the compound with a 488nm laser±mercury bulb.**

$1x10^5$ cells/well were seeded in dish plates (Ø 22mm; 2ml total volume/well). Cells were incubated at 37°C overnight before treatment. The cells were then treated with 5μM of RE84 for 2h before viewing using Olympus FV1000 confocal microscopy with a 60x oil immersion lens. Image analysis was performed using FluoView Version 7.1 Software. DsRed was excited by a 543nm argon laser, emission 583nm and the compound was excited with a 488nm laser, emission 630nm. Results are representative of three independent experiments. The orange arrow indicates the linear mitochondria, the blue one indicates the round mitochondria and the green one indicates the cell swelling

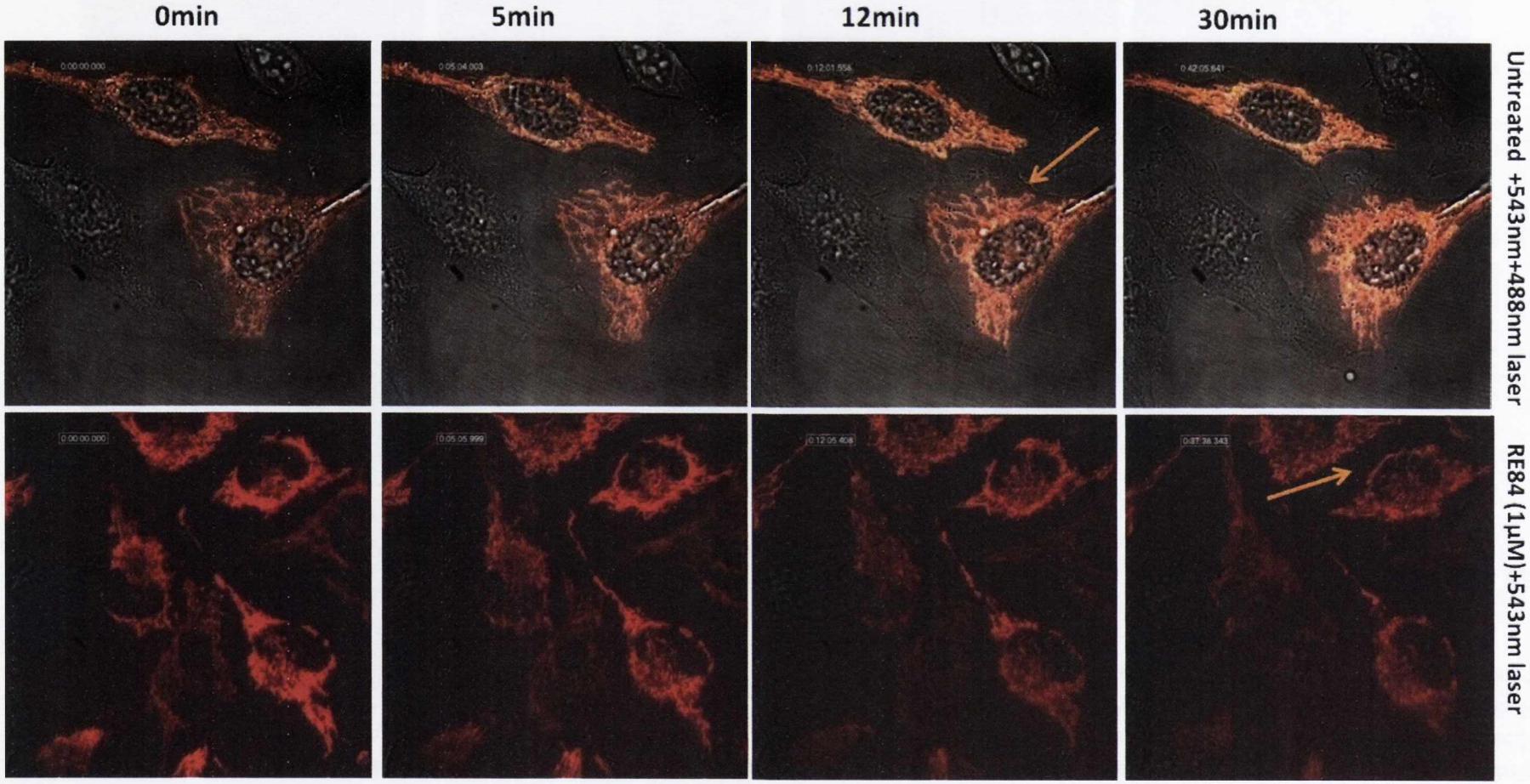
0min
5min
12min
30min
Untreated +543nm+488nm laser
RE84 (1μM)+543nm laser

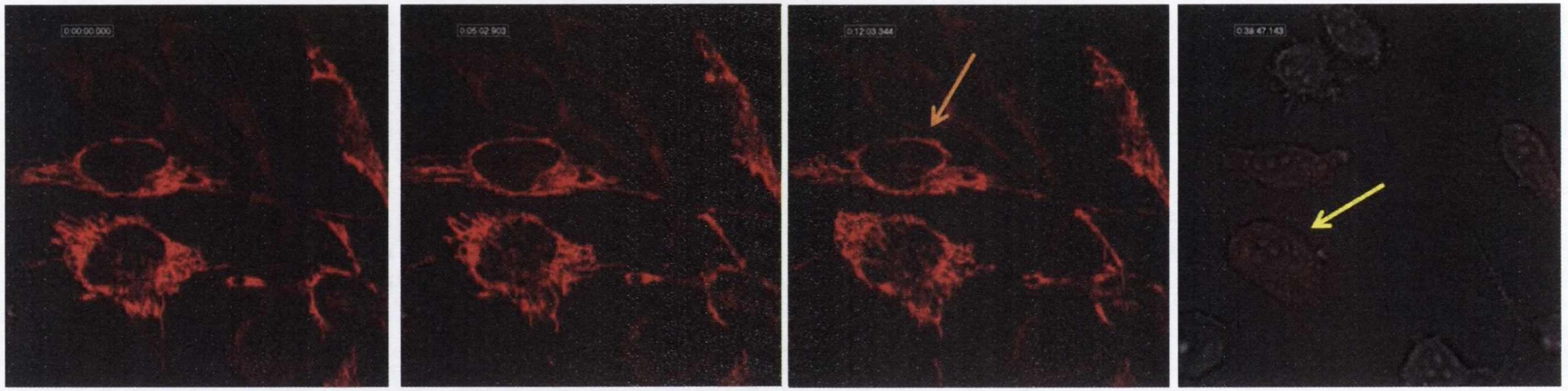

Figure 5.8: **Light-dependent mitochondria damage/cell death investigated using life video capturing.**

$1x10^5$ cells/well HeLaDsRed cells were plated in glass bottom dish plates (Ø 22 mm; 2ml total volume/well). Cells were incubated at 37°C overnight before treatment. The cells were then treated with RE84 at 1μM and incubated for 30min. Cells were washed twice in PBS followed by the addition of fresh media before viewing using Olympus IX81-DSU Spinning Disk Confocal Microscope with a 60x oil immersion lens. Image analysis was performed using IQ2 Software. During the 30min video cells were at 37°C, 5% CO_2 at 4% laser intensity for the 543nm laser and at 10% intensity for the 488nm laser (laser was only on when the images were taken). Experimental cells were irradiated with the 543nm laser ± 488nm laser. The orange arrow indicates the linear mitochondria and the yellow one indicates apoptotic bodies.

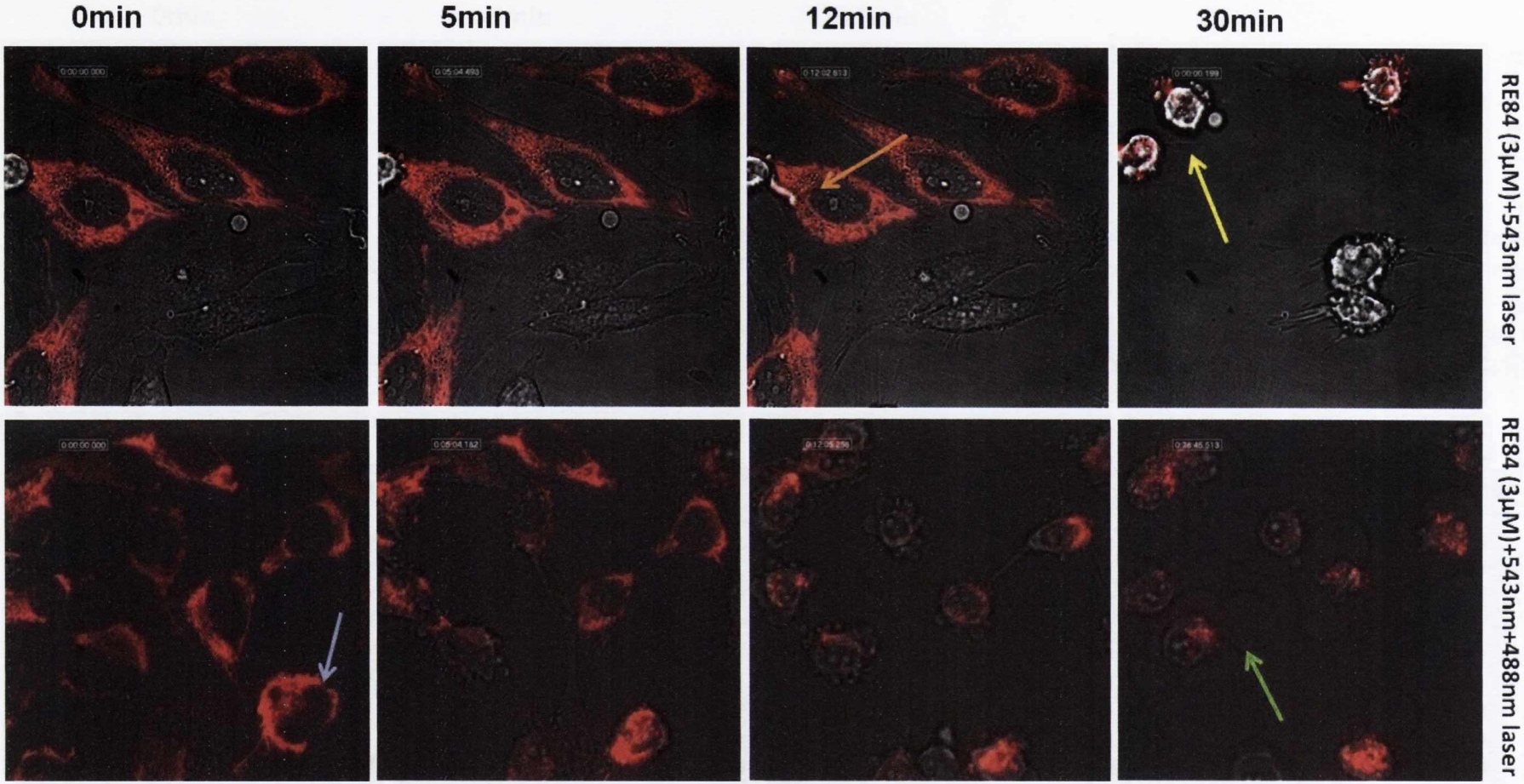
0min
5min
12min
30min
RE84 (3μM)+543nm laser
RE84 (3μM)+543nm+488nm laser

Figure 5.9: **Light-dependent mitochondria damage/cell death investigated using life video capturing.**

$1x10^5$ cells/well HeLaDsRed cells were plated in glass bottom dish plates (Ø 22 mm; 2ml total volume/well). Cells were incubated at 37°C overnight before treatment. The cells were then treated with RE84 at 3μM and incubated for 30min. Cells were washed twice in PBS followed by the addition of fresh media before viewing using Olympus IX81-DSU Spinning Disk Confocal Microscope with a 60x oil immersion lens. Image analysis was performed using IQ2 Software. During the 30min video cells were at 37°C, 5% CO_2 at 4% laser intensity for the 543nm laser and at 10% intensity for the 488nm laser (laser was only on when the images were taken). Experimental cells were irradiated with the 543nm laser ± 488nm laser. The orange arrow indicates the linear mitochondria, the green one indicates the cell swelling , the yellow one indicates apoptotic bodies and the violet one indicates mitochondria clustering.

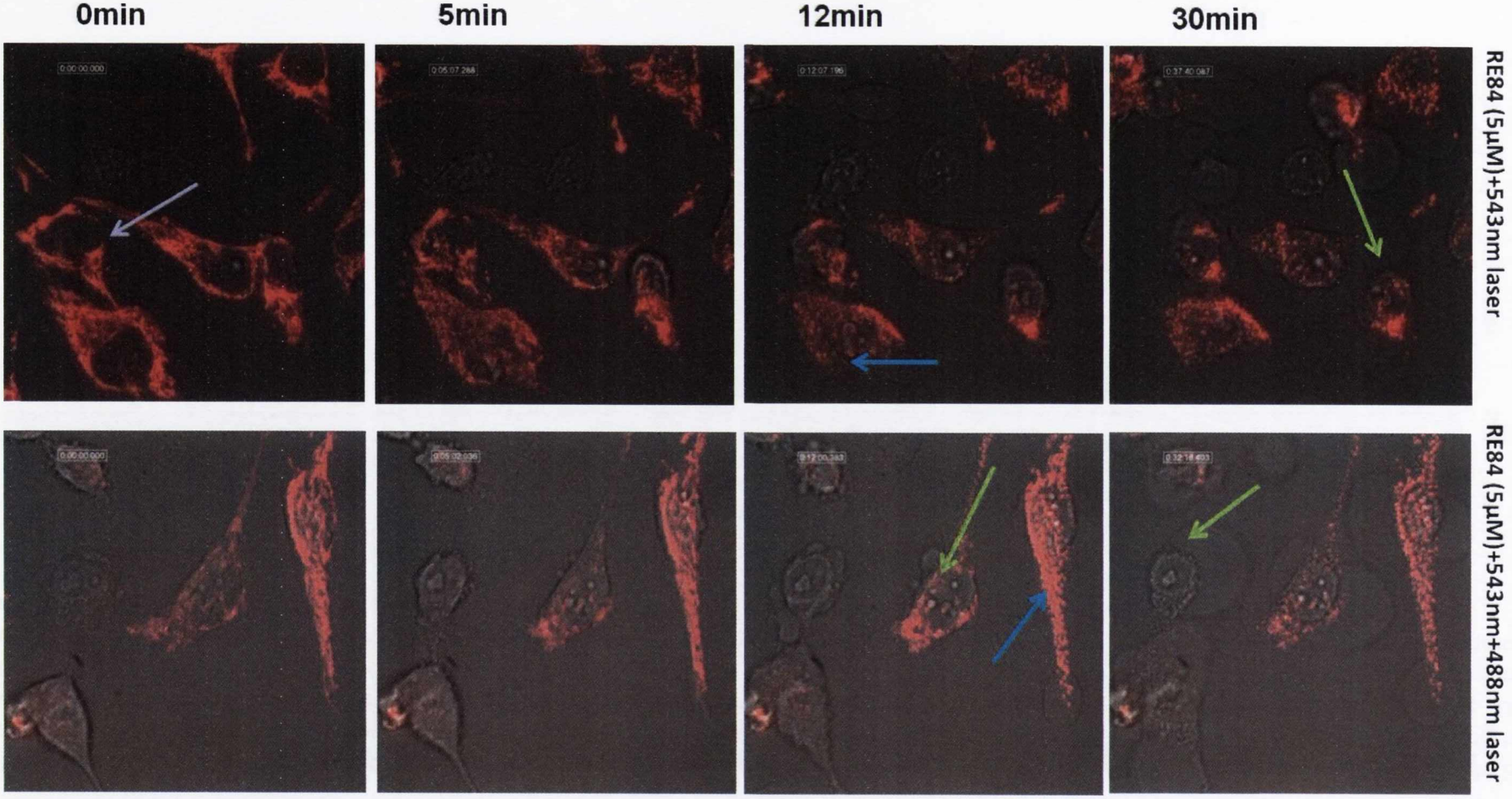
0min
5min
12min
30min
RE84 (5μM)+543nm laser
RE84 (5μM)+543nm+488nm laser

Figure 5.10: **Light-dependent mitochondria damage/cell death investigated using life video capturing.**

1x105 cells/well HeLaDsRed cells were plated in glass bottom dish plates (Ø 22 mm; 2ml total volume/well). Cells were incubated at 37°C overnight before treatment. The cells were then treated with RE84 at 5μM and incubated for 30min. Cells were washed twice in PBS followed by the addition of fresh media before viewing using Olympus IX81-DSU Spinning Disk Confocal Microscope with a 60x oil immersion lens. Image analysis was performed using IQ2 Software. During the 30min video cells were at 37°C, 5% CO2 at 4% laser intensity for the 543nm laser and at 10% intensity for the 488nm laser (laser was only on when the images were taken). Experimental cells were irradiated with the 543nm laser ± 488nm laser. The blue one indicates the round mitochondria, the green one indicates the cell swelling and the violet one indicates mitochondria clustering.

Mitochondrial photodamage, which results in mitochondrial morphology changes such as rounding and/or swelling of the mitochondria, can directly initiate the apoptosis process. Mitochondrial clustering around nucleus was also observed. Untreated cells did not show any difference in the mitochondrial morphology after light exposure to either 543 or 488nm laser as shown in figure 5.8. The videos are available in the DVD included in the back cover of the thesis.

5.5 RE84 and 85 are localized in the mitochondria

In order to have independent evidence for mitochondrial localisation/uptake of RE84 and 85 rather than nuclear localisation, fractions of cells treated with the compounds were isolated into mitochondrial and nuclear fractions.

The presence of the compounds in the fractions was determined using a fluorimeter to verify the emission of each compound per fraction. Compounds were excited using a 444nm laser (Ex: 430nm; Em: 630nm). HeLa cells were incubated with 3μM of RE84 and 85 for 4 and 24h in the dark before the emission of the fractions was determined. Spectra of the fractions are shown in figures 5.11 for compound RE84 and 5.12 for compound RE85.

In order to investigate the purity of the nuclear and mitochondrial isolated fractions, Western blot analysis was performed. Samples were prepared as described in Section 2.11.2, and Western blot was performed as described in Section 2.11.3-4 using Anti-mouse-Lamin A mAb (69KDa) and Anti-mouse-PDH E1-α mAb (Pyruvate dehydrogenase substrate E1-α, 41KDa) antibodies. Lamin A is a specific antibody for nuclear proteins and PDH E1-α is a specific antibody for mitochondrial proteins.

The pyruvate dehydrogenase complex (PDH) is at the centre of aerobic carbohydrate metabolism. It is localized in the matrix space of mitochondria where it catalyzes the irreversible oxidative decarboxylation of pyruvate entering the organelle to produce acetyl-CoA, NADH and CO_2. PDH is a complex of three different enzymes: pyruvate dehydrogenase (E1), dihydrolipoamide transacetylase (E2) and dihydrolipoamide dehydrogenase (E3).

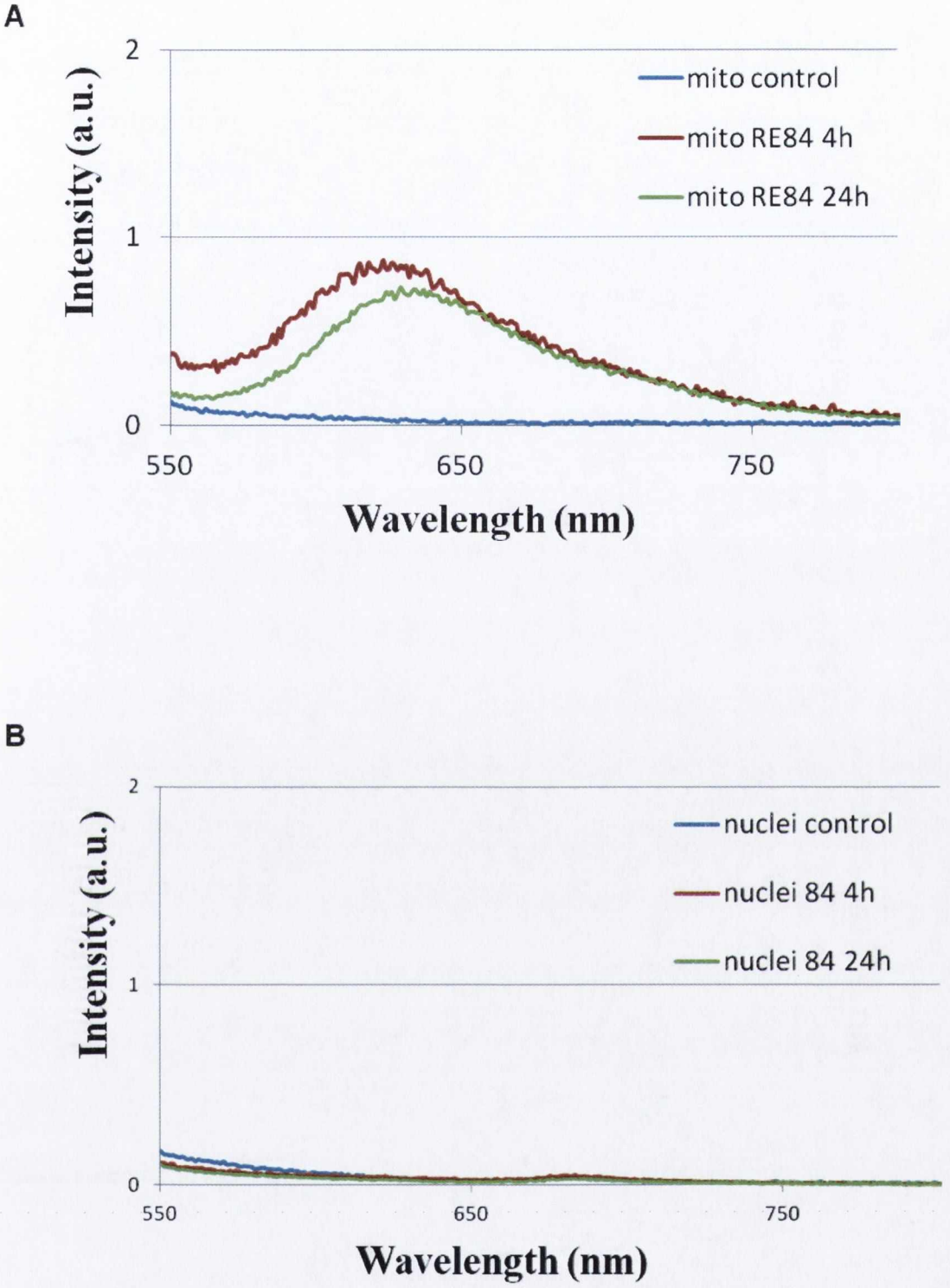

Figure 5.11: UV/Visible, excitation and emission spectra of the mitochondrial **(A)** and nuclear **(B)** fractions of HeLa cells treated with RE84 for 4h and for 24h in 10mM phosphate buffer, pH7.4.

A

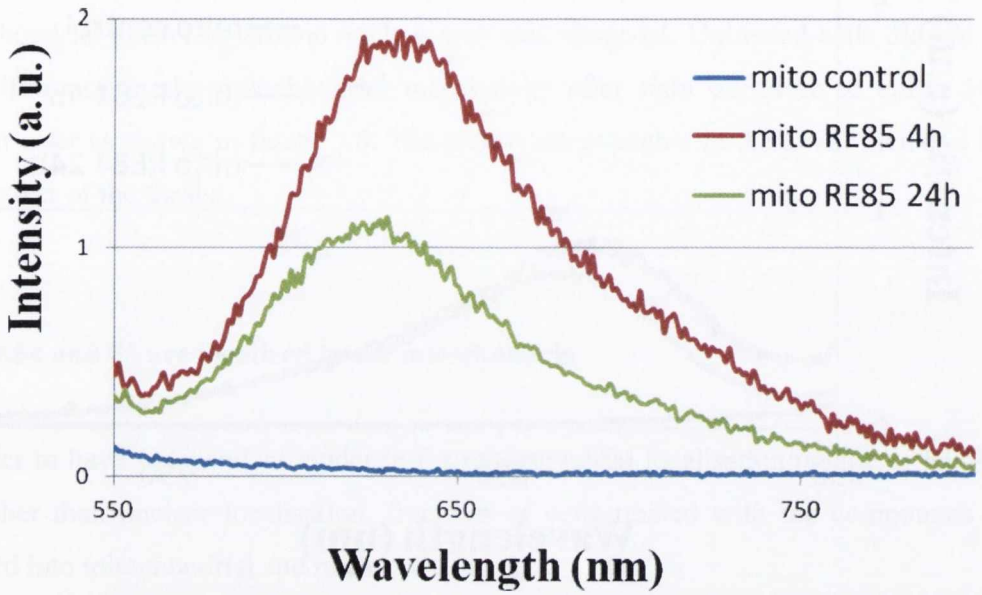

B

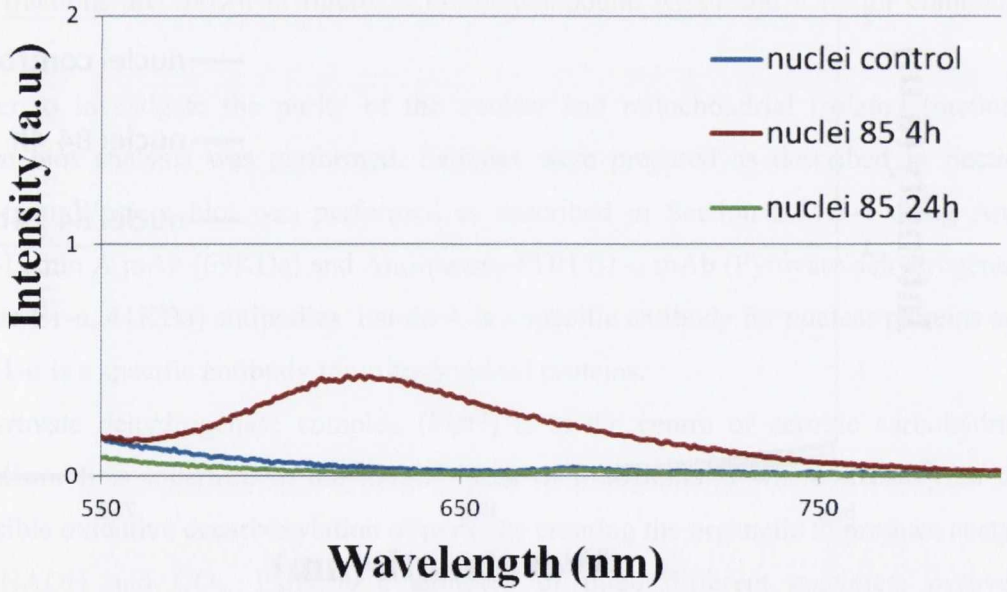

Figure 5.12: UV/Visible, excitation and emission spectra of the mitochondrial **(A)** and nuclear **(B)** fractions of HeLa cells treated with RE85 for 4h and for 24h in 10mM phosphate buffer, pH7.4.

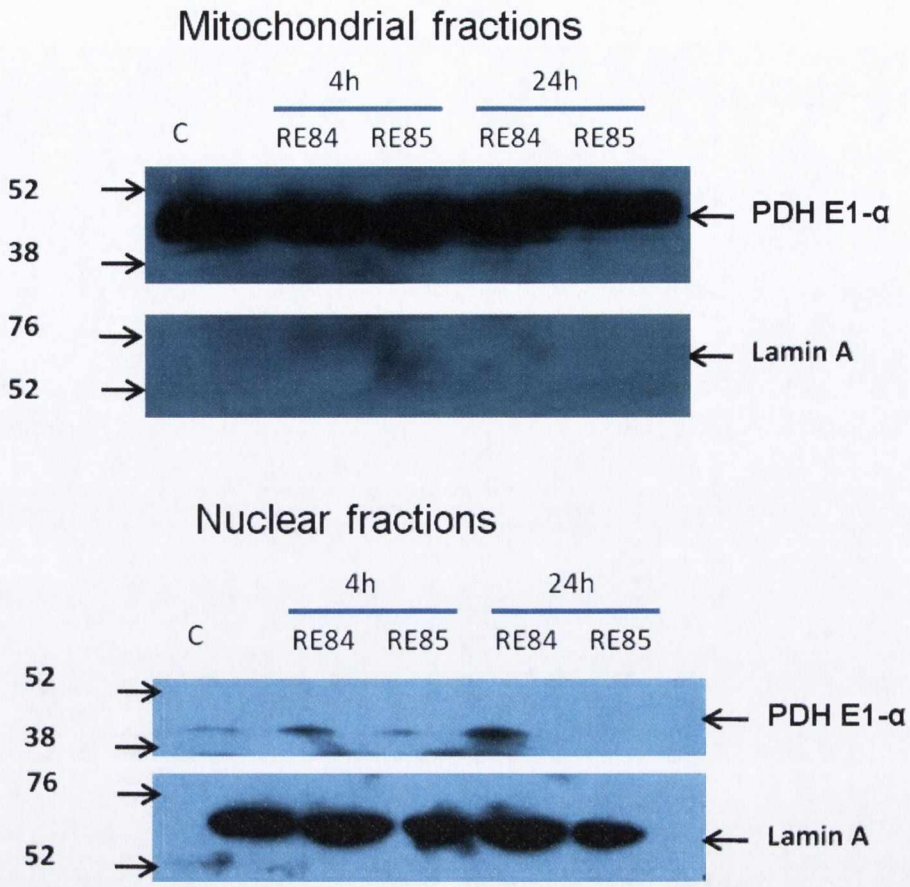

Figure 5.13: **Mitochondrial and nuclear fraction purity.**

Samples were standardised by protein concentration to 80µg/well for the mitochondrial fractions and 400µg/well for the nuclear fractions with 1x Laemmli buffer (60mM Tris-base (pH6.8), 4% SDS, 20% Glycerol) followed by sonication for 11s to shear the membranes. Then, the samples were heated in a pre-warmed heating block for 2min at 100°C followed by addition of 1M DTT (1:20; final concentration 50mM) and bromophenol blue sample buffer (1:20) for visualisation of each sample. The lysates were incubated on ice until the gel was prepared. Western blot was performed as described in Materials and Methods Section. Membranes were probed with an anti-PDH E1-α (41KDa) and an anti-Lamin A (69KDa) antibody. Results are representative of three independent experiments.

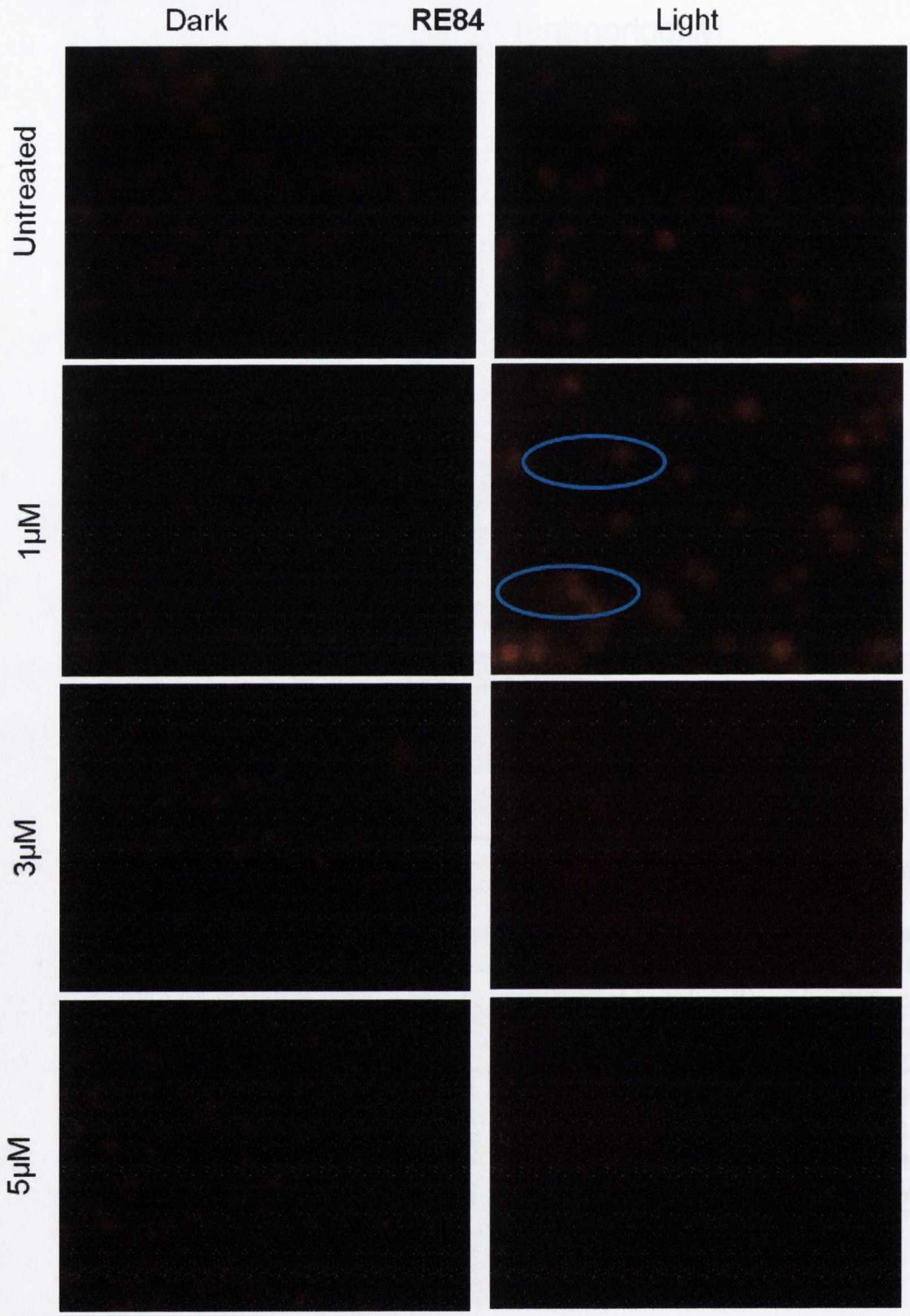
Dark
RE84
Light
Untreated
1μM
3μM
5μM

Figure 5.14: **RE84 induces DNA strand breakage at 1μM in HeLa cells.**

$0.3x10^6$ HeLa cells were seeded in a 6-well plate (3ml/well) and incubated at 37°C overnight before being treated. Cells were then treated with 1, 3 and 5μM of RE84 and incubated at 37°C for 24h before being exposed to light for 1h to give a light dose of $12.66J/cm^2$ or maintained in the dark. Following which, cells were resuspended in LMPA and added to slides pre-coated with NMPA. Samples were then lysed for 2h, subjected to electrophoresis for 30min, neutralized and stained with PI. Slides were viewed using an Olympus IX81 microscope with a 20x lens. The software Cell^P was used to collect images. Results are representative of three independent experiments. The comet tails are circled in blue.

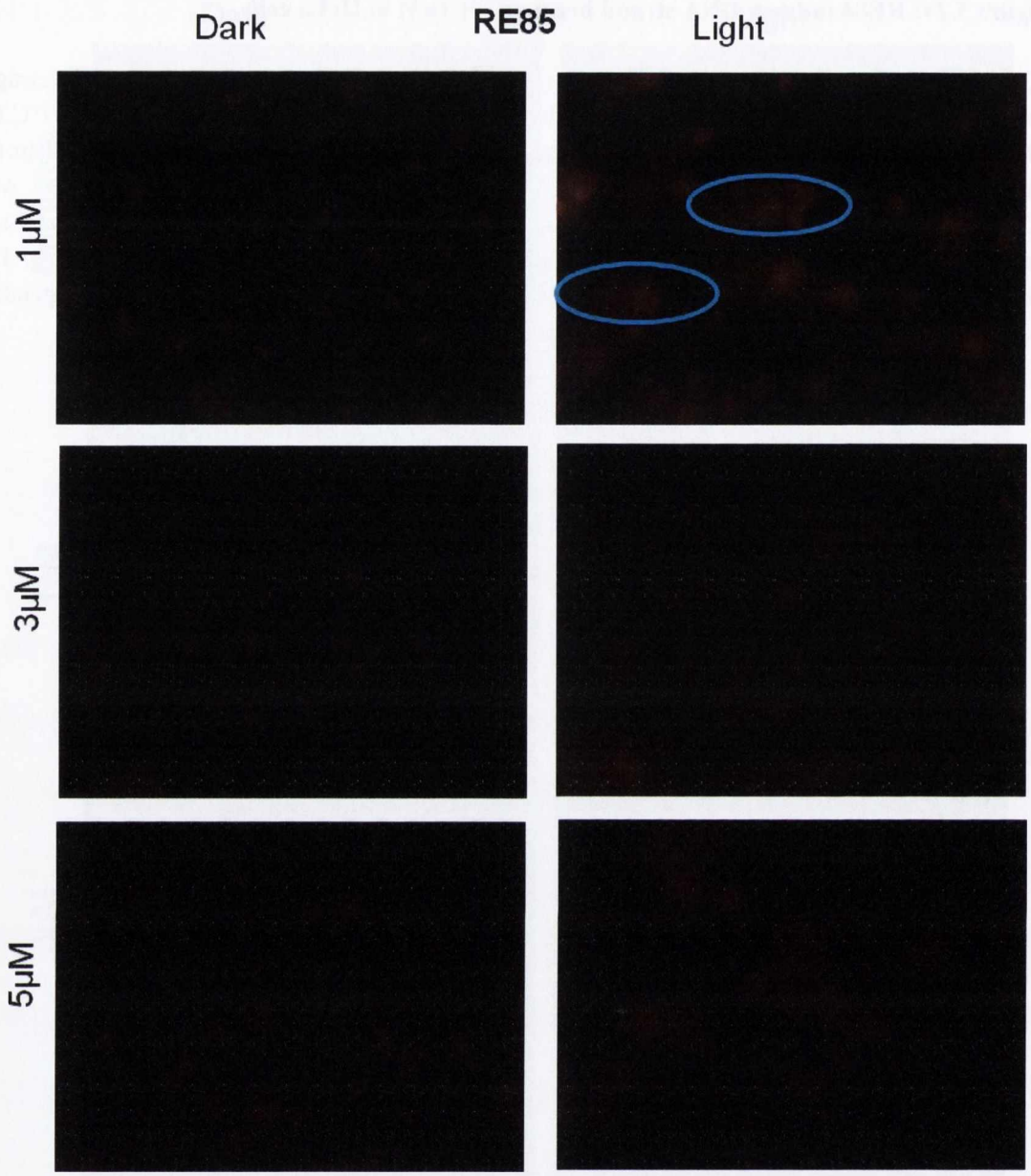

Figure 5.15: **RE85 induces DNA strand breakage at 1µM in HeLa cells.**

$0.3x10^6$ HeLa cells were seeded in a 6-well plate (3ml/well) and incubated at 37°C overnight before being treated. Cells were then treated with 1, 3 and 5µM of RE85 and incubated at 37°C per 24h before being exposed to light for 1h to give a light dose of $12.66J/cm^2$ or maintained in the dark. Following which, cells were resuspended in LMPA and added to slides pre-coated with NMPA. Samples were then lysed for 2h, subjected to electrophoresis for 30min, neutralized and stained with PI. Slides were viewed using an Olympus IX81 microscope with a 20x lens. The software Cell^P was used to collect images. Results are representative of three independent experiments. The comet tails are circled in blue.

Nuclear lamins (Lamin A, Lamin B and Lamin C, which is a splice variant of Lamin A, differing only at the carboxy-terminus), instead, are critical to maintaining the integrity of the nuclear envelope and cellular morphology. Nuclear lamins are used as nuclear markers because they can be detected only if the nucleus in the sample is intact so it is also a marker for nuclear integrity.

Lamin A protein was found in the nuclear fraction, but not in the mitochondrial fraction, suggesting that mitochondrial fraction is not contaminated with nuclei whereas the nuclear fraction might have a small amount of mitochondrial contamination as shown in figure 5.13.

These results correlate with the confocal microscopy results from Chapter 4 which showed accumulation of most if not all of the compounds in mitochondria at either 4 or 24h rather the nucleus

5.6. RE84 and 85 induce DNA single strand damage

In order to detect DNA damage, the comet assay was performed as described in Section 2.14. HeLa cells were treated with different concentrations of the compounds (1, 3 and 5μM) and incubated for 24h before being exposed to light or maintained in the dark. The results are shown in figures 5.14 and 5.15.

Only illuminated cells treated with 1μM of RE84 and 85 showed single stranded DNA migration and damage compared to dark, untreated controls as illustrated by the comet tails. At higher concentrations than 1μM (3 and 5μM), the DNA in the samples treated with the light was completely destroyed. DNA damage most likely occurs after mitochondrial damage due to the production and diffusion of ROS/$^1O_2$ from the site of production, which is mitochondria, to DNA, as confocal and spinning disk microscopy suggested. Mitochondrial DNA (mtDNA) molecules are too small (about 17 kb) to be detected using the comet assay [132]. They have been visualised by fluorescent in situ hybridisation with 'padlock' probes and appear clustered around the nucleus of embedded cells, but as soon as lysis starts, the mtDNA begins to disperse, and by the time electrophoresis begins virtually no mtDNA molecules are left [132].

5.7 Effect of RE84 and 85 with F-actin and α-Tubulin.

Considering that PDT has a strong effect on cell division, probably due to microtubule damage, it was thought to investigate on the effect of RE84 and 85 on the cytoskeleton structure, such as actin and tubulin filaments.

In relation to that, HeLa cells were incubated with 5μM of RE84 and 85 for 24h in the dark and then for one half of the replicates the cells were illuminated for 1h, and then all the cells incubated for further 23h or fixed after light exposure as described in Section 2.8.1.

After being fixed, the cells were stained for visualisation with F-actin using an Alexa Fluor 488 Phalloidin probe or with a monoclonal anti-α-tubulin antibody overnight followed by incubation with a secondary antibody anti-mouse Alexa 633. DAPI stain was again utilised to stain the nucleus. The results are shown in figures 5.16 to 5.25.

The confocal microscopy images showed no change in the actin structure after light treatment. On the other hand, a drastic tubulin disruption was shown only after light treatment with compounds RE84 and 85. In fact, cells without light stay healthy without showing morphological changes as is shown in the 3D images in figure 5.24 suggesting that cells can tolerate the compounds. Cell shrinkage was evident in the cells after light exposure but not in cells not illuminated or untreated.

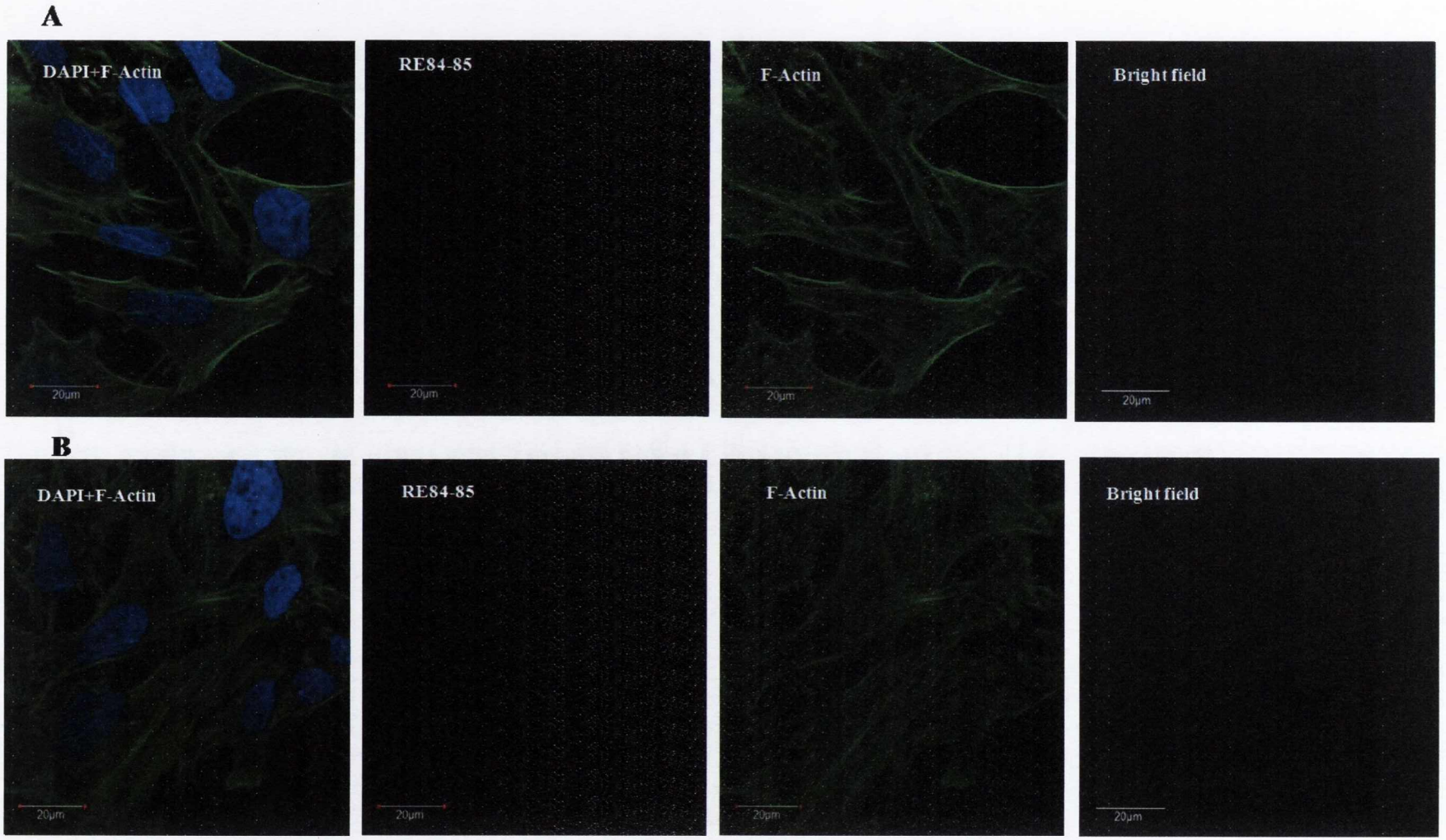
A
DAPI+F-Actin
RE84-85
F-Actin
Bright field
20μm
B
DAPI+F-Actin
RE84-85
F-Actin
Bright field
20μm

Figure 5.16: **Untreated HeLa cells stained with F-actin using Alexa Fluor 488 Phalloidin probe.**

$3x10^5$ cells/well were seeded on coverslips and placed inside a 6-well plate. Cells were incubated at 37°C overnight before adding the vehicle. Following 24h incubation the treated cells were maintained in the dark **(A)** or exposed to light for 1h to give light doses of 12.66 J/cm^2 **(B)**. Following a further 23h of incubation cells were washed twice with pre-warmed PBS, pH 7.4. Samples were fixed in 3% paraformaldehyde solution in PBS for 10min at room temperature followed by two or more washes with PBS. Staining solution + phalloidin 488 (1/40 dilution) was added to the cells for 30min at room temperature followed by two or more washes with PBS. The cells on the coverslips were then transferred onto glass slides with DAPI gel added at room temperature and left overnight at room temperature before confocal microscopy. Image viewing using Olympus FV1000 confocal microscopy with a 60x oil immersion lens and analysed using FluoView Version 7.1 Software. Phalloidin were excited by a 488nm argon laser, emission 612nm and DAPI was excited by a 405 laser, emission 461nm. Results are representative of three independent experiments.

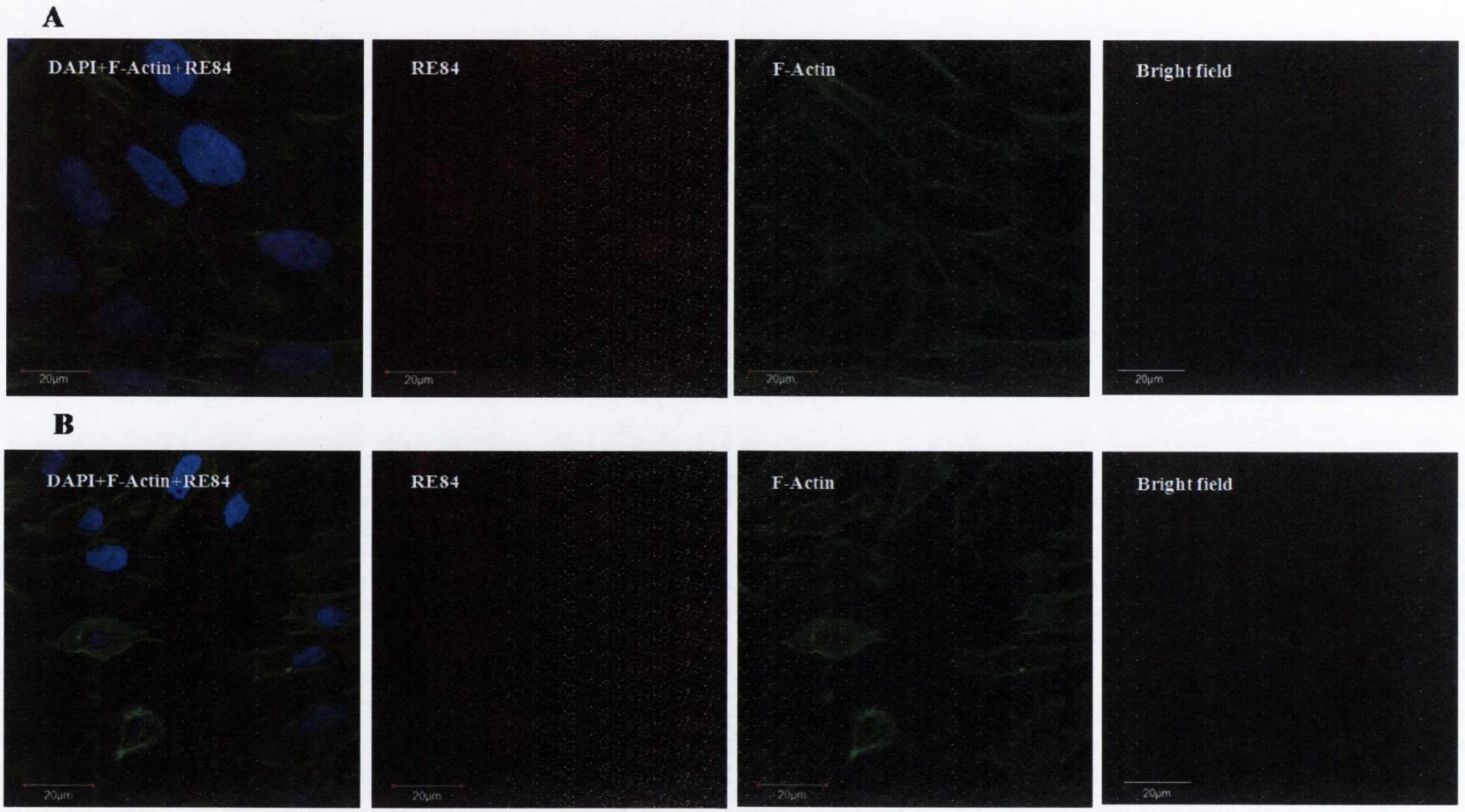
A
DAPI+F-Actin+RE84
RE84
F-Actin
Bright field
20μm
B
DAPI+F-Actin+RE84
RE84
F-Actin
Bright field
20μm

Figure 5.17: **Effect of RE84 on F-actin using Alexa Fluor 488 Phalloidin probe in HeLa cells.**

$1x10^5$ cells/well were seeded on coverslips and placed inside a 6-well plate. Cells were incubated at 37°C overnight before treatment with 5μM of RE84 and incubated for 24h. Following 24h incubation the treated cells were maintained in the dark **(A)** or exposed to light for 1h to give light doses of 12.66J/cm^2 **(B)**, cells were then washed twice with pre-warmed PBS, pH 7.4. Samples were fixed in 3% paraformaldehyde solution in PBS for 10min at room temperature followed by two or more washes with PBS. Staining solution + phalloidin 488 (1/40 dilution) was added to the cells for 30min at room temperature followed by two or more washes with PBS. The cells on the coverslips were then transferred onto glass slides with DAPI gel added at room temperature and left overnight at room temperature before confocal microscopy. Image viewing using Olympus FV1000 confocal microscopy with a 60x oil immersion lens and analysed using FluoView Version 7.1 Software. RE84 and Phalloidin were excited by a 488nm argon laser, emission 612 and 518nm respectively and DAPI was excited by a 405 laser, emission 461nm. Results are representative of three independent experiments.


A
DAPI+F-Actin+RE85
RE85
F-Actin
Bright field
20μm
B
DAPI+F-Actin+RE85
RE85
F-Actin
Bright field
20μm

Figure 5.18: **Effect of RE85 on F-actin using Alexa Fluor 488 Phalloidin probe in HeLa cells.**

$1x10^5$ cells/well were seeded on coverslips and placed inside a 6-well plate. Cells were incubated at 37°C overnight before treatment with 5μM of RE85 and incubated for 24h. Following 24h incubation the treated cells were maintained in the dark **(A)** or exposed to light for 1h to give light doses of 12.66J/cm^2 **(B)** and then cells were washed twice with pre-warmed PBS, pH 7.4. Samples were fixed in 3% paraformaldehyde solution in PBS for 10min at room temperature followed by two or more washes with PBS. Staining solution + phalloidin 488 (1/40 dilution) was added to the cells for 30min at room temperature followed by two or more washes with PBS. The cells on the coverslips were then transferred onto glass slides with DAPI gel added at room temperature and left overnight at room temperature before confocal microscopy. Image viewing using Olympus FV1000 confocal microscopy with a 60x oil immersion lens and analysed using FluoView Version 7.1 Software. RE85 and Phalloidin were excited by a 488nm argon laser, emission 612 and 518nm respectively and DAPI was excited by a 405 laser, emission 461nm. Results are representative of three independent experiments.

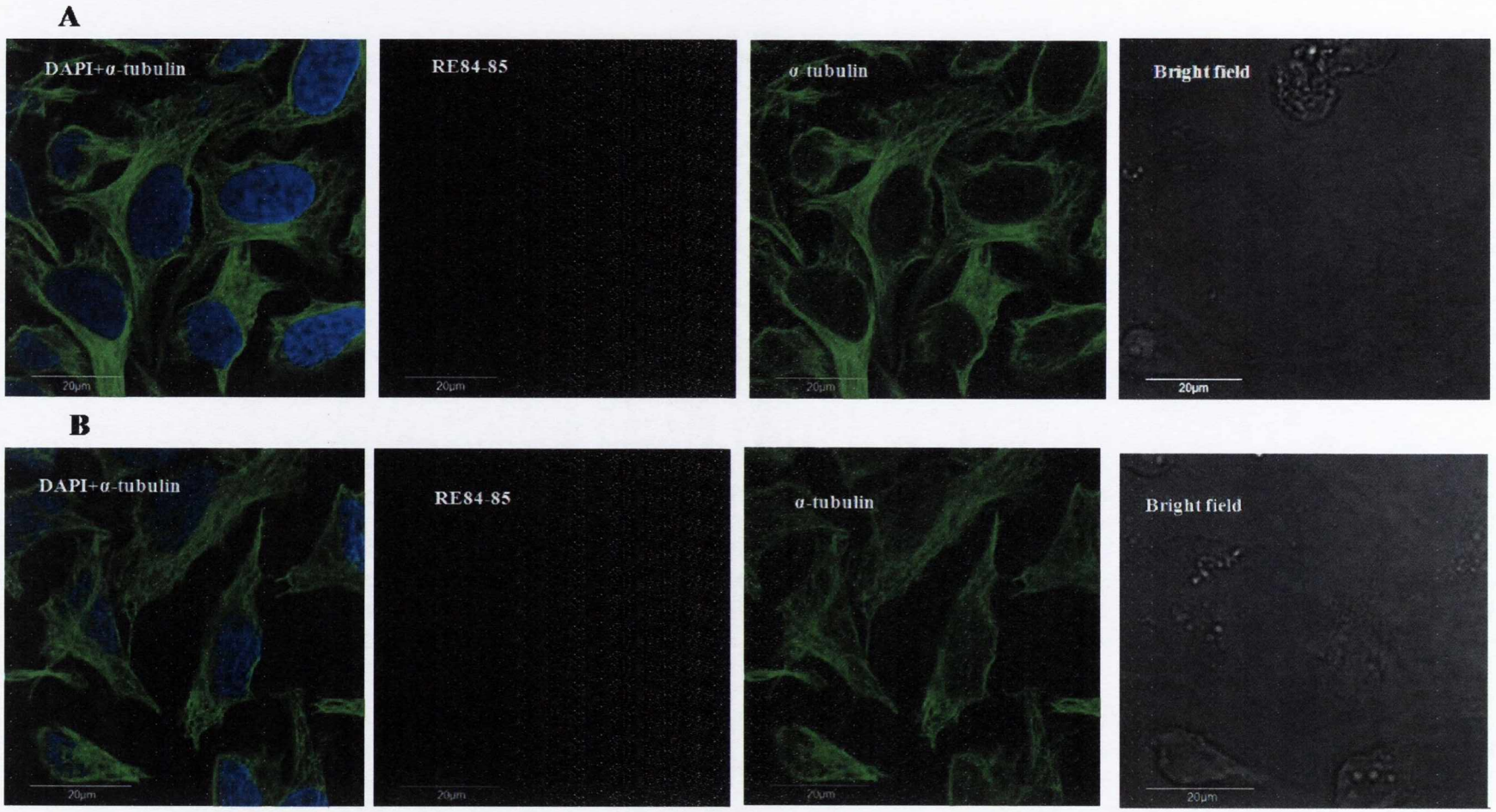
A
DAPI+α-tubulin
RE84-85
α-tubulin
Bright field
20μm
B
DAPI+α-tubulin
RE84-85
α-tubulin
Bright field
20μm

Figure 5.19: **Untreated HeLa cells stained with α-tubulin.**

$3x10^5$ cells/well were seeded on coverslips and placed inside a 6-well plate. Cells were incubated at 37°C overnight before the vehicle was added to untreated cells. Following 24h incubation the treated cells were maintained in the dark **(A)** or exposed to light for 1h to give light doses of 12.66J/cm^2 **(B)**, cells were washed twice with pre-warmed PBS, pH 7.4. Samples were fixed in 3% paraformaldehyde solution in PBS for 10min at room temperature followed by two or more washes with PBS. Staining solution + monoclonal anti-α-tubulin (1/500 dilution) was added to the cells overnight at 4°C. After two or more washes with PBS the cells on the coverslips were incubated with staining solution + anti-mouse alexa 633 (1/1000 dilution) for 1h at room temperature and then transferred onto glass slides with DAPI gel added at room temperature and left overnight before confocal microscopy. Images were viewed using Olympus FV1000 confocal microscopy with a 60x oil immersion lens and analysed using FluoView Version 7.1 Software. DAPI was excited by a 405 laser, emission 461nm and anti-mouse alexa 633 was excited by a 633nm laser, emission 647nm. Results are representative of three independent experiments.


A
DAPI+α-tubulin+RE84
RE84
α-tubulin
Bright field
20μm
B
DAPI+α-tubulin+RE84
RE84
α-tubulin
Bright field
20μm

Figure 5.20: **Effect of RE84 on α-tubulin in HeLa cells.**

$3x10^5$ cells/well were seeded on coverslips and placed inside a 6-well plate. Cells were incubated at 37°C overnight before treatment with 5μM of RE84 and incubated for 24h. Following 24h incubation the treated cells were maintained in the dark **(A)** or exposed to light for 1h to give light doses of 12.66J/cm^2 **(B),** cells were then washed twice with pre-warmed PBS, pH 7.4. Samples were fixed in 3% paraformaldehyde solution in PBS for 10min at room temperature followed by two or more washes with PBS. Staining solution + monoclonal anti-α-tubulin (1/500 dilution) was added to the cells overnight at 4°C. After two or more washes with PBS the cells on the coverslips were incubated with staining solution + anti-mouse alexa 633 (1/1000 dilution) for 1h at room temperature and then transferred onto glass slides with DAPI gel added at room temperature and left overnight before confocal microscopy. Image viewing using Olympus FV1000 confocal microscopy with a 60x oil immersion lens and analysed using FluoView Version 7.1 Software. RE84 was excited by a 488nm argon laser, emission 612nm and DAPI was excited by a 405 laser, emission 461nm and anti-mouse alexa 633 was excited by a 633nm laser, emission 647nm . Results are representative of three independent experiments.


A
DAPI+α-tubulin+RE84
RE84
α-tubulin
Bright field
20μm
B
DAPI+α-tubulin+RE84
RE84
α-tubulin
Bright field
20μm

Figure 5.21: **Effect of RE84 on α-tubulin in HeLa cells.**

$3x10^5$ cells/well were seeded on coverslips and placed inside a 6-well plate. Cells were incubated at 37°C overnight before treatment with 5μM of RE84 and incubated for 24h. Following 24h incubation the treated cells were maintained in the dark **(A)** or exposed to light for 1h to give light doses of 12.66J/cm^2 **(B)**. Following a further 23h of incubation cells were washed twice with pre-warmed PBS, pH 7.4. Samples were fixed in 3% paraformaldehyde solution in PBS for 10min at room temperature followed by two or more washes with PBS. Staining solution + monoclonal anti-α-tubulin (1/500 dilution) was added to the cells overnight at 4˚C. After two or more washes with PBS the cells on the coverslips were incubated with staining solution + anti-mouse alexa 633 (1/1000 dilution) for 1h at room temperature and then transferred onto glass slides with DAPI gel added at room temperature and left overnight before confocal microscopy. Image viewing using Olympus FV1000 confocal microscopy with a 60x oil immersion lens and analysed using FluoView Version 7.1 Software. RE84 was excited by a 488nm argon laser, emission 612nm and DAPI was excited by a 405 laser, emission 461nm and anti-mouse alexa 633 was excited by a 633nm laser, emission 647nm. Results are representative of three independent experiments.

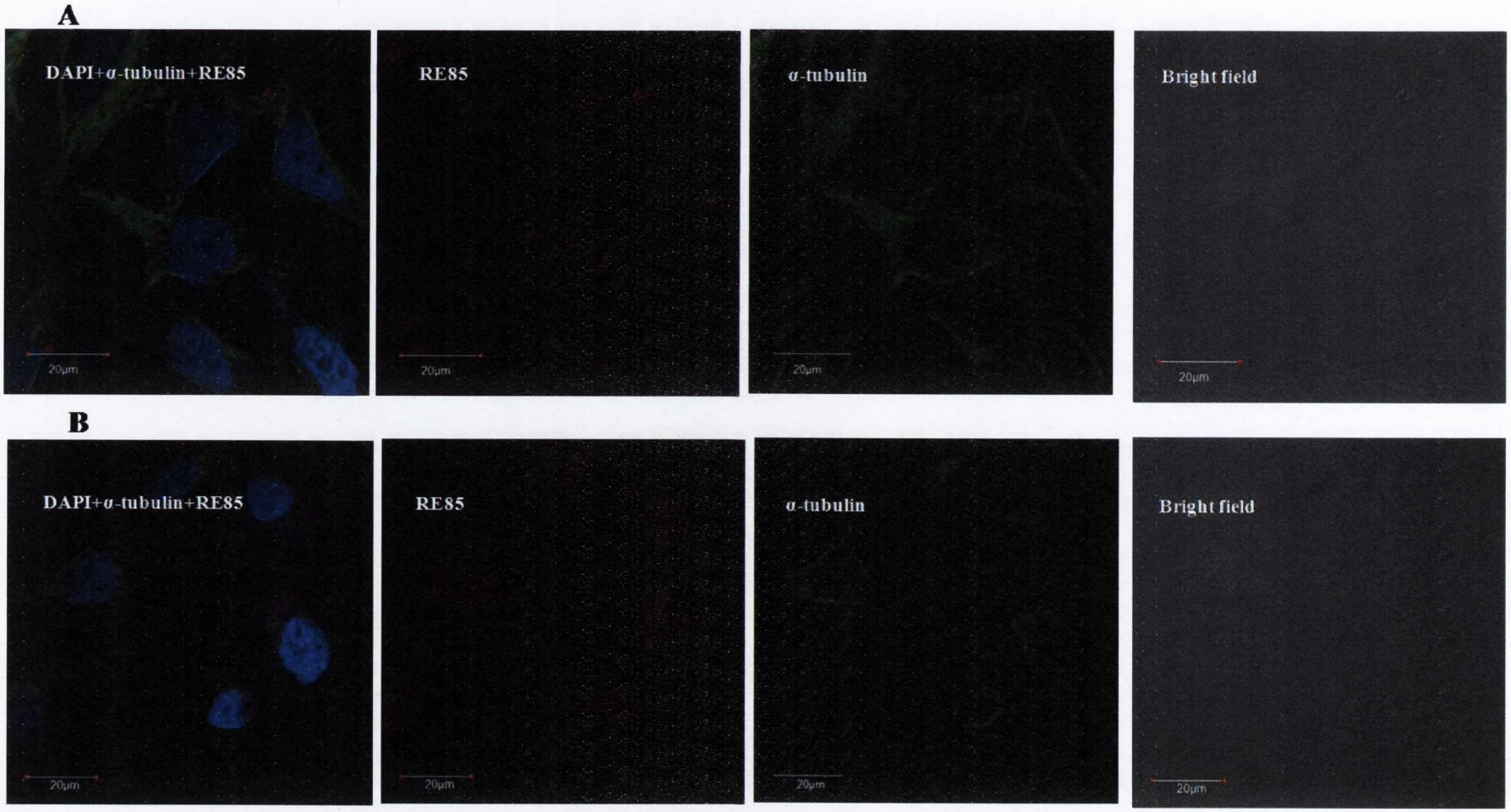
A
DAPI+α-tubulin+RE85
RE85
α-tubulin
Bright field
20μm
B
DAPI+α-tubulin+RE85
RE85
α-tubulin
Bright field
20μm

Figure 5.22: **Effect of RE85 on α-tubulin in HeLa cells.**

$3x10^5$ cells/well were seeded on coverslips and placed inside a 6-well plate. Cells were incubated at 37°C overnight before treatment with 5μM of RE85 and incubated for 24h. Following 24h incubation the treated cells were maintained in the dark **(A)** or exposed to light for 1h to give light doses of 12.66J/cm^2 **(B)**, cells were then washed twice with pre-warmed PBS, pH 7.4. Samples were fixed in 3% paraformaldehyde solution in PBS for 10min at room temperature followed by two or more washes with PBS. Staining solution + monoclonal anti-α-tubulin (1/500 dilution) was added to the cells overnight at 4°C. After two or more washes with PBS the cells on the coverslips were incubated with staining solution + anti-mouse alexa 633 (1/1000 dilution) for 1h at room temperature and then transferred onto glass slides with DAPI gel added at room temperature and left overnight before confocal microscopy. Image viewing using Olympus FV1000 confocal microscopy with a 60x oil immersion lens and analysed using FluoView Version 7.1 Software. RE85 was excited by a 488nm argon laser, emission 612nm and DAPI was excited by a 405 laser, emission 461nm and anti-mouse alexa 633 was excited by a 633nm laser, emission 647nm. Results are representative of three independent experiments.

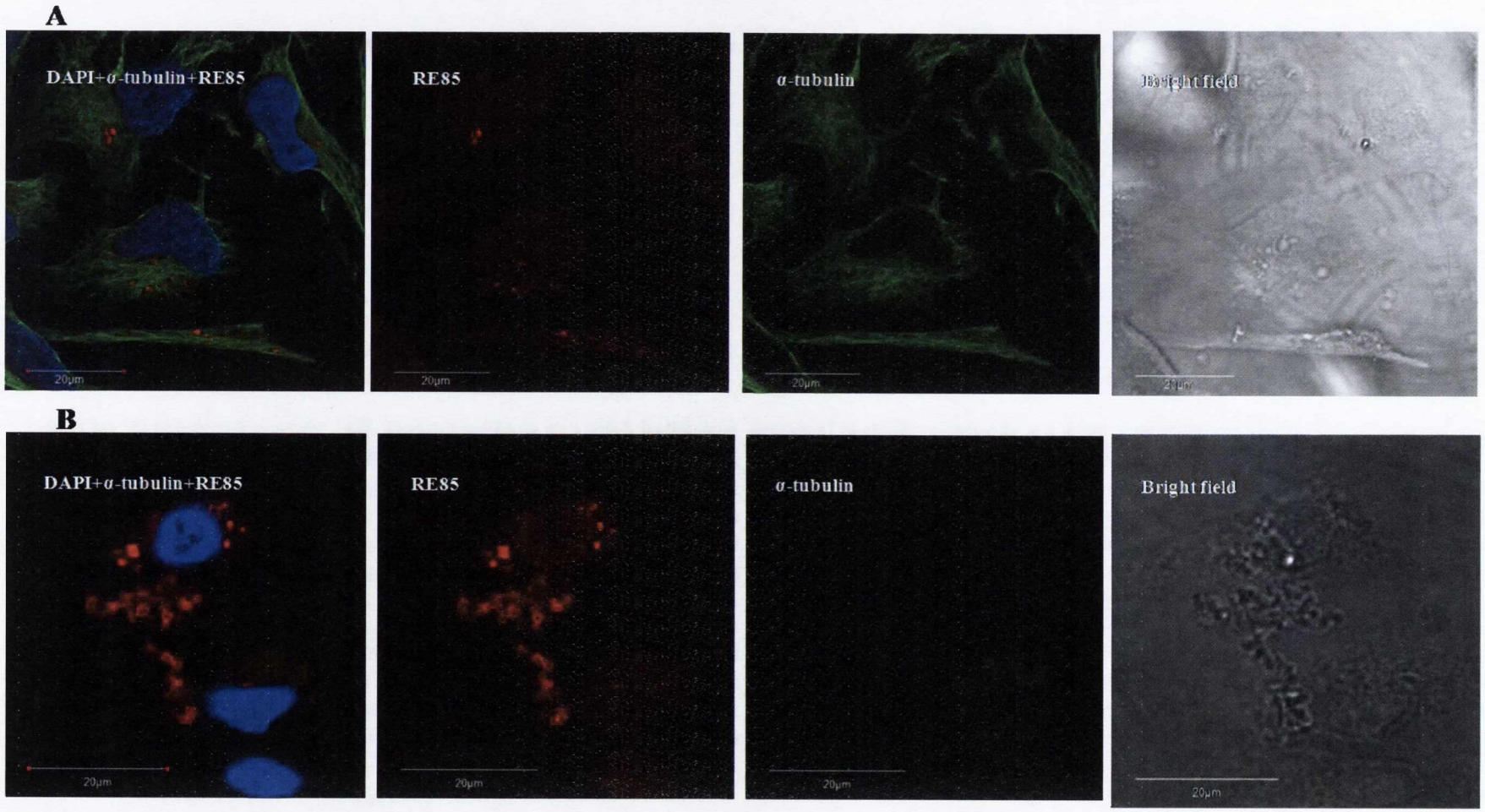
A
DAPI+α-tubulin+RE85
RE85
α-tubulin
Bright field
20μm
B
DAPI+α-tubulin+RE85
RE85
α-tubulin
Bright field
20μm

Figure 5.23: **Effect of RE85 on α-tubulin in HeLa cells.**

$3x10^5$ cells/well were seeded on coverslips and placed inside a 6-well plate. Cells were incubated at 37°C overnight before treatment with 5μM of RE85 and incubated for 24h. Following 24h incubation the treated cells were maintained in the dark **(A)** or exposed to light for 1h to give light doses of 12.66J/cm^2 **(B)**. Following a further 23h of incubation cells were washed twice with pre-warmed PBS, pH 7.4. Samples were fixed in 3% paraformaldehyde solution in PBS for 10min at room temperature followed by two or more washes with PBS. Staining solution + monoclonal anti-α-tubulin (1/500 dilution) was added to the cells overnight at 4°C. After two or more washes with PBS the cells on the coverslips were incubated with staining solution + anti-mouse alexa 633 (1/1000 dilution) for 1h at room temperature and then transferred onto glass slides with DAPI gel added at room temperature and left overnight before confocal microscopy. Image viewing using Olympus FV1000 confocal microscopy with a 60x oil immersion lens and analysed using FluoView Version 7.1 Software. RE85 was excited by a 488nm argon laser, emission 612nm and DAPI was excited by a 405 laser, emission 461nm and anti-mouse alexa 633 was excited by a 633nm laser, emission 647nm. Results are representative of three independent experiments.

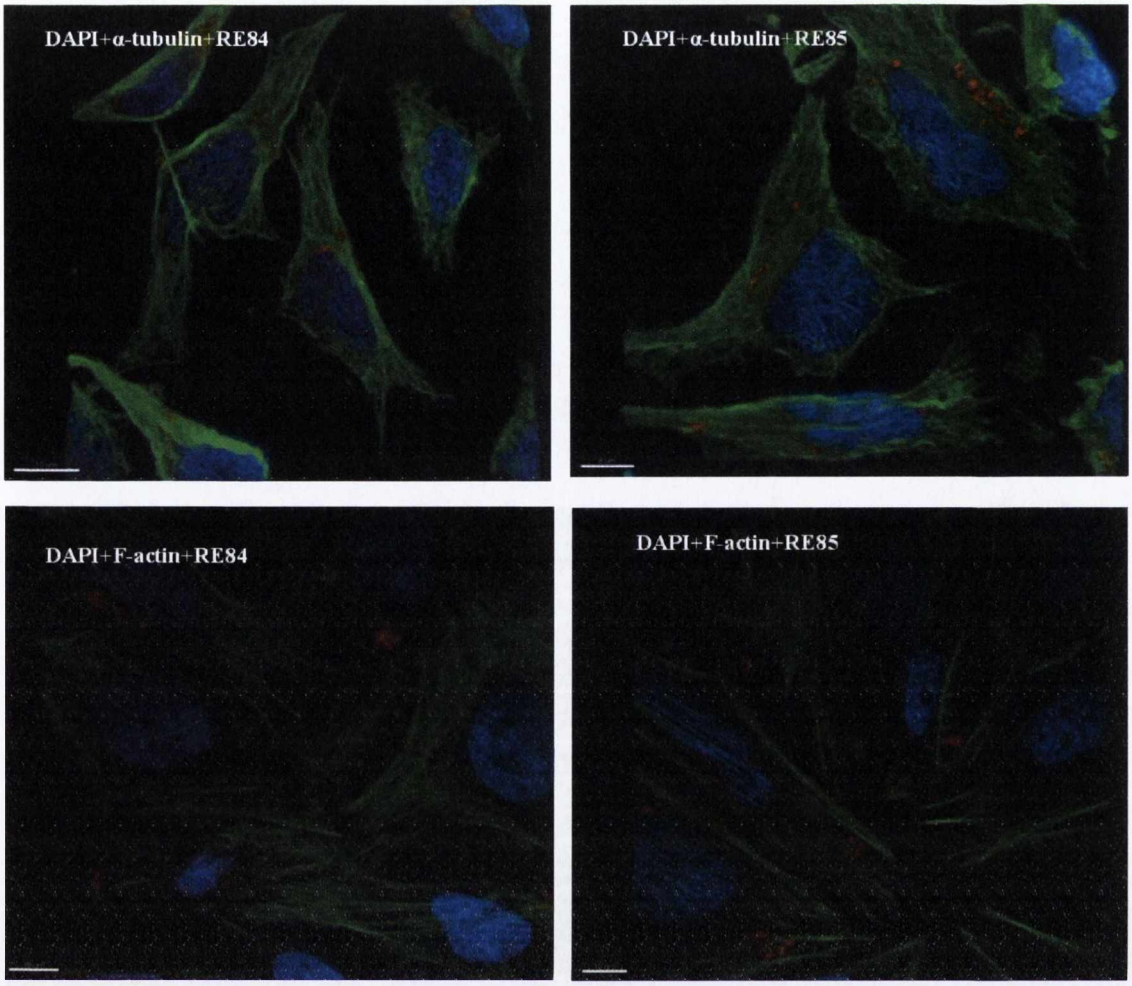

Figure 5.24: **3D images of RE84 and 85 with F-actin and α-tubulin in HeLa cells.**

$3x10^5$ cells/well were seeded on coverslips and placed inside a 6-well plate. Cells were incubated at 37°C overnight before treatment. The cells were then treated with 5μM of RE84 and 85 and incubated for 24h. Following 24h incubation the treated cells were fixed as described in Section 2.8. Image viewing using Olympus FV1000 confocal microscopy with a 60x oil immersion lens. Image were analysed using the Imaris 3D software analyser (Bitplane). Results are representative of three independent experiments.

Discussion

The aim of this Chapter was to study and understand the mechanism of action of the bimetallic Ru(II) complexes RE84 and 85. The localization of a sensitizer, which can relocate after light exposure, is important due to the fact that the site of production of $^1O_2$ can influence its lifetime and diffusion in cells from the site of production.

Similarly to the localization of compound RE37, compounds RE84 and 85 are also shown, using confocal microscopy, to localize in the mitochondria even though the compounds were synthesised to target DNA. Starting from that, a series of experiments to demonstrate the localization/effect of these compounds on mitochondria were performed.

Considering that the therapeutic effect in PDT is mediated by the generation of ROS and that the vast majority of ROS is produced by mitochondria, quantification of ROS production using CyAn was performed. Results showed an increase in ROS production in a concentration and light dependent manner suggesting ROS production as one of the causes of cell death. Furthermore, RE84 and 85 rapidly and extensively reduced the MMP in cells without light treatment at a higher extent and at lower concentration then RE37 without inducing cell death.

In 1926 Otto Warburg demonstrated that cancer cells produce most of their ATP through glycolysis even under aerobic conditions and this process is known as 'the Warburg effect'. The Warburg effect may be the reason way the reducing in the MMP in cells which are not illuminated may damage mitochondria but cells stay alive. Mitochondria photodamage may be an important step in PDT-induced apoptosis and involves ROS production after light treatment. Results suggest that ROS production is one of the causes of cell death, based on the evidence given. Moreover, mitochondrial-morphology changes suggest that mitochondrial fission occurred after light exposure, as shown in figures 5.6, 5.7 and 5.10, which suggests again that this mitochondrial damage is light dependent and that the drop in MMP alone does not induce cell death. However, investigation on the involvement of the cytosolic dynamin family member (Drp1), which mediates fission (a process that has been described in the introduction of this thesis is Section 1.6), is needed together with 3 dimensional analysis and reconstruction.

Analysis of HeLaDsRed transfected cells using spinning disk confocal microscopy showed that the form of cell death depended on the concentration of the compound and the light source used: if the concentration was high the cells started swelling which suggested that

they were dying by necrosis but, if the concentration of the compounds was low the cells appeared as shrinking apoptotic bodies. Moreover, it was shown that using the 488nm laser, cell death became faster and more dramatic than using only the 543 laser. In connection to that, AnnexinV/PI results, which have previously been already discussed in Chapter 4, together with the results from the LDH production, showed RE84 and 85 to induce apoptosis even if the mechanism of PDT-induced cell death initially appeared to have the characteristics of necrosis. It may be the different apoptotic mechanism described by Kessel *et al.*, which has been implicated in examples of phototoxicity. This mechanism implies that mitochondrial photodamage can directly initiate apoptosis followed by the generation of certain signals that lead to a series of events, resulting in DNA and cellular fragmentation with these fragments engulfed by adjoining cells, thereby avoiding inflammatory effects which result from necrosis. Further evidence of the effect of these compounds on the mitochondria showed mitochondria to become swollen and rounded in a short time depending on the concentration. It was also observed that mitochondria appeared to cluster around the nucleus, as previously mentioned in Chapter 3 for compound RE37, in a process similar to a phenomenon called mitophagy that has been described by Kim *et al.*, where gross insult of the mitochondria results in perinuclear clustering as part of the mitophagic process. However, whether this phenomenon is due to the effects of the compounds on the mitochondria or whether it is related to cell shrinkage, is hard to tell. In connection with that, further evidence on the mitophagic process is needed such as genes involved in mitophagy. For example, it has been shown that mitophagy could be prevented with a dominant negative mutant of Drp1, suggesting that fission is required in mitophagy [54] as it has been described in the introduction of this thesis in Section 1.6.

Further investigation on the localization/uptake of the compounds using isolated mitochondrial and nuclear fractions of HeLa cells treated with the compounds showed localization of Compounds RE84 and 85 in the mitochondria rather than in nuclei. Moreover, Western blot analysis showed the nuclear fractions with a small amount of mitochondrial contamination whereas mitochondrial fractions did not show any nuclear contamination. This Western blot analysis may explain why some emission has been detected in the nuclei fractions. These results are consistent with the confocal microscopy results discussed in Chapter 3 which showed again accumulation of all the compounds in mitochondria rather than nuclei.

As the compounds were designed to bind DNA, the Comet assay was performed in order to investigate intracellular nuclear DNA strand breakage with and without light treatment but while results showed some comet tails at 1μM, at higher concentrations the DNA is not even visible/is destroyed. These results together with the effect of these compounds on the mitochondria using spinning disk microscopy suggested DNA may not to be the first target for these compounds and that DNA damage is due to the production and diffusion of ROS and or $^1O_2$ from the site of production to DNA.

In Chapter 4 it has been described that RE84 and 85 are very luminescent at low concentrations making them very good compounds for imaging/localization studies. It has also been observed that cells treated with these compounds cannot be visualised for long using live confocal microscopy because the confocal laser activated the compounds and cells started dying rapidly depending on the concentration of the compound used. In order to avoid the activation of the compounds under the confocal laser, it was thought to study the compounds' localization by fixing the cells. However, results showed different localization of the compounds to live imaging, in which they appeared localised in the mitochondria, compared to fixed cells, in which they appeared localized inside the nucleus. These results suggested that cell fixation may permeabilise the nuclear membrane letting the compounds inside the nucleus or that the compounds may cross the nuclear membrane of dead cells. As a result, fixed cells could not be used to investigate the localization of the compounds but they could be used to investigate the cytoskeleton structure of the cells using tubulin and actin antibodies. PDT has a strong effect on cell division, probably due to microtubule damage. The microtubule network is also involved in mitochondrial movement inside the cells. In relation to that, studies on the effect of the compounds on the cytoskeleton structure of the cells using confocal microscopy were performed and results showed a disruption of tubulin filaments but not actin filaments after light exposure. Similar results were obtained in cells treated with compound RE37, as described in Chapter 3 but, the effect in cells treated with RE84 and 85 was more dramatic. Moreover, confocal images showed depolymerised-microtubules fragments around the nucleus after light exposure (figure 5.19B and 5.21B). These results suggested that damage of the tubulin filaments after light treatment may contribute to PDT-induced cell death. Furthermore, this study on the cytoskeleton structure showed no change in the morphological appearance of cells which were not illuminated suggesting that the presence of the compounds is not toxic to the cells as shown in figure 4.24 in Chapter 4.

In summary these results suggest that the cellular uptake of the bimetallic Ru(II) compounds RE84 and 85 leads to mitochondrial damage starting from the reduction of the membrane potential in the dark followed by ROS production upon light exposure, initiating an early step in the induction of apoptosis. The damage results in the swelling and rounding of mitochondria in a dramatic and short time followed by clustering of the mitochondria around the nucleus. Moreover, the DNA damage is likely to be an indirect effect of the ROS production and/or $^1O_2$ production and diffusion from the site of production, which are mitochondria. These results suggest that DNA is not the first target for these compounds even though they were originally synthesized to bind to DNA. The illumination process of the photosensitizer is very important for an efficient biological response in PDT as showed by the spinning disk and confocal results. In fact, by changing the concentration of the compound and by changing the laser used to illuminate the cells, the mechanism of cell death and the extent of the mitochondrial damage changed. All these results together suggested that mitochondrial photodamage can directly initiate apoptosis followed by the generation of certain signals that lead to a series of event, resulting in DNA fragmentation and cell death. This different apoptotic mechanism has been already implicated in examples of phototoxicity.

Chapter 6

Overall Discussion

6.1 Overall discussion

The first family of compounds presented in this thesis contain complexes based on a novel extended aromatic polypyridyl ligand (pdppz) which is based on the combination, in a single structure, of both pddz and TAP and is reported to insert between the base-pairs of B-form double stranded DNA [108]. The compounds were synthesised with the aim to bind DNA as compounds which form chemical bonds with DNA molecules represent several important classes of anticancer drugs [121].

Previous studies have shown the cationic derivatives of pdppz to be non-toxic in plants, have good water solubility and distinctive photophysical properties that allow interaction with DNA at relatively long wavelengths. Moreover, they exhibited an enhanced affinity for DNA with a binding constant calculated to be comparable to that of [Ru(II)(dppz)] complexes and, finally they showed more affinity for GC over AT sequences showing an increase in luminescence in the presence of $[poly(dAdT)]_2$ and a decrease in the presence of $[poly(dGdC)]_2$. Taking into consideration previous studies on pdppz, it was decided to investigate a cationic derivative of pdppz, RE33 (figure 6.1).

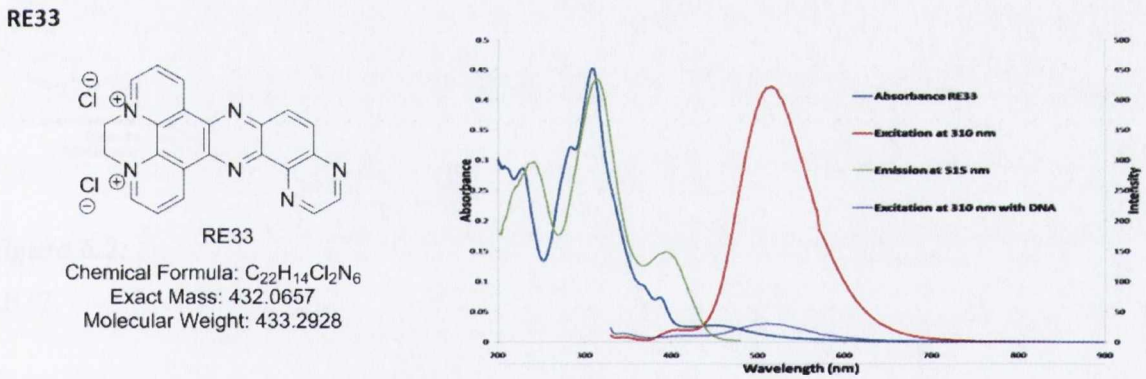

Figure 6.1: Structure and UV/Visible, excitation and emission spectra of RE33.

RE33 shows good water solubility and a distinctive set of photophysical properties [74]. Furthermore, stDNA binding affinity studies showed RE33 to have high affinity for DNA through intercalation and to have a particular preference for $[poly(dGdC)]_2$ than for $[poly(dAdT)]_2$ [73]. Moreover, it has been shown, using a DNA plasmid (pBR322 DNA), to mediate DNA cleavage [87].

It was shown by Robert B. P. Elmes, who studied the UV/Visible absorption, excitation and emission spectra of these compounds with and without stDNA, that the excited state of RE33 is quenched upon interaction with the nucleobases of DNA.

Confocal microscopy in HeLa cells treated with RE33 showed uptake of the compound into the cells and a peri-nuclear localisation was shown at 24h to the bean-shaped nucleus. However, the lack of intense luminescence within the cells, suggested RE33 would not be suitable as a molecular probe. Moreover, FACS analysis results showed RE33 to also be unsuitable as a PDT agent due to its toxicity without light treatment and due to the lack of difference in cell toxicity upon photoirradiation if incubated at high concentrations and at long time points.

With the aim to improve the DNA binding affinity of RE33 it was thought to add a Ru(II) metal centre to the structure and to vary the ligands around the metal centre and so, Ru(II) polypyridyl metal complexes, called RE30, 34 and 37 (figure 6.2), were investigated.

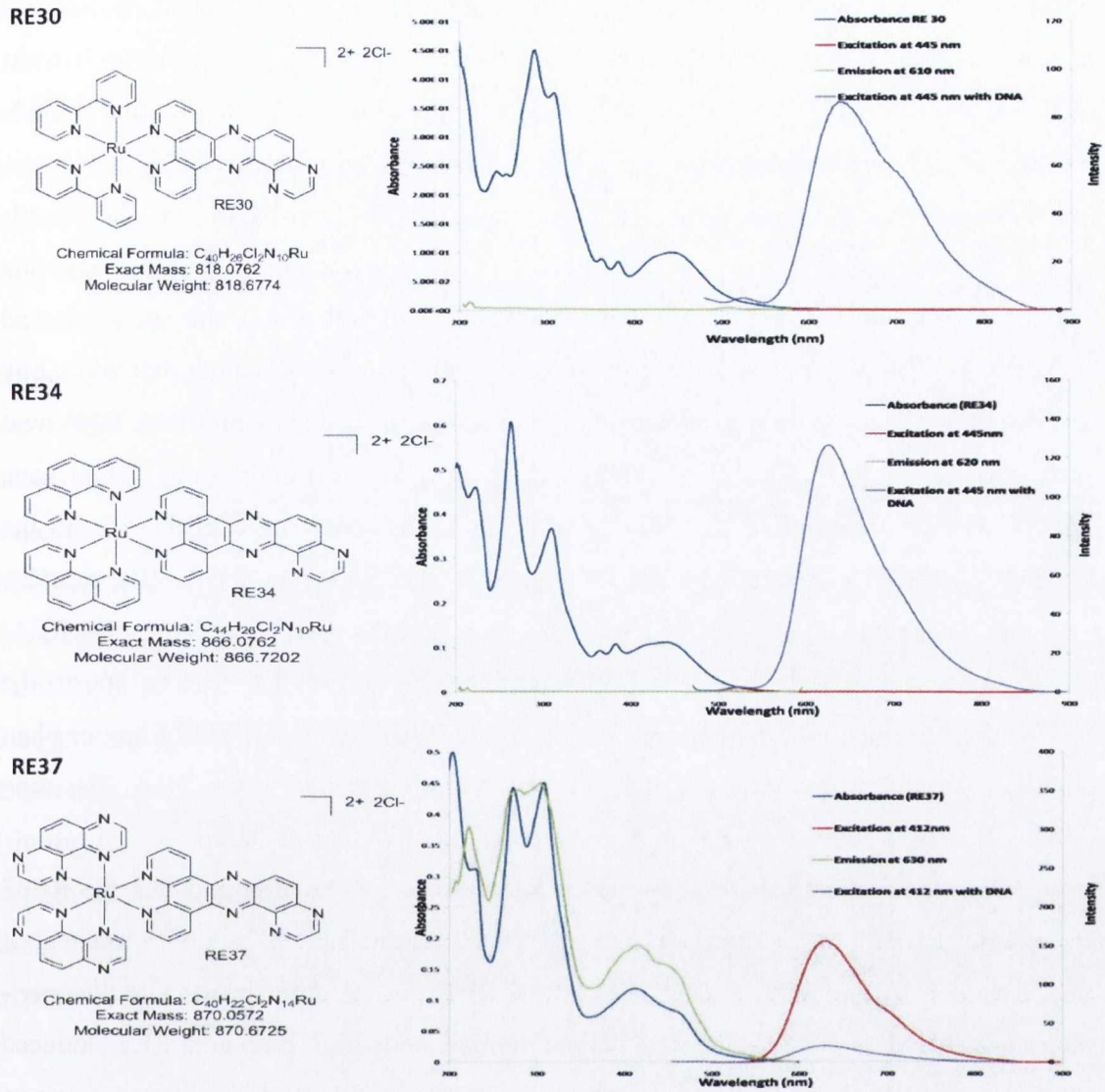

Figure 6.2: Structure and UV/Visible, excitation and emission spectra of RE30, RE34 and RE37.

The common characteristic of these compounds is the extended aromatic heterocylic ligand, dppz that allows the interaction of the complex with DNA leading to the "light switch" effect, which consists of an increase in [106] fluorescence of the compound once it is bound to DNA as has been described in the introduction to the compounds in the third chapter.

In connection with that, the excitation of the compounds with and without DNA has been determined by Robert B. P. Elmes. The UV/Visible absorption, excitation and emission spectra of these compounds have been recorded at pH 7.4 in 10mM phosphate buffer. Upon addition of stDNA, the intensity of fluoresence of RE30 and 34 in aqueous solution

was shown to increase until reaching a plateau followed by a subsequent decrease in emission. Controversially, the emission of RE37 in aqueous solution was shown to have its excited state effectively quenched by 86% upon addition of stDNA. After binding stDNA, compounds RE30 and 34 showed a 'light-switch' effect instead, whereas RE37 did not.

The differences among these compounds are the ligands. In fact, by varying the ligands around the metal centre it was possible to modify their interaction with DNA. The first ligand inserted was based on bpy, with the formation of RE30 and, the second ligand inserted was phen to form RE34. It was reported in the previous literature that while bpy bound to DNA weakly through electrostatic interaction, phen interaction with DNA was much stronger [91]. This fact may explain why, using confocal microscopy, RE34 gave more fluoresence than RE30. In order to confer a strong oxidizing excited state on the complex, an electron accepting ligand, TAP, was also added to the Ru(II) complex resulting in the formation of RE37. It was demonstrated by Robert B. P. Elmes that RE37 is highly efficient in DNA cleavage compared to RE30 and 34. This can be due to the presence of the electron accepting ligand TAP at the Ru(II) centre instead of bpy or phen because it increased the potency of the complex in binding tightly to the DNA. This may be related with the ability of RE37 to be more potent upon photoirradiation.

It has been demonstrated that RE37 is localised to the mitochondria and that the RE37 loaded mitochondria moved from the cytoplasm to a peri-nuclear localisation. Moreover, it has been shown that intracellular transport of RE37-loaded mitochondria to the peri-nuclear location was not dependent on the microtubule network. Compound RE37 induced apoptosis in a light dependent manner and results suggested that ROS production is one of the causes that induced cell death. Furthermore, RE37 is not toxic in light-untreated samples. These characteristics make RE37 a good candidate for cancer therapy in PDT. On the other hand, the other two complexes (RE30 and 34) did not have any photophysical activity without showing toxicity in light-untreated cells so they may be potentially good candidates as spectroscopic cellular probes.

Continuing in the search for new Ru(II) based DNA binding motifs in order to further increase the potency of this class of compounds in binding DNA, a combination of bis-1,8-naphthalimide derived Tröger's bases and the bimetallic Ru(II) complexes assembled by polypyridyl bridging ligands was used to synthesise compounds RE84 and 85. Based on previous studies with similar compounds, these species were expected to be capable of binding DNA with further possible applications in cellular imaging or therapeutics. It was

expected that the Tröger's base framework may orientate the two functional units, the metallic Ru(II) centers and the organic bis-1,8-naphthlaimide containing bipyridyl ligand, in a rigid architecture that may produce tight DNA binding agents. The highly positive charge of RE84 and 85 would be likely to increase the DNA binding ability of such systems through electrostatic interactions and, in addition, the bimetallic character may enable cellular localization as a nuclear DNA stain. The interest in Tröger's bases is due to the central bicyclic framework which results in two aromatic rings being fused nearly perpendicular to each other, creating a rigid V-shaped molecular scaffold. The chirality of the Tröger's base framework due to the presence of two bridgehead stereogenic nitrogen atoms in its structure plays an important role in their interaction with DNA and it is expected that such species may give rise to enantiospecific binders of DNA. The interest in bis-1,8-naphthalimides is related to the work of Veale *et al.*, in which Tröger's bases have been demonstrated as dual imaging-therapeutic agents (44 a-c) [120].

Considering all of the above, it was decided to modify the design of the 44 a-c to incorporate the bpy portion (found in RE30) that would allow the formation of the bimetallic Ru(II)-1,8-naphthalimide compounds containing Tröger's bases, RE84 and 85 (figure 6.3). In the synthesis of these bimetallic species, the Ru(II) centers and 1,8-naphthalimide units form either a meta (RE84) or para (RE85) arrangement with respect to each other. The compounds were isolated as a mixture of enantiomers, which are both expected to bind to DNA.

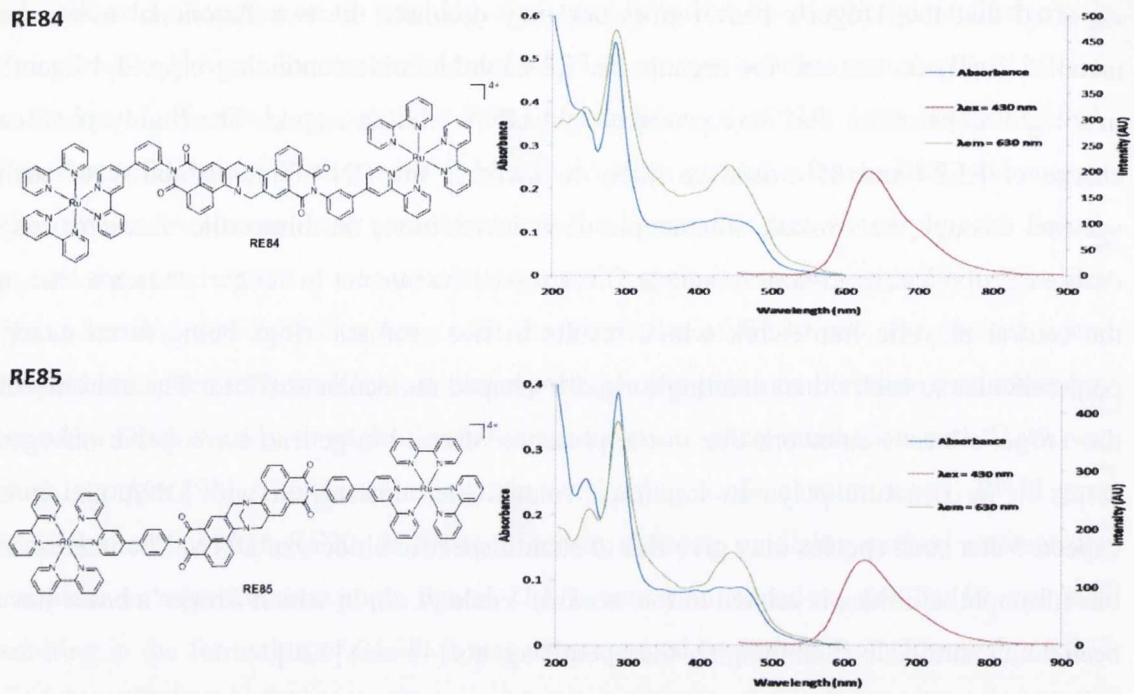

Figure 6.3: Structure and UV/Visible, excitation and emission spectra of RE84 and 85.

The UV/Visible absorption, excitation and emission spectra of these compounds was determined by Robert B. P. Elmes, which have been recorded at pH 7.4 in 10mM phosphate buffer, and results showed that upon binding of RE84 and 85 to stDNA the emission in aqueous solution is initially seen to be quenched followed by a small increase (3-5%) leading to a plateau which corresponds to a situation where the compounds are fully bound to DNA. The observed emission behaviour is most likely explained by a biphasic interaction upon addition of stDNA in relation to the hypochromic effect which is consistent with the existence of more than one site of binding. In relation to that, a binding constant could not be determined accurately from the absorption or emission data due to the small magnitude of the changes and the observed biphasic behaviour of both RE84 and 85.

Cell viability experiments showed a high tolerance of these compounds without photo-activation, but potent cytotoxicity was observed with photoactivation at lower concentrations then RE37. Localisation studies of the bimetallic Ru(II) compounds in HeLa cells using confocal microscopy showed that RE84 and 85 were substantially taken up inside the cells after only 2h. RE84 and 85 appeared visible at lower concentrations than the previous compounds (RE30, 34, 37 and 33) making them very good compounds for localization studies.

It has been shown, using various techniques that compounds RE84 and 85 are localized in the mitochondria, similarly to the localization of compound RE37, again even though the compounds where synthesised to target DNA. Despite RE84 and 85 being derived from the structure of the organic compounds 44 a-c, which have been showed to bind DNA in cells, and despite bimetallic Ru(II) complexes assembled by polypyridyl bridging ligands having found numerous applications in DNA cellular imaging [99], RE84 and 85 are not localized in the nucleus. At the moment it is not understood which difference in the structure makes the compounds localise to the mitochondria instead of the nucleus so that further experiments are being undertaken to understand this phenomena. In fact, RE84 and 85 rapidly and extensively reduced the MMP in cells not illuminated to a larger extent then cells treated with RE37 while spinning disk confocal microscopy studies showed that the compounds were inducing mitochondria to become swollen and rounded in a short time depending on the concentration. Further investigation on the localization of the compounds using isolated mitochondrial and nuclear fractions of HeLa cells showed localization of the compounds in the mitochondria. Furthermore, RE84 and 85 induced ROS production in HeLa cells in a concentration and light dependent manner suggesting ROS production as one of the causes of cell death. Compound RE37 showed a smaller increase in the intracellular ROS production then compounds RE84 and 85 which appeared again to have a more dramatic effect on the mitochondria/cells. Compounds RE84 and 85 induced DNA damage which is likely to be an indirect effect of the ROS production and/or $^1O_2$ production and diffusion from the site of production.

Photosensitizers of greatest interest in PDT bind preferentially to various organelles in the cells than the nucleus or DNA [60]. Cell studies have demonstrated that cellular phototoxicity is likely caused by the generation of reactive singlet oxygen by photosensitizers associated with organelles such as lysosomes and mitochondria. However, the initial oxidative reactions lead to damage to organelles in which the dye is bound, culminating in DNA damage, which can lead to a different extent of mutagenesis depending on the photosensitizer, the cellular repair properties and the target gene followed by cell death and destruction of the tumour or abnormal tissue [60]. Moreover, PDT also triggers the activation of several signal transduction pathways in the treated cells which are stress responses aimed at cell protection or are likely to contribute to the cell death process and apoptosis [60].

Nevertheless, studies have also demonstrated that in cells treated with several different photosensitizers, the most sensitive target site was the nucleus interphase, followed by the perinuclear cytoplasm, and finally the peripheral cytoplasm [130]. Moreover, several studies demonstrate a PDT effect on DNA, chromosomes and the mitotic spindle but, it is not clear whether these effects are due to generation of singlet oxygen elsewhere in the cell, or directly at the nuclear/mitotic spindle site [130].

Cell death may occur due to mitochondrial dysfunction. The definition of mitochondrial 'function' and 'dysfunction' is not precise. The most important physiological function of mitochondria is the ATP generation by oxidative phosphorylation. Additional functions include the generation and detoxification of ROS, involvement in some forms of apoptosis, regulation of cytoplasmic and mitochondrial matrix calcium, synthesis and catabolism of metabolites and the transport of the organelles themselves to correct location within the cell. Abnormality in any of those processes can be termed mitochondrial dysfunction [133].

A dysfunction of the mitochondrial transition pores, for example, allow for the triggered release of cytochrome c from the mitochondria to the cytosol followed by the disruption of the electron transport chain and mitochondria electron gradient. The cytosolic cytochrome c activates certain cytoplasmic proteins such as APAF-1 followed by the activation of a cascade of caspases which result in apoptotic cell death. Mitochondrial dysfunction of the ROS generation and detoxification lead to 'oxidative stress' which can cause toxic effects through the production of peroxides and free radicals that damage all components of the cell, including proteins, lipids, DNA and can cause disruptions in normal mechanisms of cellular signaling. Severe and moderate oxidative stress can trigger apoptosis, while more intense stresses may cause necrosis [133].

Investigation into the mechanism of cell death showed RE84 and 85 to induce a different apoptotic mechanism implicated in examples of phototoxicity, which has been described by Kessel *et al.*, that implies that mitochondrial photodamage can directly initiate apoptosis by certain signals that lead to a series of events, resulting in DNA and cellular fragmentation with these fragments engulfed by adjoining cells without necrotic effects. Furthermore, it has been shown that by changing the concentration of RE84 and by changing the laser used to illuminate the cells, the mechanism of cell death and the extent of mitochondrial damage changed: low concentrations of the compound led to apoptotic bodies while at high concentrations cell death appeared to have the characteristics of

necrosis and rounding and/or swelling of mitochondria. Studies on the effect of the compounds on the cytoskeleton structure of the cells using confocal microscopy showed a disruption of tubulin filaments after RE84 and 85 treatment and light exposure however this did not occur with actin filaments. Confocal images also showed damaged tubulin filaments around the nucleus after light exposure suggesting that damage of the tubulin filaments after light treatment may contribute to PDT-induced cell death.

In conclusion, we tested a novel series of compounds containing pdppz ligands or Tröger's bases conjugated to mono or bimetallic ruthenium complexes and analysed these compounds for their luminescent properties and photoirradiation effects in malignant cell lines. All compounds were successfully taken up into cells and were easily visible due to their luminescent properties. One of the compounds containing the pdppz ligand, RE37, also demonstrated the ability to actively kill cancer cells upon photoirradiation, thus making this compound potentially suitable for PDT. On the other hand, RE30 and 34, appeared to be more suitable as molecular probes due to their lack of toxicity shown in the different cell lines. RE33, instead, was shown not to be useful for either imaging or PDT. Regarding RE84 and 85 are potentially good candidates for further studies on their cancer therapeutic potential due to the low toxicity in non-irradiated cells together with the difference between light-treated and untreated samples making those compounds suitable as PDT agents.

6.2 Future work

Future work has to be done on the mechanism of cell death induced by RE84 and 85 such as investigation on the mitochondrial photodamage such as downstream effects of ROS production for example MOMP. Moreover, cytochrome c release, involvement of caspases and expression of pro-apoptotic proteins (members of the Bcl-2 family such as Bid). Furthermore, investigation on the genes involved in mitophagy and recruitment of mitochondrial fission proteins.

Moreover, future work in the search for new Ru(II) compounds that can be effective as cancer therapy in PDT, particular attention has been given to 'second generation' photosensitizers that have wavelength greater than 700nm, which is important for curing deep tumours.

Moreover, focusing on generating compounds that bind DNA and on increasing the DNA binding affinity while simultaneously displaying characteristic photophysical properties, the synthesis of new systems containing 1,8-naphthalimide units may generate more effective compounds for cancer therapy in PDT. Various families of Ru(II) complexes containing the 1,8-naphthalimide chromophore have been already designed, synthesized and photophysically evaluated [134]. Variation of the distance and flexibility of the linker connecting the naphthalimide to the Ru(II) centre, in addition to varying the substitution pattern on the chromophore allowed the establishment of important structural features for efficient DNA interaction and spectral response of these systems [73].

Bibliography

1. Patrice, T., ed. *Photodynamic therapy*. ed. Höder, D. P. and Jory, G., 2003. 8-22; 24-25.
2. Hanahan, D. and Weinberg, R. A., *Hallmarks of cancer:the next generation*. Cell, 2011. 144:646-674.
3. Negrini, S., Gorgoulis V. G. and Halazonetis, T. D., *Genomic instability-an evolving hallmark of cancer*. Nature Reviews Molecular Cell Biology, 2010. 11:220-228.
4. Hanahan, D. and Weinberg, R., A, *The hallmarks of cancer*. Cell, 2000. 100:57-70.
5. Coussens, L.M. and Werb Z., *Inflammation and cancer. Nature*, 2002. 420:860-870.
6. Sherr, C.J., *Cancer cell cycles*. Science, 1996. 274:1672-1677.
7. Sherr, C.J., *The Pezcoller lecture: cancer cell cycles revisited*. Cancer Research, 2000. 60:3689-3695.
8. Vogelstein, B., D., Lane, D. and Levine, A. J., *Surfing the p53 network*. Nature, 2000. 408:307-310.
9. Igney, F.H. and Krammer, P. H., *Death and anti-death: tumour resistance to apoptosis*. Nature Review Cancer, 2002. 2:277-288.
10. Malcolm, R.A., ed. *The cancer handbook*. ed. Nature publiscing group. 2007, 3.
11. Herbert, B., Pitts, A. E., Baker, S. I., *et al., Inhibition of human telomerase in immortal human cells leads to progressive telomere shortening and cell death*. Proceedings of the National Academy of Science U.S.A., 1999. 96:14276-14281.
12. Carmeliet, P. and Jain, R. K. *Angiogenesis in cancer and other diseases*. Nature, 2000. 407: 249-257.
13. Christofori, G. and Semb, H., *The role of the cell-adhesion molecule E-cadherin as a tumour-suppressor gene*. Trends in Biochemical Science, 1999. 24:73-76.
14. Sharman, W.M., Allen, C. M., van Lier, J. E., *Photodynamic therapeutics: basic principles and clinical applications*. Drug Discovery Today, 1999. 4:507-517.
15. Gerber, D. E., *Targeted tharapy: a new generation of cancer treatments*. American Family Physician, 2008. 77:311-319.
16. Calin, P., Parasca, S. V., *Photodynamic therapy in oncology*. Journal of Optoelectronics and Advanced Materials, 2006. 8:1173 - 1179.

17. Zhang, L., Zhou, W., Velculescu, V. E. *et.al, Gene expression profiles in normal and cancer cells*. Science, 1997. 276:1268-1272.

18. Rowinsky, E.K., *The erbB family: targets for therapeutic development against cancer and therapeutic strategies using monoclonal antibodies and tyrosine kinase inhibitors*. Annual Review of Medicine, 2004. 55:433-457.

19. Nielsen, D.L., Andersson, M. and Kamby, C., *HER2-targeted therapy in breast cancer. Monoclonal antibodies and tyrosine kinase inhibitors*. Cancer Treatment Review, 2009. 35:121-136.

20. Lierman, E., Lahortiga, I., Van Miegroet, H., *et al., The ability of sorafenib to inhibit oncogenic PDGFRbeta and FLT3 mutants and overcome resistance to other small molecule inhibitors*. Haematologica, 2007. 92:27-34.

21. Peres, J., *Recent studies show promise for treating rare pancreatic tumors*. Journal of the National Cancer Institute. 2011. 103:624-627.

22. Shah, N.P., Tran, C., Lee, F. Y., *et al., Overriding imatinib resistance with a novel ABL kinase inhibitor.* Science, 2004. 305:399-401.

23. Araujo, J.C., Trudel, G. C., Paliwal, P., *Long-term use of dasatinib in patients with metastatic castration-resistant prostate cancer after receiving the combination of dasatinib and docetaxel*. Cancer menagment and research, 2013. 5:25-30.

24. Reya, T., Morrison, S. J., Clarke M. F., et al., Stem cells, cancer, and cancer stem cells. Nature, 2001. 414:105-111.

25. Houghton, J., Morozov, A., Smirnova, I., *et al, Stem cells and cancer*. Seminars in Cancer Biology, 2007. 7:191-203.

26. Dontu, G., Abdallah, W. M., Foley, J. M., *et al., In vitro propagation and transcriptional profiling of human mammary stem/progenitor cells*. Genes and Development, 2003. 17:1253-1270.

27. Lewin, B., ed. *Il gene VIII. ed.* Zanichelli, 2006. 881-925.

28. Weinberg, R.A., *The retinoblastoma protein and cell cycle control*. Cell, 1995. 81:323-330.

29. Hitomi, M., Stacey, D. W., *Cyclin D1 production in cycling cells depends on ras in a cell-cycle-specific manner*. Current Biology, 1999. 9:1075-1084.

30. Ezhevsky, S.A., Nagahara, H., Vocero-Akbani A. M., *et al., Hypo-phosphorylation of the retinoblastoma protein (pRb) by cyclin D:Cdk4/6 complexes results in active pRb*. Proceeds of the National Academy of Science U.S.A.,1997. 94:10699-10704.

31. Giacinti, C., Giordano. A., *RB and cell cycle progression.* Oncogene, 2006. 25:5220-5227.

32. Brown, V.D., Phillips, R. A., Gallie, B. L., *Cumulative effect of phosphorylation of pRB on regulation of E2F activity.*Molecular and cellular biology, 1999. 19:3246-3256.

33. Mittnacht, S., *Control of pRB phosphorylation.*, Current Opinion in Genetics and Developement, 1998. 8:21-27.

34. Sun, A., Bagella, L., Tutton, S., *From G0 to S phase: a view of the roles played by the retinoblastoma (Rb) family members in the Rb-E2F pathway.* Journal of Cellular Biochemistry, 2007. 102:1400-1404.

35. Sherr, C.J. and Roberts, J. M., *Inhibitors of mammalian G1 cyclin-dependent kinases.* Genes and Development, 1995. 9:1149-1163.

36. Blagosklonny, M.V. and Pardee, A. B., *The restriction point of the cell cycle.* Cell Cycle, 2002. 1:103-110.

37. Kastan, M.B., Bartek, J., *Cell-cycle checkpoints and cancer.* Nature, 2004. 432:316-323.

38. Abraham, R.T., *Cell cycle checkpoint signaling through the ATM and ATR kinases.* Genes and Development, 2001. 15:2177-2196.

39. Hartwell, L.H., Weinert, T. A., *Checkpoints: controls that ensure the order of cell cycle events.* Science, 1989. 246:629-634.

40. Alberts, J., ed. *Molecular biology of the cell. Fifth Edition.* ed. Garland Science 2008. 1115-1129.

41. Ghobrial, I.M., Witzig, T. E., Adjei, A. A., *Targeting apoptosis pathways in cancer therapy.* CA A Cancer Journal of Clinitians, 2005. 55:178-194.

42. Boyer, M.J., *Apoptosis: the beginning of the end.* [cited; Available from: http://www.mednat.org/cancro/mitDNAoncogenesi.pdf], 2011. 1-40.

43. Alberts, J., ed. *Molecular biology of the cell. Fifth Edition.* ed. Garland Science, 2008. 1115-1129.

44. Yang, X., Khosravi-Far, R., Chang, H. Y., *et al., Daxx, a novel Fas-binding protein that activates JNK and apoptosis.* Cell, 1997. 89:1067-1076.

45. Yang, Y., Zhao, S., Song, J., *Caspase-dependent apoptosis and - independent poly(ADP-ribise) polymerase cleavage induced by transforming growth factor β1.* The International Journal of Biochemistry and Cell Biology, 2003. 36:223-234.

71. Copper, M. P., Tan, B.; Oppelaar, H., *et al., Meta-tetra(hydroxyphenyl)chlorin photodynamic therapy in early-stage squamous cell carcinoma of the head and neck.* Archives of Otolaryngology - Head and Neck Surgery, 2003. 129:709-711.

72. Luksiene, Z., *Photodynamic therapy: mechanism of action and ways to improve the efficiency of treatment.* Medicina (Kaunas), 2003. 12:1137-50.

73. Elmes, R.B.P., *Diquaternised and Ru(II) based polypyridyl conjugates as biological probes and phototherapeutic agents, in Chemistry.* Trinity College Dublin, 2011.

74. Dougherty, T.J., Gomer, C. J., Henderson, B. W. *et al., Photodynamic therapy.* Journal of National Cancer Institute, 1998. 90:889-905.

75. Moore, J.V., Westz, C. M L and Whitehurstyz, C., *The biology of photodynamic therapy.* Physics in Medical Biology, 1997. 42:913-935.

76. Ochsner, M., *Photophysical and photobiological processes in the photodynamic therapy of tumours.* Journal of Photochemistry and Photobiology, 1997. 33:1-18.

77. Chan, W.S., Brasseur, N., La Madeleine, C. *et al., Evidence for different mechanisms of EMT-6 tumor necrosis by photodynamic therapy with disulforated aluminum phthalocyanine or photofrin: tumor cell survival and blood flow.* Anticancer Research, 1996. 16:1887-1892.

78. Niedre, M., Patterson, M. S., Wilson, B. C., *Direct near-infrared luminescence detection of singlet oxygen generated by photodynamic therapy in cells in vitro and tissues in vivo.* Photochemistry Photobiology, 2002. 75:382-91.

79. Buettner, G.R. and Oberlby, L.W., *The apparent production of superoxide and hydroxil radicals by hematoporphyrin and light as seen by spin-trapping.* Elsevier/North -HoNand Biomedical Press, 1980. 121:161-164.

80. Spencer, N.Y., Yan, Z., Boudreau, R. L., *et al., Control of hepatic nuclear superoxide production by glucose 6-phosphate dehydrogenase and NADPH oxidase-4.* Journal of Biological Chemistry, 2011. 286:8977-8987.

81. Bergamo, A., Messori, L., Piccioli, F. *et al., Biological role of adduct formation of the ruthenium(III) complex NAMI-A with serum albumin and serum transferrin.* Investigational New Drugs, 2003. 21:401-411.

82. Levina, A., Mitra, A. and Lay, P. A., *Recent developments in ruthenium anticancer drugs.* Metallomics, 2009. 1:458-470.

83. Khalaila, I., Bergamo, A., Bussy, F., *et al., The role of cisplatin and NAMI-A plasma-protein interactions in relation to combination therapy.* International Journal of Oncology, 2006. 29:261-268.

84. Allardyce, C.S. and Dyson P. J., *Ruthenium in medicine: current clinical uses and future prospects.* Platinum Metals Review., 2001. 45:62-69.

85. Sun, Y., Collins, S. N., Joyce, L. E. *et al., Unusual photophysical properties of a ruthenium(II) complex related to [Ru(bpy)2(dppz)]2+.* Inorganic Chemistry, 2010. 49:4257-4262.

86. Leigh J. K. B., Zaleski, J. M., *Metal complex–DNA interactions: from transcription inhibition to photoactivated cleavage.* Current Opinion in Chemical Biology, 2005. 9:135-144.

87. Elmes, R.B., Erby, M, Cloonan, S., *et al., Quaternarized pdppz: synthesis, DNA-binding and biological studies of a novel dppz derivative that causes cellular death upon light irradiation.* Chem Commun (Camb), 2010. 47:686-688.

88. Phillips, T., Haq, I., Meijer, A. J. H. M., *et al., DNA binding of an organic dppz-based intercalator.* Biochemistry, 2004. 43:13657-13665.

89. Phillips,T., Rajput, C., Twyman, L., *et al., Water-soluble organic dppz analogues—tuning DNA binding affinities,luminescence, and photo-redox properties.* Chemical. Communications, 2005. 14:4327-4329.

90. Detty, M.R., Gibson, S. L. and Wagner, S. J., *Current Clinical and Preclinical Photosensitizers for Use in Photodynamic Therapy.* American Chemical Society, 2004. 47:3897-3915.

91. Friedman, A., Chambron, J. C., Sauvage, J. P., et al., Molecular ''Light Switch" for DNA Ru(bpy)2(dppz)2+. Journal of American Chemistry Society, 1990. 112:4960-4962.

92. Barton, J.K., *Targeting DNA sites with chiral metal complexes.* Pure and Applied Chemistry, 1989. 61:563-564.

93. Zhang, J., Wong, K. L,Wong, W. K., *et al., .Two-photon induced luminescence, singlet oxygen generation, cellular uptake and photocytotoxic properties of amphiphilic Ru(II) polypyridyl-porphyrin conjugates as potential bifunctional photodynamic therapeutic agents.* Organic and Biomolecular Chemistry, 2011. 9:6004-6010.

94. Chen, T., Liu, Y., Zheng, W. J., *et al., Ruthenium polypyridyl complexes that induce mitochondria-mediated apoptosis in cancer cells.* Inorganic. Chemistry, 2010. 49:6366-6368.

95. Dyson, P.J. and Sava G., *Metal-based antitumour drugs in the post genomic era.* Dalton Transactions, 2006. 28:1929-1933.

96. Fernandez-Moreira, V., Thorp-Greenwood, F. L., Coogan, M. P., *Application of d6 transition metal complexes in fluorescence cell imaging.* Chemical Communications (Camb), 2010. 96:186-202.

97. Crossley, M. J., Hambley, T. W., Mackay, L. G., *et al., Porphyrin Analogues of Troger's Base: Large Chiral Cavities with a Bimetallic Binding Site.* Journal of Chemistry Society, Chemical Communications, 1995. 1077-1079

98. Svensson, F.R., Andersson, J., Åmand, H. L., *et al., Effects of chirality on the intracellular localization of binuclear ruthenium(II) polypyridyl complexes.* Journal of Biology and Inorganic Chemistry, 2012. 17:565-571.

99. Gill, M.R., Garcia-Lara, J., Foster, S. J., *et al., A ruthenium(II) polypyridyl complex for direct imaging of DNA structure in living cells.* Nature Chemistry, 2009. 1:662-667.

100. Veale, E.B., Frimannsson, D. O., Lawler, M. *et al., 4-Amino-1,8-naphthalimide-based Tröger's bases as high affinity DNA targeting fluorescent supramolecular scaffolds.* Organic Letters, 2009. 11:4040-4043.

101. Hingorani, R., Deng, J., Elia, J. *et al., Detection of apoptosis using the BD Annexin V FITC assay on the BD FACSVers System*. Bioscience BD, [cited; Available from: http://www.bdbiosciences.com/documents/BD_FACSVerse_Apoptosis_Detection_AppNote.pdf], 2011. 1-12.

102. Qian, Y., Zhou, X., Liang, M., *et al., The altered activity of complex III may contribute to the high penetrance of Leber's hereditary optic neuropathy in a Chinese family carrying the ND4 G11778A mutation.* Mitochondrion, 2011. 11:871-877.

103. Dubikovskay, E., P*roject 1: Development of new tools for probing mitochondrial activity in cells and living animals*. Ecole polytechnique fédérale de Lausanne, [cited; Available from: http://lcbim.epfl.ch/research], 2012.

104. Thermo Scientific, *Mitochondria Isolation Kit for Cultured Cells*, [cited; Available from: http://www.piercenet.com/instructions/2161477.pdf.], 2011. 1-4.

105. Gill, M.R., Thomas, J. A., *Ruthenium(II) polypyridyl complexes and DNA-from structural probes to cellular imaging and therapeutics.* Chemical Society Reviews, 2012. 41:3179-3192.

106. Zhao,Q., Huanga, C. and Li, F., *Phosphorescent heavy-metal complexes for bioimaging.* Chemical Society Reviews, 2011. 40:2508-2524.

107. Puckett, C.A. and Barton, J. K., *Targeting a ruthenium complex to the nucleus with short peptides.* Bioorganic Medical Chemistry, 2010. 18:3564-3569.

108. Feeney, M.M., Kelly, J. M.,Tossi, A. B., *et al., Photoaddition of ruthenium(II)-tris-1,4,5,8-tetraazaphenanthrene to DNA and mononucleotides.* Journal of Photochemistry and Photobiology 1994. 23:69-78.

109. Puckett, C.A., and Barton, J. K., *Methods to explore cellular uptake of ruthenium complexes.* Journal of American Chemistry Society, 2007. 129:46-47.

110. Le Gac, S., Foucart, M., Gerbaux, P., *et al., Photo-reactive Ru(II)-oligonucleotide conjugates: influence of an intercalating ligand on the inter- and intra-strand photo-ligation processes.* Dalton Transactions, 2010. 39:9672-9683.

111. Brabec, V. and Nováková O., *DNA binding mode of ruthenium complexes and relationship to tumor cell toxicity.* Drug Resistance Update, 2006. 9:111-122.

112. Ferreira, S. D. R. M., Tedesco, A. C., Sousa,G., *et al., Analysis of mitochondria, endoplasmic reticulum and actin filaments after PDT with AlPcS4.* Lasers in Medical Science, 2004. 18:207-212.

113. Kim, S., Kim, H. Y., Lee, S., *et al., Hepatitis B virus x protein induces perinuclear mitochondrial clustering in microtubule- and Dynein-dependent manners.* Journal of Virology 2007. 4:1714-1726.

114. Marques Adade, C. and Souto-Padrón, T., *Contributions of Ultrastructural Studies to the Cell Biology of Trypanosmatids: Targets for Anti-Parasitic Drugs.* The Open Parasitology Journal, 2010. 4:178-187.

115. Cloonan, S.M. and Williams, D.C., *The antidepressants maprotiline and fluoxetine induce Type II autophagic cell death in drug-resistant Burkitt's lymphoma.* International Journal of Cancer, 2011. 128:1712-1723.

116. Yashima, E., Akashi, M., Miyauchi, N., *Chiral bis-(1, 10-phenanthroline) with Tröger's base skeleton. Synthesis and interaction with DNA.* Chemistry Letters, 1991. 6:1017-1020.

117. Van Gijte, O., Tatibouët, A., Demeunynck, M., *et al., A phenanthroline analogue of Tröger's base as bridging ligand in the synthesis of a bimetallic ruthenium (II) complex.* Tetrahedron Letters, 1997. 38:1567-1570.

118. Bresson, C., Luhmerb, M., Demeunynckc, M., *et al., The diastereoisomeric forms of a mononuclear Ru(II) complex bearing a bis-phenanthroline Tröger's base.* Tetrahedron Letters, 2004. 45:2863-2866.

119. Claessens, N., Pierard, F., Bresson, C., *et al., Optically active Ru(II) complexes with a chiral Tröger's base ligand and their interactions with DNA.* Journal of Inorganic Biochemistry, 2007. 101:987-996.

120. Veale, E.B., Gunnlaugsson, T., *Synthesis, photophysical, and DNA binding studies of fluorescent Troger's base derived 4-amino-1,8-naphthalimide supramolecular clefts.* Journal of Organic Chemistry, 2010. 75:5513-5525.

121. Beljanski, V., Marzilli, L. G., Doetsch, P. W., *DNA damage-processing pathways involved in the eukaryotic cellular response to anticancer DNA cross-linking drugs.* Molecular Pharmacology, 2004. 65:1496-1506.

122. Bullock, S.K., Kaufmann, W. K., Cordeiro-Stone, M., *Enhanced S phase delay and inhibition of replication of an undamaged shuttle vector in UVC-irradiated xeroderma pigmentosum variant.* Carcinogenesis, 2001. 22:233-241.

123. Simon, J.A., Szankasi, P., Nguyen, D. K., *et al., Differential toxicities of anticancer agents among DNA repair and checkpoint mutants of Saccharomyces cerevisae1.* Cancer research, 2000. 60:328-333.

124. Smith, P.J., Soues, S., Gottlieb, T., *et al., Etoposide-induced cell cycle delay and arrest-dependent modulation of DNA topoisomerase II in small-cell lung cancer cells.* British Journal of Cancer, 1994. 70:914-921.

125. Juarranz, A., Espada, J., Stockert, J. C., *et al., Photodamage induced by Zinc(II)-phthalocyanine to microtubules, actin, alpha-actinin and keratin of HeLa cells.* Photochemistry and Photobiology, 2001. 73:283-289.

126. Kessel, D., Luo, Y., *Mitochondrial photodamage and PDT-induced apoptosis.* J Photochemistry and Photobiology B, 1998. 42:89-95.

127. Varadi, A., Johnson-Cadwell, L. I., Cirulli, V., *et al., Cytoplasmic dynein regulates the subcellular distribution of mitochondria by controlling the recruitment of the fission factor dynamin-related protein-1.* Journal of Cell Science, 2004. 117:4389-4400.

128. Hammesfahr, B., Kollmar, M., *Evolution of the eukaryotic dynactin complex, the activator of cytoplasmic dynein.* BioMed Central Evolutionary Biology, 2012. 12:1471-2148.

129. Schmidt-Erfurth, U. and Hasan, T.; Weinreb, R., *Mechanisms of Action of Photodynamic Therapy with Verteporfin for the Treatment of Age-Related Macular Degeneration.* Survey of Ophthalmology, 2000. 45:1-20.

130. Liang, H., Do, T., Kasravi, S., *et al., Chromosomes are target sites for photodynamic therapy as demonstrated by subcellular laser microirradiation.* Photochemistry and Photobiology B: Biology, 2000. 54:175-184.

131. Granville, D.J., Cassidy, B. A., Ruehlmann, D. O., *et al., Mitochondrial release of apoptosis-inducing factor and cytochrome c during smooth muscle cell apoptosis.* American Journal of Pathology, 2001. 159:305-311.

132. Listserv, N. *Comet assay interest group.* [cited; Available from: http://www.cometassay.com/index_files/Page345.htm].

133. Brand, M.D., Nicholls, D. G., *Assessing mitochondrial dysfunction in cells.* Biochemical Journal, 2011. 435:297-312.

134. Ryan, G.J., Quinn, S, Gunnlaugsson, T., *Highly Effective DNA Photocleavage by Novel "Rigid" Ru(bpy)3-4-nitroand-4-amino-1,8-naphthalimide Conjugates.* Inorganic Chemistry, 2008. 47:401-403.